



# Parametric study of nucleate boiling in the prototypical condition of a PWR : design and construction of an experimental setup

Louise Bernadou

## ► To cite this version:

Louise Bernadou. Parametric study of nucleate boiling in the prototypical condition of a PWR : design and construction of an experimental setup. Génie civil nucléaire. Université Grenoble Alpes [2020-..], 2023. English. NNT : 2023GRALI023 . tel-04137577

**HAL Id: tel-04137577**

<https://theses.hal.science/tel-04137577>

Submitted on 22 Jun 2023

**HAL** is a multi-disciplinary open access archive for the deposit and dissemination of scientific research documents, whether they are published or not. The documents may come from teaching and research institutions in France or abroad, or from public or private research centers.

L'archive ouverte pluridisciplinaire **HAL**, est destinée au dépôt et à la diffusion de documents scientifiques de niveau recherche, publiés ou non, émanant des établissements d'enseignement et de recherche français ou étrangers, des laboratoires publics ou privés.

THÈSE

Pour obtenir le grade de

**DOCTEUR DE L'UNIVERSITÉ GRENOBLE ALPES**

École doctorale : I-MEP2 - Ingénierie - Matériaux, Mécanique, Environnement, Energétique, Procédés, Production

Spécialité : MEP : Mécanique des fluides Energétique, Procédés

Unité de recherche : CEA Cadarache

**Etude paramétrique de l'ébullition nucléée en condition prototypique d'un REP: dimensionnement et réalisation d'une maquette expérimentale**

**Parametric study of nucleate boiling in the prototypical condition of a PWR: design and construction of an experimental setup**

Présentée par :

**Louise BERNADOU**

**Direction de thèse :**

Henda DJERIDI  
PROFESSEURE DES UNIVERSITES, Université Grenoble Alpes  
Stéphane BARRE  
CHARGE DE RECHERCHE HDR, Université Grenoble Alpes  
Fabrice FRANCOIS  
CEA  
Manon BOTTIN  
CEA

Directrice de thèse  
Co-encadrant de thèse  
Co-encadrant de thèse  
Co-encadrante de thèse

**Rapporteurs :**

Michel GRADECK  
PROFESSEUR DES UNIVERSITES, Université de Lorraine  
Rémi REVELLIN  
PROFESSEUR DES UNIVERSITES, INSA Lyon

**Thèse soutenue publiquement le 28 avril 2023, devant le jury composé de :**

Henda DJERIDI  
PROFESSEUR DES UNIVERSITES, Grenoble INP  
Michel GRADECK  
PROFESSEUR DES UNIVERSITES, Université de Lorraine  
Rémi REVELLIN  
PROFESSEUR DES UNIVERSITES, INSA Lyon  
Yves DELANNOY  
PROFESSEUR DES UNIVERSITES, Grenoble INP  
Lounes TADRIST  
PROFESSEUR DES UNIVERSITES, Aix-Marseille Université

Directrice de thèse  
Rapporteur  
Rapporteur  
Président  
Examinateur

**Invités:**

Stéphane BARRE  
CHARGE DE RECHERCHE HDR, Université Grenoble Alpes  
Fabrice FRANCOIS  
CEA  
Manon BOTTIN  
CEA



# Remerciements

Tout d'abord, je tiens à remercier M. Rémi Revellin, professeur à l'INSA Lyon, ainsi que M. Michel Gradeck, professeur de l'Université de Lorraine, d'avoir accepté de rapporter mon manuscrit de thèse. Je remercie également M. Lounes Tradist, professeur à l'IUSTI, ainsi que M. Yves Delannoy, directeur de recherche au LEGI, d'avoir accepté d'examiner mon travail en tant qu'examinateur et président du Jury.

Je remercie bien évidemment mes directeurs de thèse, Mme Henda Djeridi, professeure à Grenoble INP et M. Stéphanne Barre, chercheur au LEGI à Grenoble pour leur bonne humeur et leurs conseils tout le long de ces presque quatre années laborieuses.

Je tiens particulièrement à remercier M. Rugieri, directeur de l'institut IRESNE au CEA, pour son soutien et pour m'avoir redonné confiance et enthousiasme pour la fin de ces travaux de thèse.

Je remercie également Jean Peybernes, directeur du laboratoire LTHC au CEA Cadarache, qui m'a accueilli pendant ces quatre années de stage et doctorat.

Comment éviter Fabrice François, qui m'a embarqué dans cette histoire, ces années au CEA auront été mouvementées mais il faut bien avouer que cela aura été une sacrée aventure ! Au milieu des blagues douteuses et des débats sur la manière d'effectuer un coffrage, je retiendrai les longues conversations sur le sens de la vie et du travail. Entre les modèles de Unal et les travaux du MIT, on a toujours su trouver le temps pour débattre et échanger, avec tes explications, tout semble facile en thermohydraulique. Merci pour ces presque quatre années passées ensemble. Cela n'aurait pas été pareil sans toi, tu as toujours su me guider et me remotiver même quand cela semblait impossible. Fini la jeune padawan, je pars pour de nouvelles aventure avec la force !

Manon, Manouche, je garderai ta bonne humeur et ton optimisme à toute épreuve même quand la maquette ne les passe pas (les épreuves mwahaha). Merci pour tout ces moments joyeux et animés à chercher des solutions quand je n'en voyais plus, merci d'avoir été là en soutien et pour me redonner de l'énergie quand j'étais en rade, je ne sais pas comment j'aurais pu traverser cette fin de thèse sans toi !

A la dream team de thésards, stagiaires, alternants, qui se sont succédés pendant ces quatre années sur la plateforme Poséidon : Chun-hui, Mathieu, Mira, Vivien, Maxime, Justine, Baptiste, Léna, Gaëlle et j'en oublie... Merci pour tous ces bons moments, ces fou rires et ces repas à 11h30 à la cantine parce qu'on est affamés.

Me co-bureaux préférés: Naz tout d'abord, qui nous a montré la voie et nous a préparé à ce que serait cette dernière année fatidique ! Je n'oublierai jamais les pauses sur la panic-box, les disques durs qui explosent en fin de rédaction, les photos, repas, soirées. Mes co-doctorants de l'enfer, Benjamin et Lorenzo, on a commencé ensemble on finit ensemble et je suis extrêmement fière de nous ! Merci pour les repas, les apéros et cette année passée à organiser des afterworks ensemble avec l'ASTHEC. La galère ça rapproche toujours et c'est

mieux quand on trouve des amis pour la traverser !

Merci à tous mes collègues qui m'ont accompagné et qui ont participé de près ou de loin à cette aventure, merci pour votre aide, les pauses café et les bonnes rigolades : Valérie, Jérôme, Estelle, Lionel, Guillaume, Stéphanie, Ludo, Mathieu, Mimi, Thibaut, Romu, Sylvain...

Merci à ma famille et à mes amis, toujours présents tout au long de cette grande étape de ma vie. Une thèse se construit aussi à partir du soutien qu'on trouve en dehors du travail. C'est une expérience qui prend de la place sur tout le reste et donc merci à tous d'être toujours au rendez-vous.

Anthro, je t'aime, merci d'être toi et de m'apporter autant.

## Summary in French

L'ébullition est un phénomène qui peut survenir en réacteur en conditions de fonctionnement normal ou incidentel. Dans ce dernier cas, elle peut conduire à l'apparition de la crise d'ébullition dont les mécanismes sont aujourd'hui encore non déterminés.

Le sujet proposé concerne donc la caractérisation de l'ébullition nucléée depuis l'apparition de la première bulle (Onset of Nucleate Boiling - ONB) jusqu'à l'apparition de la crise d'ébullition dans un spectre de pression large allant de la pression atmosphérique jusqu'à la pression du circuit primaire (155 bar). En effet, il semble d'après la littérature qu'il existe un changement de structure d'écoulement autour de 70 bar, l'écoulement devenant émulsif.

On s'intéressera en particulier à l'étude du couplage entre les phénomènes thermiques dans la paroi et l'écoulement dans la zone de proche paroi (taille de bulles au détachement, fréquence de détachement, taux de vide à la paroi...). Ce travail vise au final à fournir des données relatives aux différents modèles d'ébullition susceptibles d'être utilisés dans les outils de calculs numériques de type CFD.

La méthodologie qu'on se propose d'utiliser dans ce travail repose sur la conception d'un dispositif expérimental qui devra permettre une visualisation directe de l'écoulement diphasique bouillant couplée à une caractérisation du champ de température de l'élément chauffant de ce dispositif.

La caractérisation thermique devant se faire par thermographie Infra-Rouge couplée à une méthode inverse (permettant de remonter de la température mesurée à l'extérieur de la veine d'essais à la température mouillée), la détermination des caractéristiques géométriques de l'élément chauffant (en particulier son épaisseur) est donc primordiale. Une étude poussée s'appuyant sur une approche mono et bidimensionnelle de la thermique de paroi a donc été réalisée. L'originalité de celle-ci repose sur la prise en compte de conditions aux limites inhomogènes en temps et en espace afin de pouvoir simuler l'ébullition au droit de la plaque. Ce travail a permis de dimensionner l'élément chauffant afin qu'il soit d'un part représentatif du dispositif industriel (en terme d'inertie thermique et d'état de surface) et d'autre part qu'il permette les mesures souhaitées respectant une précision cible.

La visualisation dans le domaine visible a constitué un second pan important de ce travail. Elle se fera grâce à une caméra rapide (28000 i/s) couplée à des objectifs de haute précision et un éclairage performant en observant l'écoulement à travers des hublots transparents en saphir. On s'est en particulier attaché à déterminer et optimiser l'instrumentation devant être mise en œuvre afin de réaliser des mesures de précision. On a ainsi montré que l'utilisation d'un objectif bi-télécentrique associé à un montage en ombroscopie permettrait d'obtenir des résultats précis. Un focus particulier a été réalisé sur les effets de distorsion potentiel des images réalisées en proche paroi du fait du gradient d'indice optique résultant du gradient de température dans le liquide. Cette étude a montré que, d'une part, cet effet restait faible compte-tenu que, dans nos conditions d'ébullition sous-saturées, le gradient de température à la paroi reste faible et que, d'autre part, cet effet pouvait se corriger via l'utilisation de mires spécialement conçues (de taille comparable à l'objet mesuré).

Tous ces éléments ont conduit au dimensionnement d'une installation thermohydraulique et à la mise au point d'une maquette d'essais sur laquelle des tests préliminaires ont pu être réalisés.

## Summary in English

Boiling is a phenomenon that can occur in reactors under normal or incidental operating conditions. In the latter case, it can lead to the appearance of a boiling crisis, the mechanisms of which are still not fully understood.

The proposed subject therefore concerns the characterisation of nucleate boiling from the appearance of the first bubble (Onset of Nucleate Boiling - ONB) to the appearance of the boiling crisis over a wide pressure range, from atmospheric pressure to the pressure of the primary circuit of a Pressurised Water Reactor ( $155\text{ bar}$ ). Indeed, the literature indicates that there is a change in flow structure around  $70\text{ bar}$ , with the flow becoming emulsive. The study of the coupling between the thermal phenomena inside the wall and the flow in the near-wall zone (bubble size at detachment, detachment frequency, wall void rate...) is of particular interest. The final aim of this work is to provide data for the various boiling models that can be used in CFD-type numerical simulation tools.

The methodology followed in this work is based on the design of an experimental device allowing a direct visualisation of the boiling two-phase flow coupled with a characterisation of the temperature field of the heating element.

As the thermal characterisation is to be carried out by infrared thermography coupled with an inverse method (allowing the wetted temperature to be deduced from the measured wall temperature), the determination of the geometric characteristics of the heating element (in particular its thickness) is of prime importance. A detailed study based on both one- and two-dimensional approaches to wall thermics is therefore carried out. The originality of this approach lies in the consideration of inhomogeneous boundary conditions in time and space in order to simulate boiling at the plate. This work enabled the heating element to be dimensioned as both representative of the industrial device (in terms of thermal inertia and surface state) and allowing the desired measurements to be made with a target accuracy.

Visualisation in the visible range is a second important aspect of the work. This is done using a high-speed camera ( $28000\text{ fps}$ ), coupled with high-precision lenses and high-performance lighting, by observing the flow through transparent sapphire windows. Focus is placed on determining and optimising the instrumentation to be used to carry out precision measurements. It is shown that the use of a bi-telecentric lens associated with an ombroscopic setup will allow obtaining precise results. The potential distortion effects of near-wall images due to the optical index gradient resulting from the temperature gradient in the liquid is specifically studied. This effort shows that on the one hand, this effect remains weak, given that in our conditions of under-saturated boiling the temperature gradient at the wall is of small magnitude, and that on the other hand, this effect could be corrected via the use of specially designed test patterns (with size comparable to the measured object).

All these elements lead to the design of a thermal-hydraulic installation and the development of a test model on which preliminary tests can be carried out.

# Nomenclature

$q_k$	diffusive heat flux supplied to phase k
$\alpha_k$	Local void fraction for phase k
$\Delta T_{sub}$	Subcooling [ $^{\circ}C$ ]
$\dot{m}$	Mass flow rate [ $kg/s$ ]
$\epsilon$	Emissivity [-]
$\epsilon_l$	Effusivity of liquid water [ $J/Km^2s^{1/2}$ ]
$\Gamma_k$	Interfacial mass transfer term per unit of volume and time
$\lambda_l$	Thermal conductivity of the liquid phase [ $W/mK$ ]
$\overline{\overline{\tau}_k}$	Stress tensor of phase k
$\overline{\overline{\tau}_{k,T}}$	Turbulent stress tensor of phase k
$\Pi_k^E$	Interfacial energy transfer to phase k
$\rho_k$	Density of phase k
$\rho_l$	Liquid density [ $kg/m^3$ ]
$\rho_v$	Vapor density [ $kg/m^3$ ]
$\rho_{l,sat}$	Saturated liquid density [ $kg/m^3$ ]
$\rho_{v,sat}$	Saturated vapor density [ $kg/m^3$ ]
$\sigma$	Surface tension [ $N/m$ ]
$\sigma_{SB}$	Stephan Boltzmann's constant [ $W/m^2K^4$ ]
$\theta$	Contact angle [ $^{\circ}$ ]
$g$	Resultant of the volumetric forces of external origin
$I_{k,i}$	Interfacial momentum transfer to phase k without pressure contribution and mass transfer contribution
$q_{k,T}$	turbulent heat flux supplied to phase k

$V_k$	Local average velocity of phase k
$A$	Amplitude of the thermal disturbance in the area of influence of a bubble [ $^{\circ}C$ ]
$C_f$	Friction factor [-]
$d$	Size of the area of influence of a bubble [m]
$D_B$	Bubble departure diameter [m]
$D_H$	Hydraulic diameter [m]
$E_k$	Average total energy of phase k
$f$	Bubble departure frequency [ $s^{-1}$ ]
$G$	Mass velocity [ $kg/m^2s$ ]
$g$	Gravity [ $m/s^2$ ]
$h_c$	Single-phase convective heat transfer coefficient [ $W/m^2.^{\circ}C$ ]
$h_{fg}$	Latent heat of evaporation [J/kg]
$h_{l,in}$	Entry liquid enthalpy [J/kg]
$I$	Intensity [A]
$K$	Area influence factor [-]
$L_c$	Characteristic length [m]
$M$	Exitance [ $W/m^2$ ]
$N''$	Nucleation site density per unit of area [ $m^{-2}$ ]
$n$	Number of time steps [-]
$N_x$	Number of grid cells in x [-]
$N_y$	Number of grid cells in y [-]
$Nu$	Nusselt number [-]
$P$	Pressure [bar]
$Pe$	Peclet number [-]
$Pr$	Prandtl number [-]
$q_c''$	Single-phase convective heat flux [ $W/m^2$ ]
$q_e''$	Evaporation heat flux [ $W/m^2$ ]
$q_q''$	Quenching heat flux [ $W/m^2$ ]

$Re$	Reynolds number [-]
$St$	Stanton number [-]
$T_l$	Liquid temperature [ $^{\circ}C$ ]
$T_w$	Wall temperature [ $^{\circ}C$ ]
$T_{sat}$	Saturation temperature [ $^{\circ}C$ ]
$t_{sl}$	Sliding time of a bubble on the wall [s]
$W$	Thermal power transferred to the fluid [W]
$x_{eq}$	Equilibrium quality [-]
$Y_B^+$	Dimensionless distance between the top of the bubble and the wall [-]
$\alpha$	Thermal diffusivity [ $m^2/s$ ]
$\lambda$	Thermal conductivity of the heater material [ $W/mK$ ]
$\omega$	Pulsation [ $s^{-1}$ ]
$\bar{\theta}$	Adimensional temperature [-]
$\bar{\theta}_\infty$	Infinite condition of adimensional temperature [-]
$\bar{\theta}_{init}$	Initial adimensional temperature [-]
$\bar{\theta}_{wall}$	Adimensional temperature at the boundary [-]
$\rho$	Density of the heater material [ $kg/m^3$ ]
$C_P$	Thermal capacity of the heater material [ $J/K$ ]
$h_{l,sat}$	Liquid enthalpy at saturation [ $J/kg$ ]
$h_l$	Liquid enthalpy [ $J/kg$ ]
$L$	Length [m]
$l$	Width [m]
$q''$	Heat flux [ $W/m^2$ ]
$q'''$	Volumic heat source [ $W/m^3$ ]
$T$	Temperature [ $^{\circ}C$ ]
$t$	Time [s]
$T_0$	Steady state temperature [ $^{\circ}C$ ]
$T_{d,dry}$	Dry side temperature, direct calculation [ $^{\circ}C$ ]

$T_{d,initial}$  Initial temperature of the direct problem [ $^{\circ}C$ ]

$T_{d,wet}$  Wetted side temperature, direct calculation [ $^{\circ}C$ ]

$T_{dry}$  Dry side temperature [ $^{\circ}C$ ]

$t_g$  Growing time [s]

$T_H$  Higher temperature [ $^{\circ}C$ ]

$T_{i,dry}$  Dry side temperature, inverse calculation [ $^{\circ}C$ ]

$T_{i,initial}$  Initial temperature of the inverse problem [ $^{\circ}C$ ]

$T_{i,wet}$  Wetted side temperature, inverse calculation [ $^{\circ}C$ ]

$T_L$  Lower temperature [ $^{\circ}C$ ]

$T_{wet}$  Wetted side temperature [ $^{\circ}C$ ]

$t_w$  Waiting time [s]

$x$  Space direction [m]

$x_{eq}$  Equilibrium quality [-]

$y$  2D space direction [m]

$y_0$  Position of a nucleation site [m]

# Contents

<b>I Scope of the study</b>	<b>21</b>
<b>1 State of the art</b>	<b>23</b>
1.1 Scope of this study . . . . .	23
1.2 Nucleate boiling experiments . . . . .	28
1.3 High pressure data . . . . .	32
1.4 Work in progress . . . . .	39
<b>2 Litterature survey regarding nucleate boiling for forced convective flows</b>	<b>45</b>
2.1 Boiling flow study . . . . .	45
2.1.1 Single-phase heat transfer coefficient . . . . .	45
2.1.2 Correlations for ONB . . . . .	46
2.1.3 Correlations for OSV . . . . .	47
2.1.4 Correlations for $q''_{CHF}$ . . . . .	49
2.2 Boiling modeling . . . . .	53
2.2.1 Interface modelisation . . . . .	53
2.2.2 Correlations . . . . .	53
2.2.3 Orders of magnitude analysis for our study . . . . .	64
2.3 Conclusion and pre-designing . . . . .	76
<b>II Design and dimensioning of the experiment</b>	<b>77</b>
<b>3 Thermal hydraulic installation</b>	<b>79</b>
3.1 Framework . . . . .	79
3.2 Piping and Instrumentation Diagram . . . . .	79
3.3 Design and manufacture . . . . .	82
<b>4 Test section</b>	<b>87</b>
4.1 Technical requirements . . . . .	87
4.2 Test section design . . . . .	96
<b>5 Heater design</b>	<b>103</b>
5.1 Scope of the study . . . . .	103
5.1.1 Previous work . . . . .	103
5.1.2 Reminder of the problem . . . . .	108
5.2 Thermal study of the heater . . . . .	112
5.2.1 Methodology . . . . .	112

5.2.2	Direct Problem Modeling . . . . .	113
5.2.3	Inverse problem . . . . .	120
5.3	Spatial resolution of the measurements . . . . .	125
5.3.1	2D diffusion influence . . . . .	125
5.3.2	Thermal influence area of a bubble growth . . . . .	129
5.3.3	Discretization between two bubbles growing on the plate . . . . .	133
5.4	Influence of the boundary condition on the dry side . . . . .	135
5.5	Conclusion for the heater design . . . . .	138
5.6	Power supply for direct Joule heating . . . . .	139
5.6.1	Onset of Nucleate Boiling power . . . . .	139
5.6.2	Onset of Significant Void power . . . . .	141
5.6.3	Critical heat flux limit . . . . .	141
5.6.4	Power supply design . . . . .	142
<b>6</b>	<b>Instrumentation selection</b>	<b>143</b>
6.1	Shadowgraphy . . . . .	144
6.2	Reduced experimental setup . . . . .	152
6.3	First test campaign: shadowgraphy . . . . .	153
6.3.1	First test presentation . . . . .	153
6.3.2	Choice of optical assembly: lens and lighting . . . . .	153
6.3.3	Validation of the acquisition frequency and shutter time . . . . .	158
6.3.4	Evaluation of the influence of the thermal gradient . . . . .	160
6.3.5	Other comments . . . . .	161
6.3.6	First attempts at image processing . . . . .	162
6.3.7	First campaign conclusions . . . . .	167
6.4	Second test campaign: thermal gradient influence . . . . .	168
6.4.1	Second test presentation . . . . .	168
6.4.2	Transition from transient to steady state . . . . .	170
6.4.3	Deformation zone . . . . .	175
6.4.4	Impact of deformation on objects . . . . .	179
6.4.5	Effect of the thickness of hot water passed through . . . . .	181
6.4.6	Second campaign conclusions . . . . .	184
6.5	Infrared thermography . . . . .	185
6.5.1	Literature review on infrared thermography . . . . .	186
6.5.2	Strategy for IR thermography implementation . . . . .	194
<b>III</b>	<b>Experimental design and testing</b>	<b>195</b>
<b>7</b>	<b>Preparation of the experiments</b>	<b>197</b>
7.1	Test matrix . . . . .	197
7.2	Modified test facility . . . . .	197
7.2.1	Design . . . . .	199
7.2.2	Assembly and problems . . . . .	204
7.3	Back-up plan . . . . .	209
7.3.1	Design . . . . .	209
7.3.2	Hydraulic test . . . . .	216

7.4	New test matrix . . . . .	220
7.5	Test campaign . . . . .	222



# Introduction

Electricity is mainly produced by Nuclear Power Plants in France (nearly 72% of total production). The most widely used reactors are pressurised water reactors (PWR), which account for 85% of the world's installed capacity. A nuclear power plant (see Figure 1) is composed of three independent hydraulic circuits, all of which are supplied with water in the case of the PWR:

- The primary circuit (specified in the diagram Figure 2) where a coolant fluid transfers thermal energy from the nuclear reaction to the secondary circuit fluid through the steam generator.
- The secondary circuit which is mainly composed of a steam generator where water is vaporized, and then overheated using the heat from the primary circuit. The vapor then drives a turbine to produce electricity.
- A third circuit that condenses and cools the secondary circuit's fluid.

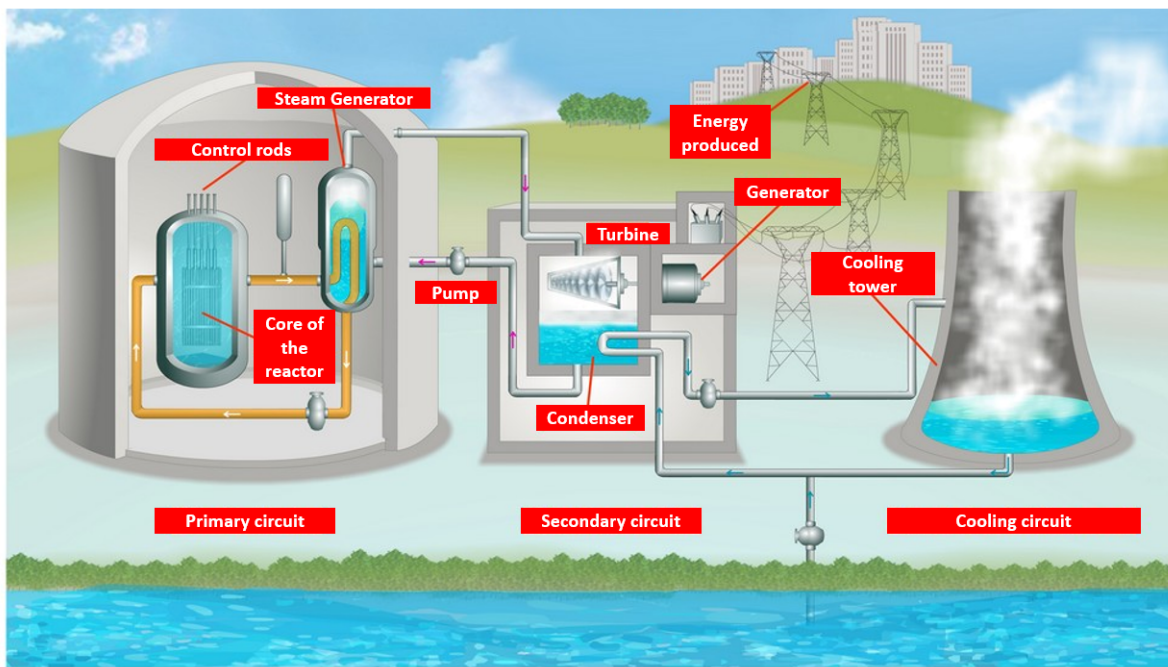


Figure 1: Operating diagram of a PWR-type nuclear installation.

The present work will focus on the primary circuit. PWRs use water as a coolant, under the following operating conditions: 155 bar and 320 °C for pressure and temperature respectively.

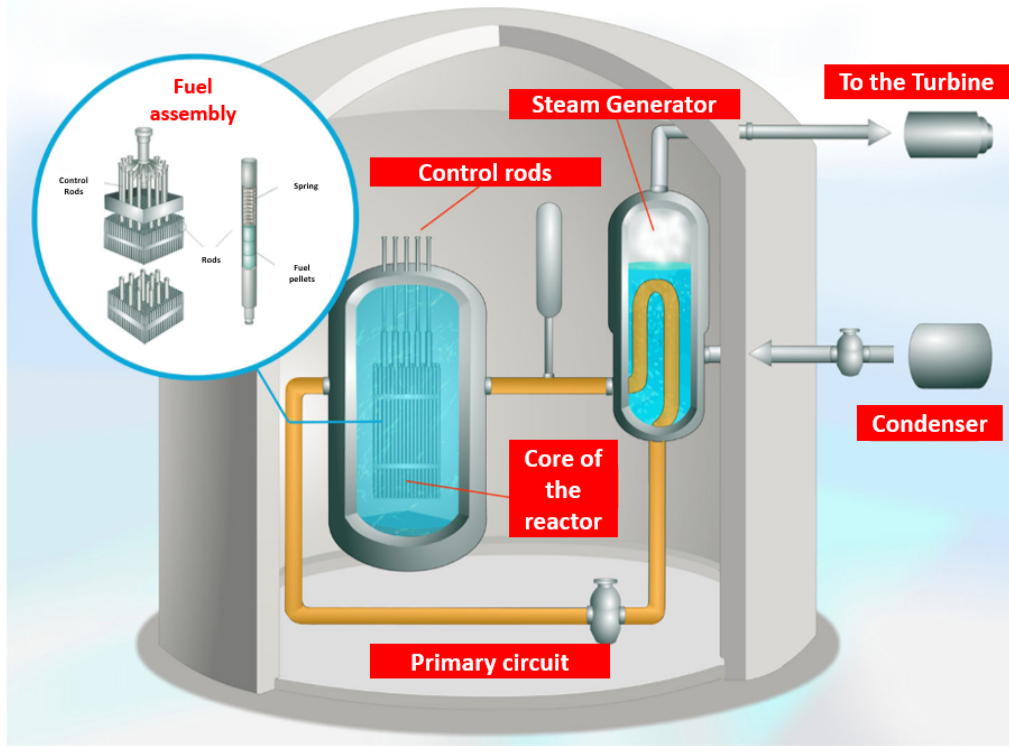


Figure 2: Operating diagram of a PWR primary circuit.

In nominal working conditions, the primary circuit is pressurised so that the coolant remains liquid despite the high temperature. However, under some certain incidental operating conditions (depressurisation, loss of coolant, withdrawal of neutron absorber, etc.), localised boiling may occur on some fuel rods.

Boiling is an efficient heat transfer method due to the creation of bubbles at the wall: the vaporisation of the fluid evacuates part of the energy and allows the wall temperature to remain constant. In addition, these bubbles create turbulence, which increases the efficiency of heat transfer.

However, this heat exchange can break down abruptly: a layer of vapour forms on the wall and thermally isolates it from the surrounding liquid. The temperature of the rod then increases rapidly (several hundred degrees per second due to the high heat source and low heat transfer coefficient), which can lead to its melting<sup>1</sup>. This phenomenon is called a boiling crisis (DNB - Departure from Nucleate Boiling).

Being able to characterise and predict the conditions leading to the occurrence of DNB is thus a major requirement for deploying and maintaining PWRs.

Nukiyama [1] has characterised the different heat transfer processes. His experimental set-up is made of a metallic wire (Tin and Nickel) immersed in saturated water (see Figure 3). The wire is heated by direct Joule effect and the wire temperature is deduced from its electrical resistance measurement.

---

<sup>1</sup>In PWR's operating conditions, heat fluxes can be high as several  $MW/m^2$ .

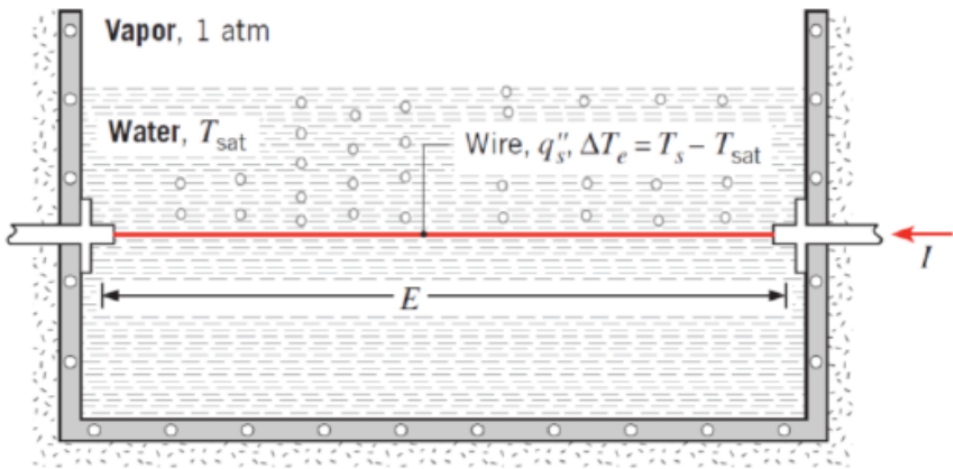
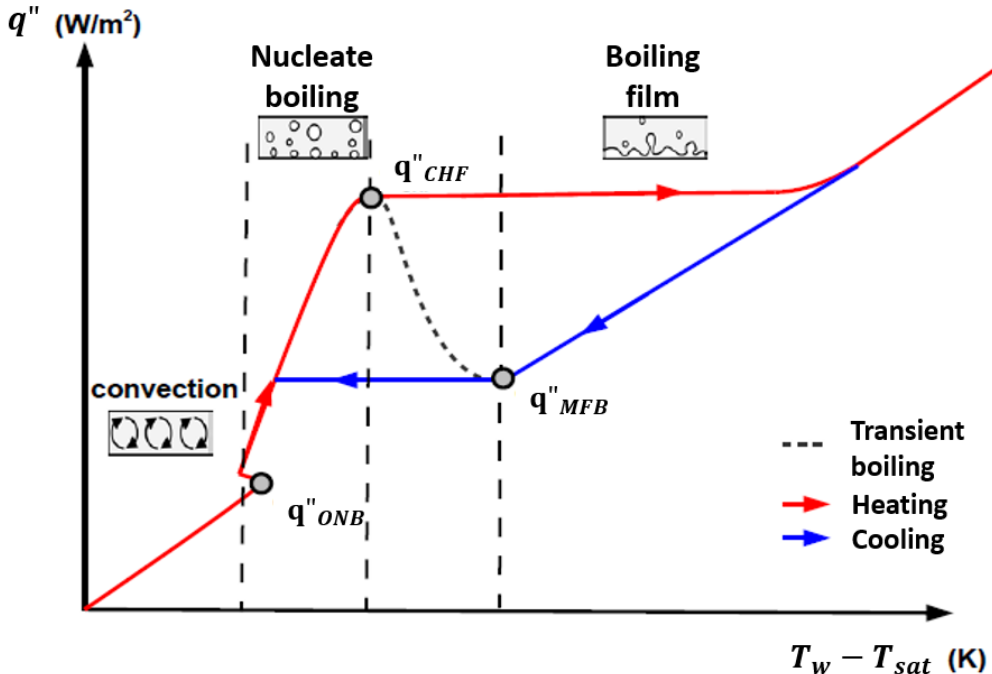


Figure 3: Nukiyama [1] curve and experiment: description of the different exchange phases of a hot wire dipped in a tank of water.

For low heat flux, the heat transfer mechanism is convection until the heat flux reaches the Onset Nucleate Boiling flux ( $q''_{ONB}$ ), at which boiling begins. As the heat flux increases, the heat transfer coefficient remains almost constant, until the heat flux reaches  $q''_{CHF}$  which is called the critical heat flux. This heat flux corresponds to the triggering of DNB for design as well as safety studies. This phenomenon is characterized by a violent increase in temperature. For safety reasons, it is then of prime importance to be able to predict as accurately as possible the thermal hydraulic conditions that may provoke the boiling crisis.

Up to now the methodology for predicting DNB is based on empirical correlations validated using experimental results. In such correlations the critical heat flux  $q''_{CHF}$  is expressed as a function of thermal hydraulic parameters (e.g. pressure, mass velocity, equilibrium

quality  $x_{eq} = \frac{h_l - h_{l,sat}}{h_{fg}}$ ) the values of which are determined at the boiling crisis occurrence using numerical tools. The current approach consists in using one-dimensional area averaged quantities as input parameters for the correlations. As an illustration, Figure 4 depicts a PWR's subchannel. It is defined as the fluid area located between four heated rods.

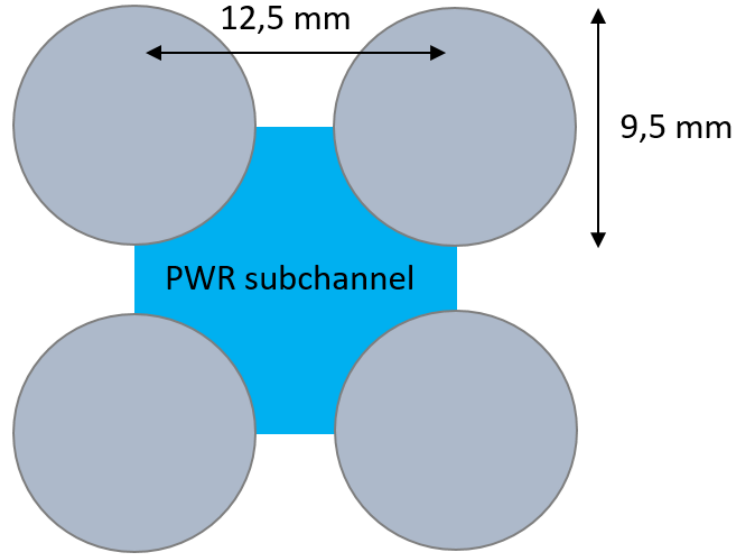


Figure 4: Schematic of a PWR subchannel.

The input parameters for the critical heat flux correlation are then averaged accross this fluid area. Nevertheless, there are at least two main drawbacks that can be underlined:

- Since the correlations are often statistical, it implies that it is difficult not to say dangerous to extrapolate those correlations beyond their range of validity. This means that every change in the design of a nuclear fuel element (geometry, working conditions, ...) implies the development a new correlation. This entails some additional experimental testings which can prove to be very expensive. Indeed, such tests need to be performed in working conditions as close as possible to the ones encountered in a PWR (high pressure, high temperature).
- The second major issue arises from the spatial scale which is used to develop such correlations. Numerous works clearly demonstrate that DNB is a local phenomenom that occurs at the wall and in its close vicinity. It then seems reasonable to assess that a local description<sup>2</sup> of the flow might be more adapted for describing and predicting the DNB. Such an approach has been developped for many years by EDF and CEA ([2], [3]). But to be successful this methodology requires some preliminary conditions, the most important being to be able to accurately determine the "local quantities". It is then necessary to use a computational tool, thoroughly validated in the proper working conditions.

This turns out to be a difficult endeavour for one major reason: whatever the considered scale (spatial, temporal...), validation of a numerical calculation tool requires data obtained

---

<sup>2</sup>Local meaning at CFD scale.

within the targetted domain. Unfortunately, because of the transient and local nature of DNB, such measurements are -up to now- unreachable, especially at CFD scale. A possible way to deal with such a problem is to try to validate the numerical tool for operating conditions as close as possible but prior to DNB triggering. In that sense, this methodology considers the boiling crisis as an expected evolution of the nucleate boiling heat transfer regime.

A classical approach to determine the local quantities is based on using the two-fluid model. A set of balance equations for mass, momentum and energy is obtained by time-averaging the local instantaneous balance equation for each phase. Other equations can also be added such as an interfacial area transport equation. Additional closure relations are needed to solve this set of equations. They mainly concern the interfacial transfer terms for mass, momentum and energy, as well as the modelling of the turbulent fluxes and the wall heat flux partitioning model. This last model is often considered to be one of the most influent model on the performances of the two-fluid model. That is why a survey of the litterature finds many studies related to this topic. Nevertheless, to our knowledge, none of these models has been validated using data prototypical for PWR operating conditions. This point will specifically be developed in the following sections.

The objective of this doctoral work is then to focus on the model of heat flux partitioning for prototypical working conditions of a PWR:

- in terms of range of thermal hydraulic parameters: pressure ranging from 20 to 120 bar, mass flux ranging from 500 to 2000  $kg/m^2.s$ , heat flux density ranging from  $10^5$  to  $10^6 W/m^2$ , equilibrium quality  $x_{eq} \sim 0^-$ ;
- in terms of representativeness of the heater (and especially its surface state). Indeed, some studies ([4]) have shown that the surface roughness of the heater has a strong influence on the boiling phenomenon.

This work will be organised in three sections as follows:

- In Section 1,
  - Chapter 1 will be devoted to a litterature review concerning the heat flux partitioning model and the experiments that are used to validate such a model. This analysis will justify the need for a specific set-up.
  - Chapter 2 will present some correlations and pre-calculus in order to design a new experimental set-up whose description will be given in Section 2.
- In Section 2,
  - Chapter 3 will focus on the thermal hydraulic loop where the future test section is to be implemented.
  - Chapter 4 will provide first elements of the design of the test section.
  - Chapter 5 and 6 will be devoted to the implementation of the instrumentation that will be used to perform the measurements of interest. The first one will focus on thermal measurements which will be performed using IR thermography. A specific study based on an innovative model describing the thermal behaviour of the heater will be introduced. This model will be used to determine the geometry

of the heating system and in particular its thickness. Chapter 6 will focus on the implementation of the shadowgraphic measurement technique and its use for boiling flows.

- In section 3,
  - Chapter 7 will introduce the experimental plan and some preliminary tests including measurements at high pressure.

A general conclusion will draw up the work carried out during this doctoral job and will offer some perspectives on the work still to be done in order to achieve the initial goal of this thesis.

# **Part I**

## **Scope of the study**



# Chapter 1

## State of the art

The aim of this thesis is to characterise nucleate boiling for prototypical thermal hydraulic conditions of a Pressurized Water Reactor (PWR), from the onset of nucleate boiling (ONB) to the triggering of the boiling crisis (DNB). There are several works on the subject. Some consider what happens in boiling flows, while others focus on the study of a nucleation site and the phenomena occurring around a bubble. In this chapter, we will review these experimental investigations to evaluate the existing panel and to identify the gaps that remain to be investigated.

### 1.1 Scope of this study

The boiling crisis is an important issue for the safety of nuclear installations and is considered in the incidental scenarios. The physical origin of this phenomenon is still poorly understood.

Two approaches exist to predict the boiling crisis: **(i)** the correlative approach, based on experiments and the building of a correlation based on variables, presumed to explain the phenomenon, or **(ii)** the modelling approach which involves identifying the physical mechanisms responsible for the boiling crisis. Modelling approaches are not sufficiently mature to date. Questions remain about the mechanisms involved and the scales of the phenomena (time and space). The problem with correlative approaches as stated above is their statistical aspect. Every change of the assembly configuration leads to develop a new correlation and therefore to implement an, often costly, experiment. Up to now, the input parameters are quantities that are 1D area-averaged over a subchannel (Delhaye [5]). This results from the fact that this scale is a good compromise between the accuracy of the codes that calculate those quantities and the accuracy of the flow behaviour description.

A third alternative was presented ([2], [3]), consisting in a correlative approach but replacing the 1D quantities by local quantities (on the CFD scale) to take into account the local character of the boiling crisis: this is the Local Predictive Approach (LPA). Through this approach, researchers hope to extend the domains of validity of the correlations.

This change of scale should theoretically allow a better understanding of the local nature of the phenomenon and in particular the links between the local structure of boiling two-phase flows especially in the vicinity of the heated wall and the onset of the boiling crisis. This approach could also make it possible to limit the need for experiments that are costly and complex to carry out because of the operating conditions (high pressure/high temperature). As the boiling crisis is considered as a transition between nucleate boiling and film boiling,

its characterisation and understanding necessarily relies on specific flow data under critical heat flux conditions. With the LPA, the hope is to be able to identify precursors to the occurrence of the boiling crisis. The LPA is therefore not intended to predict the value of the critical flux for a set of given thermal hydraulic conditions but rather to identify a set of elements that herald the onset of the boiling crisis. The prerequisite for this approach is therefore to have calculation tools qualified at the CFD scale under our operating conditions (known as PWR).

The success of LPA relies on the accurate description of the considered boiling flows. In this study, the focus is put on the phenomenon of nucleate boiling from the appearance of the first bubble (ONB) to the occurrence of the critical heat flux.

Boiling is a physical process impacted, on the one hand, by what happens at the wall, and on the other hand, by what happens in the core of the flow. Three distinct zones can therefore be identified in the boiling flow (see Figure 1.1): the wall, a boiling boundary layer (where boiling starts) and a so-called core zone.

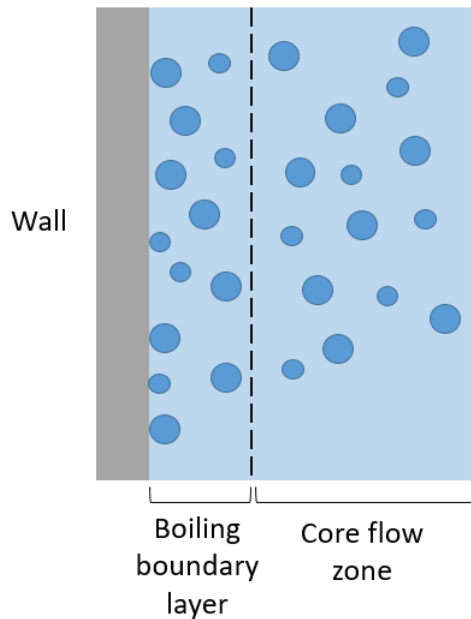


Figure 1.1: Boiling flow zone: wall, boiling boundary layer, core flow zone.

The study of the core flow zone is widely documented in the literature ([6], [7], [8], [9]). On the other hand, the boundary layer zone is less easily studied as boiling is a localised phenomenon in the vicinity of the wall. This study focuses on this area, where the boiling phenomenon arises.

The boundary layer here refers to a zone that can be seen as an interface between the core and the wall and is different from the thermal boundary layer considered for single-phase flows. Characterising the behaviour of the zone of interest therefore requires characterising the flow in this zone but also the boundary conditions in the domains bordering this boundary layer (in particular the wall).

A classic forced convection boiling flow goes through a specific sequence of stages. Let us consider a vertical tube uniformly heated as presented in Figure 1.2. In the lower part of the tube, the flow is a single-phase flow, the heat transfer regime corresponds to forced

convection. The heat transfer coefficient remains almost constant. The temperature of the fluid and the wall increase simultaneously.

When the wall temperature reaches the necessary superheat (above the saturation temperature of the fluid) for the activation of the nucleation sites, bubbles appear. This is called the Onset of Nucleate Boiling (ONB). The flow corresponds to a subcooled boiling regime. The wall temperature stabilises while the fluid temperature is still increasing.

In a second phase, the bubbles gradually detach from the wall and migrate towards the center of the flow. The transition is called the Onset of Significant Void (OSV).

From this point onwards, the bubbles may coalesce to form slugs. Then these slugs may join themselves to reach the annular flow regime. The heat transfer is then forced convection through the liquid film which tends to disappear because of evaporation and arrachement. The complete disappearance of the liquid film leads to a drying out of the wall and a droplet flow takes place. Single phase vapour flow occurs when all droplets have evaporated. The heat exchange is then single-phase convection with vapour phase.

Up to now, the two-fluid model is the reference calculation tool to perform CFD calculation. This model consists in solving the time-averaged local phase balance equations (for each phase: liquid and vapour) to which are added the balance conditions at the interfaces ([11]). NEPTUNE CFD ([3]) is based on those equations.

The mass conservation equation can be defined as:

$$\frac{\partial(\alpha_k \rho_k)}{\partial t} + \nabla \cdot (\alpha_k \rho_k \underline{V}_k) = \Gamma_k \quad (1.1)$$

where  $\alpha_k$  is the local void fraction for k-phase,  $\rho_k$  is the density of phase k,  $\overline{V}_k$  is the local average velocity of phase k and  $\Gamma_k$  is the interfacial mass transfer term per unit of volume and time.

The momentum balance equation can be written as:

$$\frac{\partial \alpha_k \rho_k \underline{V}_k}{\partial t} + \nabla \cdot (\alpha_k \rho_k \underline{V}_k \otimes \underline{V}_k) = \alpha_k \rho_k \underline{g} - \alpha_k \nabla(P) + \Gamma_k \underline{V}_{k,i} + \alpha_k \rho_k \underline{g} + \nabla \cdot (\alpha_k (\overline{\tau}_k + \overline{\tau}_{k,T})) + I_{k,i} \quad (1.2)$$

where  $P$  is the pressure,  $\underline{g}$  the resultant of the volumetric forces of external origin,  $\underline{V}_{k,i}$  is the interfacial velocity,  $\overline{\tau}_k$  and  $\overline{\tau}_{k,T}$  the stress tensor of phase k and the turbulent stress tensor of phase k respectively,  $I_{k,i}$  the interfacial momentum transfer to phase k without pressure contribution and mass transfer contribution.

The total energy balance equation can be written as:

$$\frac{\partial \alpha_k \rho_k E_k}{\partial t} + \nabla \cdot (\alpha_k \rho_k E_k \underline{V}_k) = \nabla \cdot (\alpha_k (\overline{\tau}_k \underline{V}_k - \underline{q}_k - \underline{q}_{k,T})) + \alpha_k \rho_k \underline{g} \cdot \underline{V}_k + \Pi_k^E \quad (1.3)$$

where  $E_k$  is the average total energy of phase k,  $\underline{q}_k$  and  $\underline{q}_{k,T}$  the diffusive heat flux supplied to phase k and the turbulent heat flux supplied to phase k respectively,  $\Pi_k^E$  the interfacial energy transfer to the k-phase.

To be solved, these equations require closure relations such as turbulence modelling, expressions for the interfacial forces as well as interfacial heat transfer. Among these relations, we focused on the heat flux partitionning model at the wall which describes the distribution of the wall heat flux between liquid and vapor phases. According to us, as this model acts as a boundary condition, it seems reasonable to begin with understanding this physical phenomenon before studying the impact of closure laws for example on the core flow behaviour, such as turbulence.

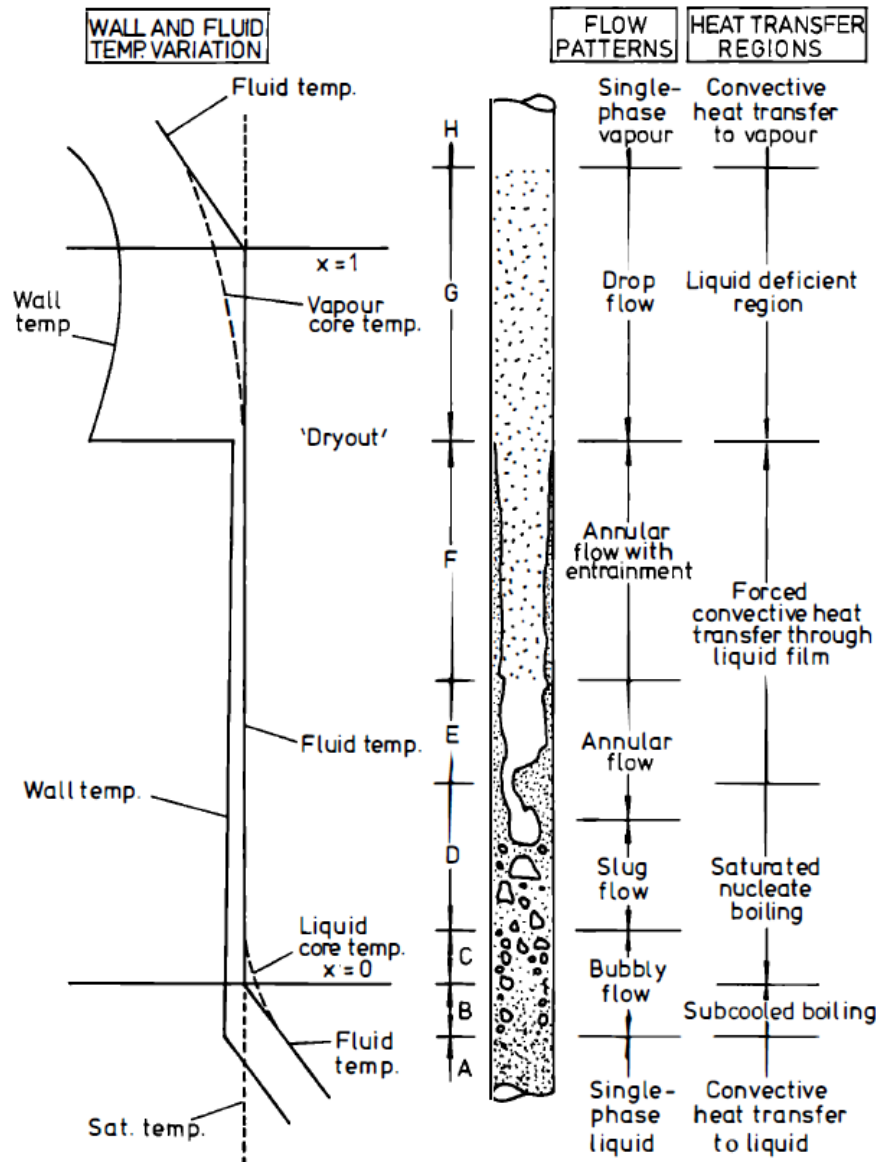


Figure 1.2: Flow configurations and associated thermal regimes. Flow in a vertical heating tube with low heat flux, reprinted from Collier and Thome [10].

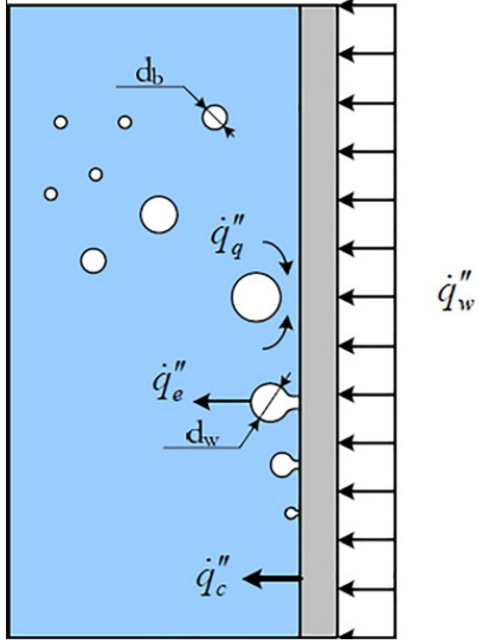


Figure 1.3: Heat flux partitionning model, from Kurul and Podowski [12].

The reference model for heat flux partitioning model is based on the work of Kurul and Podowski [12].

This model assumes that the wall heat flux  $q''_w$  can be divided in three components (see Figure 1.3) that are:

- the single-phase convective heat flux  $q''_c$ , which represents the fraction of the energy input used to heat the subcooled liquid to saturation conditions. This term can be expressed as:

$$q''_c = (1 - N'' K \frac{\pi}{4} D_B^2) h_c (T_w - T_l) \quad (1.4)$$

- the evaporation heat flux  $q''_e$ , which represents the fraction of the energy supplied to vaporise the liquid by creating a liquid-vapour interface,

$$q''_e = f N'' \frac{\pi}{6} D_B^3 \rho_v h_{fg} \quad (1.5)$$

- the quenching heat flux  $q''_q$ . After the bubble detaches from the wall, it drags away superheated liquid which is replaced by a colder liquid. This phenomenon is associated with an increase in heat transfer and is classically modelled by transient conduction.

$$q''_q = f N'' K \frac{\pi}{4} D_B^2 2\epsilon_l \sqrt{\frac{T_w}{\pi}} (T_w - T_l) \quad (1.6)$$

In equations (1.4), (1.6) and (1.5),  $N''$  is the nucleation site density per unit of area [ $m^{-2}$ ],  $K$  is the area influence factor [-],  $D_B$  is the bubble departure diameter [ $m$ ],  $h_c$  is single-phase convective heat transfer coefficient [ $W/m^2 \cdot ^\circ C$ ],  $T_w$  is the wall temperature [ $^\circ C$ ],  $T_l$  is the liquid temperature [ $^\circ C$ ],  $f$  is the bubble departure frequency [ $s^{-1}$ ],  $\epsilon_l$  is effusivity of liquid

water [ $J/Km^2s^{1/2}$ ],  $t_w$  is the waiting time [s],  $\rho_v$  is the vapor density [ $kg/m^3$ ], and  $h_{fg}$  is the latent heat [ $J/kg$ ], respectively.

The evaporation heat flux  $q_e''$  (1.5) depends on three important parameters that are the **nucleation site density**  $N''$ , the **bubble departure frequency**  $f$  and the **bubble departure diameter**  $D_b$ . These parameters are often provided with different correlations ([13], [14], [15]). Nevertheless, most of those correlations are based on experimental measurements performed at low pressure and low temperature conditions or for different fluids. Moreover, when performing experiments to validate the model, all those parameters are not simultaneously measured. From a practical point of view, that means that two parameters are measured (for example the bubble diameter  $D_b$  and the bubble detachment frequency  $f$ ) and the remaining parameter (in our example, the nucleation site density  $N''$ ) is fitted by comparing the model calculations to some secondary experimental measurements like the wall temperature or the void fraction. This approach may be risky: even if the final calculations seem to be good, they may result from errors compensations within the model. To ensure the validity of the partitioning model, **it then seems necessary to perform direct and complete measurements of all the aforementioned sub-models parameters, in operating conditions as close as possible to the targeted ones (PWR)**.

In this study the focus will be drawn on measuring those three parameters in order to completely characterise the heat flux partitionning model for PWR prototypical conditions: (i) the bubble departure frequency  $f$ , (ii) the active nucleation site density  $N''$  and (iii) the bubble departure diameter  $D_b$ .

PWR's prototypical conditions (including normal and incidental conditions) are summarised here. They involve high pressure and high temperature water convective flow as indicated below.

- Pressure: 80 to 155 bar
- Liquid temperature: close to 300°C
- Liquid mean velocity: 500 to 5000 kg/m<sup>2</sup>s.

As a first step, a litterature survey was carried out regarding nucleate boiling studies in order to determine if some data concerning the targeted thermal hydraulic conditions might be available.

## 1.2 Nucleate boiling experiments

Despite the interest of the present work lying on convective boiling flow, it is worth mentioning some work related to pool boiling. Indeed, they may enlight some physical processes in order to understand the underlining boiling mechanisms. A lot of theoretical and experimental work has been done to try to define and quantify the boiling phenomenon in order to understand the boiling crisis. Transient and nucleate boiling have been studied to understand and predict the behaviour of the fluid during the boiling crisis.

Several approaches are proposed in the literature: one can find mechanistic models proposing a physical vision of the phenomenon but they are often at a macroscopic scale and rely on

averaged experimental data (averaged over the section [15]), but there are also several authors who are interested in the local predictive approach (LPA) which aims at getting back to the local scale of the phenomenon. For this work, the experimental data are obtained in the vicinity of the heated wall for operating conditions as close to the boiling crisis as possible ([2], [3]). In this work, we are interested in nucleate boiling, from the Onset of Nucleate Boiling to the boiling crisis, for pressure ranging from atmospheric pressure to the primary circuit pressure (155 bar). In particular, the coupling between the thermal phenomena in the heated wall and the flow in the near-wall zone (bubble size at detachment, detachment frequency, nucleation site density) will be studied.

A targeted literature review was conducted and studies were identified. They are classified (Table 1.1) according to the area studied (core flow or boundary layer) and their field of study (modelling or experimental aspects).

Table 1.1: References classification.

	Core flow studies	Boiling Boundary layer studies
Modeling	Bricard [16] Manon [7] Guéguen [2] Kwon and Chang [19] Inoue et al. [20] Lee and Mudawwar [22] Kurul and Podowski [12] Groenveld et al. [25]	Levy [17] Unal [18] Montout [3] Sugrue and Buongiorno [21] Cole [23] Stephan and Hammer [24] Gu et al. [26] Yoo et al. [27]
Experiments	Hosler [28] Roy et al. [29] Edelman and Elias [32] Lee et al. [35] Scheiff [36] Baudin [39] Yadav and Roy [40] Dix [43] Hapke et al. [44] Garnier et al. [47] Hassan [48] Maitra and Raju [49] François et al. [8] Bartel et al. [52] Arik and Bar-Cohen [53] Oleknovitz [56] Visentini [57]	Euh et al. [30] Yun et al. [31] Lin and Chen [33] Klédy et al. [34] Estrada and Hassan [37] Yuan et al. [38] Langlard et al. [41] Situ et al. [42] Ooi et al. [45] Semeria [46] March [4] Inoue [20] François et al. [50] Richenderfer et al. [51] Sarker et al. [54] Han and Griffith [55]

The majority of nucleate boiling studies are carried out at low pressure with measurements of void fraction ([58], [35], [59], [40]) and velocity measurements for each phase ([60], [59]) but also liquid temperature profile to characterize the flow ([8] [31] [29]). These measurements are made with several types of instrumentation, most of the time with optical probes ([58]), conductivity probes ([35], [59]), capacitance probes ([49]) or direct flow visualisation ([61]). Table 1.2 summarises the data measured by the different studies that were identified.

In Table 1.2 two things can be noted: **(i)** the measurements often concern **low-pressure flows** and **(ii)** they focus on one boiling parameter in particular (very few studies present **simultaneous measurements** of the three parameters of interest to the present work). For example, the only work where measurements were done simultaneously for departure diameter, departure frequency, nucleation site density and wall temperature is the one of Richenderfer et al. [51]. Nevertheless, this study was performed with low pressure conditions.

The few studies presenting measurements of wall boiling parameters often use the same instrumentation: characterisation of boiling at the heated wall/fluid interface is performed by high-speed imaging with direct visualisation of the flow.

To illustrate we can mention the work of Yun et al. [31] with a visualisation of a boiling

Table 1.2: Parameter measurements in litterature.  $P_{eq}$  for Equivalent water pressure range: LP for Low pressure, HP for High pressure ( $> 70\text{ bar}$ ). Every measurements is specified. Instrumentation: PT for Pitot tube, DSCP for Double sensor conductivity probe, CP for Capacitance probe, TH for Thermocouple, DSOP for Double sensor optical probe, OP for Optical probe, PTV for Particle Tracking Velocimetry, IR for Infrared thermography, HSV for High-speed visualisation, HA for Hot-film anemometry

References	Fluid	$P_{eq}$	$D_B$	$f$	$N_a$	$v_l$	$v_v$	$\alpha$	$T_l$	$T_w$	$T_v$	Instrumentation
Situ [59]	Water	LP	$\times$				$\times$	$\times$				DSCP
Lee [35]	Water	LP				$\times$	$\times$	$\times$				DSCP, PT
Edelman [32]	Water	LP						$\times$				X-ray, $\gamma$ -ray
Maitra [49]	Water	LP						$\times$	$\times$	$\times$		CP, TH
François [50]	R12	HP	$\times$					$\times$				DSOP
Yun [31] [62]	Water	LP	$\times$			$\times$	$\times$	$\times$	$\times$			OP, PT, TH
Dix [43]	R114	HP						$\times$	$\times$	$\times$		HA, HSV
Roy [60] [58] [29]	R113	LP	$\times$			$\times$	$\times$		$\times$	$\times$	$\times$	DSOP, TH, PTV
Hapke [44]	Water	LP									$\times$	IR
Sugrue [61]	Water	LP	$\times$									HSV
Lin [33]	R134a	LP	$\times$		$\times$							HSV
Yuan [38]	Water	LP	$\times$									HSV
Richenderfer [51]	Water	LP	$\times$	$\times$	$\times$						$\times$	HSV, IR
Yadav [40]	Water	LP						$\times$				$\gamma$ -ray
François [8]	R12	HP				$\times$	$\times$	$\times$				Thermal-HA
Cole [13]	Water	LP	$\times$	$\times$								HSV
Scheiff [63]	HFE7000	HP								$\times$		HSV, IR
Sarker [54]	Water	LP	$\times$	$\times$						$\times$		HSV
Ooi [45]	Water	LP	$\times$	$\times$	$\times$							HSV
Semeria [46]	Water	HP	$\times$									HSV
Han [55]	Water	LP	$\times$	$\times$						$\times$		HSV, TH
March [4]	Water	HP	$\times$									HSV
Euh [30]	Water	LP		$\times$								HSV
Estrada [37]	HFE301	HP				$\times$						PTV
Estrada [64]	HFE301	HP	$\times$			$\times$	$\times$			$\times$		HSV, IR, PTV
Hassan [65]	HFE301	HP				$\times$	$\times$			$\times$		PTV, IR
Garnier [47]	R12	HP				$\times$	$\times$	$\times$				DSOP
Baudin [39]	HFE7000	HP				$\times$				$\times$		PIV, IR, HSV
Inoue [20]	Water	HP	$\times$			$\times$		$\times$		$\times$		TH, X-ray
Thorncroft [66]	Water	LP	$\times$	$\times$								HSV
Bibeau [67]	Water	LP	$\times$	$\times$								HSV
Klausner [68]	R113	LP	$\times$									HSV
Bartel [52]	Water	LP	$\times$			$\times$	$\times$	$\times$				DSCP
Chu [69]	Water	LP	$\times$	$\times$								HSV

flow in an annular test section. The test section allows the visualisation of the evolution of the flow along the heating element as shown in Figure 1.4. Experiments were performed with water at atmospheric pressure. These visualisations lead to answers on the radial distribution of the void fraction measured with a double sensor optical fiber probe. Indeed, visualisation allows then an external point of view on the flow and a better understanding of the objects measured by an intrusive instrumentation.

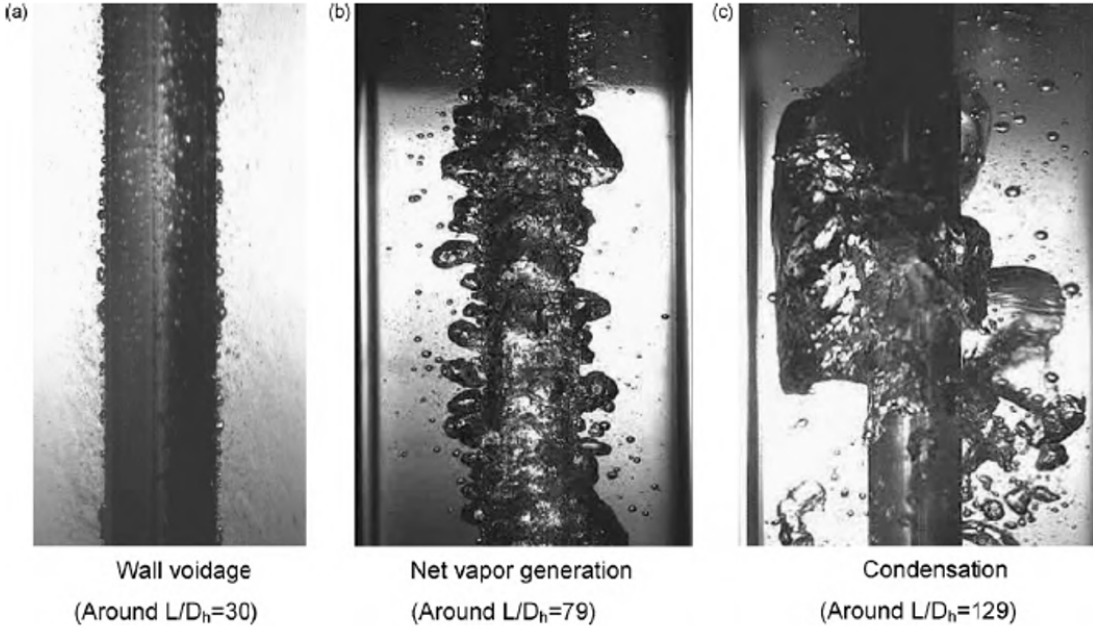


Figure 1.4: Visual observations along the SUBO test section, reprinted from Yun et al. [31].

Optical access to the flow seems to be the key to understanding the phenomenon. It gives access to the phenomenological behaviour more easily than intrusive instrumentation that requires interpretation.

Another example is the work of Sugrue and Buongiorno [61], who performs bubble diameter measurements with direct flow visualisation. The angle of orientation of the test section can be changed to study a vertical upward flow ( $0^\circ$ ) to a vertical downward flow ( $180^\circ$ ). The heating element is a  $1\text{ cm}$  thick 316L stainless steel plate. Bubble diameters at detachment are measured with direct visualisation (see Figure 1.5). These measurements are made at low pressure (from  $1$  to  $5\text{ bar}$ ). It can here be noticed that it is possible to perform more accurate visualisations on an identified active nucleation site. The results show an increase in measured diameter with increasing heat flux, decreasing flow velocity, decreasing subcooling and decreasing pressure.

Moreover, some studies have highlighted important phenomena with visualisation setups in the growth and detachment phases of bubbles. It was indeed possible to detect the sliding of bubbles in the wall before they detach. Thorncroft et al. [66] conducted an experimental study using flow visualisation to measure boiling characteristic parameters such as bubble size, growth rate, bubble departure and lift-off diameters, and waiting time from isolated nucleation sites. The studies were conducted for FC-87 refrigerant, for ascending and descending flows. The results are different according to the orientation of the flow but the visualisation allowed to highlight the effect of the sliding of the bubbles along the heated

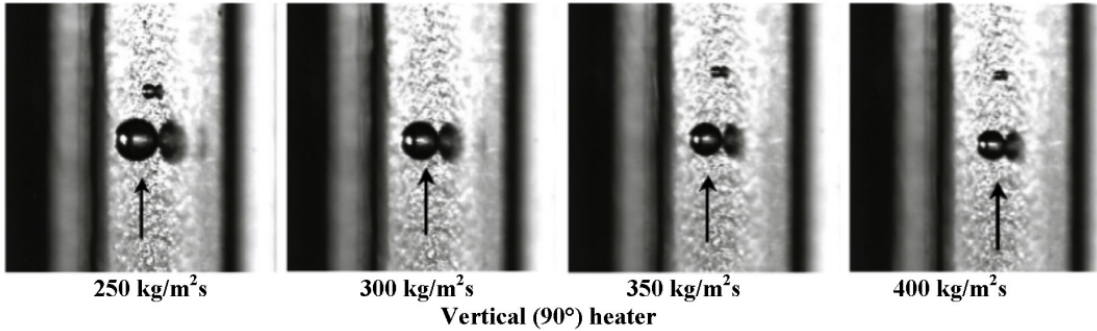


Figure 1.5: Images of bubbles departure, the degree of subcooling is  $10\text{ }^{\circ}\text{C}$  and the heat flux is  $0.05\text{MW}/\text{m}^2$ , reprinted from Sugrue and Buongiorno [61].

wall. This result was also identified by Bibeau and Salcudean [67] who found that bubbles were still growing as they滑 along the heating surface until reaching a maximum size when the condensation rate equals the evaporation rate. Yoo et al. [70] proposed a model to take into account the bubble growth during this sliding period.

The coupling between direct visualisation and infrared thermography is also proposed as an interesting solution to characterise near wall boiling ([39], [51], [64]). Measuring the evolution of the wall temperature with time can give important indications of the detachment frequency and nucleation site density and also helps to determine the instant of bubble detachment from the wall. This time measurement coupled with direct visualisation allows more accurate diameter measurements. Especially if the bubble slides down the wall before leaving the wall for flow, it can prove that the bubble left its nucleation site. In addition, works that carried out bubble diameter measurements in convective flow under PWR conditions ([4]) noted difficult access to the interface with optical index gradient effects due to near wall temperature gradients. These two coupled methods overcome this difficulty.

For a short pressure range Sugrue shows a variation in bubble diameter with pressure. Euh et al. [30] also points out the effect of pressure on the boiling parameters. They investigated bubble nucleation in vertical forced-convective subcooled boiling for pressure values from 1.7 to 3.5 bar. The results indicated that bubble departure frequency increased with heat flux and pressure but decreased with increasing mass flux and subcooling. One should notice that if detachment frequency varies for a small pressure variation, it is legitimate to wonder whether those correlations can be extrapolated to much higher pressure.

Because of the obvious pressure dependency, the review is going to focus on specific high pressure works in the following section. But first, a definition of what is meant by "high pressure" is needed.

### 1.3 High pressure data

In order to identify existing high pressure measurements, a review of the literature was carried out to create a non-exhaustive summary of available experiments. In his paper Hosler [28] carried out a summary of pattern investigations which is presented in Table 1.3. The studies listed are carried out for pressure values ranging from atmospheric pressure to  $2000\text{ psia}$  ( $\sim 138\text{ bar}$ ). However, a single study (from Hosler himself) reaches this pressure, most of the tests being performed below  $1000\text{ psia}$  ( $\sim 70\text{ bar}$ ).

Investigator	Reference	Date	Fluids	Pressure (Psi)	Temp. (°F)	Flow Rates (lb/hr.-ft <sup>2</sup> )	Heat Fluxes (Btu/hr.-ft <sup>2</sup> )	Geometry and Orientation	Remarks
Kosterin	6	1949	Air - Water	15-60	70	$1.2 \times 10^5$ to $4.2 \times 10^5$	Adiabatic	Vertical, Inclined, Horizontal, Tube	Observations beyond end of heated tube
Dengler	7	1952	Steam - Water	< 30	Sat.	$5.4 \times 10^5$ to $1.2 \times 10^6$	0 to 4000	Vertical Tube	
Johnson, Abou - Sabe	8	1952	Air - Water	< 50	70-140	$0.6 \times 10^3$ to $2.4 \times 10^6$	$3.5 \times 10^4$ to $1.75 \times 10^5$	0.87" Horizontal Tube	
Krasil'ko, Krastakova,	9	1952	Air - Water	Atmospheric	70	$3.7 \times 10^4$ to $1.1 \times 10^6$	Adiabatic	Horizontal Tube	
Schneider	10	1953	Kerosene - Gas	Atmospheric	60	$1.0 \times 10^3$ to $8.0 \times 10^4$	Adiabatic	Horizontal Tube	
Alves	11	1954	Air - Water	1000	70	$2.5 \times 10^4$ to $2.4 \times 10^7$	Adiabatic	1" Horizontal Pipe	
Baker, O.	12	1954	Air - Oil	1000	75	$1.0 \times 10^4$ to $2.28 \times 10^5$	Adiabatic	Large Horizontal Pipe	
Kozlov	13	1954	Air - Water	23	70	$8.0 \times 10^4$ to $1.6 \times 10^6$	Adiabatic	Vertical Tube	
Leppert, et al.	14	1955	Steam - Water	30-200	Sat.	$4.0 \times 10^5$ to $1.3 \times 10^6$	$0$ to $3.5 \times 10^5$	Horizontal Tube	
White, Huntington	15	1955	Kerosene - Gas	Atmospheric	70	$2.0 \times 10^3$ to $8.0 \times 10^4$	Adiabatic	Horizontal Tubes	
Berglin, Gorley	16	1956	Air - Water	22	180	$6.8 \times 10^5$	$2.0 \times 10^4$ to $1.25 \times 10^5$	1" Horizontal Tube	
Govier, Redford, Dunn	17, 18	1957	Air - Water	36	70	$1.3 \times 10^4$ to $1.6 \times 10^5$	Adiabatic	Vertical Tube	
Iabin, et al.	19	1958	Steam - Water	25-1850	Sat.	$6.4 \times 10^5$ to $1.2 \times 10^6$	Adiabatic	Horizontal Tube	
Janssen	20	1960	Steam - Water	< 30	Sat.	$1.8 \times 10^4$ to $0.6 \times 10^5$	$1.57 \times 10^5$ to $7.5 \times 10^5$	Vertical & Rod	
Johnsons, Schrock	21	1960	Water	800	Subcooled	$2.2 \times 10^5$ to $3.1 \times 10^6$	$1.5 \times 10^4$ to $1.0 \times 10^5$	7/8" by 7/8" Vertical Channel	
Vohr	22	1963	Steam - Water	< 50	Sat.	$1.8 \times 10^5$ to $3.6 \times 10^5$	$2.6 \times 10^4$ to $8.2 \times 10^4$	Vert. - Rect. Channel, 3/8" x 3 1/4" x 48"	Subcritical heat flux, one side heated, photography
Govier, Gomer	23	1962	Air - Water	36	70	$2.0 \times 10^3$ to $1.1 \times 10^6$	Adiabatic	1.03" Horizontal Tube	
Hartmann	24	1962	Steam - Water	1000	Subcooled	$1.1 \times 10^6$ to $5.5 \times 10^6$	$1.0 \times 10^4$ to $2.7 \times 10^6$	Vertical, Rectangular channel	
Quandt	25	1962	Air - Water	to 1800	70	$1.6 \times 10^4$ to $6.5 \times 10^4$	Adiabatic	Vertical, Rectangular channel	
Styrkovich, Surkov	26	1962	Steam - Water	1000	Sat.	$6.0 \times 10^4$ to $7.5 \times 10^6$	Adiabatic	Vertical, Rectangular channel	
Tippets	27	1962	Steam - Water	n Pentane	Sat.	$1.8 \times 10^5$ to $1.44 \times 10^6$	$5.9 \times 10^5$ to $1.14 \times 10^6$	Vertical, Rectangular channel	
Gouwe, Huang	28	1963	Steam - Water	1000	Sat.	$7.6 \times 10^4$ to $1.3 \times 10^6$	$0$ to $5500$	Vertical, Rectangular channel	
Hsu, Graham	29	1963	Air - Water	Atmospheric	Sat.	$4.1 \times 10^4$ to $8.0 \times 10^4$	$0$ to $52000$	Vertical, Rectangular channel	
Bennett, et al.	30	1965	Steam - Water	500, 1000	Subcooled	$3.0 \times 10^5$ to $3.0 \times 10^6$	$1.6 \times 10^4$ to $3.9 \times 10^5$	0.4" Vert. Tube, 12" long	
Berenson, Stone	31	1965	Freon 113	55	Sat.	$1.0 \times 10^4$ to $4.0 \times 10^4$	$0$ to $4.0 \times 10^4$	Horiz. 0.236" Tube, 40" long	
Bergles, et al.	32	1965	Steam - Water	150-2000	Sat.	$0.4 \times 10^6$ to $4.0 \times 10^6$	$0$ to $7.5 \times 10^5$	24" heated length	
Hosler	33	1966	Air - Water	200-600	70	$3.8 \times 10^4$ to $7.6 \times 10^4$	Adiabatic	Vertical 0.4" Tube	
Haberstroh, Griffith	34	1965	Steam - Water	< 10 <sup>4</sup>	Sat.	$0.2 \times 10^6$ to $2.4 \times 10^6$	$9.6 \times 10^5$ to $1.7 \times 10^6$	Horizontal and Vert. Tube, 0.09" and 0.242" diameter	
Fiori, Bergles	35	1965	Freon 11	50-350	Sat.	$0.2 \times 10^6$ to $2.0 \times 10^6$	Adiabatic	0.36" x 1.05" Vert. Rect. Channel	
Baker, J. L. L.	36	1965	Steam - Water	25-185	Subcooled	$0.1 \times 10^6$ to $1.5 \times 10^6$	$0.1 \times 10^6$ to $1.1 \times 10^6$	1" x 1" x 6" Vert. Channel	
Kirby, et al.	37	1965						0.2" x 6" Heater	Vapor generated in heated tube upstream

Table 1.3: Previous flow pattern investigation, reprinted from Hosler [28].

When trying to draw up a summary of the high pressure experiments, it was made obvious that there are very few studies which have been performed since the ones listed by Hosler. Table 1.4 lists the experiments that may be of interest regarding our context.

Table 1.4: High pressure experiments with water or simulant fluid. Note that some data identified by “-” are not available in the articles.

Author	Fluid	Geometry	Equivalent pressure	Temperature	Flow rate	Heat flux
-	-	-	[bar]	[°C]	[kg/m <sup>2</sup> s]	[kW/m <sup>2</sup> ]
Hosler, 1968	Water	Rectangular	10 – 140	65 – 310	1.2 – 46.8	0 – 138
Dix, 1971	R114	Annular	27 – 70	15 – 20.5	51.53 – 821.8	9.42 – 170.35
Inoue, 1995	Water	Rod bundle	1 – 86	-	284 – 1988	-
March, 1999	Water	Rod bundle	26 – 150	196 – 330.2	1650 – 2200	600 – 960
Garnier, 2001	R12	Circular	100 – 180	20 – 70	1000 – 5000	50 – 650
Perez, 2010	HFE 301	Rectangular	10 – 140	25.5	-	0 – 64
Scheiff, 2015	HFE 7000	Semi-annular	100 – 180	25 – 30	-	25 – 320
François, 2011	R12	Circular	100 – 160	20 – 70	400 – 1600	50 – 500
Semeria, 1969	Water	Rectangular	1 – 137	saturation	-	22 – 2230

The experiments listed here are performed for high pressure steam/water flows or with a simulating fluid. It can be noted that there are few experiments in the pressure ranges of a reactor. This list is not exhaustive but clearly demonstrates a lack of data at high pressure.

Several authors have also tried to provide a summary of existing measurements and data under the relevant conditions. In his doctoral work, Klédy [9] was also interested in experiments at high pressure doing an inventory of experimental databases on boiling convective flows. He found only three references for high pressure measurements: DEBORA experiment in R12, Perez and Hassan experiments in HFE-301 and Inoue experiments in water but with a maximum pressure of 86 bar.

One should notice that measurements performed with simulant fluids (Freon R12, R134a, R113) of HFE-301 are interesting. Indeed, they generally allow to perform experiments at much lower temperature and pressure, while maintaining characteristics (density, enthalpy) that are close to those of water at high pressure. Nevertheless, as a consequence this raises the question of the transposition of those results to steam/water conditions. Furthermore, the experiments carried out and described in the literature (as can be identified on the various summaries) often provide results at low pressure or in similarity with another fluid than water (simulating fluid: R12, R113, HFE).

For example, the DEBORA installation (CEA/Grenoble)<sup>1</sup> was designed to study, on a local scale, the evolution of the structure of a two-phase flow from the beginning of boiling (Onset of Nucleate Boiling) to the onset of the boiling crisis (Departure from Nucleate Boiling). This experimental loop uses R12 as simulant fluid. To determine the equivalent range of parameters between water and Freon the following scaling parameters have been used. They are introduced in Equation (1.7) to (1.10) (Stevens and Kirby (1964), Ahmad (1973)).

<sup>1</sup>Installation which is now dismantled.

$$\left( \frac{\rho_{l,sat}}{\rho_{v,sat}} \right)_{simulant} = \left( \frac{\rho_{l,sat}}{\rho_{v,sat}} \right)_{water} \quad (1.7)$$

$$\left( \frac{q''}{Gh_{fg}} \right)_{simulant} = \left( \frac{q''}{Gh_{fg}} \right)_{water} \quad (1.8)$$

$$\left( \frac{G^2 D_H}{\rho_{l,sat} \sigma_l} \right)_{simulant} = \left( \frac{G^2 D_H}{\rho_{l,sat} \sigma_l} \right)_{water} \quad (1.9)$$

$$\left( \frac{h_{l,in} - h_{l,sat}}{h_{fg}} \right)_{simulant} = \left( \frac{h_{l,in} - h_{l,sat}}{h_{fg}} \right)_{water} \quad (1.10)$$

Equation 1.7 derives the water equivalent pressure from the refrigerant pressure. Equation 1.8 determines the equivalent heat flux obtained from the refrigerant data. The Equation 1.9 determines equivalent mass velocities. Finally, the inlet temperature is obtained using Equation 1.10.

The DEBORA database is known to provide relatively good data (local void fraction, gas velocity and radial profiles of liquid temperature measurements). However, it should be noted that the liquid temperature is rarely measured, contrary to the wall temperature which has also been measured during DEBORA experiments.

Nevertheless, if the validity of the aforementioned scaling criteria is widely admitted for critical heat flux, nothing at date guarantees that those non dimensionnal numbers might be used to transpose other results as for example void fraction or bubble diameter. This is a real problem regarding the validation of calculation tools like NEPTUNE CFD for example since this code like many others use the DEBORA database to improve its modelling and closure laws. Concerning the transposition of results obtained using simulant fluids for quantities that differ from the critical heat flux, it is worth mentionning the doctoral work of François [71] who performed local void fraction measurements in a rectangular channel in Freon R12 using an optical probe. He compared similar measurements using steam/water for high pressure and high temperature. The tests used are those of Martin (1967) concerning the measurement of void fraction profiles in a vertical rectangular test section for high pressure steam/water flows. The geometry of the test channel used by Martin was similar to that of the Patricia channels used by François. The void ratio measurements were made using a radiation attenuation (X-ray) method. François' results with an optical probe are therefore integrated across the width and compared between two plates with Martin's steam/water tests. The thermal hydraulic conditions of the DEBORA tests were transposed into equivalent water conditions using the established similarity in order to be able to compare Martin's experimental results with those obtained by François. In the exemple Figure 1.6, it appears that the measured void fraction profiles are quite comparable, both in terms of space and amplitude and tends to confirm that critical heat flux scaling parameters could be used to transpose much more quantities than the only critical heat flux.

In order to build up on these promising results, it seems necessary to build a data bank using steam/water for the targeted prototypical thermal hydraulic conditions.

Concerning the parameters of interest pointed before, bubble diameter at detachment, detachment frequency and nucleation site density, few measurements have been presented for high pressure conditions. High pressure data banks are scarce as pointed out by Mali et al. [72] in his work on bubble diameter measurements. In his summary, only one reference

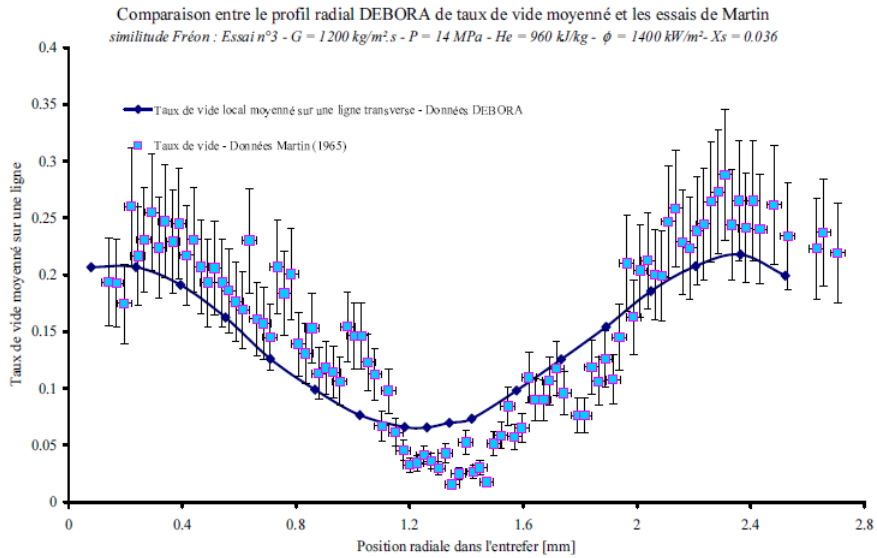


Figure 1.6: One of the comparison of the averaged DEBORA void rate profile with the measurement made by Martin (1967), reprinted from François [71]

shows measurements above 70 bar. Sugrue and Buongiorno [21] also propose a summary of the experiments available in the literature. The presented databases correspond to measurements carried out with simulating fluids (R113, R12), or to steam/water low pressure experiments.

Through the literature review, a clear lack of data on high pressure boiling flows is noticeable. There is also a lack of measurement of the characteristic parameters of wall nucleate boiling, especially under the harsh conditions of a PWR. This study aims at filling this gap in order to validate the initial observations presented below.

Several studies exist that guide and justify moving towards experimental studies at high pressure.

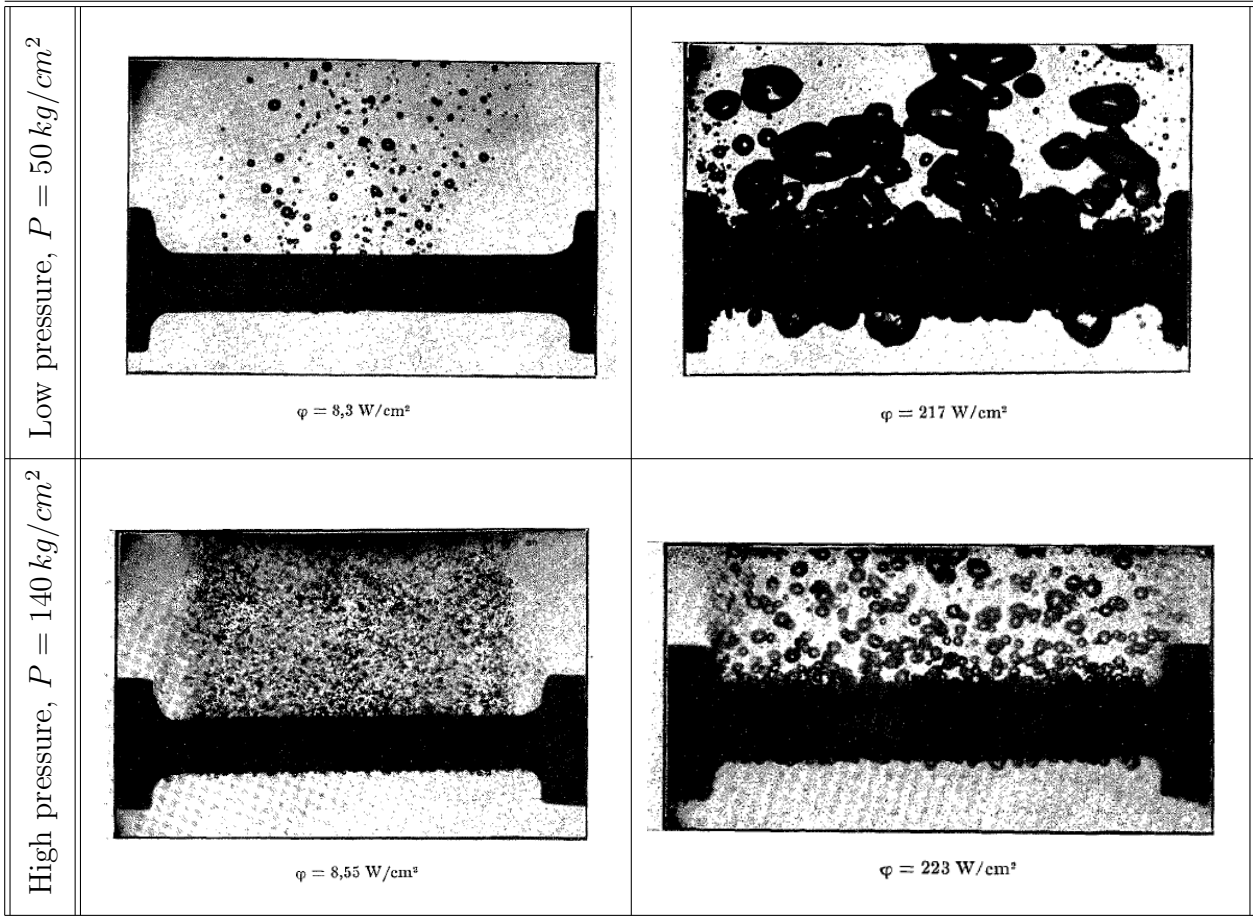
Semeria [46] visualised boiling in low and high pressure through fluorite and quartz windows. The tests were conducted in pool and with forced convection. For high pressure tests, Semeria identifies several types of bubbles: equilibrium bubbles of large diameter that remain on the wall for a long time (in boiling vessels only, these bubbles do not exist in forced convection), so-called boiling bubbles whose starting diameter decreases sharply with pressure, and coalescence bubbles encountered in low-quality flows for moderate heat flux, which he considers to play a preponderant role in the nuclear applications. The Figures presented in Table 1.5 show the evolution of the observations as a function of the heat flux for a pressure of 50 bar and a pressure of 137 bar. Semeria notes that bubble size decreases rapidly with pressure and bubble population increases on the wall with finer grain size.

Hosler [28] experiments were performed in a rectangular test section with one wall heated by direct current. The other face of the test section is made of quartz or sapphire windows.

The test matrix is given in Table 1.6: flow visualisations were done for a wide range of pressure from atmospheric pressure to high pressure ( $\sim 137$  bar) by sweeping the void fraction in order to draw flow maps for several mass velocity ranges.

Hosler results are shown in Figure 1.7. Flow maps (equilibrium quality vs mass velocity) are presented. Whatever the thermal hydraulic conditions, the same flow regimes are encountered. Nevertheless, the boundaries between those flow regimes vary as a function of the pressure.

Table 1.5: Boiling for two pressure ranges (at  $P = 50 \text{ kg/cm}^2$  ( $\sim 49 \text{ bar}$ ) and  $P = 140 \text{ kg/cm}^2$  ( $\sim 137 \text{ bar}$ )) on a  $2 \text{ mm}$  diameter horizontal tube, in this table  $\varphi$  is the heat flux injected through the tube, reprinted from Semeria [46].



Hosler's maps (see Figure 1.7) show that as pressure increases, bubbles are observed to be smaller and the transition between the boiling and pocket/stopper flow regimes occurs later (at higher void rates). These observations show that pressure has a direct effect on the nature of the flow regime: instead of a pocket/plug flow, an emulsive type flow is observed at high pressure. Coalescence seems to slowed down when pressure increases. As a consequence, the physical mechanism driving boiling flow may differ as a function of the pressure.

Moreover, increasing mass velocity leads to a flow pattern transition at lower bulk enthalpy. This is leading to a direct transition from bubble to annular flow. Similarly, at lower inlet temperature and higher heat flux, the transition from bubble to slug happens at lower enthalpy. Hosler comparison of his measurements with existing flow maps (Baker et al. [73], Kozlov [74] and Quandt [75]) shows that the proposed maps do not give a correct prediction of the observations he made. None of the three flow maps satisfies the predictions of these observations, the transitions from bubble to slug flow is often poorly predicted. These elements confirm that high pressure, high temperature boiling is specific and that its prediction cannot be based on results at low pressure. This study supports the need for credible high pressure, high temperature measurements under the conditions of interest and in an independent manner.

Pressure P, lb./sq. in. abs.												
	150		300		600		800		1,400		2,000	
Run No.	Inlet temp.	Run No.	Inlet temp.	Run No.	Inlet temp.	Run No.	Inlet temp.	Run No.	Inlet temp.	Run No.	Inlet temp.	
Mass Velocity, G, lb./hr.-sq. ft.	$0.1 \times 10^6$	28	350	29	425							
$0.25 \times 10^6$	11 150 10 300	27 150 12 250 13 350 19 350	22 300 23 400	42 270 35 370 36 370 37 470	43 335 44 435	74 385 38 485 73 485 70 585						
$0.5 \times 10^6$	2 150 3 150 8 300	18 250 14 350	25 300 32 300 24 400	39 370 40 470	45 335	48 485 49 585 71 585						
$1.0 \times 10^6$		58 300 59 350	33 300 34 435	41 370 55 470	46 435 47 535 61 535	66 485 67 585 72 585						
$2.0 \times 10^6$		60 350		50 370 54 470	62 535	68 485 69 585						
$4.0 \times 10^6$				56 470								

Table 1.6: Summary of photographic runs ranges of conditions tested in Hosler work, reprinted from Hosler [28].

Other works also observed this type of behaviour changes with the variation of pressure, as for example François [71]. This work concerns the study and characterisation of two-phase flows in an inclinable rectangular channel of small hydraulic diameter. The experimental work consisted in carrying out measurements using optical probes to characterise the local structure of the flow (local void fraction, bubble diameter, bubble speed). Given the real operating conditions of a nuclear propulsion reactor (high pressure and temperature), these tests were carried out in Freon similarity (substitute fluid with a low heat of vaporisation). The interpretation of the tests showed that whatever the range of void fraction investigated (from 5 to 95%), the liquid phase remained the continuous phase. At high void fraction, the flow seems to behave like a foam. These observations (through intrusive instrumentation and with a simulating fluid) appeared to be identical to the observations made by Hosler [28] presented just before.

A high pressure measurement, through a non-intrusive instrumentation, will allow the validation of these observations.

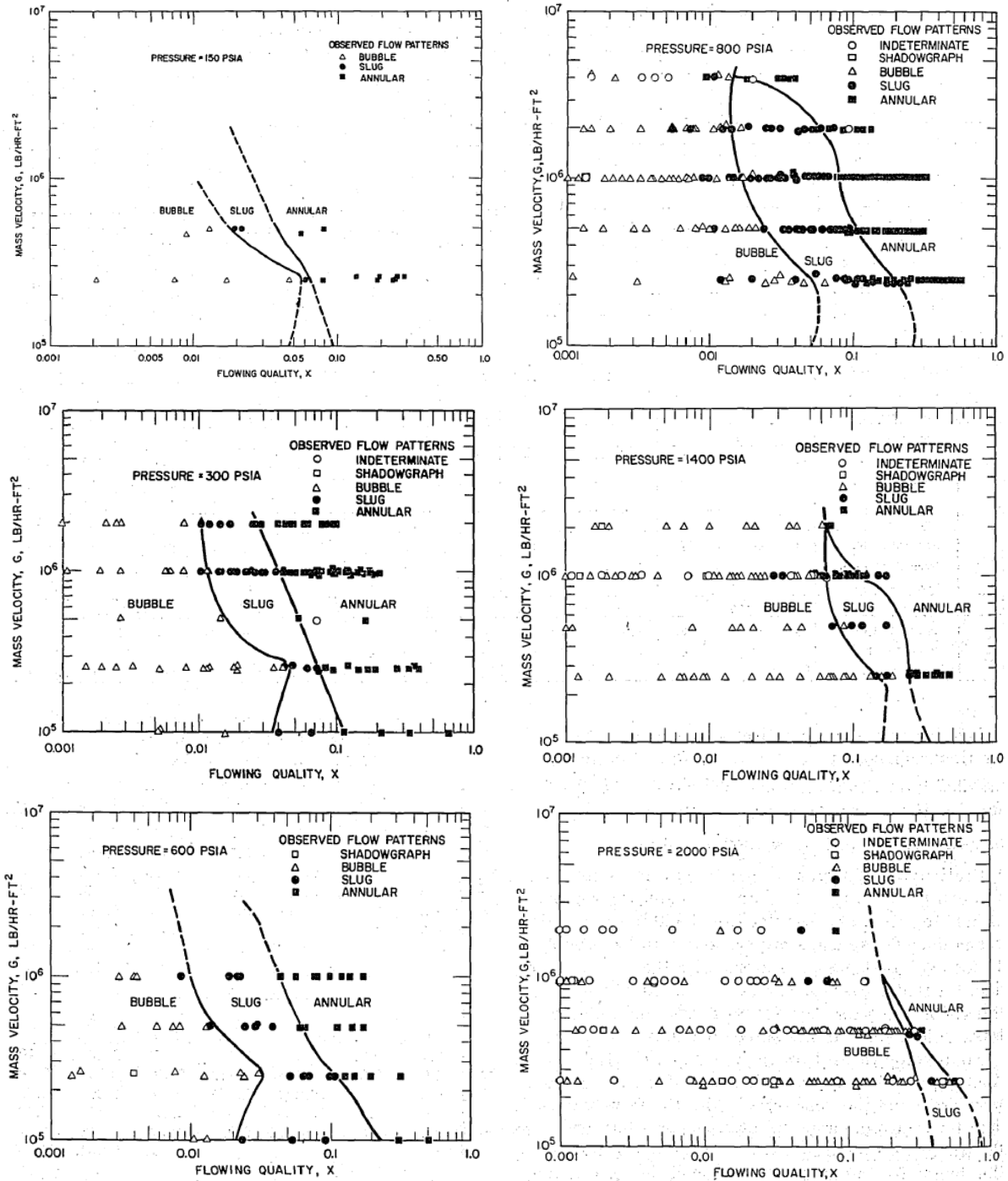


Figure 1.7: Flow pattern data and correlation, reprinted from Hosler [28].

## 1.4 Work in progress

The need for high pressure measurements is now clearly confirmed. Several works are leading the way towards such high pressure measurements and it is important to study them to provide a basis for further work in this work. From this point of view, it is interesting to mention the work carried out at MIT and in particular that of Richenderfer et al. [51] concerning the study of boiling with the implementation of a complete measurement system for the

three parameters that we intend to measure (bubble diameter at detachment, detachment frequency, nucleation site density) as well as the wall temperature. All those measurements are performed simultaneously.

For this purpose, the test section was designed to allow optical access to the flow and to carry out measurements using an ombroscopic setup. The test section is described in Figure 1.8. The heating element was also designed to allow infrared measurements. It consists in a thin layer of Indium Tin Oxide (ITO) deposited on a sapphire window that allows infrared radiation to pass through (see upper right part of the figure). The resulting heating element has a thickness of  $0.7\mu m$ , heated by direct Joule effect.

The optical arrangement (see lower right part of Figure 1.8) provides: (i) a direct view of the flow in front of the heater with the lighting going through the heater, (ii) a direct view of the boiling flow grazing the heater with a shadowgraphic arrangement and (iii) an infrared thermography measurement at the back of the heater through the sapphire.

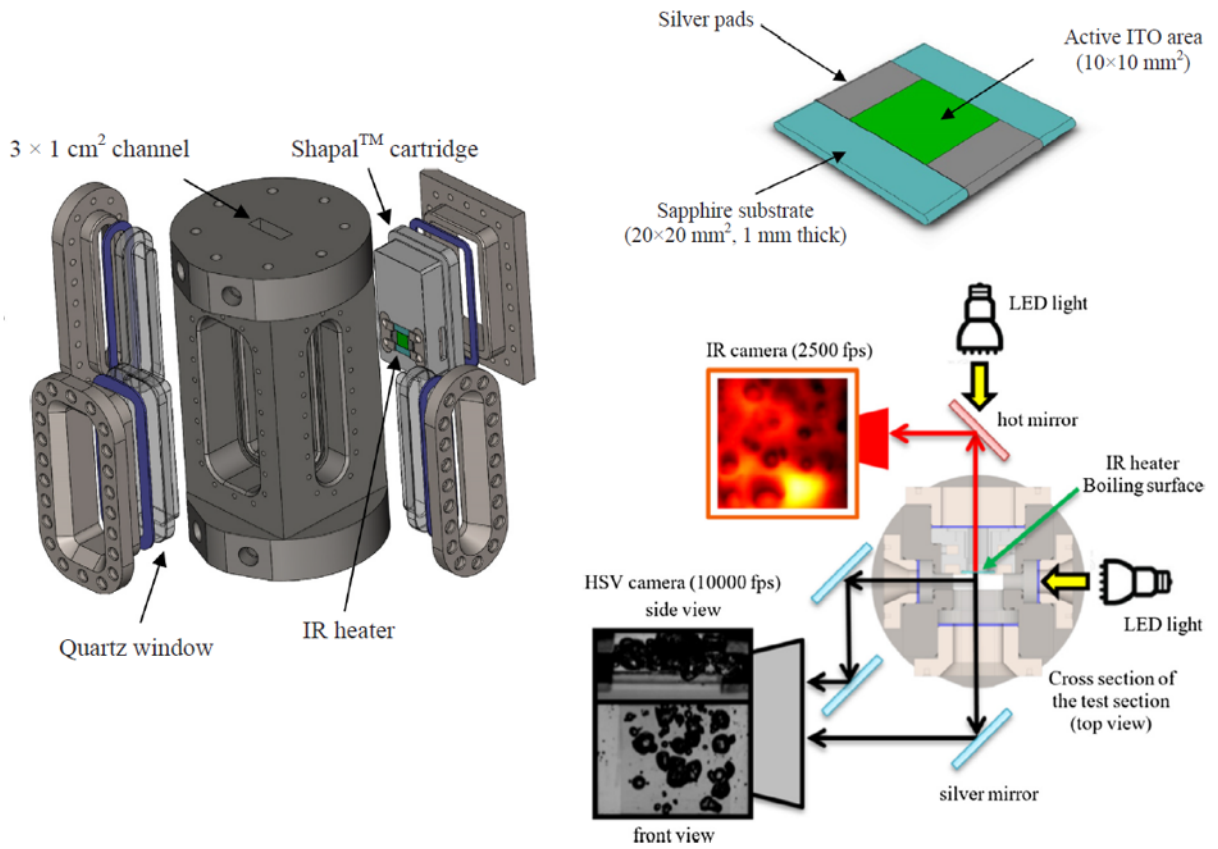


Figure 1.8: Exploded view of the flow boiling test section (upper left). IR heater consisting of a sapphire substrate ( $20 \times 20 \text{ mm}^2$ ,  $1 \text{ mm}$  thick), a  $700 \text{ nm}$  thick, electrically-conductive, IR-opaque ITO coating acting as Joule heater, and silver pads (upper right). Cut-view of the test section with optical arrangement (bottom right). Reprinted from Richenderfer et al. [51].

Infrared measurements allow the determination of heat flux density as well as temperature distribution on the heating element. The nucleation site density is deduced from the varia-

tion of temperature on a nucleation site. Indeed, when a bubble is growing on a site, there is a temperature drop on this position as it is presented Figure 1.9. In addition, it allows a better accuracy concerning the bubble departure diameter measurements by shadowgraphy, indicating when the bubble is really detached from the wall, the instant of detachment corresponding to a minimum temperature reached before going back up.

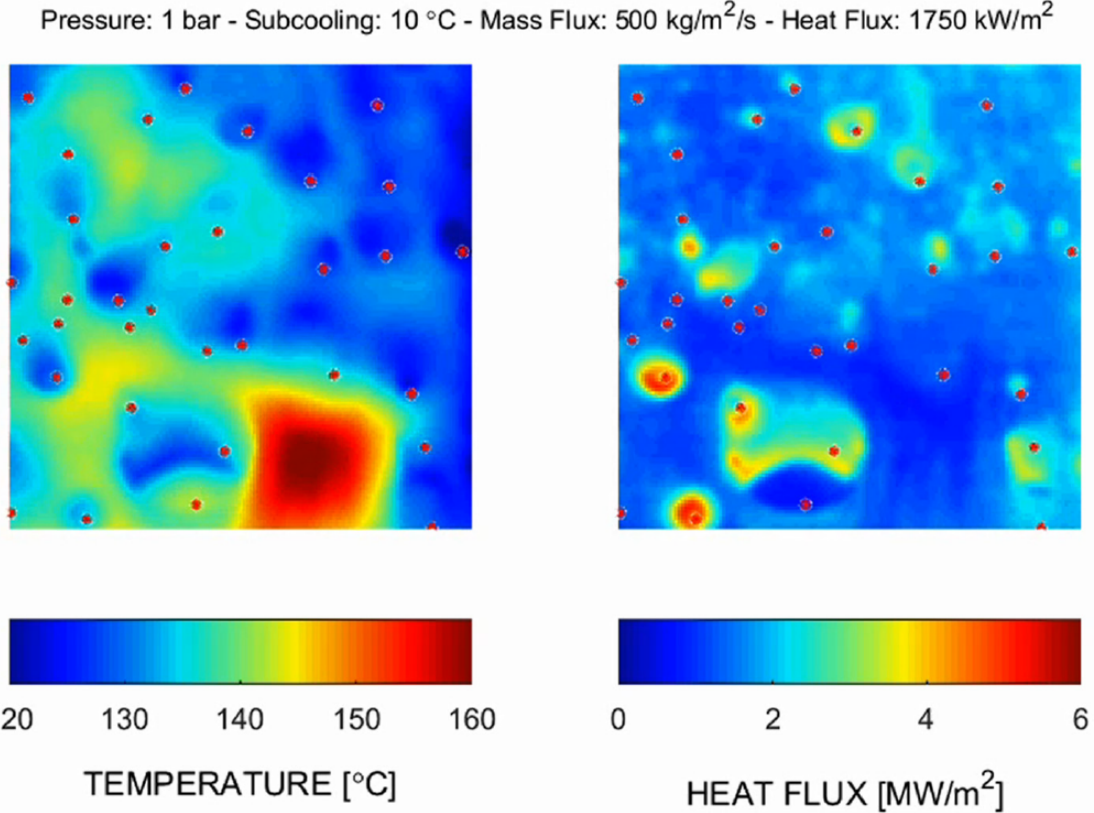


Figure 1.9: Sample validation of the nucleation site detection algorithm on the test with a mass flux of  $500 \text{ kg/m}^2/\text{s}$  (the fluid flows upward) and an average heat flux of  $1750 \text{ kW/m}^2$ . Red dots identify the nucleation sites. Reprinted from Richenderfer et al. [51].

It is important to notice that the heating element does not consist in a metal element but it is made of metallic deposit. This type of deposit follows the roughness of the material on which it is deposited (here sapphire substrate). In this study, Richenderfer presents in Figure 1.10 a qualification of his surface in order to qualify the type of surface where the boiling will take place.

The ITO surface of this heater is nano-smooth (see left Figure 1.10), but localised imperfections are pointed on the sapphire substrate in the range of a few microns (see middle Figure 1.10), which might act as nucleation sites during boiling. It is expected that the number of nucleation sites on such surface is much lower compared to commercial metallic surfaces, resulting in a lower heat transfer coefficient and a higher CHF value.

The representativeness of such a surface condition can therefore be questioned. Several studies exist and point out the dependency of boiling phenomenon and critical heat flux to the roughness of the heater ([76], [54]). All the more so when the work of March [4] is put under consideration. March's thesis focuses on fuel assembly corrosion and the impact of this

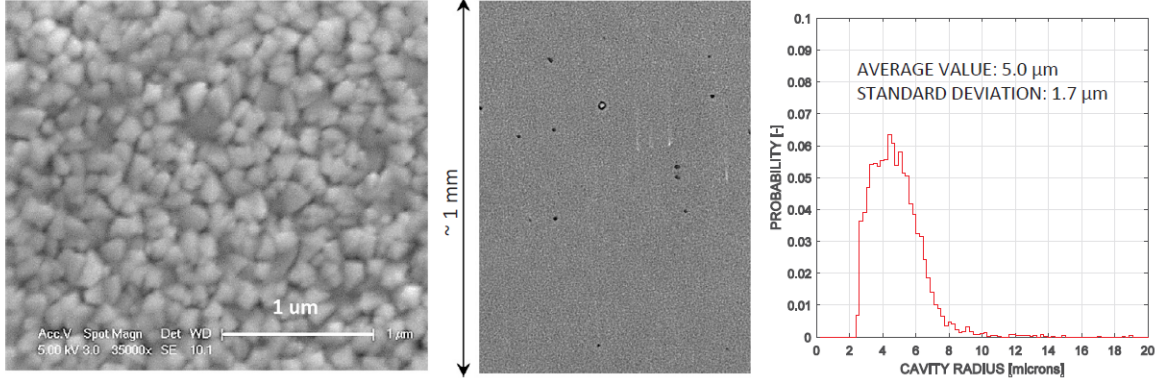


Figure 1.10: View of the ITO surface with different magnification (left and middle) and size distribution of imperfections serving as potential nucleation sites (right). The left figure is taken with an SEM and reveals a granular, nano-smooth surface. The picture in the middle was taken with an optical microscope: cavities that might act as nucleation sites appear as black dots or rings, reprinted from Richenderfer et al. [51].

corrosion on nucleate boiling. In this work a test section (Figure 1.11) was designed to allow optical access to the flow around heated rods through sapphire and zirconia windows. The fuel assembly consists of nine heated rods. Two types of cladding were considered: a first type A with a typical commercial surface roughness ( $R_a = 0.2 \mu\text{m}$ ) and a second type B with an oxidised condition ( $R_a = 3.9 \mu\text{m}$ ). The visualisation of boiling for those two configuration is presented in Figure 1.12 for a pressure of 155 bar and a local quality equal to  $-0.031$ . The left figure corresponds to the A type of surface, the right figure to the B type.

A change in the flow structure can be observed as a result of the change in surface roughness of the heating surface: the rougher the surface is, the smaller the bubbles are. Bubbles grow and detach from the wall with a smaller size than for a smoother surface. The surface condition directly influences the size of the bubbles on the wall. It therefore seems important to check the representativeness of a surface in order to draw conclusions about boiling under PWR conditions.

The evidence presented here reinforces the need for measurements for prototypical PWR conditions, including high pressure exploration. The importance of controlling the boundary conditions, in particular the surface roughness of the heating element, was identified as crucial to ensure representative measurements. In the following chapter, the parameters to be measured will be investigated and orders of magnitude determined in order to do a pre-sizing of the test section and the associated instrumentation.

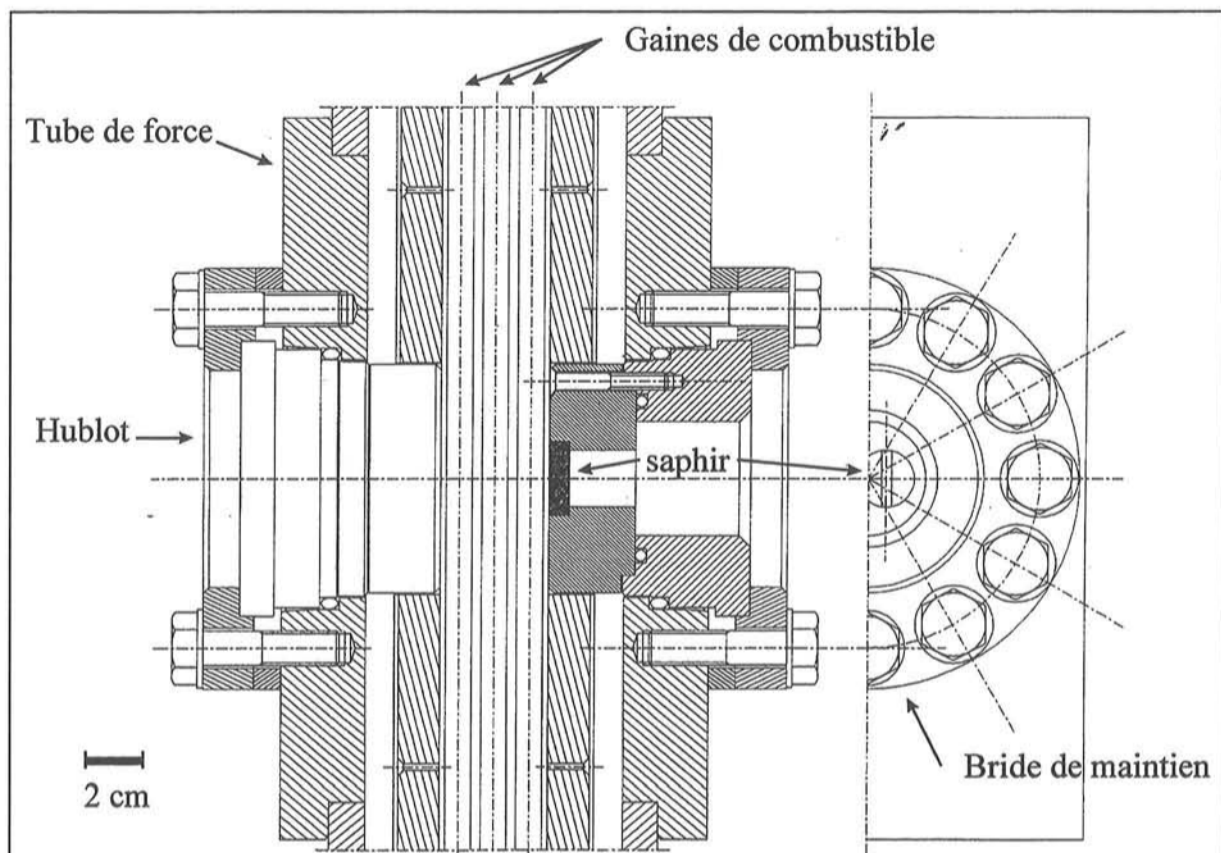


Figure 1.11: Experimental setup of March, reprinted from March [4].

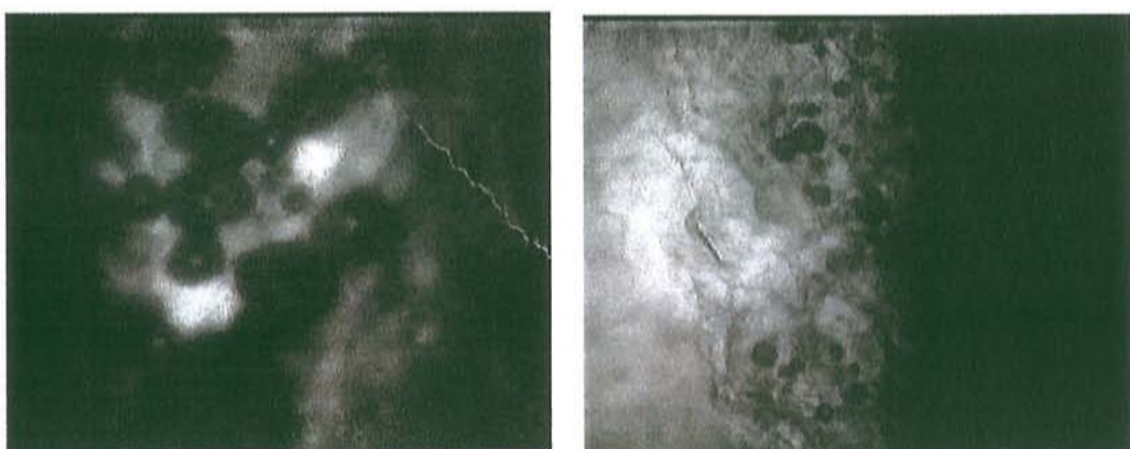


Figure 1.12: Visualisation of type A- $R_a = 0.2 \mu\text{m}$  (left) and B- $R_a = 3.9 \mu\text{m}$  (right) surface state influence over boiling on a heated rod. Reprinted from March [4].



# Chapter 2

## Litterature survey regarding nucleate boiling for forced convective flows

As introduced previously, high pressure measurements are required to inform and compare the boiling models. In order to design a facility and its associated instrumentation to measure the bubble detachment frequency, the bubble detachment diameter and the nucleation site density, it is important to determine an order of magnitude of those parameters. This may be helpful to determine the characteristics as well as the performances of the future instrumentation.

### 2.1 Boiling flow study

As presented in the previous chapter, boiling process is characterized by particular conditions from ONB that correspond to the appearance of the first bubble to the onset of significant void where bubble begin to detach from the heated wall. We present here some models to predict the occurence of those conditions.

Identifying the ONB, OSV and critical heat flux points will lead us to frame our study and to be able to correctly define this work ongoing. Several correlations can be found in the litterature that depend on the flow, the operating conditions and the geometry of the test section. In his thesis, Manon [7] summarises these models and defines the best set by comparing them to the DEBORA databank. Also several studies are trying to define the most accurate (in terms of trends and values) correlations to describe boiling flow (Hapke et al. [44], Fang et al. [77], Cong et al. [78], Rogers et al. [79]). Some models are presented in the incomming section.

#### 2.1.1 Single-phase heat transfer coefficient

The first step is to be able to calculate the single phase heat transfer coefficient, which then allows to calculate the temperature of the fluid and of the wall as a function of the energy injected in the test section through the heated wall. Several correlations are available to calculate this heat transfer coefficient. The best known is that of Dittus and Boelter [80] which expresses Nusselt as a function of Reynolds and Prandtl calculated at the bulk temperature. This correlation is valid for Prandtl number  $0.6 \leq Pr \leq 160$  and Reynolds number  $10^4 \leq Re \leq 10^6$ , where  $Re = \frac{GD_H}{\mu_l}$  and  $Pr = \frac{\mu_l C_{pl}}{\lambda_l}$ .

$$Nu_{Dittus} = 0.023 Re^{0.8} Pr^n \quad (2.1)$$

with  $n$  value is given for a heated wall as  $n = 0.4$ . Gnielinski [81] also expresses Nusselt in terms of the same quantities but for different conditions:  $0.5 \leq Pr \leq 2000$  and  $2300 \leq Re \leq 5.10^6$ .

$$Nu_{Gnielinski} = \frac{\frac{C_f}{2}(Re - 1000)Pr}{1 + 12.7 \left(\frac{C_f}{2}\right)^{0.5} (Pr^{2/3} - 1)} \quad (2.2)$$

where  $C_f$  is the friction factor determined with Moody diagram or Colebrook equation. Fluid properties are calculated at liquid bulk temperature.

### Wall temperature

Once the heat transfer coefficient is determined, the fluid temperature can be calculated from the heat balance energy within the fluid. The wall temperature is given by the formula as follows:

$$T_w = T_l + \frac{q'' D_H}{\lambda_l Nu} \quad (2.3)$$

where  $Nu$  is the Nusselt number given by Equation 2.2 or 2.1 for example.

#### 2.1.2 Correlations for ONB

The location of the Onset of Nucleate Boiling (ONB) corresponds to the onset of activation of the first nucleation sites. In order to determine this point, the first step is to define a criteria for the wall temperature reaching this point.

To determine the superheat temperature at the wall necessary to see boiling start, several authors propose expressions taking into account for the pressure, the heat flux density as well as the fluid characteristics at its mean temperature.

Bergles and Rohsenow [82] obtained a graphic solution by postulating that the bubbles in the nucleation cavities grow only if the temperature of the interface located the furthest from the wall is higher than the saturation temperature. They propose to write this superheat as:

$$\Delta T_{ONB,BG} = (T_w - T_{l,sat})_{ONB,BG} = 0.556 \left( \frac{q''}{1082 P^{1.156}} \right)^{0.463 P^{0.0234}} \quad (2.4)$$

$P$  is the system pressure in bar,  $q''$  is the heat flux density in  $W/m^2$

Davis and Anderson [83] propose an analytical solution that leads to:

$$\Delta T_{ONB,DA} = (T_w - T_{sat})_{ONB,DA} = \left( \frac{8\sigma q'' T_{sat}}{\lambda_l h_{fg} \rho_g} \right)^{0.5} \quad (2.5)$$

Finally, Frost and Dzakowic [84] have extended the range of validity of the equations proposed by Davis and Anderson, including in particular fluids like Freon R12.

$$\Delta T_{ONB,FD} = (T_w - T_{sat})_{ONB,FD} = \left( \frac{8\sigma q'' T_{sat}}{\lambda_{l,sat} h_{fg} \rho_v} \right)^{0.5} Pr_{l,sat} \quad (2.6)$$

The validity range of those models are summarised in Table 2.1.

Table 2.1: ONB correlations validity range

Author and Year	Fluid	Pressure	Heat flux	Mass velocity
-	-	[bar]	[MW/m <sup>2</sup> ]	[kg/m <sup>2</sup> .s]
Bergles and Rohsenow 1964	Water	[1-138]	[0.12-15]	[3600-15000]
Davis and Anderson 1966	Water	[4-138]	[0.5 - 15]	[1000-5000]
Frost and Dzakowic 1967	Water/R12	[1-200]	0.15	-

After determining the wall superheat, the coordinate  $z_{ONB}$  is determined by solving the heat balance in the fluid written as:

$$h_l(z) = h_{l,in} + \frac{W}{\dot{m}} \quad (2.7)$$

with  $W$  the heat transferred to the fluid,  $\dot{m}$  the mass flow rate. The turbulent single-phase heat transfer coefficient may be given by the Dittus-Boelter (2.1) or Gnielinski (2.2) relation.

### 2.1.3 Correlations for OSV

The Onset of Significant Void is less obvious to define. It is commonly accepted that OSV corresponds to the incipience of an increased vapor production, where bubbles begin to migrate toward the flow core.

Several models are available to predict OSV: some are empirical and other ones analytical. Empirical correlations express the superheat characterising the OSV from the hydraulic parameters. Analytical models express the subcooling at the OSV as a function of  $Y_B^+$  which is a dimensionless distance between the top of the bubble and the wall. Martinelli proposed in 1947 the following model purely empirical:

$$\begin{cases} \Delta T_{OSV} = Q * Pr * Y_B^+ & \text{if } 0 \leq Y_B^+ \leq 5 \\ \Delta T_{OSV} = 5Q \left( Pr + \ln \left( 1 + Pr \left( \frac{Y_B^+}{5} - 1 \right) \right) \right) & \text{if } 5 < Y_B^+ \leq 30 \\ \Delta T_{OSV} = 5Q \left( Pr + \ln(1 + 5Pr) + 0.5 \ln \left( \frac{Y_B^+}{30} \right) \right) & \text{if } 30 < Y_B^+ \end{cases} \quad (2.8)$$

where  $Q$  is defined as:  $Q = \frac{q''}{\rho_l C p_l \sqrt{\tau_w / \rho_l}}$

The expression for  $Y_B^+$  varies according to the author:

- Levy [17] postulates the OSV occurrence is possible if the temperature at the bubble top is equal to saturation temperature. This leads for  $Y_B^+$  to the following relation:

$$Y_B^+ = 0.015 * \frac{\sqrt{\sigma D_B \rho_l}}{\mu_l} \quad (2.9)$$

- Staub [85] suggests a dependence of  $Y_B^+$  to the inlet liquid velocity. The following equation was then proposed:

$$Y_B^+ = \frac{D_B}{2} * \frac{\rho_l v_l \sqrt{f/8}}{\mu_l} \quad (2.10)$$

- Rogers et al. [79] takes into account the static contact angle  $\theta$  into this formulation:

$$Y_B^+ = \frac{D_B}{2} * \frac{\rho_l}{\mu_l} * \sqrt{\frac{\tau_w}{\rho_l}} (1 + \cos(\theta)) \quad (2.11)$$

These three models are very similar because they consider the same boundary condition for the temperature at the top of the bubble. The difference lies in that they assumed different bubble shapes: spherical for Levy, hemispherical for Staub and truncated spherical with a contact angle for Rogers.

The empirical correlations found in the literature directly express the subcooling at the OSV. Saha and Zuber [86] supposed that the point of net vapor generation only depends on local thermal conditions. Evaporation is set proportional to heat flux and condensation proportional to the local subcooling. Saha and Zuber considered two distinct situations based on the flow rate: for low mass flow rate, Nusselt number is presented as the similarity parameter, whereas at high mass flux rates, the local Stanton number is considered to be as the appropriate scaling group. Stanton number is defined as  $St = \frac{h}{v_l \rho_l C_p}$ . The data used by Saha and Zuber correspond to several types of studies (working fluid: water or Freon 114 or Freon 22), with pressure values ranging from atmospheric up to 138 bar.

These two distinct regions are identified in Figure 2.1.

The subcooling  $\Delta T_{OSV}$  defined by  $\Delta T_{OSV} = T_{sat} - T_{l,OSV}$  is then given by:

$$\begin{cases} \Delta T_{OSV, SZ} = 0.0022 \left( \frac{q'' D_H}{\lambda_l} \right) & \text{if } Pe \leq 70000 \\ \Delta T_{OSV, SZ} = 153.8 \left( \frac{q''}{G_{in} C p_l} \right) & \text{if } Pe > 70000 \end{cases} \quad (2.12)$$

where Peclet number is defined as  $Pe = \frac{GD_H C p_l}{\lambda}$ .

Unal [18] suggests the following empirical relation, assuming that the OSV can be predicted from a balance between the number of bubbles that condense and the number of bubbles created in a subcooled nucleate flow regime:

$$\Delta T_{OSV, Unal} * \frac{h_l}{q''} = a = cte \quad (2.13)$$

where  $a = 0.24$  if  $v \geq 0.45 \text{ m.s}^{-1}$ , or  $a = 0.11$  if  $v < 0.45 \text{ m.s}^{-1}$ .

According to the litterature, the most accurate models are the Saha and Zuber for the empirical model and Levy for the analytical one. However, Levy's model is qualified at low pressure (up to 4 bar maximum). The Saha and Zuber model seems therefore to be the most suitable model regarding our thermal hydraulic conditions. The range of validity of each of those models is summarised in Table 2.2.

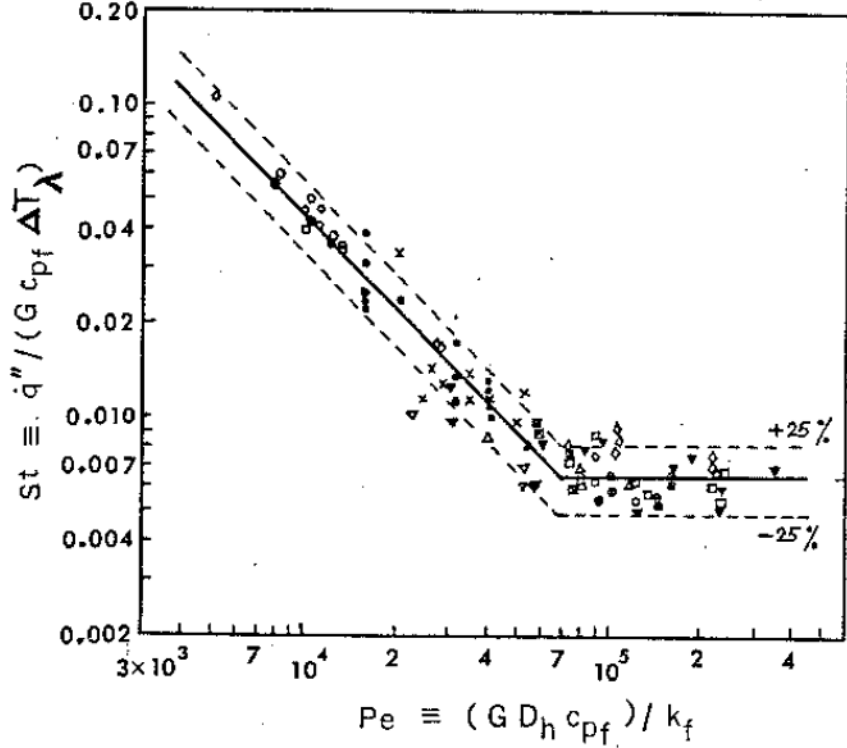


Figure 2.1: Peclet number vs Stanton number at the point of net vapor generation, after Saha and Zuber [86].

Table 2.2: OSV correlations validity range

Author and Year	Fluid	Pressure	Heat flux	Velocity	Subcooling
-	-	[bar]	[kW/m <sup>2</sup> ]	[m/s]	[°C]
Levy	-	4.1	-	0.15	-
Staub 1968	Water	1.7	-	-	-
Rogers 1987	Water	[1.5-1.55]	[300-1200]	[0.07-0.45]	-
Saha and Zuber 1974	Water, Freon 114, Freon 22	[1-138]	-	-	-
Unal 1975	Water and R-22	[1-150]	[150-1920]	[0.2-4.65]	[3.7-42]

#### 2.1.4 Correlations for $q''_{CHF}$

Observations of CHF (Critical Heat Flux) have been conducted since the 1900s, whereas studies regarding its prediction began for around 1940. Measurements took into account several parameters as pressure, inlet temperature, flow rate, diameter and heating length, but also secondary parameters such as orientation, material, type of heating, plate thickness, roughness, diameter change, dissolved gases, this list may not be exhaustive. Unfortunately, those studies suffer from a lack of reproducibility since similar studies (with the same parameters at first glance) can show completely ambivalent results.

Most of pool boiling CHF models are based on hydrodynamic mechanism leading to an interruption of the liquid supply to the heater. Zuber [87] assumed that CHF occurred when

the interface water/steam become unstable, proposing the following expression:

$$q''_{CHF,Z} = \frac{\pi}{24} h_{fg} \sqrt{\rho_v} (\sigma_l g (\rho_l - \rho_v))^{1/4} \quad (2.14)$$

Lienhard [88] and Kutateladze [89] proposed similar correlations using the same describing parameters.

Regarding convective boiling, Groeneveld et al. [25] gives an overview of existing correlations and models. He counted almost 5 000 references. One major issue sticks to the fact that some thermal hydraulics domains are difficult to access like for example the domain of high flow rates associated with high equilibrium quality.

Different approaches exist to determine the critical heat flux. The first is entirely based on experimental data: after identifying the parameters influencing the critical heat flux, the best mathematical expression correlating the data is proposed. One can cite for example the correlation of Bowring [90]:

$$q''_{CHF,B} = \frac{A + B(h_l - h_{l,in})}{C + L_c} \quad (2.15)$$

where  $A$ ,  $B$  and  $C$  are defined as:

$$A = \frac{0.5793 h_{fg} D_H G F_1}{1 + 0.0143 F_2 D_H^{0.5} G} \quad (2.16)$$

$$B = 0.25 D_H G \quad (2.17)$$

$$C = \frac{0.077 D_H G F_3}{1.0.347 F_4 \left(\frac{G}{1356}\right)^n} \quad (2.18)$$

The exponent  $n$  is given by the relation  $n = 2 - 0.5p'$ , where  $p' = P/69$ , with  $P$  in [bar].

The quantities  $F_1$ ,  $F_2$ ,  $F_3$  and  $F_4$  are expressed as:

- If  $p' < 1$

$$F_1 = \frac{p'^{18.942} \exp(20.8(1 - p')) + 0.917}{1.917} \quad (2.19)$$

$$F_2 = \frac{p'^{1.316} \exp(2.444(1 - p')) + 0.309}{1.309} \quad (2.20)$$

$$F_3 = \frac{p'^{17.023} \exp(16.658(1 - p')) + 0.667}{1.667} \quad (2.21)$$

$$\frac{F_4}{F_3} = p'^{1.649} \quad (2.22)$$

- If  $p' > 1$

$$F_1 = p'^{-0.368} \exp(0.608(1 - p')) \quad (2.23)$$

$$F_2 = \frac{F_1}{p'^{-0.448} \exp(0.254(1 - p'))} \quad (2.24)$$

$$F_3 = p'^{0.219} \quad (2.25)$$

$$\frac{F_4}{F_3} = p'^{1.649} \quad (2.26)$$

Notable correlation is the one of Katto [91, 92, 93]: this correlation has a phenomenological basis, a large database and a wide range of validity.

$$q''_{CHF,K} = XG(h_{fg} + K(h_l - h_{l,in})) \quad (2.27)$$

where  $X$  and  $K$  depend on three non-dimensional numbers:

$$\begin{cases} L' = \frac{L_c}{D_H} \\ R' = \frac{\rho_v}{\rho_l} \\ W' = \frac{\sigma \rho_l}{G^2 L_c} \end{cases} \quad (2.28)$$

The coefficient  $X$  depends on five particular values.

$$\begin{cases} X_1 = \frac{CW^{0.043}}{L'} \\ X_2 = \frac{0.1 * R'^{0.133} * W'^{0.333}}{1 + 0.0031L'} \\ X_3 = \frac{0.098R'^{0.133} * W'^{0.4333} * L'^{0.27}}{1 + 0.0031L'} \\ X_4 = \frac{0.0384R'^{0.6} * W'^{0.173}}{1 + 0.28W'^{0.233}L'} \\ X_5 = \frac{0.234R'^{0.513} * W'^{0.433} * L'^{0.27}}{1 + 0.0031L'} \end{cases} \quad (2.29)$$

where  $C$  is defined as:

$$\begin{cases} C = 0.25 & \text{if } L' < 50 \\ C = 0.25 + 0.0009(L' - 50) & \text{if } 50 < L' < 150 \\ C = 0.34 & \text{if } L' > 150 \end{cases} \quad (2.30)$$

The  $K$  coefficient depends on three values:

$$\begin{cases} K_1 = \frac{0.261}{CW^{0.043}} \\ K_2 = \frac{0.833(0.0124 + 1/L')}{R'^{0.133} * W'^{0.333}} \\ K_3 = \frac{1.12(1.52W'^{0.233} + 1/L')}{R'^{0.6}W'^{0.173}} \end{cases} \quad (2.31)$$

The values of  $X$  and  $K$  follow the following rules:

- For  $R' < 0.15$ :
  - If  $X_1 < X_2$  then  $X = X_1$
  - If  $X_1 > X_2$  and  $X_2 < X_3$  then  $X = X_2$
  - If  $X_1 > X_2$  and  $X_2 > X_3$  then  $X = X_3$
  - If  $K_1 > K_2$  then  $K = K_1$

- If  $K_1 < K_2$  then  $K = K_2$
- For  $R' > 0.15$ :
  - If  $X_1 < X_5$  then  $X = X_1$
  - If  $X_1 > X_5$  and  $X_5 > X_4$  then  $X = X_5$
  - If  $X_1 > X_5$  and  $X_5 < X_4$  then  $X = X_4$
  - If  $K_1 > K_2$  then  $K = K_1$
  - If  $K_1 < K_2$  and  $K_2 < K_3$  then  $K = K_2$
  - If  $K_1 < K_2$  and  $K_2 > K_3$  then  $K = K_3$

Another way to calculate critical heat flux is the look up table provided by Groeneveld, including DeBortoli [94] (1 000 tube-CHF data) which was the earliest CHF database available, one of the most recent being Hall and Mudawar [95] with 30 000 CHF data tubes.

This method consists in constructing a table containing experimental values of critical heat flux as a function of hydraulic parameters. The tests are performed on tubes whose inner diameter is 8 mm and uniformly heated. This table is updated regularly and contains more than 20,000 points. From this table, Groeneveld proposes relations that allow extrapolation to different situations (different diameter or heated length, different heating conditions) respecting the parametric trends.

Another way is to determine the mechanisms responsible for the critical heat flux and to give a mathematical description (analytical model). One of the most famous CHF model is the bubble crowding model initially proposed by Weisman and Pei (1983).

The three models presented will be used to define the upper limit of the flow injected into the test section. For each of these models, the conditions of validity of these relationships are summarised in the Table 2.3.

Table 2.3:  $q_{CHF}$  models and correlations validity range

Author and Year	Fluid	Pressure	Velocity
-	-	[bar]	[kg/m <sup>2</sup> .s]
Zuber 1958	-	1	-
Bowring 1972	Water	[2-190]	[136-18600]
Groeneveld (data) 1983	-	[11-200]	[6-8000]
Katto 1990	Water	[1-200]	[350-40600]

## 2.2 Boiling modeling

### 2.2.1 Interface modelisation

As presented in the previous chapter, the modelling of nucleate boiling using the two fluid model require to specify several closure relations and in particular the wall heat flux partitionning.

As presented in Chapter 1, Kurul and Podowski [12] model assumes that the heat flux  $q_w''$  can be divided in three components that are the evaporation heat flux  $q_e''$ , the quenching heat flux  $q_q''$  and the single-phase convective heat flux  $q_c''$ , respectively.

As a reminder, the evaporation heat flux  $q_e''$  (1.5) depends on three parameters that are the nucleation site density  $N''$ , the bubble departure frequency  $f$  and the bubble detachment diameter  $D_b$  respectively. These parameters are often provided with different correlations (Cole [13], Unal [15]). Most of those correlations are based on experimental measurements performed at low pressure and low temperature conditions or for different fluids (R12, R114, R113). For example, the bubble diameter  $D_b$  is often calculated using the well-known correlation of Unal [15]. Despite this correlation being often used for high pressure and high temperature steam/water flows, one should notice that the experimental data base used by Unal to build his correlation is based on De Munk experiments that were performed with Sodium [96]. Moreover, considering that this correlation is dimensional, it is legitimate to wonder about the applicability of this model for PWR thermal hydraulic conditions.

As a first approach and in order to define the setup and the instrumentation for such measurements. We propose in the following section a litterature survey regarding the previously mentionned parameters ( $f$ ,  $D_b$  and  $N''$ ).

### 2.2.2 Correlations

Several correlations can be found in the literature for each of the quantities to be measured<sup>1</sup>. These correlations often have a range of validity in pressure that does not include PWR conditions. Nevertheless, by comparing them, we believe that some reliable orders of magnitude can be exhibited. Those orders of magnitude will be helpful to specify for example the instrumentation we intend to use for future experiments.

#### Correlations for bubble detachment diameter

Several references that model the bubble diameter at detachment can be found. The best known and most widely used is that of Unal [15] who proposes a model based on an energy balance of a bubble growing on a heated wall. It expresses the bubble detachment diameter as:

$$D_{B,Unal} = \frac{2.42 \cdot 10^{-5} P^{0.709} A_{Unal}}{(B_{Unal}\phi)^{0.5}} \quad (2.32)$$

---

<sup>1</sup>Nucleation dnesity, buble detachment diameter and detachment frequency

where  $P$  is the pressure expressed in  $[Pa]$  and with  $A_{Unal}$  and  $B_{Unal}$  as:

$$A_{Unal} = \frac{(q'' - h\Delta T_{sub})^{1/3} \lambda_l (\frac{\lambda_s C p_s \rho_s}{\lambda_l C p_l \rho_l})^{0.5}}{2C_1^{1/3} \rho_v h_{fg} (\pi \frac{\lambda_l}{\rho_l C p_l})^{0.5}} \quad (2.33)$$

$$B_{Unal} = \frac{\Delta T_{sub}}{2(1 - \frac{\rho_v}{\rho_l})} \quad (2.34)$$

where  $q''$  is the heat flux,  $\Delta T_{sub} = T_l - T_{sat}$  is the subcooling,  $\lambda_s$  is the thermal conductivity of the heater material,  $C p_l$  is the thermal capacity of the heater material,  $\rho_l$  is the density of the heater material,  $\lambda_l$  is the thermal conductivity of the liquid,  $C p_l$  is the thermal capacity of the liquid,  $\rho_l$  is the liquid density,  $\rho_v$  is the vapour density and  $h_{fg}$  is the latent heat.  $\phi$  and  $C_1$  are expressed as:

$$\phi = \begin{cases} \left(\frac{v_l}{v_0}\right)^{0.47} & \text{if } v_l > 0.61 m/s \\ 1 & \text{if } v_l < 0.61 m/s \end{cases} \quad (2.35)$$

where  $v_l$  is the liquid velocity and  $v_0 = 0.61 m/s$ .

$$C_1 = h_{fg} \mu_l \sqrt{\frac{(\rho_l - \rho_v)g}{\sigma}} \left( \frac{C_p l}{0.013 h_{fg} P r^{1.7}} \right)^3 \quad (2.36)$$

where  $g$  is the gravity. Borée [97] then improved this model to extend its domain of validity to very weakly subcooled flows<sup>2</sup>. The parameter  $B$  is now defined in terms of the Stanton number.

$$B_{Borée} = \frac{q''}{2(1 - \frac{\rho_v}{\rho_l}) S t_{lim} \rho_l C p_l v_l} \quad (2.37)$$

$S t_{lim}$  is the limit value for Stanton number above which correlation of Borée is no longer valid. This limit is fixed at 0.0065.

Tolubinski and Kostanchuk [98] carried out experimentations on heated stainless steel plate with water. This correlation (Equation 2.38) was checked for high pressure boiling water experiment (see Table 2.4).

$$D_{B,TK} = \min \left( 0.0006 \exp \left( \frac{-\Delta T_{sub}}{45} \right); 0.014 \right) \quad (2.38)$$

where  $\Delta T_{sub} = T_l - T_{sat}$ .

Fritz assumed static balance between buoyancy and surface tension forces and gives good results at atmospheric pressure (Equation 2.39).

$$D_{B,Fritz} = 0.0208 \theta \sqrt{\frac{\sigma}{g(\rho_l - \rho_v)}} \quad (2.39)$$

where  $\theta$  is the contact angle fixed by the author to  $41^\circ$ . Kocamustafaogullari [99] modified Fritz correlation [72] in order to extend it to the highest pressure values (Equation 2.40).

---

<sup>2</sup>i.e. when  $\Delta T_{sub}$  tends toward 0.

$$D_{B,KI} = 0.0012 \left( \frac{\rho_l - \rho_v}{\rho_l} \right)^{0.9} D_{B,Fritz} \quad (2.40)$$

Cole model [23] is only validated at low pressure condition for pool boiling, pressure ranges from 0.06 bar to 1 bar.

$$D_{B,Cole} = \left( \frac{\sigma}{g(\rho_l - \rho_g)} \right)^{0.5} \frac{\rho_l C p_l \Delta T_{sub}}{\rho_g h_{fg}} \quad (2.41)$$

Yoo et al. [70] proposed a model that takes into account the sliding of the bubble on the wall. Indeed, several observations have shown that the bubble, when leaving its nucleation site, does not necessarily take off from the wall but may slide on it and can continue to grow as presented in Figure 2.2. While sliding, the bubble is still in the superheated liquid layer and take energy from this layer and the heated wall.

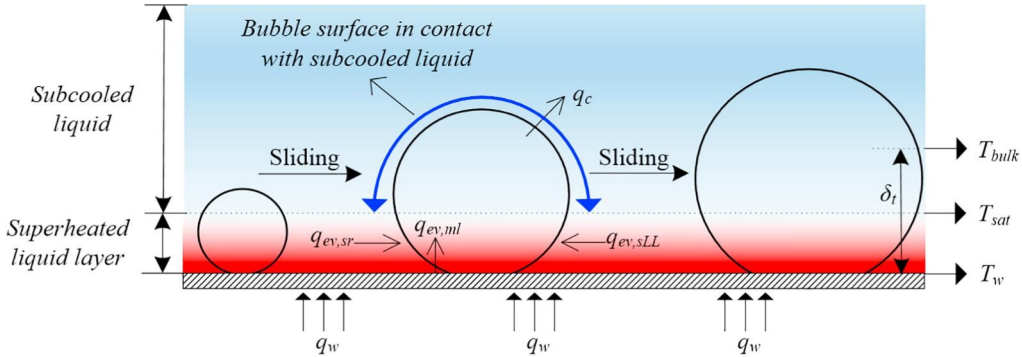


Figure 2.2: Heat transfer mechanism associated with the growth of sliding bubble, reprinted from Yoo et al. [70].

Yoo and Estrada-Perez correlation is defined by Equation 2.42.

$$D_{YE} = \frac{2A't_{sl}^{0.5} \left( 1 + \frac{B't_{sl}}{3} \right) + D(0)}{1 + B't_{sl}} \quad (2.42)$$

with  $t_{sl}$  the sliding time of the bubble on the wall, and:

$$A' = 2\gamma Pr^{-0.5} Jan_h^{0.5} \left( \frac{A_{ml}}{A_{tot}} \right) + (1-f) \frac{2b\lambda_l(T_w - T_{sat})}{\rho_v h_{fg} \sqrt{\pi\eta_l}} \quad (2.43)$$

$$B' = \frac{f \Delta T_{sub} C}{1 - \frac{\rho_v}{\rho_l}} \quad (2.44)$$

$$\gamma = \sqrt{\frac{\lambda_s \rho_s C p_s}{\lambda_l \rho_l C p_l}} \quad (2.45)$$

$$Ja = \frac{\rho_l C p_l (T_w - T_{sat})}{\rho_v h_{fg}} \quad (2.46)$$

$$\eta = \frac{\lambda}{\rho C p} \quad (2.47)$$

$$\frac{A_{ml}}{A_{tot}} = 1.22\gamma^{-0.79}e^{-0.204Ja} \quad (2.48)$$

with  $C = 0.1$ ,  $f = 0.3$ ,  $b = 0.24$  and  $D(0) = 25\mu m$ .

The range of validity of those models are summarised in the Table 2.4.

Table 2.4: Diameter correlations validity range

Author and Year	Fluid	Experiment	Pressure	Heat flux	Velocity	Subcooling
-	-	-	[bar]	[MW/m <sup>2</sup> ]	[m/s]	[°C]
Unal 1975	Water	Convective/vertical	[1-177]	[0.47-10.64]	[0.08-9.15]	[3-86]
Cole 1960	Water	Pool boiling	[0.06-1]	[0.022-0.067]	-	[3-12]
Yoo and Estrada 2018	R113	Convective	1	[0.0028-0.031]	-	[0.3-13.5]
Tolubinsky and Kostanchuk 1970	Water	Convective/horizontal	[1-10.13]	0.47	[0.08-0.2]	[5-20]
Kocamustafaogullari and Ishii 1983	Water	Pool boiling	[0.067-141.8]	-	-	-

## Correlations for bubble detachment frequency

Classically, models for detachment frequency are highly correlated to the bubble departure diameter models following a general equation  $f \times D_B = cte.$

The frequency of bubble detachment can be expressed as the inverse of the sum of the growth time  $t_g$  of a bubble on the heated wall and the waiting time  $t_w$  between two nucleations (2.49).

$$f = \frac{1}{t_g + t_w} \quad (2.49)$$

Two families of models can be identified: some authors try to model the detachment frequency  $f$  directly, while others try to model the growth and detachment times ( $t_g$  and  $t_w$ ) of the bubble.

The Cole [13] bubble departure frequency (Equation 2.50) was derived assuming a force balance between buoyancy and drag forces (drag coefficient constant). Cole performed experiments on heated zirconium ribbon suspended in a water beaker at saturation. Observations were carried out with high-speed camera, for pool nucleate boiling.

$$f_{Cole} = \sqrt{\frac{4g(\rho_l - \rho_v)}{3\rho_l D_B}} \quad (2.50)$$

The model of Ivey [100] was developed to be specifically used for coalesced bubbles and is shown in equation 2.51.

$$f_{Ivey} = 0.9 * \sqrt{\frac{g}{D_B}} \quad (2.51)$$

The Stephan and Hammer [24] model includes the effect of surface tension and was developed as Cole's correlation for pool boiling according to the author. Equation (2.52) can also be used for low-pressure subcooled flow boiling cases.

$$f_{Stephan} = \frac{1}{\pi} \sqrt{\frac{g}{2D_B}} \left( 1 + \frac{4\sigma}{\rho_l g D_B^2} \right) \quad (2.52)$$

Zuber [101] established a correlation at atmospheric pressure with water and CC14 in pool boiling on an horizontal surface. This correlation, as Cole's correlation (2.50), depends on bubble diameter (see Equation 2.53) which was analytically deduced assuming a thermal boundary layer around the bubble.

$$f_{Zuber} = \frac{1.18}{2D_B} \left( \frac{\sigma g(\rho_l - \rho_v)}{\rho_l^2} \right)^{0.25} \quad (2.53)$$

Basu et al. [102] proposes an expression for the characteristic times derived from experimental data obtained for water/steam subcooled flows (Equation 2.54 and 2.55).

$$t_{g,Basu} = \frac{D_{Basu}^2}{45e^{-0.02Ja_{sub}} Ja_{sub} \eta_l} \quad (2.54)$$

where  $Ja_{sub} = \frac{\rho_l C p_l \Delta T_{sub}}{\rho_v h_{fg}}$ .

$$t_{w,Basu} = 139.1(T_w - T_{sat})^{-4.1} \quad (2.55)$$

Unal [15] expresses the growth time in terms of the same parameters as his departure diameter correlation (2.56).

$$t_{g,Unal} = \frac{1}{1.46CB_{Unal}\phi} \quad (2.56)$$

with C as:

$$C = 65 - 5.69 \cdot 10^{-5}(P - 10^5) \quad for : 1 < P < 10 \text{ bar} \quad (2.57)$$

and with  $B_{Unal}$  and  $\phi$  defined by Equation (2.34) and (2.35).

Yeoh et al. [42] proposed another expression for the waiting time and assumed that  $t_w = 3t_g$ .

$$t_{w,Yeoh} = \frac{1}{\pi\eta} \frac{(T_w - T_l)C_1r_c}{(T_w - T_{sat}) - \frac{2\sigma T_{sat}}{C_2\rho_v h_{fg} r_c}} \quad (2.58)$$

with:

$$r_c = \left( \frac{1}{C_1 C_2} \right)^{0.5} \left( \frac{2\sigma T_{sat} k_l}{\rho_v h_{fg} q''} \right)^{0.5} \quad (2.59)$$

$$C_1 = \frac{1 + \cos(\theta)}{\sin(\theta)} \quad (2.60)$$

$$C_2 = \frac{1}{\sin(\theta)} \quad (2.61)$$

where  $\theta$  is the contact angle.

The range of validity of those models are summarised in Table 2.5.

Table 2.5: Frequency correlations validity range

Author and Year	Fluid	Experiment/Data	Pressure	Heat flux	Velocity	Subcooling
-	-	-	[bar]	[MW/m <sup>2</sup> ]	[kg/m <sup>2</sup> .s]	[°C]
Cole 1960	Water	Pool boiling	1	-	-	-
Stephan 2014	Water		1	-	-	-
Basu 2005	Water	Convective/Vertical	[1.03-3.2]	[0.025-1.13]	[124-926]	-
Ivey 1967	Water	Pool boiling	[0.006-1]	-	-	[18-49]
Yeoh 2008	Water	Convective/Vertical	1	[0.06-0.206]		[2.5-20]
Zuber 1962	Water/CCl <sub>4</sub>	Pool boiling	1	[0.557 - 2.09]	-	-

## Correlations for nucleation site density

Active nucleation site density mainly depends on the nature of the heated wall, the local fluid parameters as well as the superheat and wettability.

Lemmert and Chawla [103] formulated it for low pressure conditions.

$$N_{LC} = C^n(T_w - T_{sat})^n \quad (2.62)$$

with  $C = 210$  and  $n = 1.805$ .

Krepper et al. [104] modified the values of  $C$  and  $n$  constant in order to extend it for high pressure boiling conditions.

Kocamustafaogullari and Ishii [14] propose to express the nucleation site density as a function of cavity radii and physical properties of the fluid (Equation 2.63).

$$N_{a,KI} = \frac{f(\rho^*) R_c^{-4.4}}{D_{KI}^2} \quad (2.63)$$

with  $\rho^* = (\rho_l - \rho_v)/\rho_v$  and:

$$f(\rho^*) = 2.15710^{-7} \rho^{*-3.2} (1 + 0.0049 \rho^*)^{4.13} \quad (2.64)$$

$$R_c^2 = \frac{4\sigma T_{sat}}{\Delta T_{sub} \rho_v h_{fg} D_B} \quad (2.65)$$

Basu et al. [105] propose an empirical correlation from experimental data obtained for water/steam and Freon 113 flows for different heaters materials (copper, zirconium and nichrome).

$$N_{a,Basu} = \begin{cases} 0, 34.10^4(1 - \cos(\theta))\Delta T_{sat}^2 & \text{if } T_{w,ONB} - T_{sat} < \Delta T_{sat} < 15^\circ C \\ 0, 34.10^{-1}(1 - \cos(\theta))\Delta T_{sat}^{5.3} & \text{if } \Delta T_{sat} > 15^\circ C \end{cases} \quad (2.66)$$

with  $\theta$  the contact angle between the bubble and the wall.

Yang and Kim [106] proposes a correlation (Equation 2.67) based on wall superheat condition and validated at low pressure for superheat between  $5^\circ C$  and  $12^\circ C$ .

$$N_{a,Yang} = 0.28 \Delta T_w^{2.66} \quad (2.67)$$

where  $\Delta T_w = T_w - T_{sat}$  is the wall superheat.

Hibiki and Ihsii [107] propose a mechanistic model (Equations 2.68 to 2.70) as a function of the size and cone angle distributions of cavities present on the heated surface. This model was validated for different types of flow (pool boiling and convective). Comparison of this model with high pressure water data over wall superheat is presented Figure 2.3.

$$N_{a,Hibiki} = \bar{N}_n \left( 1 - \exp \left( \frac{\theta^2}{8\mu^2} \right) \right) \left( \exp \left( f(p^+) \frac{\lambda'}{R_c} \right) - 1 \right) \quad (2.68)$$

where  $\bar{N}_n = 4.72 \times 10^5 \text{ sites/m}^2$ ,  $\mu = 0.722 \text{ rad}$ ,  $\lambda' = 2.5 \times 10^{-6} \text{ m}$  and  $R_c$  and  $f(p^+)$ :

$$f(p^+) = -0.01064 + 0.48246\rho^+ - 0.22712\rho^{+2} + 0.05468\rho^{+3} \quad (2.69)$$

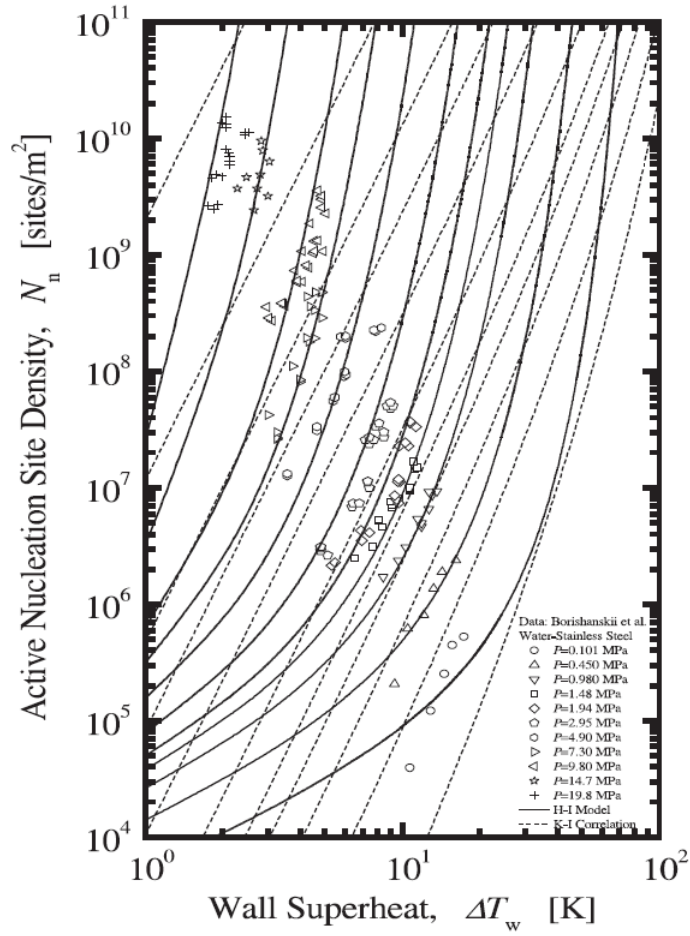


Figure 2.3: Comparison of Hibiki active nucleation site density model with high pressure water data, reprinted from Hibiki and Ihsii [107].

where  $\rho^+ = \log(\rho^*)$  and  $\rho^* = \Delta\rho/\rho_g$ .

$$R_c = \frac{2\sigma(1 + (\rho_g/\rho_f))/P_f}{\exp(h_{fg}(T_g - T_{sat})/(RT_gT_{sat})) - 1} \quad (2.70)$$

Most of the correlations that determine the nucleation site density exhibits a dependence on wall superheat (as well as comparative studies as the one proposed by Vadlamudi and Nayak [108]). This justifies that in order to develop and validate a model for the nucleation site density, an accurate and real time monitoring of the wall temperature is necessary. The range of validity of those models are summarised in Table 2.6.

Table 2.6: Nucleation site density correlations validity range

Author and Year	Fluid	Experiment/Data	Pressure	Heat flux	Velocity	Subcooling
-	-	-	[bar]	[MW/m <sup>2</sup> ]	[kg/m <sup>2</sup> s]	[°C]
Lemmert and Chwala 1977	Water	Pool boiling	1	-	-	0
Basu 2005	Water/R113	Convective	[1.03-1.3]	[0.019-0.963]	[186-886]	[6.6-46.5]
Kocamustafaogullari 1983	water	Pool boiling	[1 - 198]	-	-	-
Hibiki	Water	Convective	[1 - 198]	[0.058-1.16]	[0 - 886]	-
Yang 2016	Water	Convective	1	[0.017 - 0.289]	[122 - 657]	[4.7 - 12]

### 2.2.3 Orders of magnitude analysis for our study

Those models offer us the access to a wide database that should allow us to determine some orders of magnitude for the size of the bubbles at detachment and the frequency of detachment for our operating conditions. These orders of magnitude will help us to determine the characteristics of the instrumentation that will be used in our future test section.

In his thesis, Stéphane Pujet [109] considered three operating conditions that covers the whole range of working conditions for a PWR (from atmospheric pressure up to normal condition  $P \sim 15.8\text{ MPa}$ ). Those three configurations are described in Table 2.7. For each of those thermal hydraulic conditions, Pujet have determined some orders of magnitude for several parameters that are important to characterize the boiling process. One should notice that the case 1 does correspond, in terms of thermal hydraulic range, to the experiments conducted by Gunther (1951). Some parameters like the bubble diameter or the growth time are then directly measured, those experimental values being considered as reliable orders of magnitude for the concerned parameters. During his experiments, Gunther measured various parameters like the bubble size and their time evolution, the number of bubbles formed at the wall by unit area and time, the fraction of wall wetted by bubbles. For those experiments, the fluid velocity is closed to  $3\text{ m/s}$  which is prototypical of the velocity encountered in industrial configurations.

Some results in Table 2.7 were obtained from correlations extrapolated beyond their range of validity. They appear in italic. Underlined values means that several models were tested, the retained value being considered as the most reliable. In his work, Pujet used this scale analysis to identify the most important mechanisms while studying the bubble growth over a heated surface. We propose here to use a similar approach to determine the characteristics of the instrumentation of our incoming experimental setup.

The models mentionned in the previous section can be used outside their field of validity and give a first order of magnitude for predimensioning the test model and instrumentation.

Several authors have gathered existing models for comparison and selection to find the best combination with the CFD tools for PWR applications. Montout [3] described some empirical and mechanistic models, then analysed them, compared them and selected the most accurates for NEPTUNE code.

Mali et al. [72] study different associations of models for bubble departure diameter, detachment frequency and nucleation site density (see the simulation matrix Table 2.8), but also boiling-induced turbulence, heat transfer and drag force models, in order to study subcooled boiling in a vertical tube using the two-fluid model.

Using the CFD software (ANSYS-Fluent), Mali shows by comparing his simulations (in terms of void fraction distribution or fluid temperature) with Bartolomei's results that the best model combination seems to be: KI-KI (Kocamustafaogullari correlation for diameter, Cole correlation for frequency and again Kocamustafaogullari for density).

In his work, Murallidharan [110] proposes to use various existing models, often outside their range of validity, to combine them and model subcooled boiling flows at high pressure using Star-CCM+ code. The simulations are then compared to Bartolomei's experimental results (bubble diameter, detachment frequency and nucleation site density see Table 2.9). By fixing a combination and varying only one model at a time, Murallidharan identified models with significant deviations outside their range of validity. With this method, the following models are recommended: Hibiki and Ishii correlation for nucleation site density and Cole correlation for bubble departure frequency.

Table 2.7: Analysis of three flow configuration for nucleate boiling, reprinted from Pujet [109].

		Case 1	Case 2	Case 3
<b>Thermal hydraulic parameters</b>				
Pressure	[bar]	1	25	158
Liquid velocity	[m/s]	3.06	2	3.57
Local thermodynamic titre	[-]	-0.095	-0.056	-0.037
Heat flux	[kW/m <sup>2</sup> ]	4500	640	450
<b>Intermediate variables</b>				
Reynolds number	[-]	61200	142259	300000
ONB parietal overheating	[K]	30	2.3	0.5
Unal parietal overheating	[K]	39	5	4.2
Jens-Lottes parietal overheating	[K]	36	14.9	1.7
Monophasic heat exchange coefficient $h_{1\phi}$	[W/m <sup>2</sup> ]	21000	18338	27880
Two-phase flow exchange coefficient $h_{2\phi}$	[W/m <sup>2</sup> ]	52941	23704	55556
$y+$ bubble top	[-]	391	84	181
Bubble production	[m <sup>2</sup> /s]	1.1e9	1.5e10	8.7e8
<b>Length scales</b>				
Experimental bubble diameter	[μm]	700	120-140	140
Unal bubble diameter $D_{Unal}$	[μm]	761	130	142
Sliding distance	[μm]	560	1e4	8e5
<b>Time scales</b>				
Experimental growth time	[μs]	200	-	-
Unal growth time $t_{g,Unal}$	[μs]	198	16890	776189
Kolmogorov scales $t_k$	[μs]	113	69	31
Integral scale $t_{int}$	[μs]	552	157	102

Model combination name	Bubble departure diameter model	Bubble departure frequency model	Nucleation site density model
TK-LC	Tolubinsky-Kostanchuk	Cole	Lemmart-Chawla
KI-LC	Koca-Ishii	Cole	Lemmart-Chawla
Unal-LC	Unal	Cole	Lemmart-Chawla
TK-KI	Tolubinsky-Kostanchuk	Cole	Koca-Ishii
KI-KI	Koca-Ishii	Cole	Koca-Ishii
Unal-KI	Unal	Cole	Koca-Ishii

Table 2.8: Simulation matrix for boiling parameter models used in Mali's study, reprinted from Mali et al. [72].

Simulation matrix		
$N$ (sites/m <sup>2</sup> )	$f$ (1/s)	$D$ (m)
<i>BASE simulation</i>		
HI	Cole	Koca
<i>N models simulation matrix</i>		
LC-M	Cole	Koca
WD	Cole	Koca
BB	Cole	Koca
<i>f models simulation matrix</i>		
HI	Stephan	Koca
HI	Zuber	Koca
HI	KQ	Koca
HI	KD	Koca
<i>D models simulation matrix</i>		
HI	Cole	Fritz
HI	Cole	Cole
HI	Cole	TK
HI	Cole	KQ
HI	Cole	KD

Table 2.9: Simulation matrix for boiling parameter models used in Murallidharan's study, reprinted from Murallidharan [110].

The problem in our case is not to find the best model association to establish orders of magnitude on a result such as parietal superheat, void ratio or other but to select these models independently. In this type of study, one can imagine that a model association gives a good result on the global characteristics of the flow but that this result comes from error compensation. One cannot stop at these results.

In this work, we intend to get some reliable orders of magnitude of the parameters we wish to measure. To do this, we propose to test some of the previously introduced models by considering each of them as independant from the others. Those tests will be performed on a large range of parameters in terms of pressure and subcooling. Despite most of those models not being valid at high pressure (prototypical of PWR), their behaviour outside their range of validity will be studied, to see in particular if some trends can be exhibited.

### Comparison for bubble diameter correlations

In order to determine orders of magnitude of the bubble size we expect to measure, we used the models presented above. In order to study the relevance of these different models, we carried out a sensitivity study. We focused on the effect of the pressure on this parameter. The temperature of the fluid as well as the flow rate and the thermodynamic equilibrium quality are imposed while the pressure is varying. Figure 2.4 shows the results obtained.

Comparing the diameters between the different models/correlations, it appears first that models seems to show consistant behaviour predicting a bubble size decrease with pressure increase, except for the model of Tolunbinski-Konstanchuk which exhibits an opposite trend. This behaviour sounds inconsistent and confirm that this model is not worth being used for high pressure operating conditions. One should also notice that the model of Fritz predicts much larger bubble size than the others models while the model of Cole tends to overestimate

the bubble size at low pressure and underestimate it at high pressure compared to other models. Those observations, coupled to the fact the models of Unal and Kocamustafaogullari have *a priori* the closest ranges of validity compared to our targeted conditions, confirm our choice of focusing on those two models.

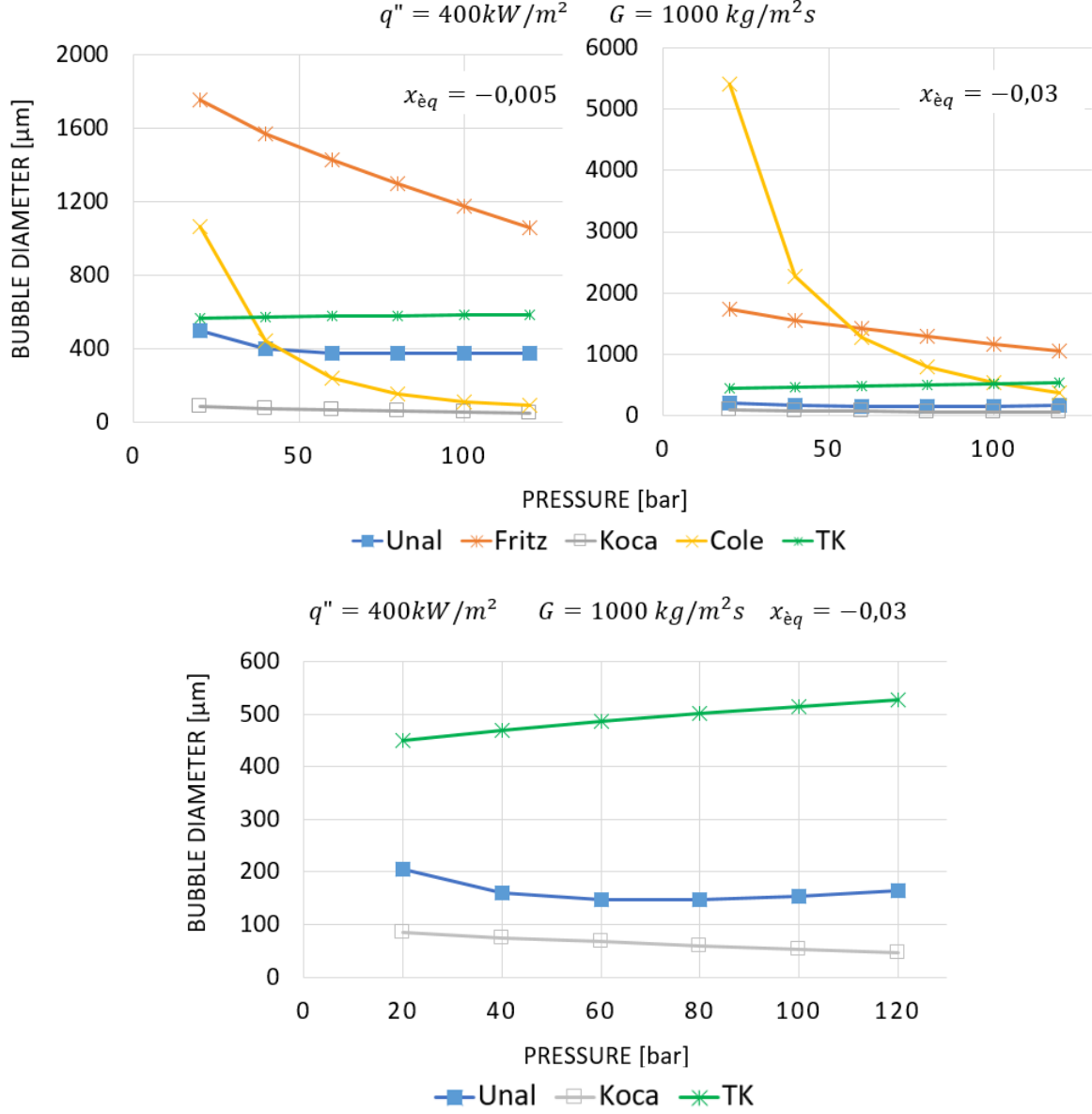


Figure 2.4: Comparison between correlations for departure bubble diameter as a function of pressure for a fixed heat flux of  $400 \text{ kW/m}^2$ , fixed mass velocity of  $1000 \text{ kg/m}^2\text{s}$  and equilibrium quality of  $-0.005$  (upper left) and  $-0.03$  (upper right). Zoom on the three most accurate models (bottom).

Results from Unal and Kocamustafaogullari and Ishii models are closer but show a difference at high pressure: the order of magnitude changes from a few microns for Kocamustafaogullari and Ishii to several tens of microns for Unal (see Figure 2.5). In CFD, in particular in the NEPTUNE code used to simulate boiling flows, it is known that coupling Unal model with the model of Kurul and Podowski for nucleation site density [3] does not

lead to good predictions of wall superheat. The model of Kocamustafaogullari and Ishii for bubble diameter coupled with the Ishii nucleation site density model gives better results [72]. However, Unal's model is widely used in the literature, and in the studies carried out, it is noticed that it is quite close to the experimental values in PWR conditions [4] as well as in atmospheric pressure range [51]. As the bubble size predicted by Kocamustafaogullari model is much lower than the one predicted by Unal it might indicate that Kocamustafaogullari model predicts the bubble size when it detached from its nucleation site whereas Unal model might predict the bubble lift-off diameter. This last one is probable larger because of potential coalescence while sliding along the heated wall before detaching.

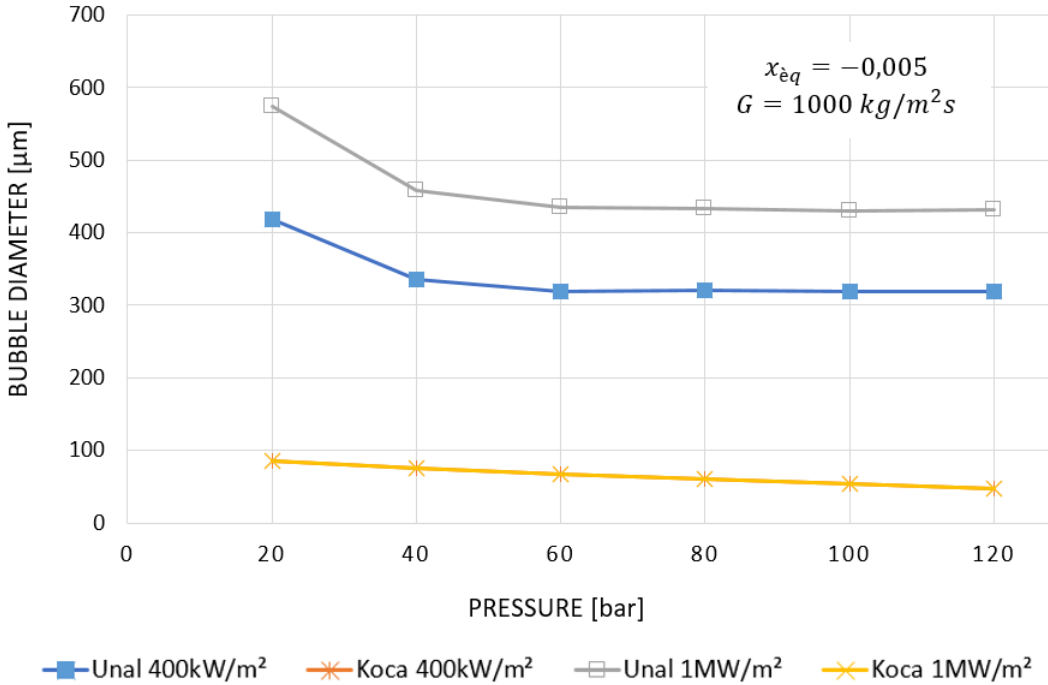


Figure 2.5: Focus on the Unal and Kocamustafaogullari models and their evolution with pressure and heat flux (for  $400 \text{ kW/m}^2$  and  $1 \text{ MW/m}^2$ ).

The Kocamustafaogullari and Ishii model only takes into account for pressure effects for the prediction of the bubble size. Figure 2.5 shows that a change in the value of heat flux or subcooling -all other parameters being equal- does not influence the evolution of diameter. In contrast, Unal's model exhibits a dependency of the diameter to heat flux or equilibrium quality. One should notice that Unal model is purely empirical and unfortunately dimensional. In contrast, Kocamustafaogullari's model is semi-empirical in that sense it is based on dimensionless numbers.

In order to determine the characteristics of the instrumentation that will be required for the future experimental program, it is essential to have a reliable model to determine the bubble size. Indeed, having to measure bubbles of  $300 \mu\text{m}$  or  $10 \mu\text{m}$  does not lead to the same instrumentation constraints. Given the discrepancies in bubble diameters predicted by the two correlations, it seems interesting to study these models in detail. Montout [3] carried out a critical analysis of Unal model. The relative deviations of the bubble diameter calculated from Unal's correlation compared to his experimental validation data show a maximum deviation

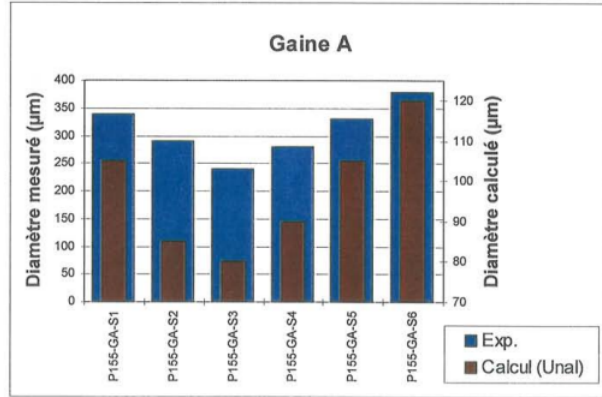
of  $\pm 67\%$ . At high pressure, Montout noticed that this deviation decreases to  $\pm 30\%$ . As a consequence, Unal seems to be more accurate at high pressure.

March [4] compared bubble diameter measurements with Unal diameter correlation. His results are given in Figure 2.6. For both surface roughness (A- $R_a = 0.2 \mu m$  or B- $R_a = 3.9 \mu m$ ), the correlation seems to correctly capture the variation of the experimental diameter. Nevertheless, for the smooth surface (A), the diameter is underestimated by Unal (see upper Figure 2.6). March explains these inconsistencies by the fact that Unal's model does not take account for subcooling. Another explanation for these inconsistencies can also be proposed: the bubble sizes measured by March do not necessarily correspond to the moment when they detach from the wall. However, after detaching from the wall, a bubble can - depending on the subcooling - coalesce with the surrounding bubbles and increase in diameter. This behaviour, observed by Roy et al. [58], could explain why the diameters measured by March are systematically underestimated by the Unal correlation. Whatever the flowrate, the roughness seems to have an impact on the bubble size. This confirm that in order to be representative of industrial targeted configuration, this parameter will have to be taken into account.

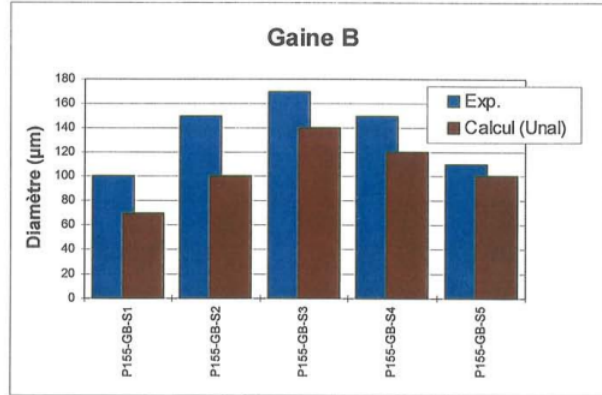
Using the database established by March [4], we can compare the results of the above correlations with some experimental bubble size data. These measurements were performed at different pressure, at  $26 \text{ bar}$  and  $155 \text{ bar}$ . All the models presented above are compared to March's experimental measurements. The aim here is to confirm that the elimination of previous model was legitimate and to establish more substantiated conclusions. As we can see on Figure 2.7, Cole's correlation does not follow the evolution of the bubble diameter as a function of subcooling, the data at low pressure is greatly overestimated and does not appear on the graph. The Tolubinsky and Kostanchuk correlation [98] follows the correct evolution with subcooling but overestimates the experimental values of bubble diameters. Kocamustafaogullari correlation underestimates the high pressure diameter values, results being in a good agreement for the lowest pressure. Nevertheless at constant pressure, the effects of subcooling or thermodynamic equilibrium quality on the bubble size are not taken into account in the Kocamustafaogullari correlation. Unal correlation seems to be much more accurate, and well reproduce the influence of the subcooling. Nevertheless, one can notice that March measurements were performed with a low quality camera ( $25 \text{ fps}$ ). One might expect that high speed and high performance technology will lead to more precise and maybe, different diameter measurements.

All these elements lead us to no longer consider for the Kocamustafaogullari's model and to use the Unal model to determine the orders of magnitude of the bubble diameters at detachment.

The Yoo et al. [70] model calculates the bubble departure diameter taking into account for a time during which the bubble is sliding on the wall  $t_{sl}$  (Equation 2.42). In this model, the bubble diameter at detachment depends on the sliding time, starting from an initial bubble diameter of  $25 \mu m$ . Using March's data, one can therefore calculate the sliding time corresponding to the bubble diameter measured by March. For March's data, we determine a sliding time ranging from  $0.3 \text{ ms}$  to  $7 \text{ ms}$  (see Figure 2.8).



a) Gaine A



b) Gaine B

Référence	Gaine	Flux (MW/m <sup>2</sup> )	Débit (kg/m <sup>2</sup> s)	Tentrée (°C)	Xéq local	ΔT <sub>sub</sub> (K)	Vliq (m/s)	Dmoy (μm)
P26-GA-S1	A	0,60	2120	196,0	-0,046	16,9	2,48	40
P26-GA-S2	A	0,60	2100	202,0	-0,031	10,9	2,48	140
P26-GA-S3	A	0,60	2100	198,5	-0,039	14,4	2,47	55
P26-GA-S4	A	0,60	2100	198,5	-0,039	14,4	2,47	65
P26-GA-S5	A	0,75	2100	198,5	-0,032	11,4	2,48	320
P26-GB-S1	B	0,60	2100	202,0	-0,030	10,7	2,48	35
P26-GB-S2	B	0,63	2100	198,5	-0,038	13,7	2,47	30
P26-GB-S3	B	0,77	2100	198,5	-0,031	11,0	2,48	65
P26-GB-S4	B	0,78	2100	198,5	-0,030	11,0	2,48	75

Référence	Gaine	Flux (MW/m <sup>2</sup> )	Débit (kg/m <sup>2</sup> s)	Tentrée (°C)	Xéq local	ΔT <sub>sub</sub> (K)	Vliq (m/s)	Dmoy (μm)
P155-GA-S1	A	0,77	1800	330,3	-0,031	3,4	2,98	340
P155-GA-S2	A	0,77	1990	329,8	-0,042	4,6	3,27	290
P155-GA-S3	A	0,77	2200	330,5	-0,045	4,8	3,61	240
P155-GA-S4	A	0,85	2210	330,2	-0,04	4,3	3,63	280
P155-GA-S5	A	0,95	2200	330,2	-0,031	3,3	3,64	330
P155-GA-S6	A	0,96	1990	329,8	-0,023	2,7	3,31	380
P155-GB-S1	B	0,77	1810	326,1	-0,061	6,6	2,93	100
P155-GB-S2	B	0,78	1790	330,1	-0,031	3,4	2,96	150
P155-GB-S3	B	0,96	1790	330,0	-0,011	1,8	2,99	170
P155-GB-S4	B	0,95	1990	330,1	-0,022	2,6	3,31	150
P155-GB-S5	B	0,96	2200	329,2	-0,037	4,7	3,61	110

Figure 2.6: Comparison between Unal correlation and March measurements over bubble departure diameter for two different types of rod surface quality, A- $R_a = 0.2 \mu\text{m}$  B- $R_a = 3.9 \mu\text{m}$ , from March [4].

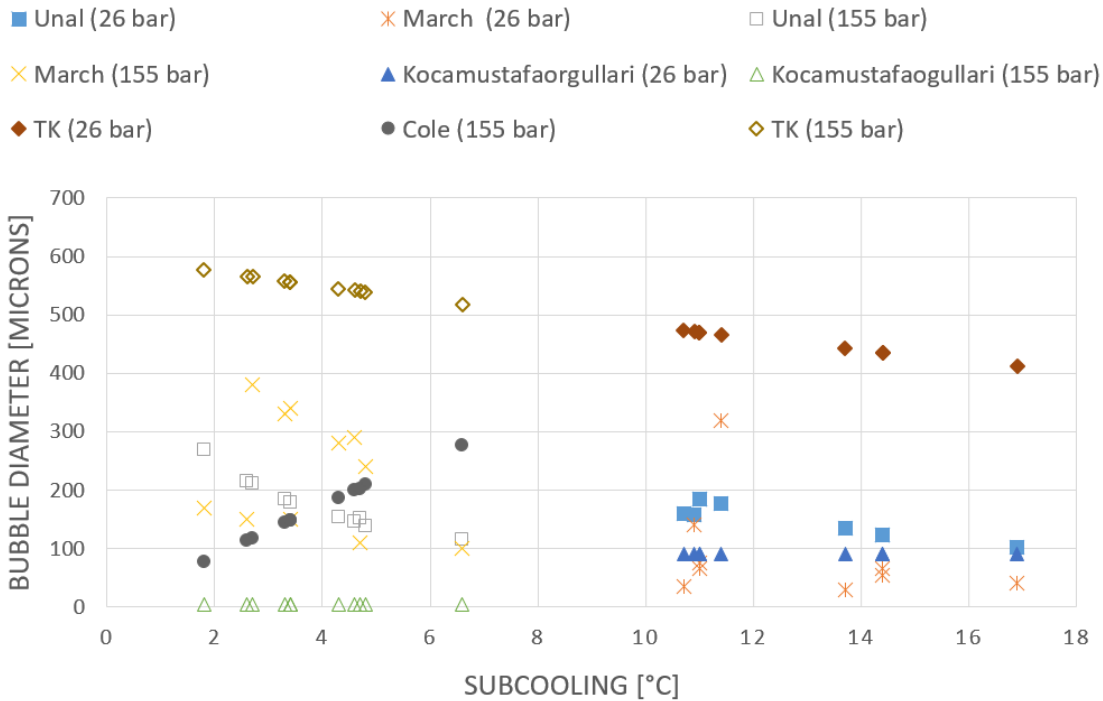


Figure 2.7: Comparison between March bubble diameter data [4] and several correlations function of the subcooling.

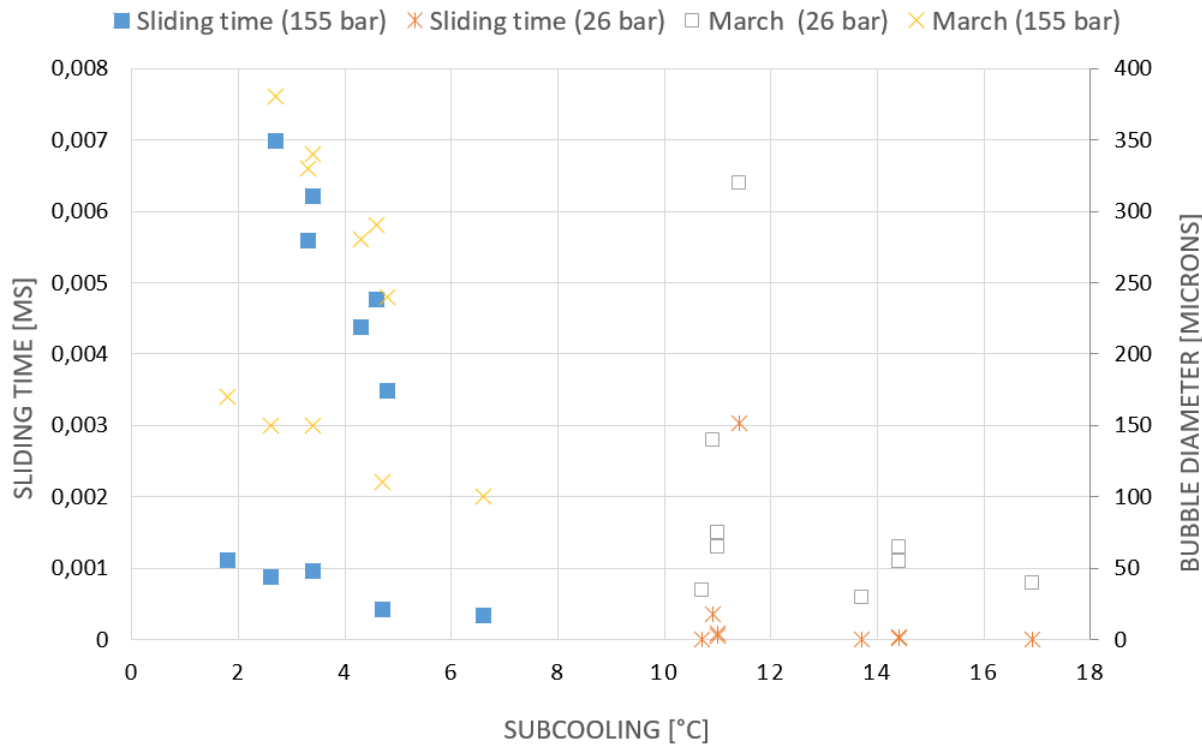


Figure 2.8: Calculation of the sliding time required to obtain the bubble diameter measured by March from the Yoo correlation.

## Comparison for bubble frequency departure correlation

In the same way as above for diameter, detachment frequency models will be evaluated through a parametric study with respect to pressure. As these models are all established at atmospheric pressure, their behaviour at high pressure is sometimes questionable. Depending on the bubble size model which is considered, the results may differ. Using Unal's model for bubble diameter, a detachment frequency can be calculated and the results from the different available correlations can be compared.

Figure 2.9 shows the prediction of the models as a function of pressure. One can see that Stephan's model strongly overestimates the detachment frequency compared to other models. Stephan's model will therefore not be retained due to its behaviour which strongly differs from the other models. The other models compared in Figure 2.10 show very variable

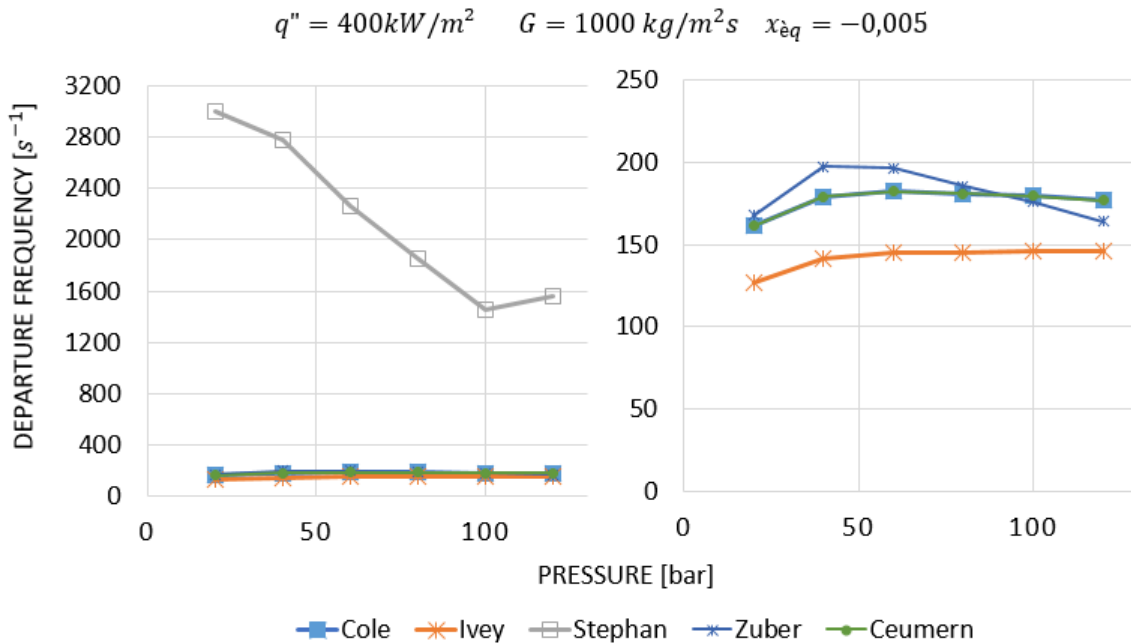


Figure 2.9: Comparison between correlations for bubble departure frequency as a function of pressure for a fixed heat flux of  $400 \text{ kW/m}^2$ , fixed mass velocity of  $1000 \text{ kg/m}$  and equilibrium quality of  $-0.005$ .

results: Cole's model predicts frequencies between  $150 \text{ Hz}$  and  $300 \text{ Hz}$  while Zuber's model can predict detachment frequencies of up to  $500 \text{ Hz}$ . Ivey model seems to predict lower detachment frequency compared to other models. The Cole model is the one used today in CFD calculation codes (Neptune CFD, [3]). Even if these models have not been validated at high pressure -the lack of experimental data limiting such validations- we will retain this reference as an order of magnitude for the detachment frequency. Nevertheless, it is important to keep Zuber's order of magnitude in mind, which gives frequencies that can go up to  $500 \text{ Hz}$ . As these models have not been validated at high pressure, different orders of magnitude can be expected, but only accurate measurements could complete this information.

Other experimental studies are worth being mentionned to get some additional informations about detachment frequency. Richenderfer et al. [51] performed bubble departure frequency measurements presented Figure 2.11. These curves show the experimental results.

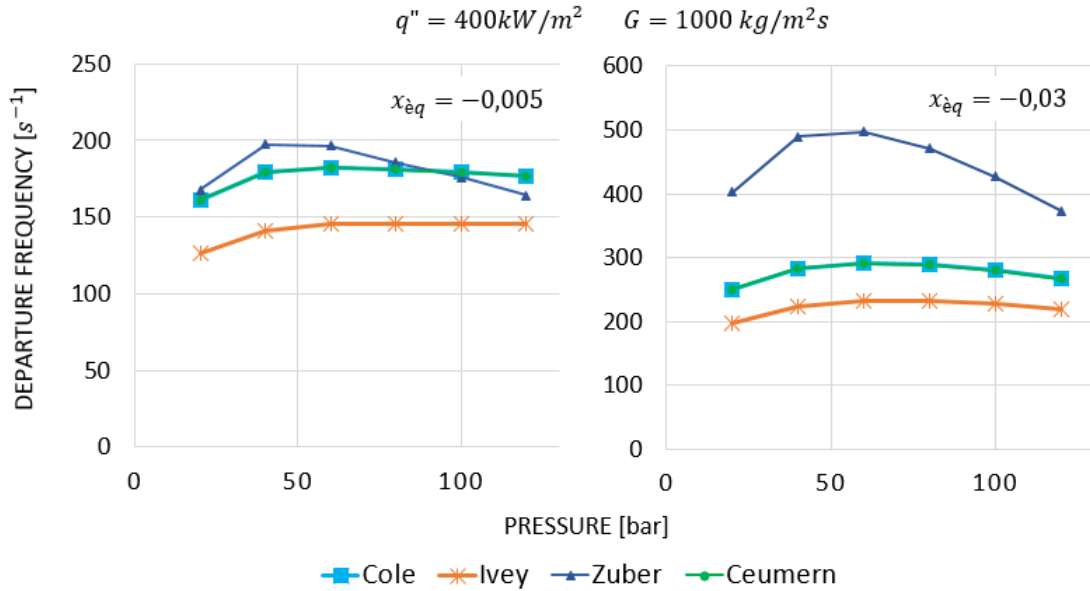


Figure 2.10: Zoom on the four most accurate correlations for bubble departure frequency as a function of pressure for a fixed heat flux of  $400 \text{ kW/m}^2$ , fixed mass velocity of  $1000 \text{ kg/m}$  and equilibrium quality of  $-0.005$  and  $-0.03$ .

These curves indicate that the detachment frequency increases from  $100 \text{ Hz}$  to  $450 \text{ Hz}$  when the heat flux increases from  $500$  to  $3250 \text{ kW/m}^2$ . Despite these data were measured at atmospheric pressure, they tend to show that the detachment frequency may strongly depends on heat flux.

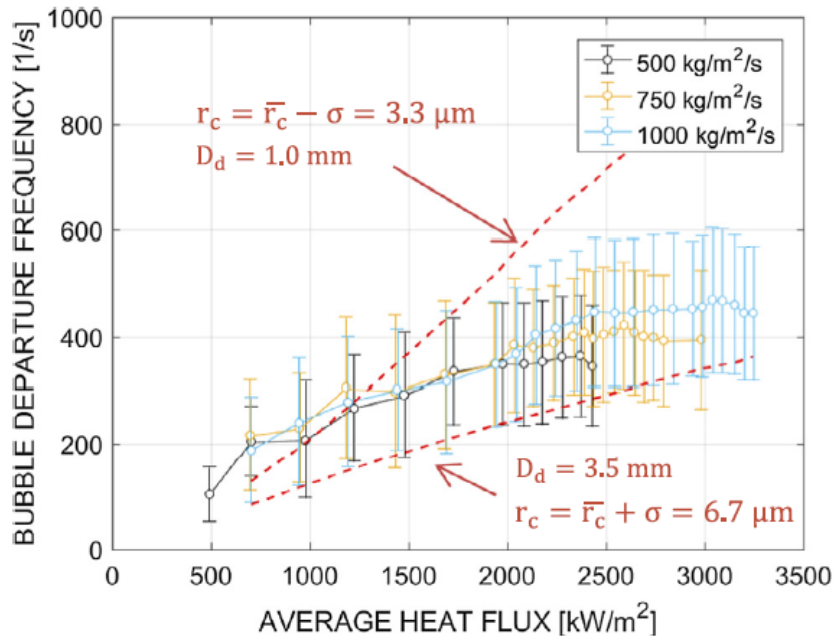


Figure 2.11: Bubble departure frequency for tests at  $1.01 \text{ bar}$ ,  $10^\circ\text{C}$  of subcooling and mass fluxes of  $500$ ,  $750$  and  $1000 \text{ kg/m}^2\text{s}$ , reprinted from Richenderfer et al. [51].

It is also worth mentionning Ooi et al. [45] work. In his work, Ooi proposes a benchmark on existing models in terms of bubble size at detachment and detachment frequency. The experiment consists in a square section ( $1.27 \times 1.27 \text{ cm}^2$ ) with an upward flow allowing measurements in subcooled boiling flow. The test section is made of stainless steel,  $99.8 \text{ cm}$  long, with quartz windows allowing visual access to the flow. Measurements are made by direct visualisation. Nine flow conditions are proposed with various subcooling, flow velocity, injected flow, and with a pressure variation ranging from 1 to 5 bar. The measurements are carried out on several nucleation sites simultaneously and make it possible to highlight the differences which can appear between several nucleation sites. Each point on the Figure 2.12 represents a bubble detachment at a nucleation site for the first condition studied. For each of these sites, we can see that the frequency of detachment can vary from one nucleation site to another one and these variations can be quite large with sites activating and deactivating during the same trial. By removing the inactivity times on the sites, we can obtain a well-defined frequency (see upper right Figure 2.12) but this does not represent reality of successive activation and deactivation. To account for these variations Ooi proposes a different formula with an average made on the differences of time observed on a site. Comparing these results with some models, the active departure frequency seems to fit with the model calculations (here Cole example see lower Figure 2.12). This work demonstrates the importance of taking into account for several nucleation sites to determine a correct order of magnitude of the detachment frequency and then compare it to existing models.

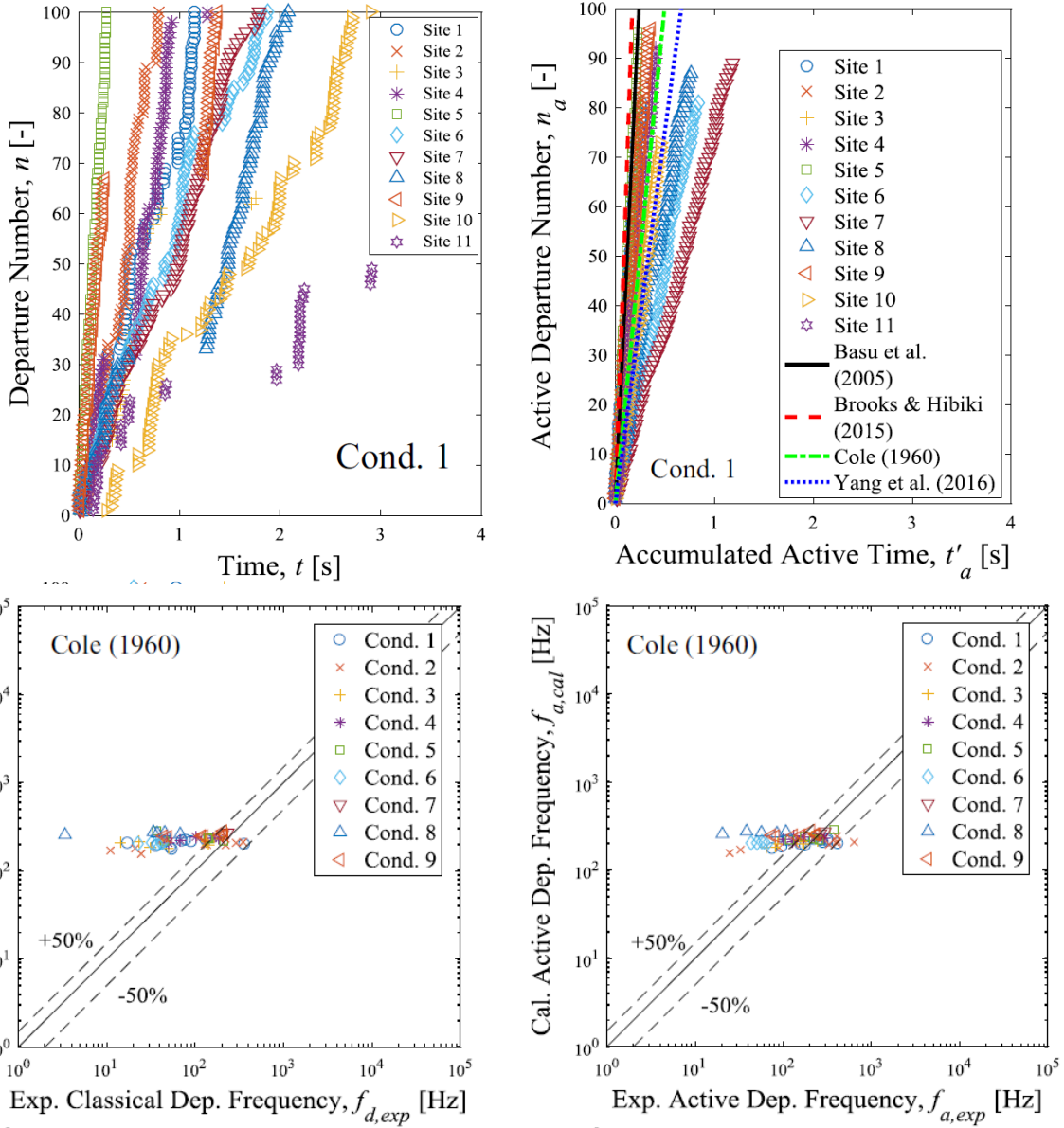


Figure 2.12: Time sequence of bubble departure for all active nucleation sites and for Condition 1 (Upper left). Time sequence of bubble departure for all active nucleation sites without considering periodic dormancy (Upper right). Comparison of classical (Lower left) and active (Lower right) active departure frequencies with predicted values by Cole correlation.

## 2.3 Conclusion and pre-designing

In this chapter, we identified the models that are important to the understanding of the boiling flow we intend to observe. The calculation methods for identifying the different characteristic stages of a boiling flow have been presented and will be used in the rest of this study.

Furthermore, some models describing the parameters we want to measure were presented. These correlations are not always defined or validated for the conditions we are interested in but their study can help us to determine first orders of magnitude in the absence of reliable data regarding our targeted operating conditions.

The Unal model can thus be defined as a reference for the size of the bubble at detachment and we can expect to measure bubbles of a few tens of microns to a few hundreds of microns. This will require high-performance instrumentation with a high spatial resolution. In addition, it has been identified that the detachment frequency can reach several hundred Hertz (despite the models being used outside their range of validity), so it will be necessary to implement a fast and reactive instrumentation. These first data make it possible to define the needs inherent in the measurements that we wish to carry out. The designing of the experiment, taking into account those results, will be presented in the next part of this work.

## **Part II**

# **Design and dimensioning of the experiment**



# Chapter 3

## Thermal hydraulic installation

### 3.1 Framework

The ambition of this project is to be able to carry out measurements under the thermal hydraulic conditions corresponding to those of PWRs, thus requiring an installation capable of providing said conditions at the boundaries of its test section. Within the CEA Cadarache Poseidon platform, several loops fulfill this criterion, in particular CIRENE, BIKINI and CORAIL.

However, the availability of these test facilities due to the projects underway at the CEA for its partners could have been a problem. Indeed, both the planned measurements and the development of the instrumentation and settings require significant availability of a facility. It was then decided to design a new facility that would allow more precise tests and autonomy with regard to the planning of existing projects.

The PWR conditions are as follows:

- Pressure: 155 bar
- Temperature: inlet - 286 °C; outlet - 323.2 °C
- Flow rate: 68 350 m<sup>3</sup>/h

values from Delhaye [5].

This installation is meant to accommodate the future test section developed in the framework of this thesis as well as future facilities requiring forced convection and prototypical PWR conditions of pressure and temperature.

### 3.2 Piping and Instrumentation Diagram

A thermal hydraulic loop consists of several basic components. The design process begins by considering the thermal hydraulic conditions required to perform the desired measurements, and determining the pressure, temperature and flow rate required to obtain such conditions. An accumulator is used to set the pressure of the primary circuit at the specified value. The pump drives the fluid and the flow rate can be regulated by a bypass system and valves. A pre-heater is installed in order to control the temperature of the circuit. Then, boiling is triggered by heating the fluid through the test section heater (by direct Joule effect). In addition, the power injected into the test section must be evacuated from the hydraulic

components, especially the pump, for safety reasons. It is therefore necessary to install a heat exchanger at the outlet of the test section. The fluid must be conditioned upstream: demineralised water is used, degassed by the circuit upstream of the primary circuit using a thermal degasser. The quality of the water can be checked (in terms of pH, demineralisation quality, dissolved gas level) before the loop is filled.

The following PID (Piping and Instrumentation Diagram) Figure 3.1 summarises the various elements required.

The blue circuit is the primary circuit composed of a pump P01, a pre-heater section REC01, the test section, an heat exchanger ECH01 which removes the heat injected into the test section (in red), the accumulator AQ01 which pressurises the circuit and regulates pressure variations. The column upstream of the accumulator is equipped with a heat exchanger ECH02 because this type of equipment cannot stand a temperature higher than 80 °C.

The green circuit is the injection circuit, where the fluid is conditioned: the demineralised water passes through a resin RE01 to control the quality of the water. It is degassed using a thermal degasser and then cooled by two heat exchangers ECH03A and ECH03B before being injected into the circuit using a charge pump P02. A measuring section allows the water quality to be sampled and monitored in terms of pH and redox potential using the VM13 valve. A drain line is provided in the primary circuit for draining the system or for hot discharges. For this purpose, a heat exchanger ECH04 is installed, which allows the pressure in the steam projection to be evacuated.

The purple circuit is the secondary industrial water circuit that feeds the various heat exchangers.

Moreover, several parameters need to be controlled and measured during the tests such as inlet and outlet pressure, inlet temperature and inlet flow rate. Measuring instruments must therefore be installed upstream and downstream of the test section. Each of these instruments can add use constraints to the design process, such as required length of straight pipe for flow meters, or the presence of condensate pot for pressure sensors. For each exchanger, a flow meter is installed on the secondary circuit with valves to control the exchange and allow heat balance calculations.

Several safety items are also installed: two safety valves protect the primary circuit from overpressure in case of an incident. A safety valve also protects the filling circuit. They are connected to a common discharge network (orange circuit). In addition, safety sensors are installed on the primary circuit: two safety pressure and temperature measurements that stop the heater if thresholds are exceeded; two control pressure and temperature measurements upstream of the accumulator to protect the equipment. A pressure differential sensor is also installed on the P01 pump to protect it with a threshold defined by its NPSH (Net Positive Suction Head). A temperature sensor is installed in the discharge line of the primary circuit to monitor the temperature when discharging.

The design of the installation was initially done in-house and then subcontracted to an engineering company for the final design plans and flexibility calculations.

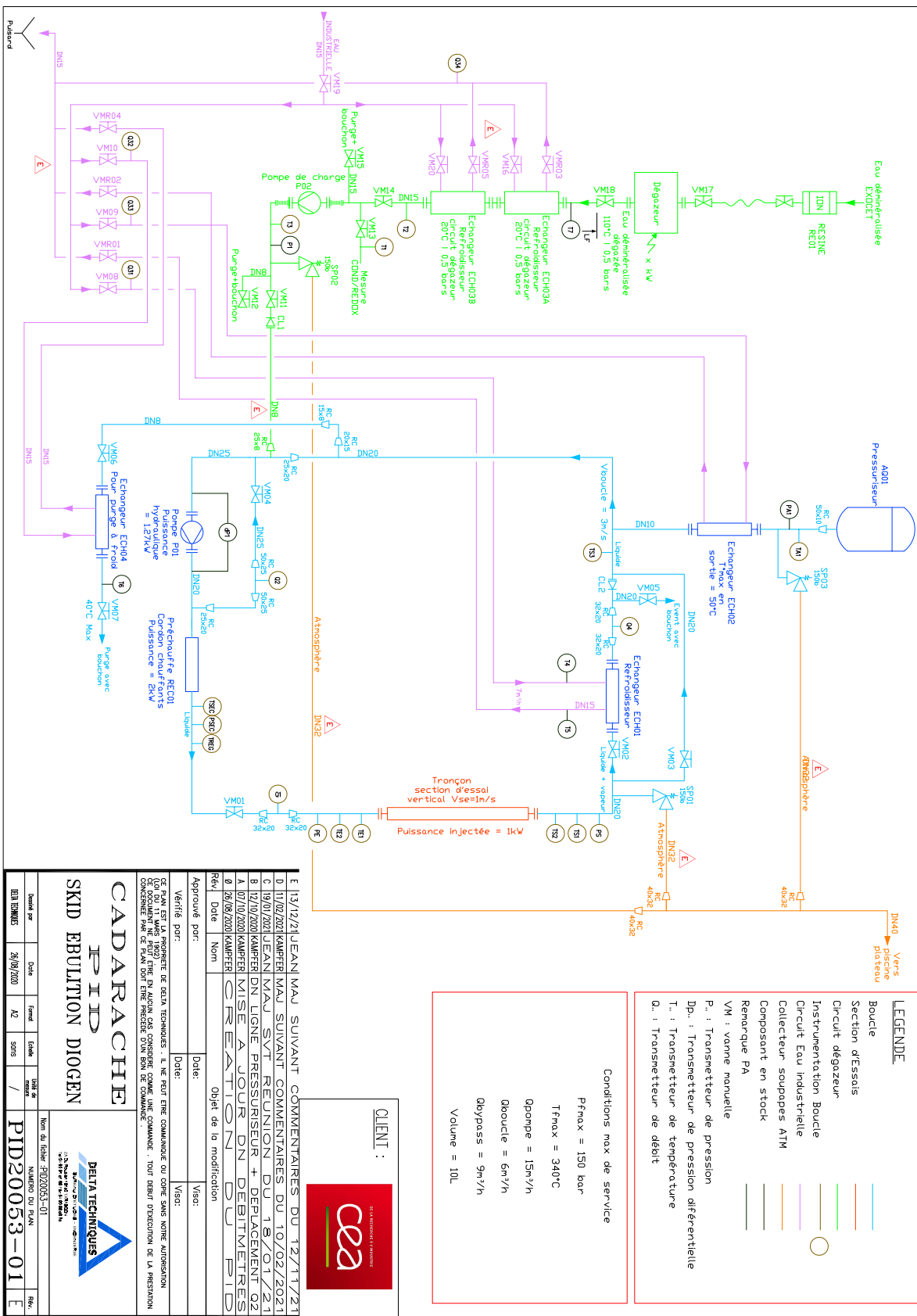


Figure 3.1: Piping and Instrumentation Diagram of the thermal hydraulic DIOGEN loop.

### 3.3 Design and manufacture

This loop, named DIOGEN for Dispositif Instrumenté d’Observation d’Ébullition Nucléée (Instrumented Device for Nucleate Boiling Observation), is to be installed in the pit of an existing building. The DIOGEN system is designed to fit on a  $2 \times 2 \times 2 m^3$  skid for easy handling and relocation (primary circuit) as presented on the plan Figure 3.2. This type of architecture is easy to manufacture and modify, and consists of an assembly of mechanically welded 304L stainless steel elements. The weight of this frame is 350 kg. An additional skid is then provided to accommodate the loop conditioning and filling circuit (see Figure 3.3). It is also made from welded 304L stainless steel components and weighs 69 kg. On these two skids, several attachment elements are added to support the elements of the loop: pump, accumulator, instrumentation.

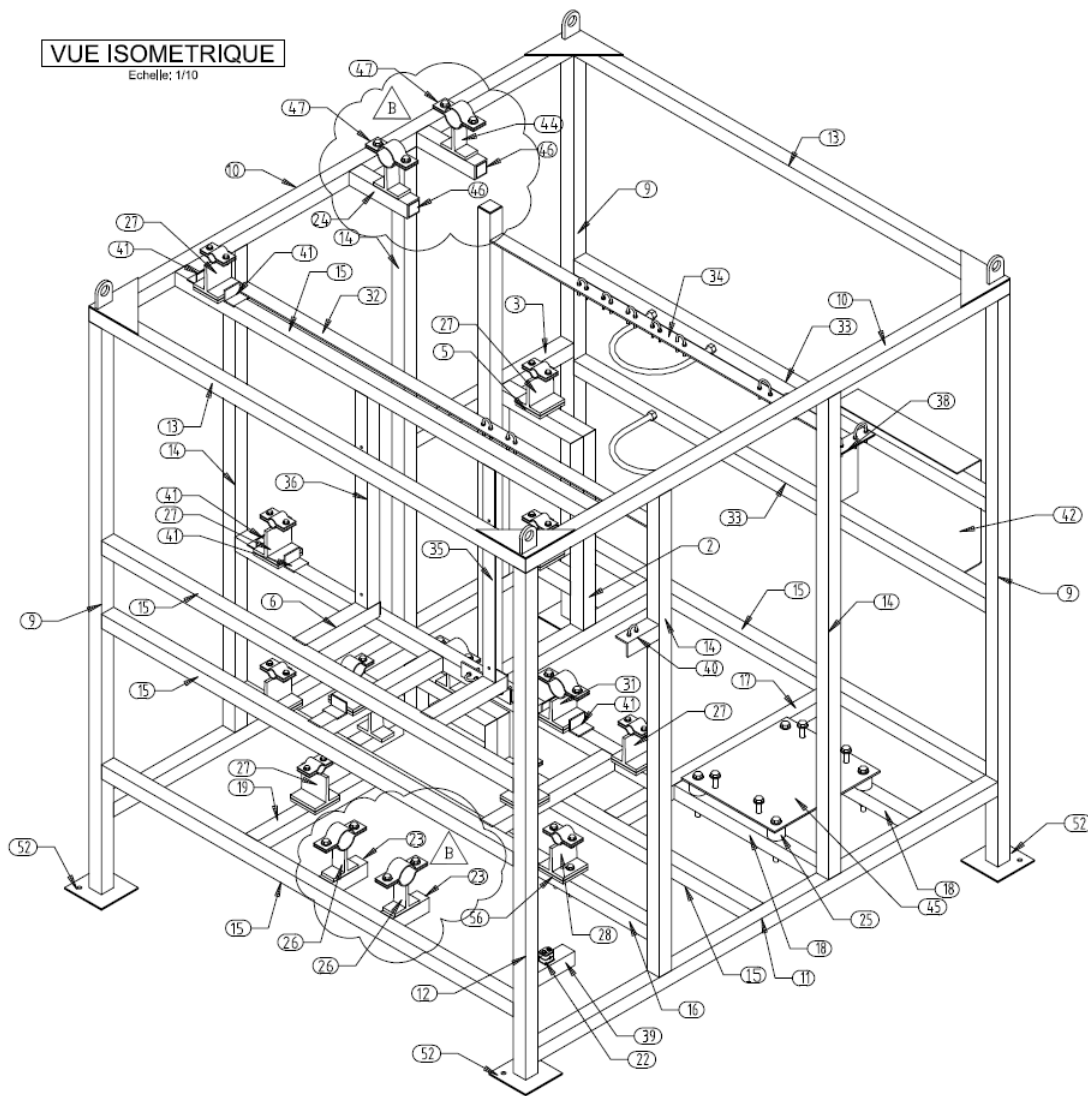


Figure 3.2: Skid housing the primary circuit of the installation.

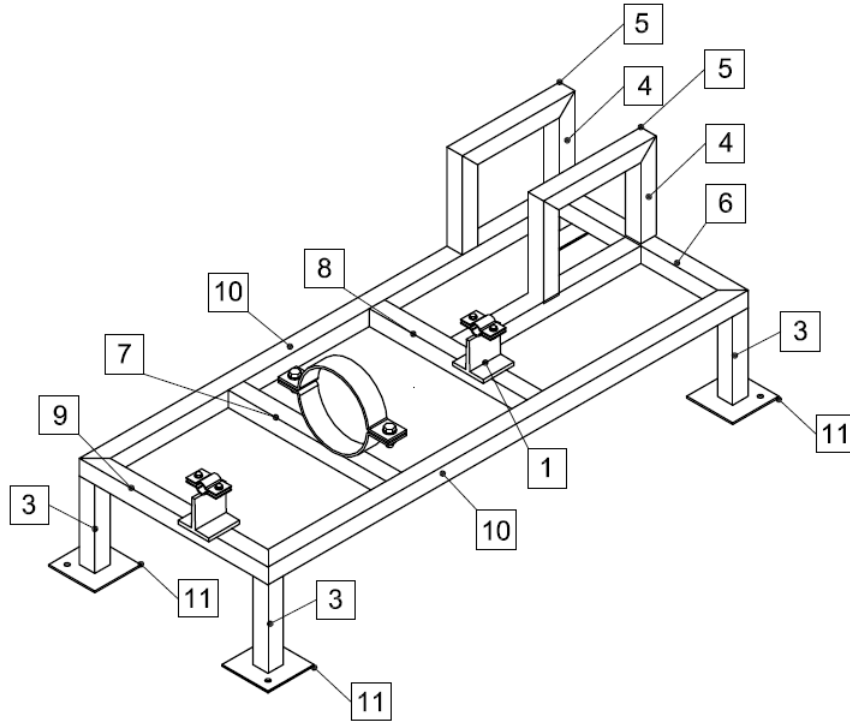


Figure 3.3: Skid housing the filling circuit of the system.

The pit installation of this facility can be verified in 3D (see Figure 3.4). The interactions required for the operation, such as access to the valves or the electrical panel on the outside of the skid, are checked (see Figure 3.5).

The future test section will have a square section of  $3 \times 3 \text{ cm}^2$  and will be connected to a circular pipe section with a diameter of DN20.

The different heat exchangers were then sized according to the temperature constraints.

Different conservative operating configurations were taken into account. From these configurations, the inlet and outlet temperature of the exchanger on the primary side (hot source) were calculated, taking into account the various components of the loop (preheater, pump, etc.). The inlet and outlet temperature of the secondary side (cold source corresponding to the industrial water circuit) are imposed: 20 and 40°C. The exchange coefficients were computed using the Nusselt correlation. Once this coefficient was calculated, the overall exchange coefficient in this exchanger was determined: convection on the primary (hot) side, conduction in the thickness of the pipe, convection on the secondary (cold) side.

Several calculation methods were used:

- A first calculation was made considering that locally, the exchange surfaces are equivalent,
- A second method consisting in considering a cylindrical thermal resistance for the conduction between the two fluids was applied,
- Finally, the calculation was carried out by considering a flat exchange surface for con-

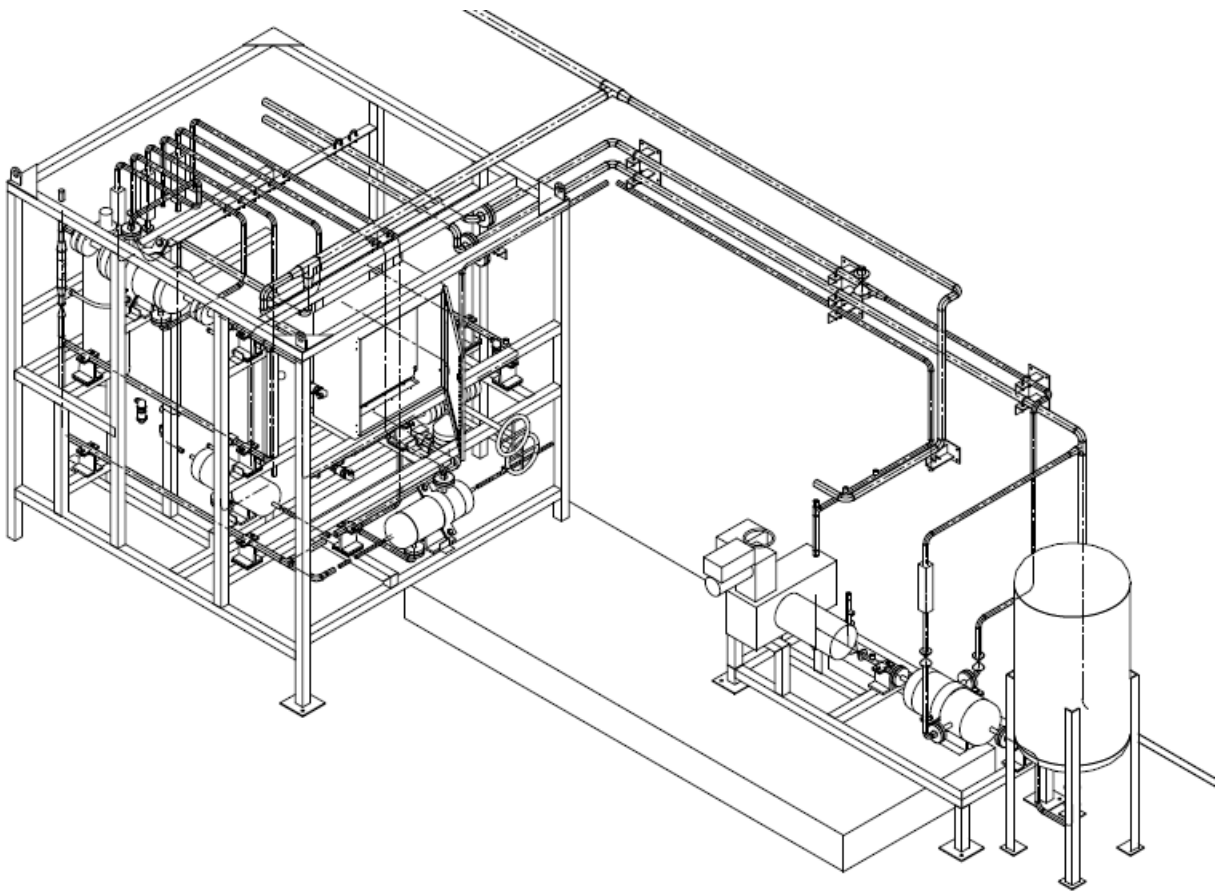


Figure 3.4: 3D visualisation of the equipped installation in the building pit.

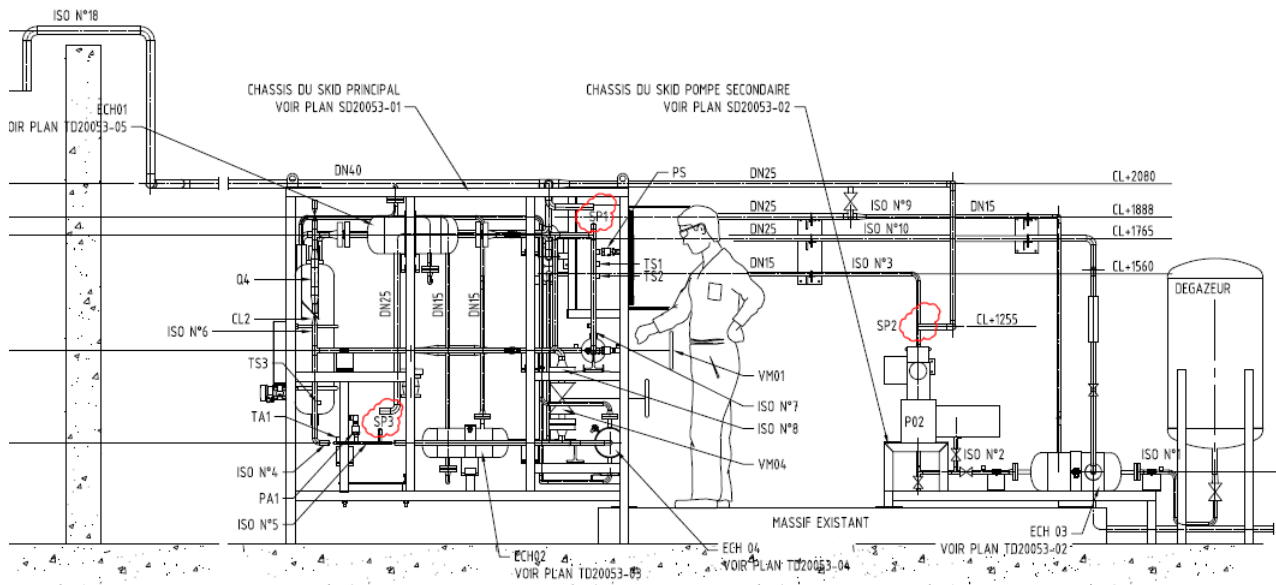


Figure 3.5: Visualisation of the installed loop and access for operations on the installation.

duction.

For each of these three methods, the logarithmic temperature difference was calculated for a counterflow exchanger as shown in Equation 3.1.

$$\Delta T_{Log} = \frac{(T_e - t_s) - (T_s - t_e)}{\ln\left(\frac{T_e - t_s}{T_s - t_e}\right)} \quad (3.1)$$

where  $T_e$  and  $T_s$  are the entry and exit temperature of the primary circuit (hot source),  $t_e$  and  $t_s$  are the entry and exit temperature of the secondary circuit (cold source).

The exchange surface  $S_e$  is then calculated according to the power to be extracted  $W$ , the exchange coefficient  $h$  and the logarithmic temperature difference  $\Delta T_{Log}$  as presented in Equation 3.2.

$$W = hS_e\Delta T_{Log} \quad (3.2)$$

These calculations are based on the assumption that there is no fouling in the pipes in view of the operating times. The calculation with the three methods makes it possible to determine an envelope exchange surface. A first design of corkscrew exchanger was proposed but the bends were too important on a schedule 80S pipe and were not technically feasible. All the exchangers (see example Figure 3.6) were sized in a straight line to avoid ESP qualification of each element. In fact, the primary pipe is kept and a shell is added around it to serve as a secondary network. An expansion compensator is added to the outer shell to take up the thermal expansion on the primary pipe to which it is welded.

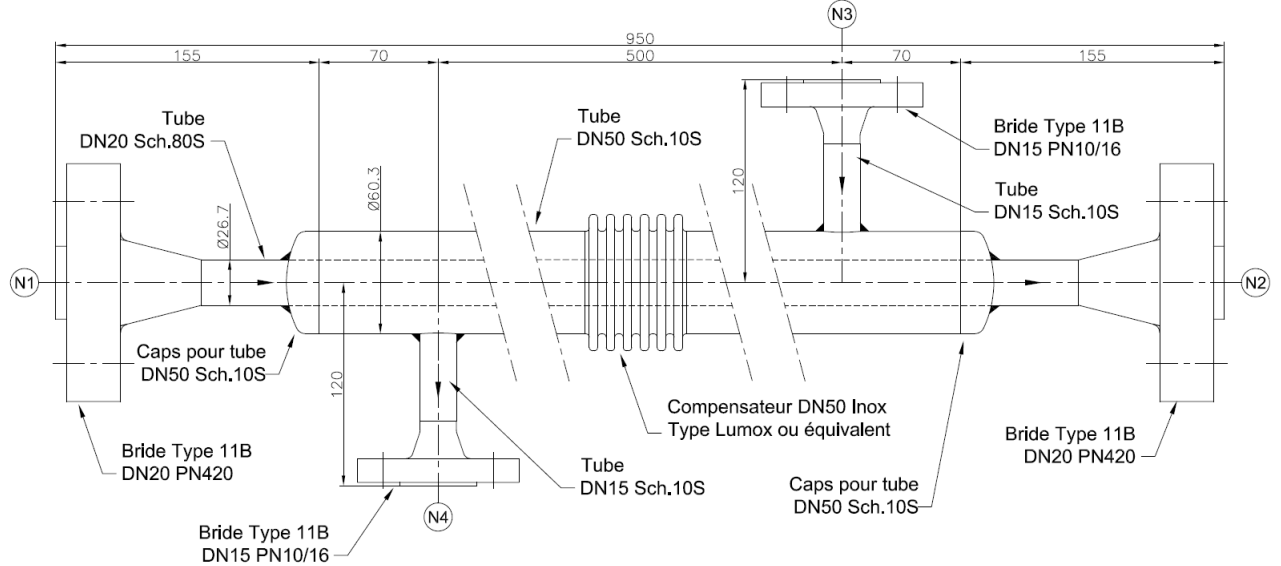


Figure 3.6: Heat exchanger design.

A hydropneumatic accumulator has been dimensioned to allow the main circuit to be pressurified and to absorb the pressure variations due to the temperature variations of the system.

Within CEA Cadarache and more precisely on the Poseidon platform, several installations were dismantled in recent years for various reasons. Some of these facilities operated under the thermal hydraulic conditions of interest. The components of these test loops, some of which were in working order, were stored on the platform. It was therefore decided to make

an inventory of the elements that could correspond to the project's needs. The associated data sheets were also collected thanks to the platform's archive.

A pump operating at PWR conditions was retained, which meets the operating conditions of this new loop for the main circuit (Pump P01). The capabilities of this pump allow the implementation of a bypass to fine tune the flow in the test section: this bypass has a larger pipe diameter DN25 to accommodate the flow sent by the pump. Two valves allow adjusting the distribution of water circulating in the by-pass and the circuit of the test section, thus regulating the flow rate. The main pump (P01) was sent for an overhaul, as some repairs were necessary for its proper functioning. A second pump was found to act as a filling and booster pump if required (Pump P02). A deaerator, a tank that can operate under pressure up to  $5\text{ bar}$ , was also recovered. This equipment is to be decommissioned and used at  $1.5\text{ bar}$  to degas the demineralised water before injecting it into the primary circuit. Three valves were also recovered. They are sized to the correct operating conditions with a  $2500\text{ lbs}$  rating.

As far as instrumentation is concerned, several technologies require specific implementations. For example, each flowmeter requires a straight length of pipe before the orifice where the differential pressure measurement is made. Some pressure measurements should be made in condensate pots, especially downstream of the test section where boiling is bound to occur. Tapping of several locations in the circuit is required for temperature measurements by thermocouple.

Finally, to allow the operation of such an installation, a safety file must be provided. This type of file must describe the operation of the entire pressure installation. It must contain the detailed composition of the circuits, as well as the installed power and associated instrumentation. Procedures should be described for each situation: pressure and temperature rise, ignition checks, safety sensors, thresholds, emergency stop, shutdown, etc. A risk analysis must also be provided with the associated regulatory aspects and the treatment of these risks must be presented.

On this installation, the element considered as a Category IV Pressure Equipment (ESP) and requiring special attention (monitoring in service) is the hydropneumatic accumulator. All the other equipment in the loop is considered Category 0, manufactured and used according to the rules of the art, meaning that no further controls are needed.

The small volume of this facility ( $60\text{ L}$  in the primary circuit) allows precise handling of the conditions, which is valuable for the upcoming trial.

At the present time, the manufacture of this installation has begun with the manufacture of the various skids. Maintenance of the primary circuit pump was performed, revealing damaged parts that were replaced. The fabrication is planned and should continue outside the framework of the thesis for future work on this topic.

# Chapter 4

## Test section

In this chapter, the technical constraints inherent of the measurement techniques and operating conditions of the future test section are detailed. The facilities used in the literature for this type of study and the associated feedback are presented. The design and initial technical solutions for the high pressure, high temperature test section are then described.

### 4.1 Technical requirements

The main constraint for the choice of the measurement techniques to be used is to be non-intrusive. Several types of measurements are possible, but direct visualisation of the flow is the most widely used technique for this type of study nowadays. Indeed, indirect measurements through optical probes or sensors leave certain uncertainties because of calibration and can disrupt the flow. With direct visualisation, the measurement is carried out directly without an interface that can lead to a loss of information. Similarly, for the temperature measurement of the heating plate, the use of infrared thermography allows to measure in time and space the temperature distribution. With other techniques such as the use of thermocouples or probes, the measurement is discretised to a higher order of magnitude.

The aim is to implement two measurement techniques on the future facility (Figure 4.1): a measurement by direct visualisation of the flow with a shadowgraphic setup and a measurement of the temperature distribution of the heated plate by infrared thermography. The implementation of these two measurement techniques needs to be taken into account from the initiation of the test section concept.

This facility will use water as working fluid, under pressure from 1 to 150 bar and temperature up to 350 °C.

To enable the shadowgraphy measurements, this facility must have an optical access to the flow. It is therefore necessary to determine the best material to resist to the required conditions (pressure and temperature) and also to provide the best optical access allowing to carry out measurements in shadowgraphy.

Several types of test section can be found in the literature, allowing optical access to the flow. Most of these sections were designed for low pressure conditions, but the fixtures can provide guidance on how to assemble visualisation windows and gain access to the flow. Several of the mock-ups presented in this section have different geometries: circular, annular, square, sub-channel, cluster assembly.

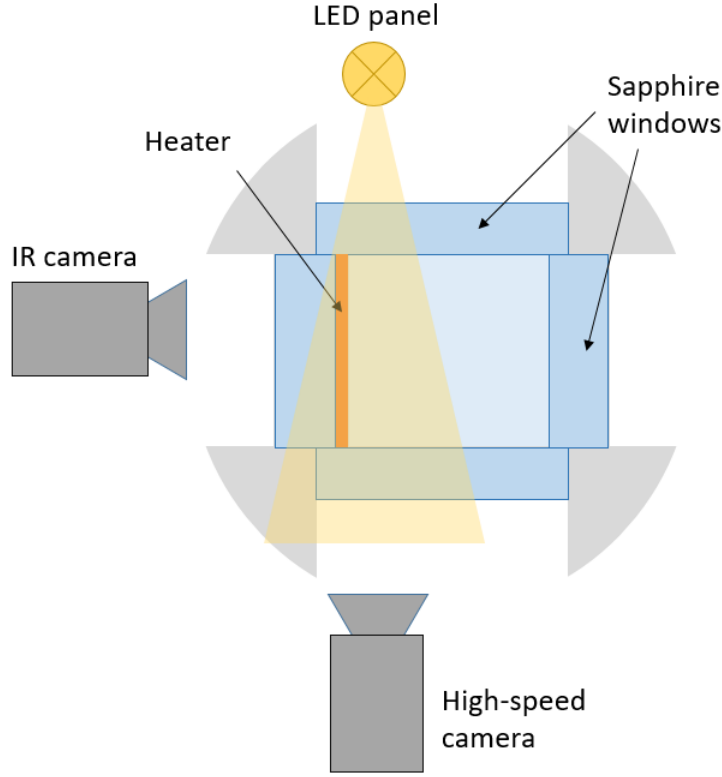


Figure 4.1: Shadowgraphy and thermography measurements diagram.

Lin and Chen [33] used a test facility working with refrigerant R-134a (tetrafluoroethane). The test section (Figure 4.2) is 1.35 m long, with a 10 cm long heated section. Two types of test section are implemented: a flat one and an augmented one (technical name "hypervapotron"). Three crystal glass windows are installed to allow visualisation. The test section is fabricated from a block of copper. It is heated by six cartridges delivering 4500 W power to the test section, this is an indirect heating.

The annular test section of Roy et al. [60, 58, 29] is presented Figure 4.3. This facility is composed of a heated 304 stainless steel inner wall and an insulated transparent pyrex glass outer wall. The measurement section is made of quartz. The inner stainless steel tube is heated by direct current. Refrigerant R-113 is used as the working fluid. A jacket was installed around this test section: consisting of an anodized aluminium box with front and back quartz windows and a glass side window to be filled with R-113 (trichlorotrifluoroethane) and avoid laser beam refraction at the outer wall of the quartz tube.

The test section of the SUBO facility is presented Figure 4.4. The test section is a vertically arranged annulus with a heated rod at the channel center. The rod is heated by direct Joule effect. This facility can work with water under a maximal pressure of 50 bar. Several parts of the test section are made of cylindrical windows forming the channel and allowing visualisation measurements of the boiling flow.

Sugrue et al. [61] used another type of test section to study the effect of orientation angle of the channel over bubble departure diameter. This test section is presented Figure 4.5, it is a rectangular 316L stainless steel body equipped with two viewing windows and a heater insulated with MACOR ceramic. MACOR part serves as thermal and electrical

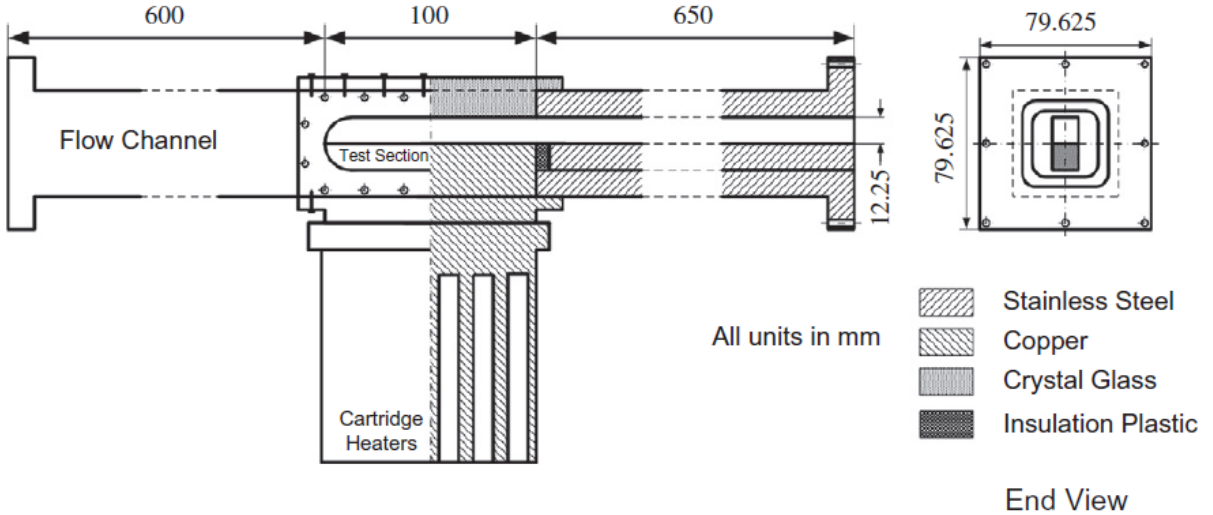


Figure 4.2: Experimental R-134a facility, reprinted from Lin and Chen [33].

insulator. This test section was designed to be oriented during the test up to  $180^\circ$  working at atmospheric pressure. Copper studs are used as connections to the power supply lines that provide DC current and are screwed into the ends of the heater.

In Richenderfer et al. [51] work, the test section used up to 10 bar is a  $3 \times 1\text{ cm}^2$  flow channel. The main body is fitted with four sides: three quartz windows to provide a direct access to the flow and a cartridge made of Shapal as electrical insulator for the IR heater (see Figure 4.6). The quartz windows are mounted on the body of the test section and held in place with gaskets and a counter flange. The IR heater is composed of a sapphire substrate coated with indium-tin-oxyde (ITO) and installed inside the cartridge. This deposit is heated by direct Joule effect through silver pads wrapped around the filleted edges of the sapphire substrate.

March [4] uses a high pressure mock-up with the visualisation of a 9-rod fuel assembly (see Figure 4.7). Two circular portholes are mounted on the test section and allow visualisation of boiling on the rods. March determined diamond to be the strongest material to withstand the pressure, however he selected sapphire for cost and ease of fabrication. The section is encircled by a pressure tube to take up the stresses and hold the pressure. A clamp is used to hold the window in place on the test section.

The mounting of the two sight glasses requires the insertion of a spacer on the test section. The port holders pass through the half-shells constituting the fluid passage section and re-establish the continuity of the channel so as not to disturb the flow. The port holders are removable and allow the portholes to be replaced by steel plugs for use without viewing. Both windows have a diameter of 19.5 mm and a thickness of 7 mm. The size of the sapphire is determined by the width of the soldering on its support. The port holders are machined from an alloy whose characteristics are compatible with the thermal expansion of the sapphire. Sealing is provided by graphite gaskets. The sightglass manufacturer recommends a temperature rise and fall rate of  $20^\circ\text{C}/\text{h}$  to limit thermal stress.

Another high pressure experimental facility was used by Hosler [28]. It consisted of a long vertical rectangular flow channel (see Figure 4.8). This channel was formed by two quartz side prisms, a quartz front window and a stainless steel heater strip. The plate was heated

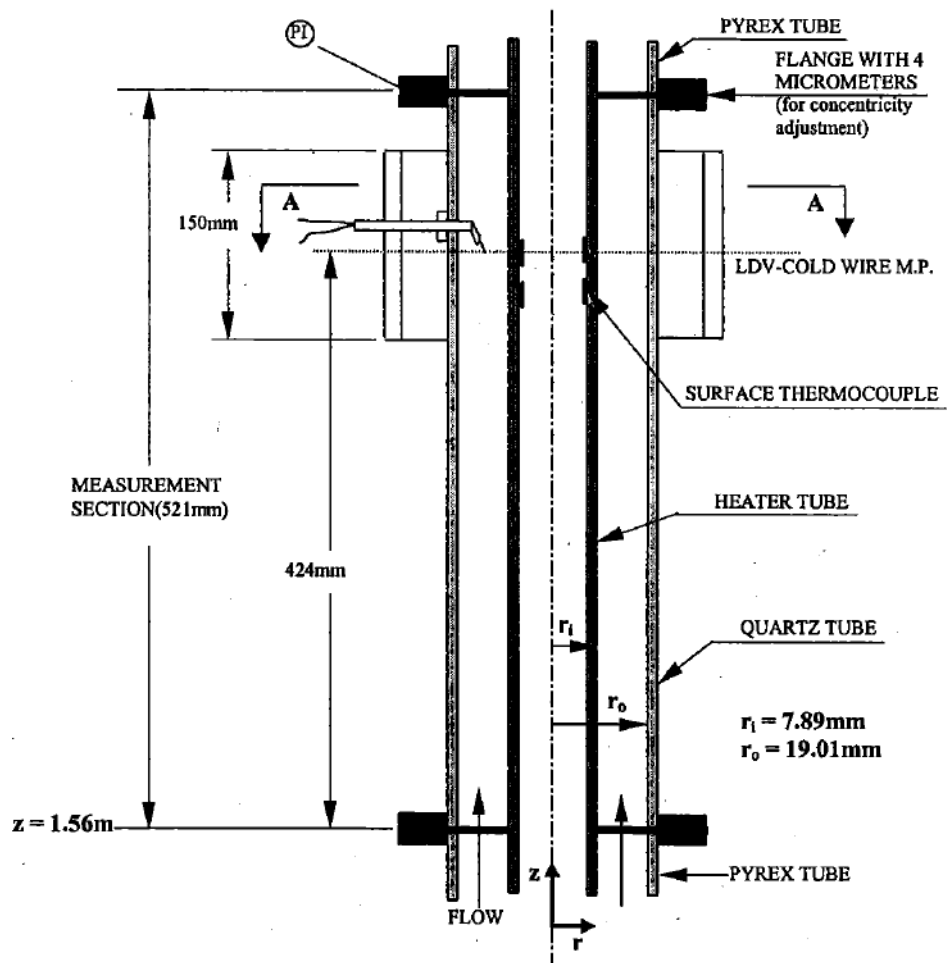
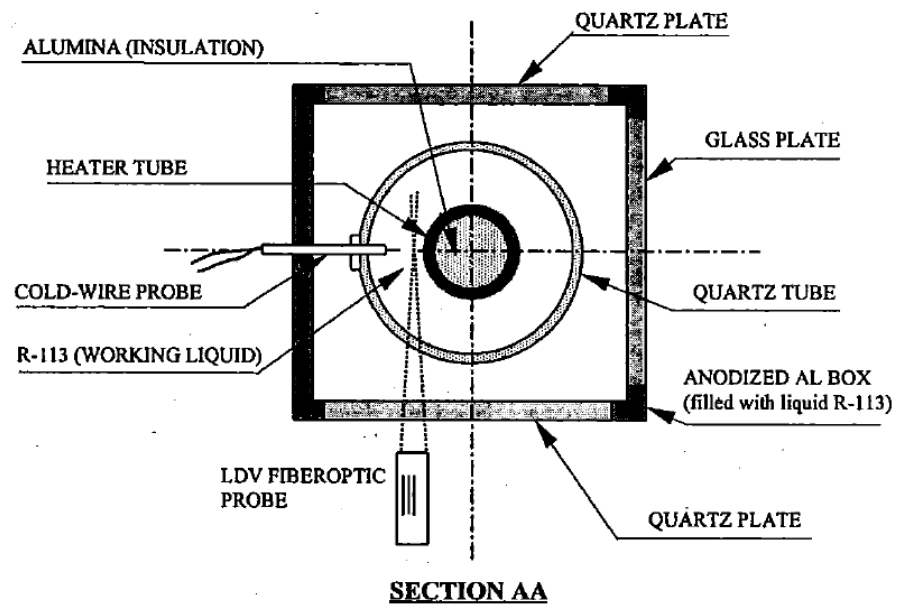


Figure 4.3: Experimental R-113 facility, reprinted from Roy et al. [58].

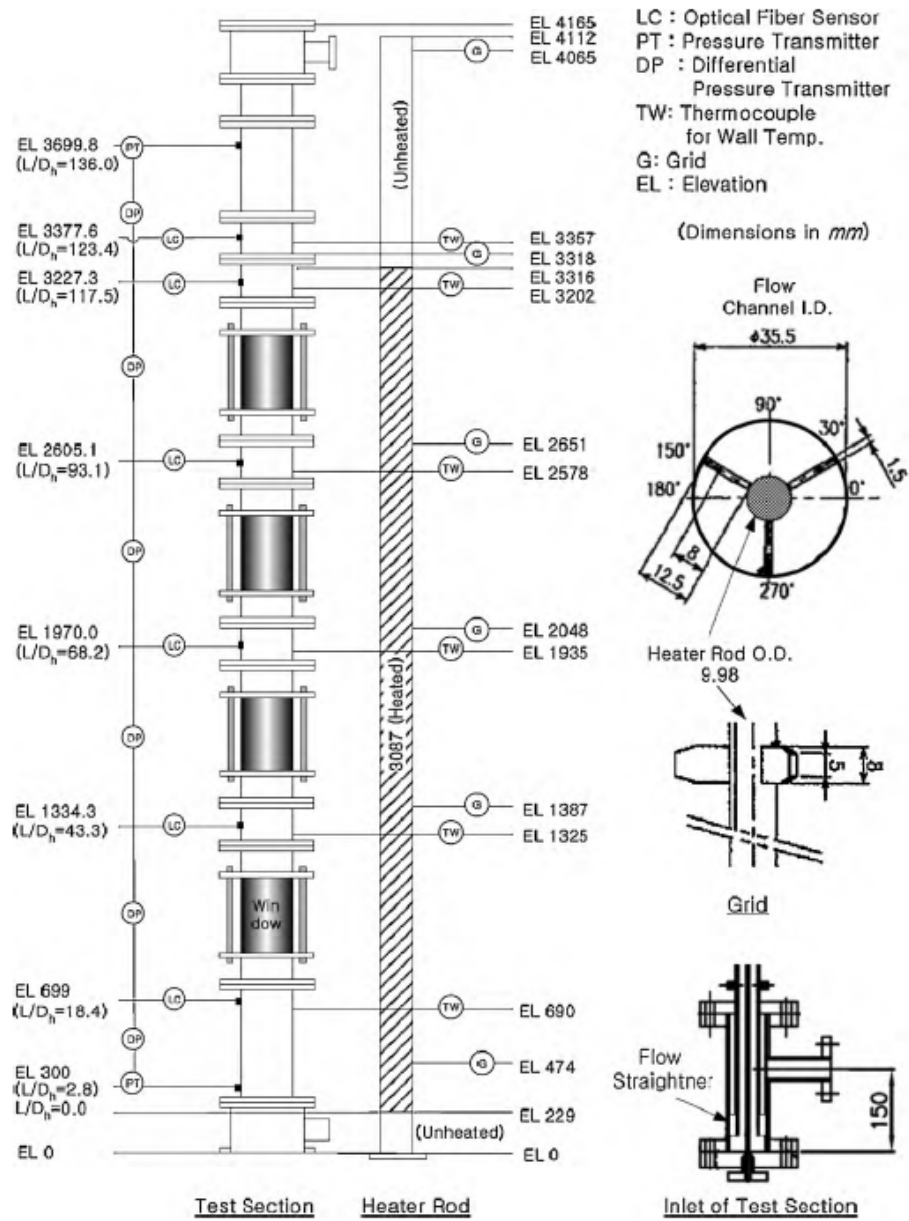


Figure 4.4: SUBO experimental facility, reprinted from Yun et al. [31].

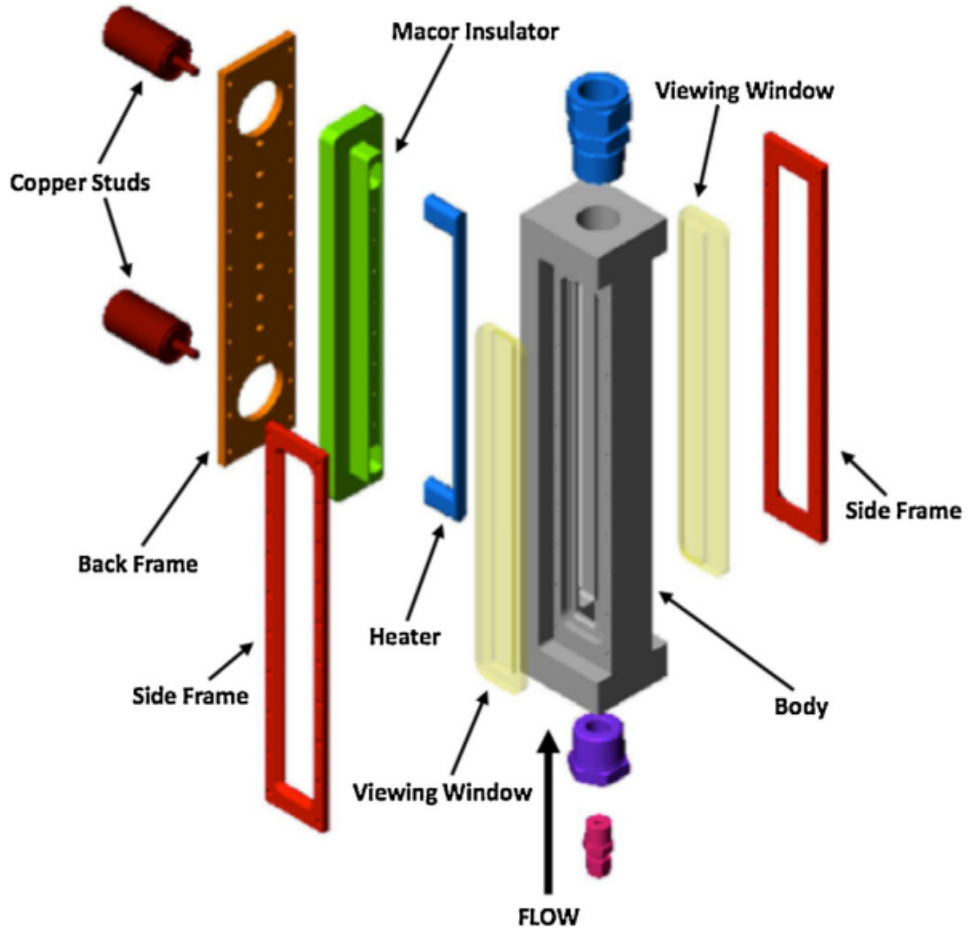


Figure 4.5: Experimental water facility, from Sugrue et al. [61].

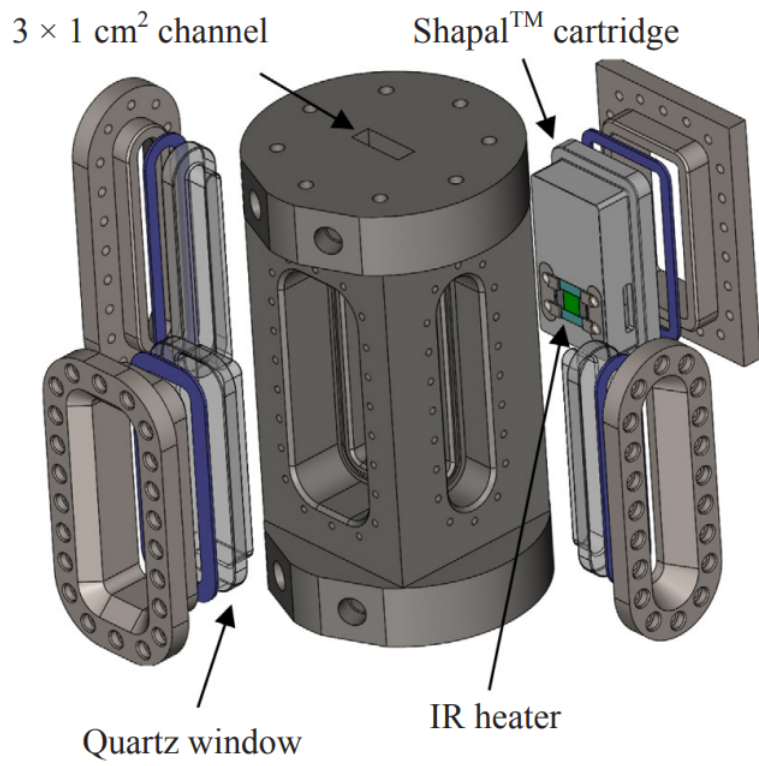


Figure 4.6: MIT test section facility, reprinted from Richenderfer et al. [51].

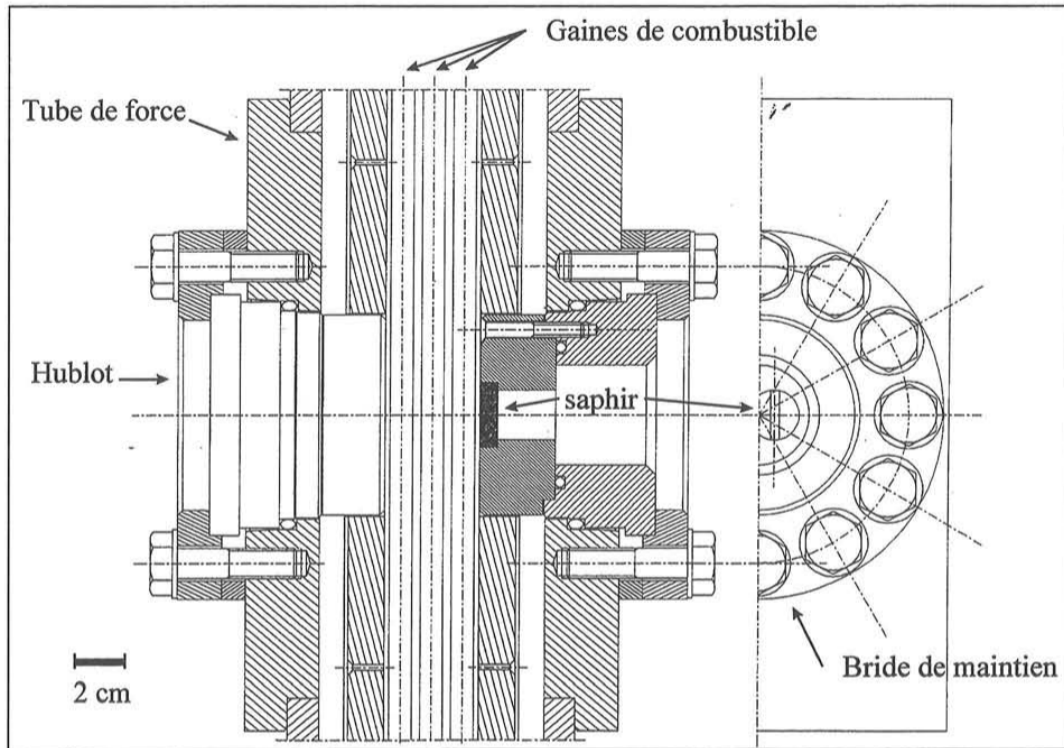


Figure 4.7: March test section facility, reprinted from March [4].

by ohmic dissipation. This facility was installed in a high pressure water flow loop. The combination of ceramic insulator and sapphire surface to protect the quartz windows form the test section. Gaskets around each window and also around the counter flange ensure that the test section is sealed.

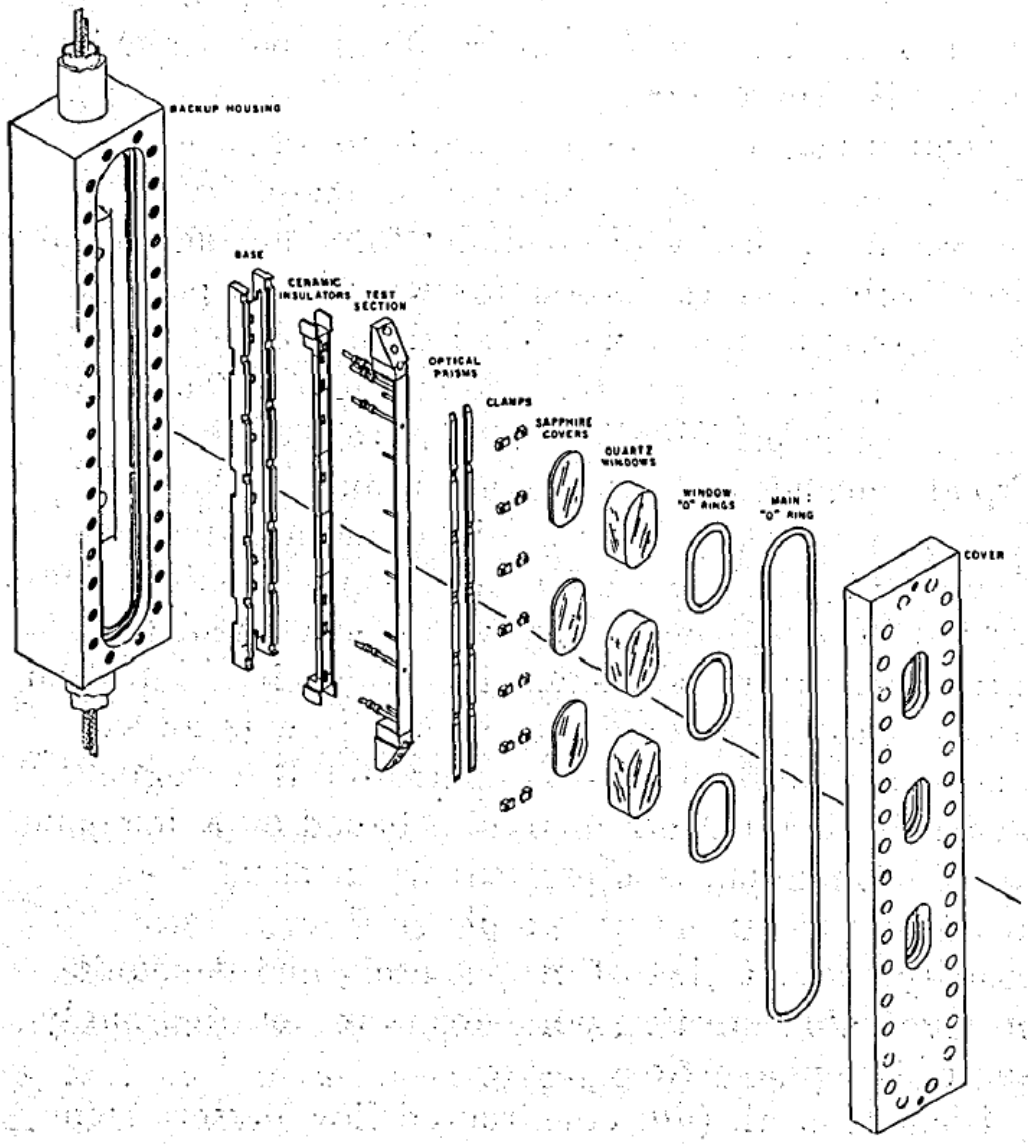


Figure 4.8: Hosler test section facility, reprinted from Hosler [28].

The setup to be made should allow an optical access with a square fluid passage section and allow the tangential visualisation of a flat plate. As seen previously by the review of existing facilities in the literature, sapphire and quartz seem to be the best materials to resist the pressure and temperature constraints of our study. Several other materials are used, such as pyrex or crystal but for low pressure applications. March [4] believes in his study that diamond is the best material for these high pressure, high temperature applications, but given the high cost of manufacturing an all-diamond window, sapphire is the selected material.

Sapphire is a material that is often used as a window. The window should be mounted loosely. Direct contact with the metal bearing surfaces is not recommended (insertion of

teflon or metal seals depending on the operating pressure and temperature). The metal chosen for the cell must have a coefficient of thermal expansion close to that of sapphire to avoid problems of differential expansion. The surface finish of the metal and sapphire must be controlled, ground for the former and optically polished for the latter, to allow visualisation.

Quartz has interesting optical qualities but is less resistant to pressure than sapphire. Moreover the coefficient of linear thermal expansion of quartz is  $5.5 \times 10^{-7} K^{-1}$ , the one of sapphire is  $5.8 \times 10^{-6} K^{-1}$ , which is closer to stainless steel coefficient  $16.5 - 19.5 \times 10^{-6} K^{-1}$  and limits the differential expansion stress.

The second argument in favour of sapphire is its ability to be brazed, being an alumina. It is thus possible to imagine being able to ensure a seal or the support of parts by brazing.

Sapphire was therefore selected for the windows for measurements in the visible range.

## 4.2 Test section design

Making a high pressure facility with optical access is not easy. Sapphire can be machined with special diamond tools. Several solutions have been proposed to make a facility with four optical ports: three for the visible part, one for the IR part with the plate.

First of all, a model solution made entirely of sapphire was devised after discussions with professionals. From a block of sapphire, the pipe can be machined to form the fluid flow section. The problem with this all-sapphire block test section is that the machining frosts the material. Sapphire must be polished to be used as a viewing window, otherwise it is not transparent. To achieve this, polishing is carried out with increasingly fine-grained tools, but this polishing is done flat or in a circular pipe. A circular sapphire pipe is therefore feasible. The square duct desired here to limit the optical effects cannot be polished. The use of quartz for a test section machined from a block is more appropriate. Quartz is flame polished and therefore allows internal polishing of the test section. However, this material has been discarded earlier because of differential thermal expansion. Moreover, internal machining with milling machines has its limitations: the corner is formed with a milling radius and therefore not a sharp corner on the edges of the section. This can be problematic as one wishes to look at the interface of the heating plate and therefore at the end of the fluid flow section. This solution was therefore dropped.

The second solution proposed is the one often found in the literature: a fluid flow section formed by sapphire windows with a stainless steel structure presented in Figure 4.9.

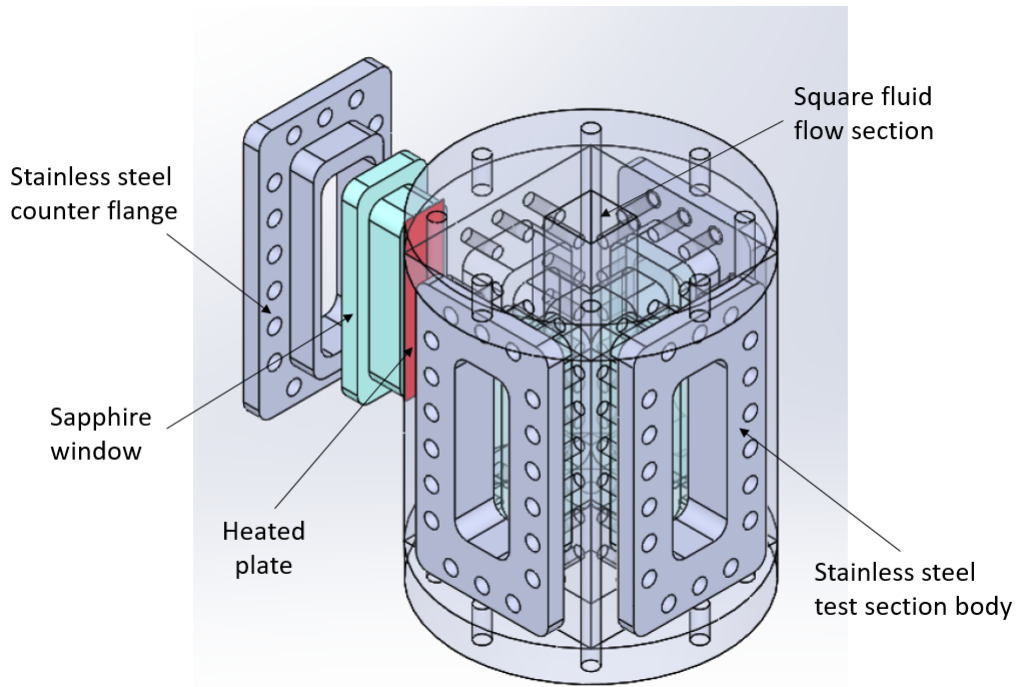


Figure 4.9: Test section design.

This test section consists of a stainless steel body allowing the insertion of sapphire windows held in place by stainless steel counter-flanges and gaskets to ensure watertightness.

In order to measure the temperature of the heating wall with an IR camera, a solution

must be found to ensure that the pipe can withstand 155 bar while having a plate (Joule effect heating) thin enough to limit the conduction time and therefore the phase shift or attenuation of the thermal information. A first solution proposed is to create a pressurised enclosure to place the infrared camera as close as possible to the plate (see Figure 4.10).

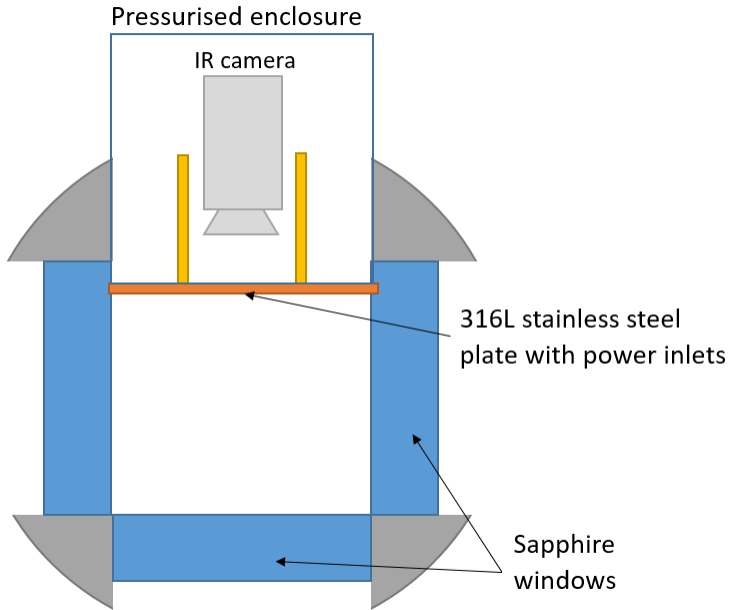


Figure 4.10: Pressurised enclosure solution for IR measurements.

This method presents several constraints. It is necessary to guarantee the pressure balance to ensure that the plate of a few tens of microns is not deformed. It is also necessary to succeed in insulating it thermally and electrically. This solution was too complicated to be implemented.

Another solution is to use a window as for the other three faces to guarantee the hold and to insulate the heating plate as presented Figure 4.11.

Several materials correspond to the infrared bandwidth to be targeted for these measurements. Nevertheless, the problem of pressure resistance remains the same as the choice of materials for the portholes. Sapphire has a fairly wide bandwidth (see Figure 4.12) and is retained for the porthole equipped with the heating plate.

Sapphire is a good electrical insulator with a resistivity of  $10^{12} \Omega m$ . As sapphire is an infrared-transparent material, we will not have any problems with the transmission of the radiation we are interested in. It allows light to pass through well with a wavelength range of 150 to 6500 nm, which encompasses part of the infrared range. Our plate emits radiation in the infrared range which, once recovered by the camera, allows us to map the temperature distribution on the plate and its temporal evolution. It is therefore necessary to know the wavelength range of the emissions for the temperature ranges studied and to check that the sapphire plate allows these emissions to pass through so that they can be captured by the camera.

For pressure values from 1 to 150 bar, the saturation temperature is between 100 and 342 °C. A temperature range between 100 and 350 °C is therefore selected (the plate having a parietal superheat of a few degrees for boiling to occur). Considering the hot plate as a

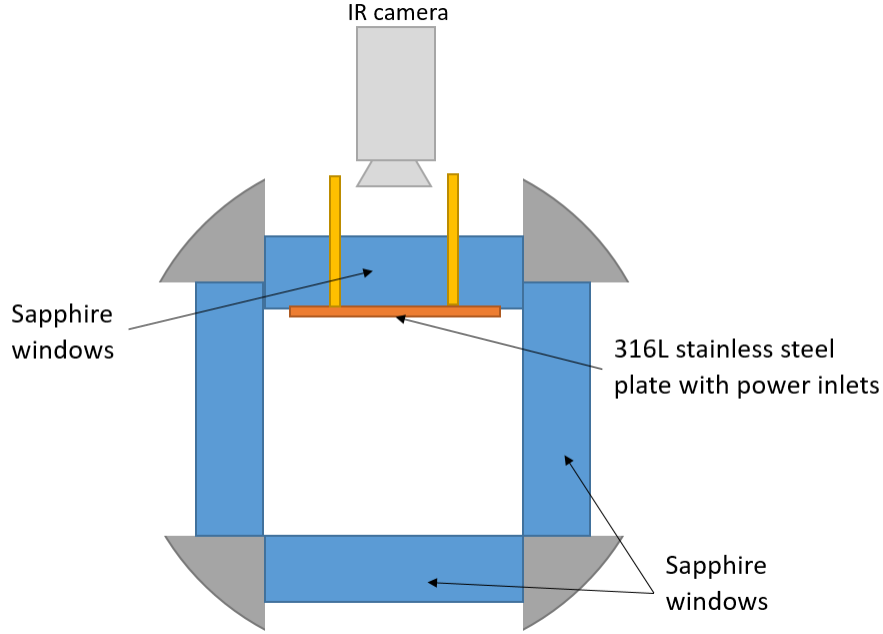


Figure 4.11: Sapphire window solution for IR measurements.

black surface at temperature  $T$ , surrounded by a transparent medium, in this case sapphire of index  $n$ , Planck's law is written as shown in Equation 4.1.

$$E_{b,\lambda} = \frac{C_1 \lambda^{-5}}{n^2 (e^{C_2/n\lambda T} - 1)} \quad (4.1)$$

$$C_1 = 2\pi h c_0^2 \quad (4.2)$$

$$C_2 = \frac{hc_0}{k} \quad (4.3)$$

with  $h$  Planck constant in [ $J.s$ ],  $n$  is the refractive index of sapphire,  $c_0$  the light velocity in [ $m/s$ ] and  $k$  the Boltzmann constant in [ $J/K$ ].

With a temperature range of  $100 - 350^\circ C$  the emittance can be plotted against the wavelength presented Figure 4.13, with the bandwidth limit of the sapphire (yellow line).

The bandwidth of sapphire allows the desired infrared thermography measurements over the temperature range of interest. This equipped window will be made of sapphire.

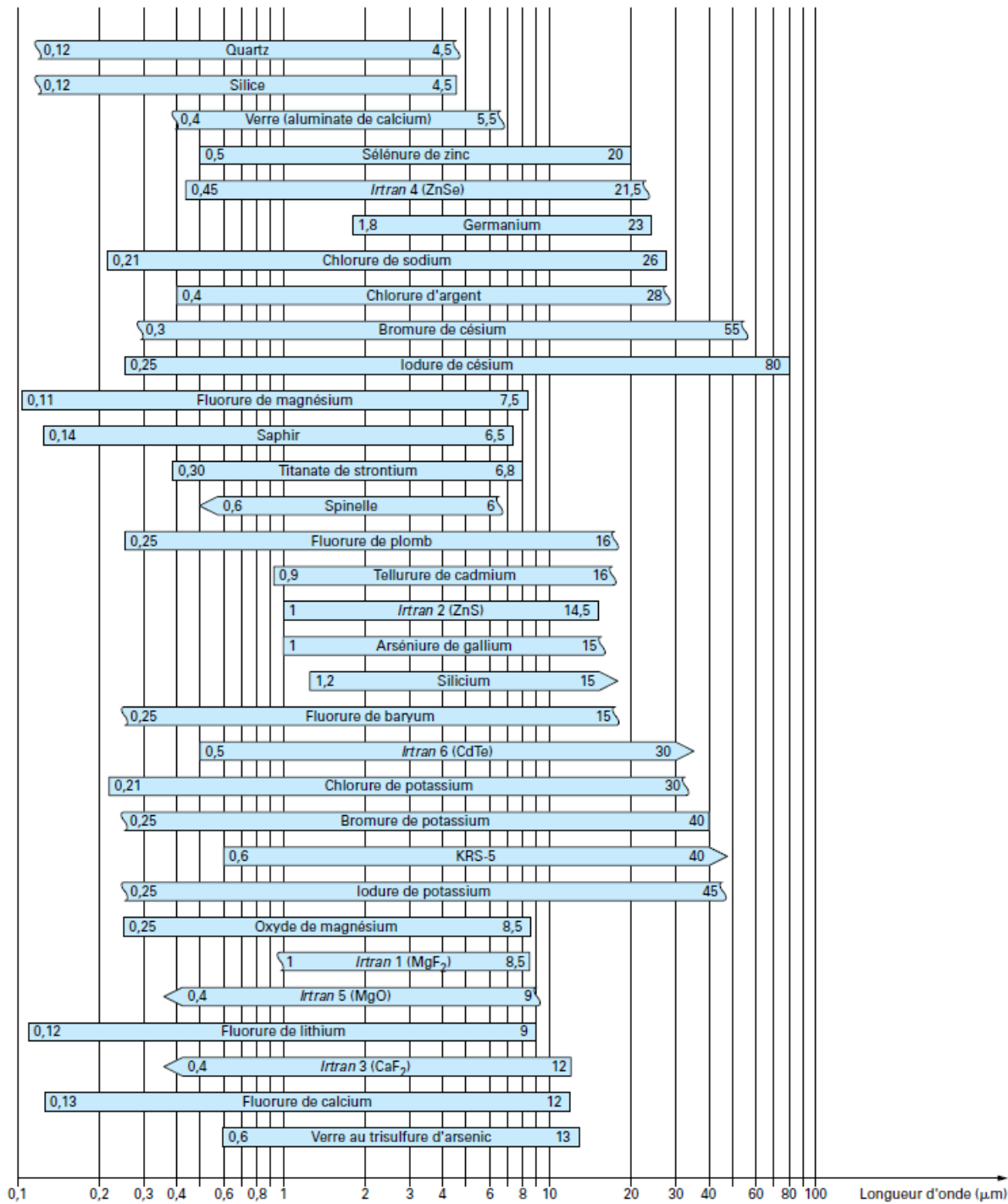


Figure 4.12: Spectral areas of optical transmission for different optical materials with a thickness of 2 mm, from Cojan et al. [111].

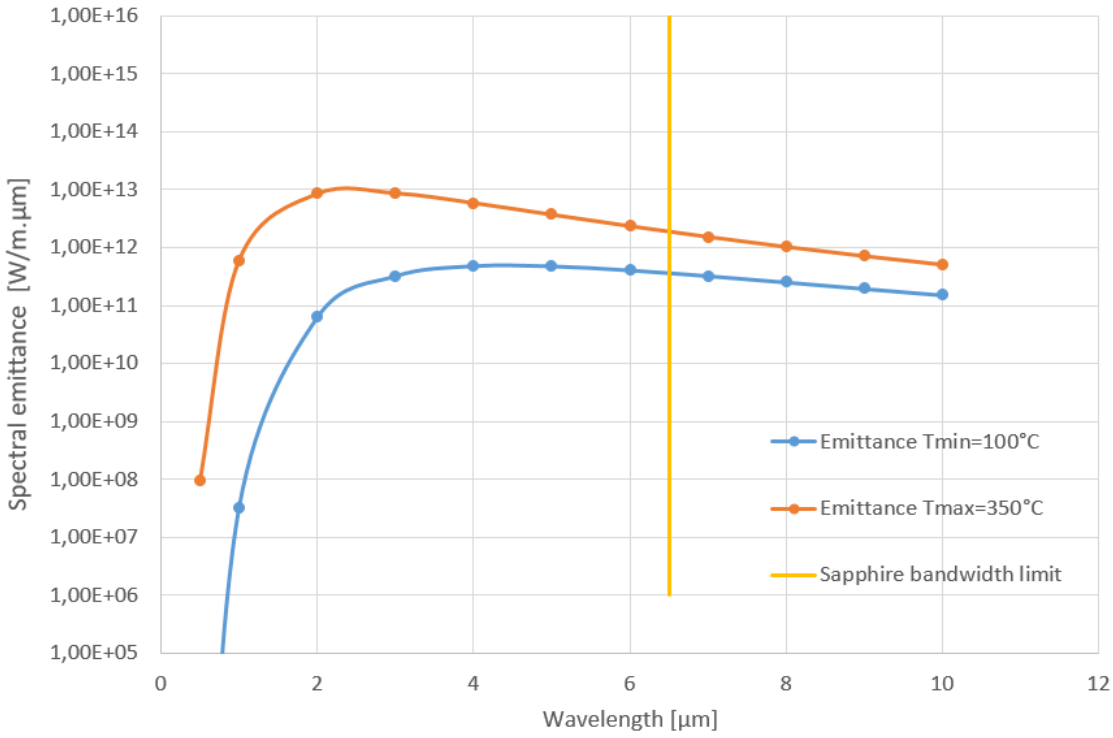


Figure 4.13: Spectral emittance of the stainless steel plate for minimum and maximum temperature range.

Sapphire is an alumina and can be brazed with other materials. Brazing requires the addition of a different material to make the link between the two parts: it is carried out in a vacuum furnace at a high temperature but lower than the melting temperature of the two parts to be brazed (carried out at 400 or 700°C). It can also be said to be active with a chemical bond (between sapphire and titanium for example). A metallization of the sapphire surface can be applied to braze the stainless steel plate and limit the brazing area. For a thin layer such as the plate of a few tens of microns, the sapphire will impose its thermal expansion on cooling.

A first concept of a window equipped with the hot plate has been proposed (see Figure 4.14). The sapphire window is machined to allow the power supply to pass through. The heating plate is soldered to the sapphire to ensure waterproofing. Some drawbacks arised with this first concept: the solder has a high electrical conductivity and the current distribution is not controlled. Moreover, the thickness of the solder will be around 30 microns, for a plate estimated at a few tens of microns to limit the phase shift by conduction, this added thickness may pose a problem for the measurements envisaged. Furthermore, for thermography measurements it is often necessary to apply a layer of constant emissivity paint to the target element. This layer of paint will not allow soldering over the entire heating plate

A solder tape on the plate contour can be considered to limit the impact of its thermal conductivity on the measurement. This solution was discarded: the addition of solder around the edge of the plate can cause problems. Indeed, as the plate is a few microns thick, the pressure will press this stainless steel sheet against the sapphire window and push the central part (not brazed) a few microns. The measurement by shadowgraphy visualisation is carried

## CONCEPT 1

### Stainless steel brazed to sapphire

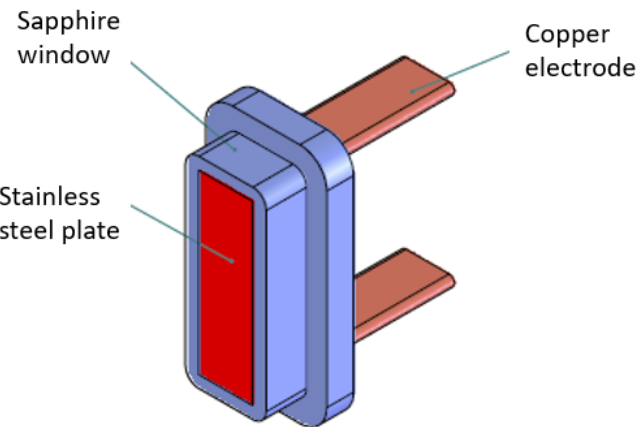


Figure 4.14: First equipped window design: brazed hot plate on sapphire window.

out in a tangential way with the plate to capture bubbles of a diameter of a few tens of microns. If the central part is pressed in, information on the thickness of the outer braze is lost. The additional thickness will hinder correct visualisation. This solution cannot therefore be retained.

Soldering at the power inlets can also be considered. The solder has a high conductivity and will allow a distribution on the plate at each current inlet. However, during the brazing process, the stainless steel foil may become taut (differential expansion) and exert a significant force on the brazing material, which could break.

A second concept of window was then proposed by adding a skirt system on the copper electrodes (see Figure 4.15). This skirt can provide a seal and accommodate differential expansion between the sapphire window and the copper electrodes. One issue was raised: if water is allowed to flow between the heating plate and the sapphire window, IR thermography measurements are impossible. Moreover, the copper electrodes will expand and may distort the plate and interfere with visualisation.

Research and discussions with sapphire professionals have led to the conclusion that technological developments are needed to implement this concept of a sapphire window equipped with a stainless steel power plate. Soldering tests and the development of a solution to ensure watertightness are necessary and inappropriate for the timing of a thesis.

Nevertheless, the definition of the geometry of the heating plate as well as the instrumentation required for the desired measurements have been studied in the following chapters.

**CONCEPT 2**  
With copper / sapphire  
sealing skirt

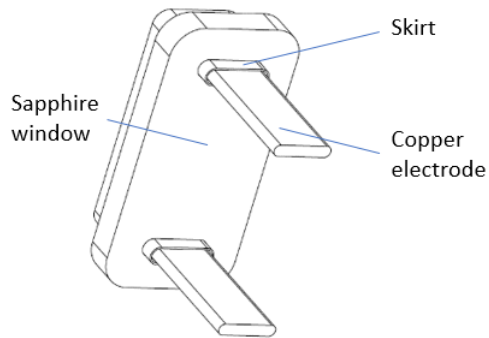


Figure 4.15: Second equipped window design: skirt system to limit differential expansion.

# Chapter 5

## Heater design

This chapter is dedicated to the determination of the heating plate thickness in order to perform infrared thermography measurements. Indeed, as previously mentioned, the thickness of the plate directly influences the feasability as well as the quality of the measurement. Thus, the thermal behaviour of the heating plate as a function of its thickness will be studied. The thermal study presented here was the subject of a paper and presentation at the NURETH19 conference [112] and a paper published in Applied Science [113].

### 5.1 Scope of the study

#### 5.1.1 Previous work

To ensure the validity of the partitioning model, it seems necessary to perform direct and complete measurements of all the sub-models parameters (bubble diameter  $D_b$ , bubble detachment frequency  $f$  and nucleation site density  $N''$ ) in operating conditions as close as possible to the targeted ones (PWR).

As a reminder, Richenderfer's work [51] on the visualisation of nucleate boiling tends to move towards high pressure to study boiling under typical PWR conditions. In this work, Richenderfer proposes a heating element consisting of a sapphire substrate on which indium-tin oxide ITO is deposited in a thin layer. The thickness of this heating element is less than 1 micron. They designed an experimental setup that allows measurements of each parameter mentioned in previous chapter. This setup is made of a test section (square cross-sectional) equipped with quartz windows to get an optical access to the flow. The heater (where nucleate boiling occurs, see Figure 5.1) is made of a sapphire plate (substrate) coated with a thin layer of indium-tin-oxide (ITO). The thickness of this ITO coating is  $0.7 \mu\text{m}$  and is heated by direct Joule effect. Operating conditions of this study were low pressure and low temperature conditions but with the objective of improving the setup to measure the parameters under PWR conditions. The optical setup is presented Figure 5.2 (top).

They managed to visualise the bubbles through the sapphire beneath the heater and collect the data related to the heated plate temperature and heat flux. An infrared high-speed camera measures the temperature of the heated plate on its external face and the temperature of the wetted side of the plate is obtained solving a conduction-radiation inverse problem. An exemple of these thermal measurements is presented Figure 5.2 (bottom), with the temperature result (left) and the heat flux result (right). The red dots represent the identified

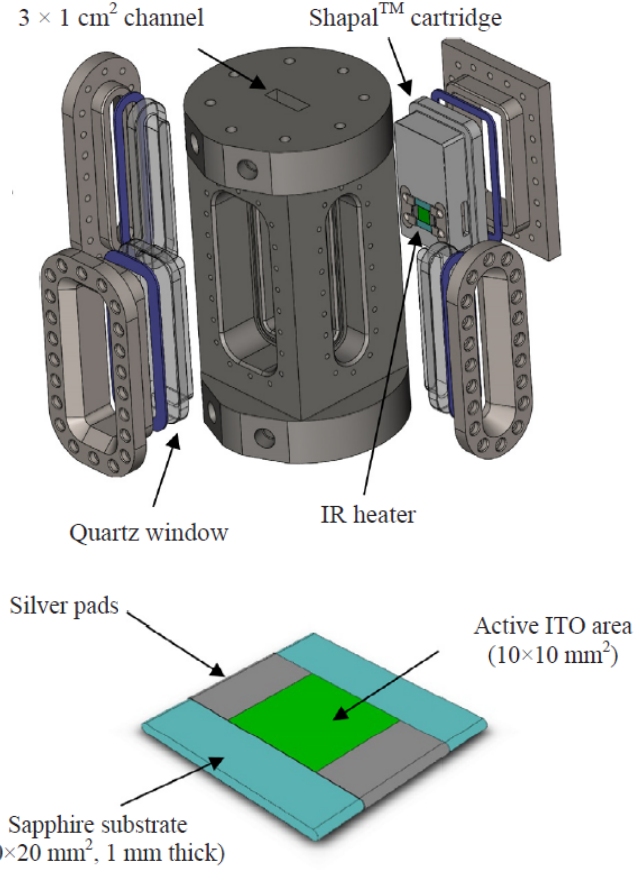
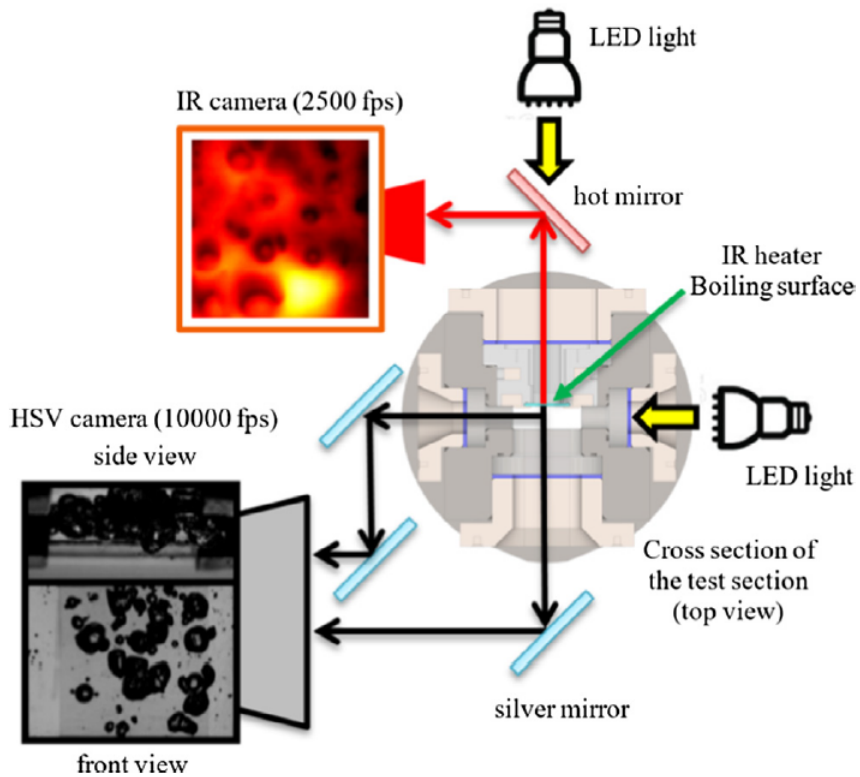


Figure 5.1: Richenderfer facility, Sapphire substrate coated with ITO, from Richenderfer et al. [51].

active nucleation sites.

Despite the obvious interest in such experiment, the representativeness of the heated surface is questionable, in particular due to its thickness. One should notice that for classical industrial plates (*e.g.* metallic plate), the characteristic size of an active nucleation site is of the same order of magnitude, not to say larger [114], than the thickness of the ITO layer used by Richenderfer et al. [51]. This may have an influence on the correct development of a bubble.



Pressure: 1 bar - Subcooling: 10 °C - Mass Flux: 500 kg/m<sup>2</sup>/s - Heat Flux: 1750 kW/m<sup>2</sup>

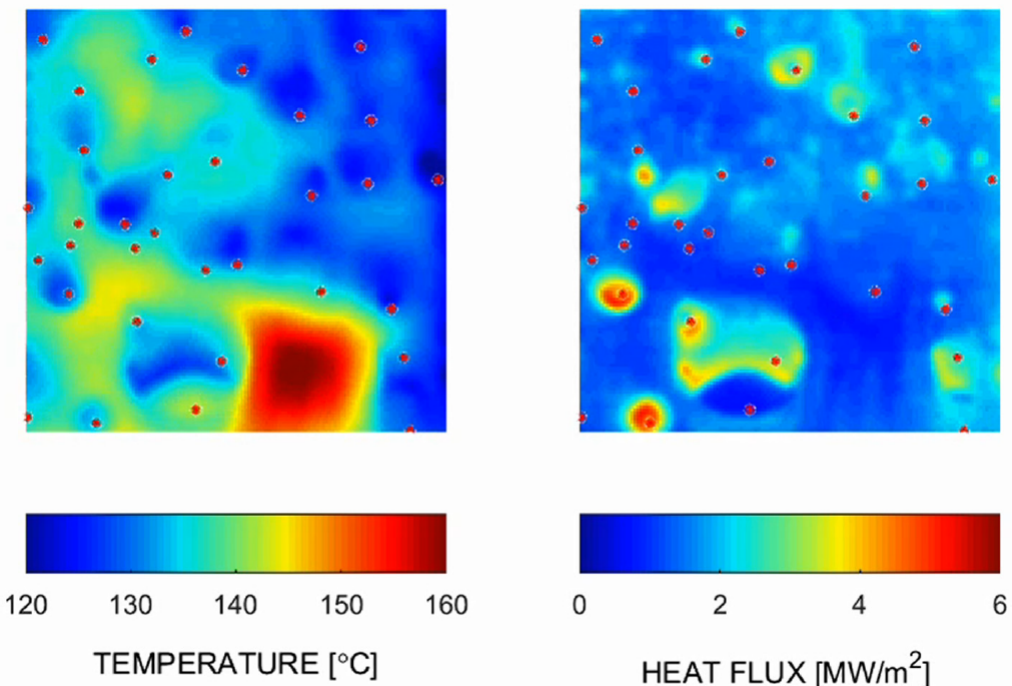


Figure 5.2: Cut-view of the test section with optical arrangement and sample validation of the nucleation site detection algorithm on the test with a mass flux of  $500 \text{ kg/m}^2\text{s}$  (the fluid flows upward) and an average heat flux of  $1750 \text{ kW/m}^2$ . Red dots identify the nucleation sites, from Richenderfer et al. [51].

To confirm this statement, let us consider the work of March [4]. An experimental setup was designed to study the two-phase flow characteristics for PWR thermal hydraulic working conditions.

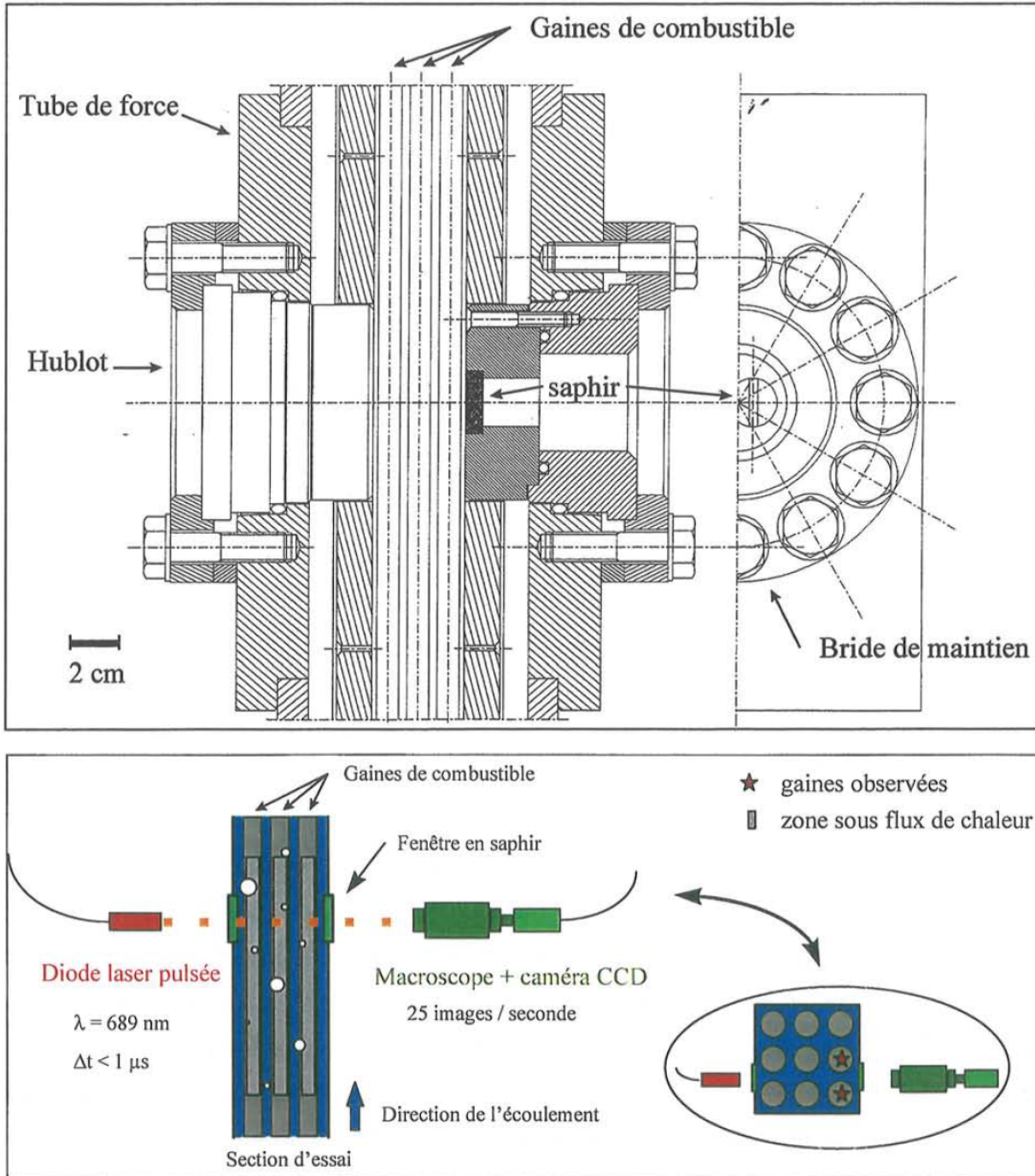


Figure 5.3: March facility, reprinted from March [4].

The test section is composed of a rod bundle with nine rods heated by direct Joule effect (see Figure 5.3). Those rods (external diameter  $9.5\text{ mm}$ , formed by two layers of stainless steel and zircaloy, thickness  $1.17\text{ mm}$ , length  $70\text{ mm}$ ) are put inside a vessel (square channel  $38.2\text{ mm}$ ) that can support the pressure. The vessel is equipped with two sapphire windows

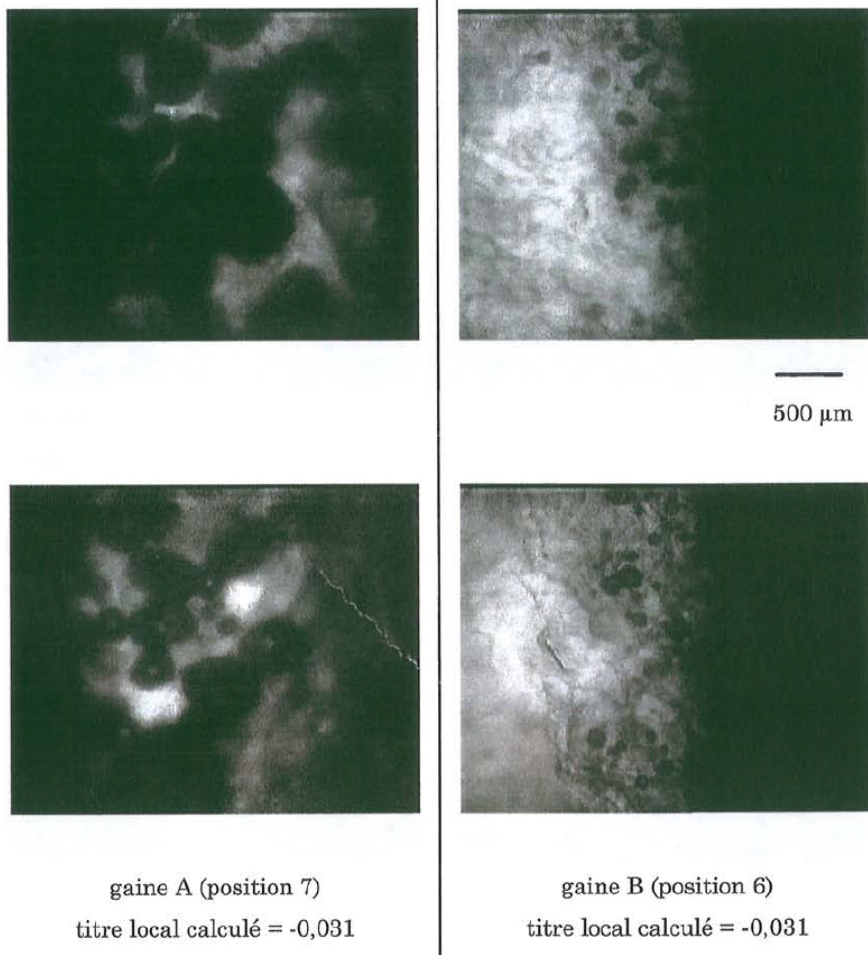


Figure 5.4: March result, reprinted from March [4].

that allow a direct visualisation of the two-phase flow along the heated rods and particularly the bubbles that are created at the surface of the rods. Pictures of the flow are obtained using shadowgraphy (see Figure 5.4). Experiments have been performed within the following thermal hydraulic parameters range:

- pressure from 26 *bar* up to 155 *bar*
- mass velocity ranging from 1000 to 3500  $kg.m^{-2}.s^{-1}$
- equilibrium exit quality  $x_{eq}$  corresponding to sub-cooled conditions (ranging from ONB up to  $x_{eq} \approx 0$ );

where  $x_{eq}$  is defined by :

$$x_{eq} = \frac{h_m - h_{l,sat}}{h_{fg}} \quad (5.1)$$

where  $h_{fg}$  is the phase change enthalpy,  $h_{l,sat}$  is the liquid enthalpy at saturation) and  $h_m$  is the mixture enthalpy given by a one dimensional heat balance.

During the tests, March [4] focused on the impact of the roughness of the heated surface on nucleate boiling and especially the size of the bubbles. He observed strong changes in the

flow structure and especially in the bubble size as a function of the roughness. For a smooth surface (that can be characterised by a roughness close to  $0.2 \mu\text{m}$ , left Figure 5.4) and for the same set of thermal hydraulic conditions, the bubbles are quite larger than the bubbles created at the surface of the rough rod (characterised by a higher roughness close to  $3.9 \mu\text{m}$ , right Figure 5.4). Thus, it appears that the roughness largely influences the nature of the boiling flow, particularly in terms of bubble size [76]. This result confirms that it is necessary to consider a realistic heated plate in order to ensure a good representativeness.

If March's work [4] clearly demonstrates the technical feasibility of such measurements, some limitations worth being pointed. In this study, discussions on the image analysis method are missing, in particular the problem of optical distortion noted in the vicinity of the heated wall due to the thermal gradient (refractive index) was not addressed. In addition, only about twenty tests are presented in this study for the measurement of the average bubble diameter (nine tests at  $26 \text{ bar}$  and eleven tests at  $155 \text{ bar}$ ). The resulting database needs to be completed to perform parametric studies (bubble diameter as a function of thermal hydraulic parameters e.g. pressure, equilibrium quality, subcooling...). One can also notice that there were no thermal measurements ( $T_w$ ) concerning the heater. Finally, to the best of our knowledge, data collected by March [4] are unique but haven't been challenged by anyone else and their reproducibility as well as their accuracy still needs to be demonstrated.

The present work performed at CEA/Cadarache aims to extend the initial work performed by March [4]. To measure parameters of interest in PWR's conditions, as an answer to what has just been pointed previously, a realistic heater needs then to be designed.

### 5.1.2 Reminder of the problem

The future experimental setup was presented in the previous chapter. This setup will involve a specific test section (presented Figure 5.5) which will allow **(i)** a direct visualisation of the boiling flow using the same technique as the one used by March [4] (shadowgraphy), but also **(ii)** a characterisation of the temperature field of the wetted side of the heated plate, similar to Richenderfer et al. work [51].

Nevertheless, in order to account for the representativeness of the heating surface, we choose to consider a thick metallic plate (Stainless steel) as the heater instead of a thin metallic coating proposed by Richenderfer et al. [51], **plate whose thickness needs to be determined.**

Figures 5.5 and 5.6 depict a schematic of the future test section and its measurement systems.

Three sapphire windows, located on three external faces of the test section, will allow a direct visualisation of the bubbles created along the heated plate, which will be soldered on a fourth sapphire window. As a reminder, sapphire was selected in the previous chapter for several reasons:

- pressure resistance,
- transparency to IR,
- possibility of fixing the heating plate by brazing.

The metallic plate will be heated by **direct Joule effect**.

The temperature of the heated plate will be measured on its external face (dry side  $T_{dry}$ )

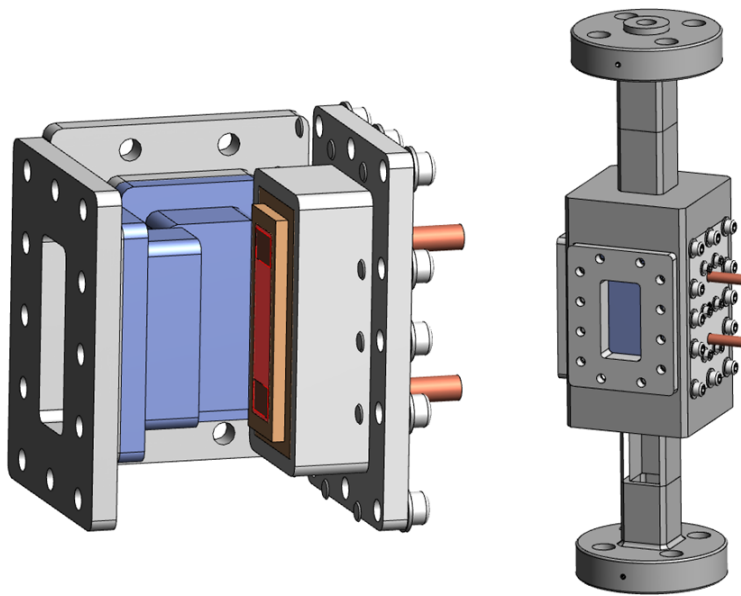


Figure 5.5: 3D schematic of the future test section. The heated element is drawn in red:  
Heated length  $L \approx 5.10^{-2}m$  - Heated width  $l \approx 1.10^{-2}m$  - Thickness of the metallic plate :  
*to be determined.*

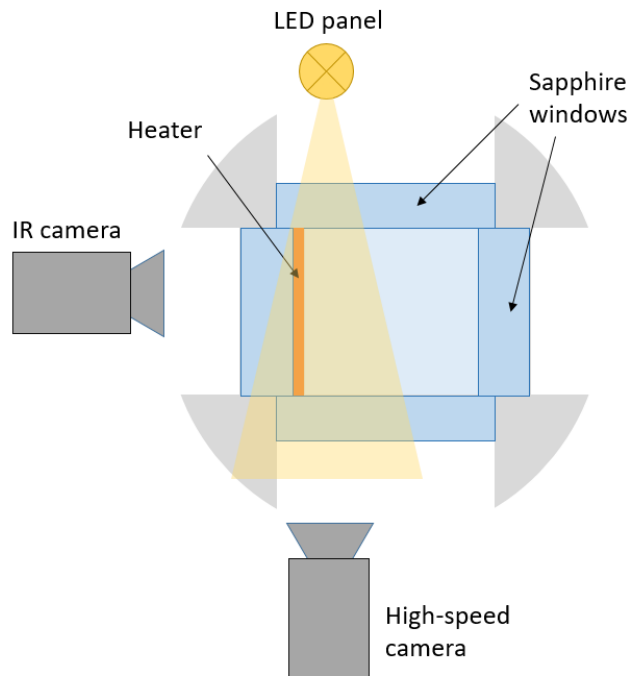


Figure 5.6: Operating measurements principles.

using an infrared camera and the temperature of the wetted side of the plate  $T_{wet}$  will be deduced from the dry temperature by solving the heat diffusion equation within the plate.

Knowing the wetted temperature is useful to analyse the data collected by shadowgraphy through the sapphire windows. Indeed, as mentioned before, due to the thermal gradients in the vicinity of the heated wall ([4] [65]), pictures obtained by shadowgraphy can be distorted, making the identification of the bubble detachment time and, as a consequence, the bubble lift off diameter difficult. As an exemple, Figure 5.7 shows the difficulty of identifying the state of attachment of the bubble.

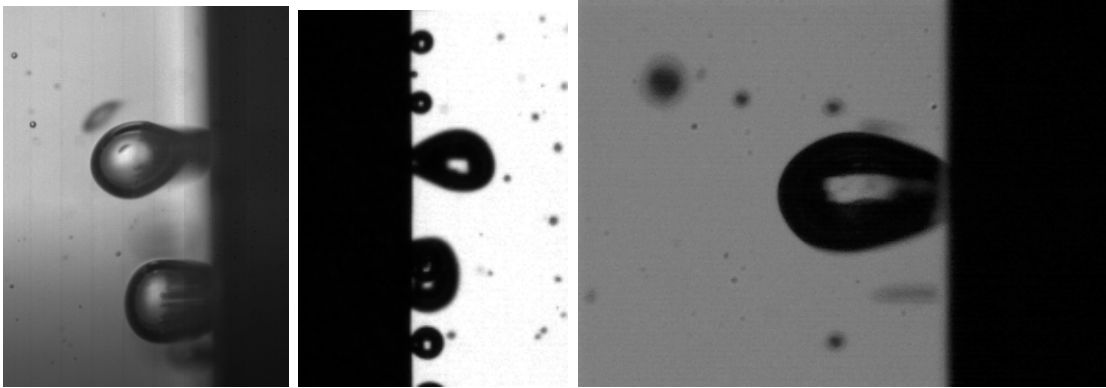


Figure 5.7: Visualisation by shadowgraphy of bubble growing on the heating wall. On these pictures, the bubble cannot be identified as still attached to the wall or detached. Images from the preparatory tests presented in the next chapter.

Moreover, for active nucleation site density, shadowgraphy does not give the information because of the reduced depth of field, infrared measurement can provide this information. It is believed that thermal imaging will be helpful as the bubble detachment should correspond to a local variation of the temperature field on the wetted side of the heated plate.

As an illustration, one can cite the recent work of Wang and Podowski [115], who calculated the temperature profile as a function of time under a nucleation site. In this work, the heat transfer of a wall subjected to boiling is presented. Two types of experimental heating wall are studied, greater than 1 mm thick, they are associated with a semi-infinite wall, whereas of the order of a micrometer thick the surface heat flux is defined as quasi constant, they consider that there is no thermal inertia. For both types of plate, with an internal or external heat source, they solve conduction in the liquid boundary layer to determine the influence of heating on the temperature variation on the plate (boiling interface). The analytical resolution of the heat transfer between a plate and its environment during the waiting period between two nucleations is summarised and compared to experimental measurements of the temperature variation at the wall (in vessel boiling measurements). It is this representation that interests us: the temperature drop at the moment of nucleation (until the growth time,  $t_g$ ) and the return to its initial state during the waiting period (waiting time,  $t_w$ ). Figure 5.8 describes the prototypical behavior of the wall temperature beneath a nucleation site as a function of time. One can observe two distinct stages. First, while the bubble is still attached to its nucleation site and is growing, the temperature decreases because of the vaporisation. Then, the bubble detaches from the heated wall at  $t_g$  (called growing time), and the temperature increases until a new bubble begins to grow on the nucleation site.  $t_w$  is called waiting time, as the time between one bubble lift-off and a new nucleation to appear. Thermal imaging may help us to identify the time when the bubble effectively detaches from the wall ( $t_g$ ).

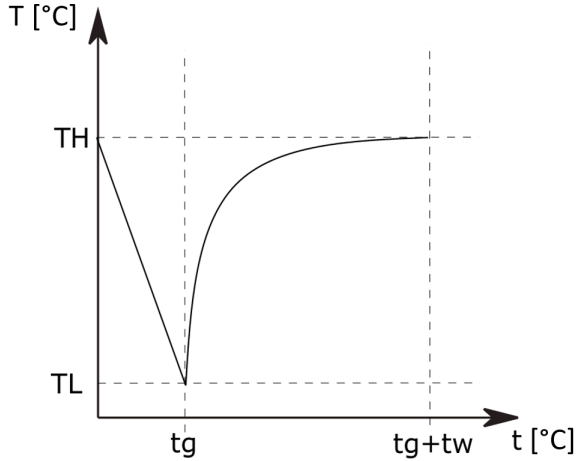


Figure 5.8: Prototypical time evolution of the temperature beneath a nucleation site,  $t_g$  is the growth time -  $t_w$  is the waiting time between a bubble take-off and the appearance of a new nucleation, based on Wang and Podowski [115].

Determining the plate thickness should then result from a compromise. On the one side, the thickness should be large enough to ensure a good representativeness of the heating surface regarding the topic of roughness and fully developed boiling. However, on the other side, the thickness should be thin enough to allow an accurate determination of the temperature on the wetted side of the heating plate. Figure 5.9 depicts the problem to be solved. The problem that is solved here is an unsteady heat conduction problem which is classically characterised by a Fourier number and therefore a characteristic conduction time (see Equation 5.2).

$$t_{cond} \sim \frac{e^2}{\alpha} \quad (5.2)$$

where  $e$  is the thickness of the plate and  $\alpha$  is the thermal diffusivity of the material. This characteristic time  $t_{cond}$  must therefore be sufficiently low so as not to dephase the unsteady phenomena that we wish to capture.

As a preliminary stage, assuming that the plate thickness will be likely much lower than the other characteristic dimensions of the heater, a one-dimensional approach will be considered.

By solving the diffusion equation within the plate for a given set of boundary conditions (here the problem is one-dimensional), it is possible to determine the wetted temperature  $T_{wet}$ . During experiments, all the IR measurements will be performed on the external side. So the boundary conditions, that are necessary to solve the heat conduction problem through the heater, will be expressed on the same face (dry side of the plate).

The associated heat conduction problem is then qualified as an inverse problem where the major characteristic is to be an ill-posed problem (from a mathematical point of view). As a consequence, the wetted temperature, which is calculated by solving the diffusion equation will be very sensitive to the boundary conditions uncertainties (dry temperature, and heat flux on this face).

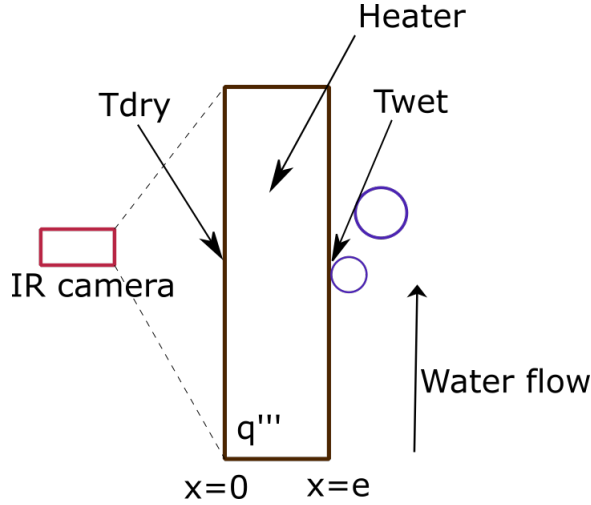


Figure 5.9: Schematic diagram of IR thermography measurements and thermal conductive problem.

## 5.2 Thermal study of the heater

### 5.2.1 Methodology

To determine the thickness of the plate, a three steps methodology was used (see Figure 5.10).

1. In a first step, the direct heat conduction problem is solved within the plate. This problem is characterized by a given couple of boundary conditions expressed on both sides of the calculation domain which do correspond to both faces of the heated plate:
  - (a) On the dry side:  $x = 0, q'' = 0$ .
  - (b) On the wetted side:  $x = e, T_{d,wet} = f(t)$ .

The objective is to calculate :  $T_{d,dry} = T(x = 0, t)$ . The subscript  $d$  indicates that the direct problem is being solved.  $x$  is the space variable,  $e$  the plate thickness and  $q''$  the heat flux.

2. In a second step, the associated inverse heat conduction problem is studied. This problem is characterized by a given couple of boundary conditions expressed on the dry side of the plate. This configuration will correspond to the experimental configuration, all the measurements being performed on the external (dry) face of the heater.
  - (a) On the dry side:  $x = 0, q'' = 0$ .
  - (b) On the dry side:  $x = 0, T_{i,dry}(0, t) = T_{d,dry}(0, t)$ .

The objective is to calculate the wetted temperature  $T_{i,wet}$  and to check whether  $T_{i,wet} = T_{d,wet}$ . The subscript  $i$  means that the inverse problem is being solved.

3. In a third step, a sensitivity analysis to the uncertainties of  $T_{d,dry}$  will be performed.

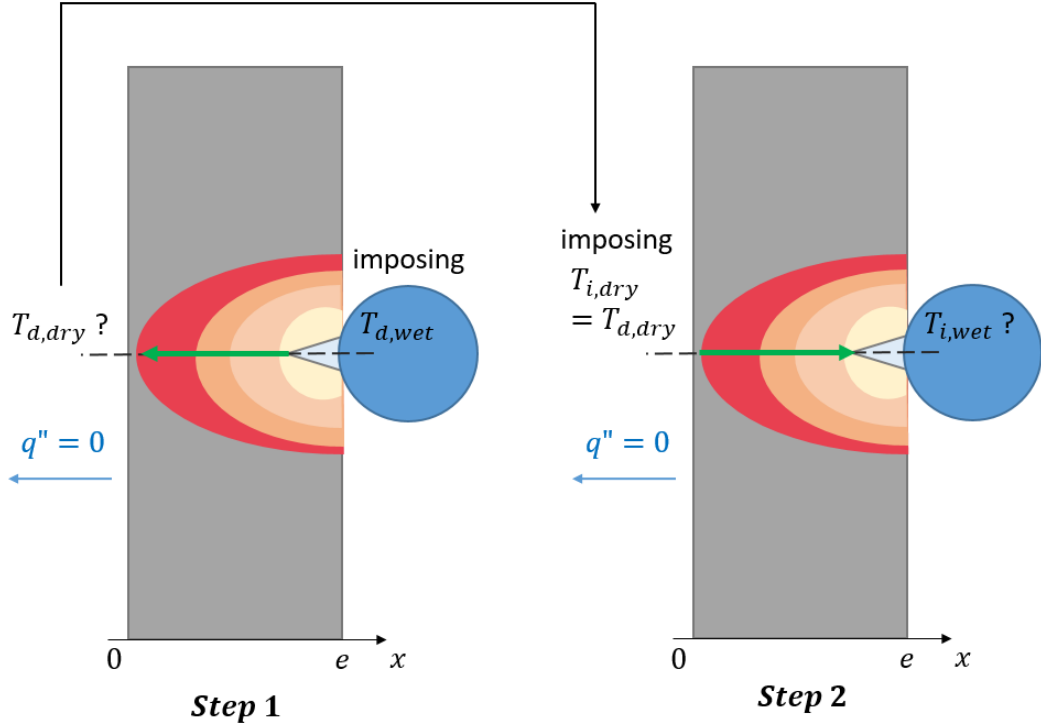


Figure 5.10: Step 1 and 2 of the thickness determination methodology.

### 5.2.2 Direct Problem Modeling

#### Modeling

The heat diffusion equation can be written as:

$$\rho C_P \frac{\partial T}{\partial t} = \lambda \nabla^2 T + q''' \quad (5.3)$$

where  $\rho$  is the density of the heater material,  $C_P$  is the thermal capacity of the heater material,  $T$  is the temperature,  $t$  is time,  $\lambda$  is the thermal conductivity of the heater material supposed to be constant and  $q'''$  is the volumic heat source due to direct Joule effect. The power input is calculated as the product of the electrical resistance of the plate  $R_{elec}$  and the current supplied squared  $I$ . The intensity is imposed by an electrical power source in order to heat the plate through direct Joule effect. The volumic heat source is then calculated as Equation 5.4.

$$q''' = \frac{R_{elec} I^2}{l \times H \times e} \quad (5.4)$$

The time dependent temperature profile on the wetted side of the plate  $T_{wet}$ , described in Figure 5.8. To simulate boiling on the wetted face, we consider:

$$\boxed{\begin{aligned} \text{for } t < t_g & \quad T_{d,wet}(x = e) = \frac{T_L - T_H}{t_g} t + T_H \\ \text{for } t_g < t < t_g + t_w & \quad T_{d,wet}(x = e) = T_L + \frac{T_L - T_H}{1 - e^{-1}} \left(1 - e^{-\frac{t - t_g}{t_w}}\right) \end{aligned}} \quad (5.5)$$

where  $t_g$  and  $t_w$  are respectively the growth time of a bubble on his nucleation site and the waiting time between two nucleations on the same site.

The initial condition is expressed as the solution of the steady problem:

$$\boxed{\lambda \nabla^2 T + q''' = 0} \quad (5.6)$$

$$\boxed{\text{Boundary conditions: } \frac{\partial T}{\partial x}(x=0) = 0 \\ T(x=e) = T_H} \quad (5.7)$$

### Preliminary estimation of thickness through analytical analysis

In order to determine a first order of magnitude of the thickness, a simple analytical analysis has been done. The attenuation and phase shift properties of a metal plate subjected to a variable temperature field as a boundary condition are to be estimated in a simple configuration. By considering a harmonic variation, one can analytically determine this behaviour and identify the skin thickness at which the information can no longer be identified.

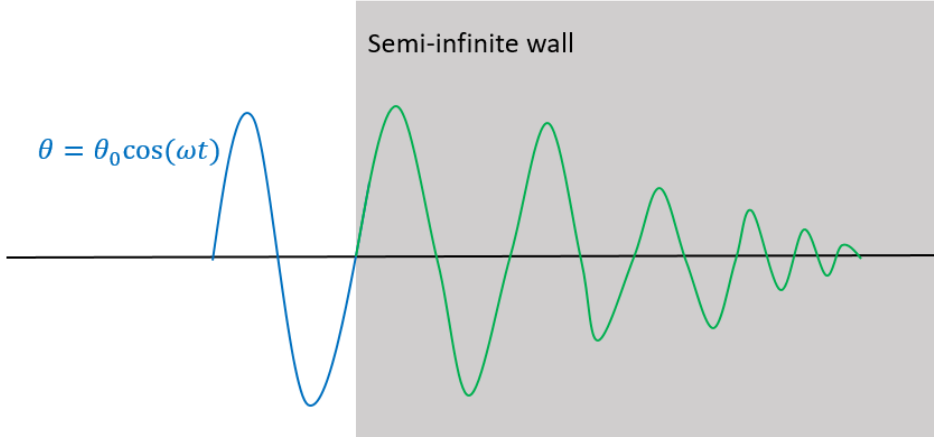


Figure 5.11: Harmonic time-dependent variation imposed at the boundary of a semi-infinite wall.

As a first approach, an harmonic time-dependent temperature is applied on the boundary of a semi-infinite wall (see Figure 5.11) with the following thermal equations 5.8 to 5.11.

$$\boxed{\rho C_P \frac{\partial \bar{\theta}}{\partial t} = \lambda \frac{\partial^2 \bar{\theta}}{\partial x^2}} \quad (5.8)$$

with  $\bar{\theta} = T - T_0$ ,  $T$  the temperature,  $T_0$  the initial temperature.

The boundary condition at  $x = 0$ ,  $\bar{\theta}_{wall}$ , is defined as:

$$\boxed{\bar{\theta}_{wall}(x=0, t) = \theta_0 \cos(\omega t)} \quad (5.9)$$

where  $\omega = 2\pi f$  and  $f$  the frequency.

The boundary condition for an infinite wall is defined as:

$$\bar{\theta}_\infty(x = \infty, t) = 0 \quad (5.10)$$

The initial condition  $\bar{\theta}_{init}$  is:

$$\bar{\theta}_{init}(x, t = 0) = 0 \quad (5.11)$$

The solution of Equations (5.8) to (5.11) can be written as:

$$\bar{\theta}(x, t) = e^{i\omega t} f(x) \quad (5.12)$$

Using boundary and initial conditions, the solution  $\bar{\theta}$  can be expressed as:

$$\boxed{\bar{\theta}(x, t) = \bar{\theta}_0 e^{\sqrt{\frac{\omega}{2\alpha}}x} \cos\left(\omega t - \sqrt{\frac{\omega}{2\alpha}}x\right)} \quad (5.13)$$

where  $\alpha$  is the thermal diffusivity.

With this simple expression, the temperature attenuation within the plate can be calculated. The signal frequency is deduced from time  $t_g$  and  $t_w$  characterizing the temperature variation under a nucleation site (see Figure 5.12).

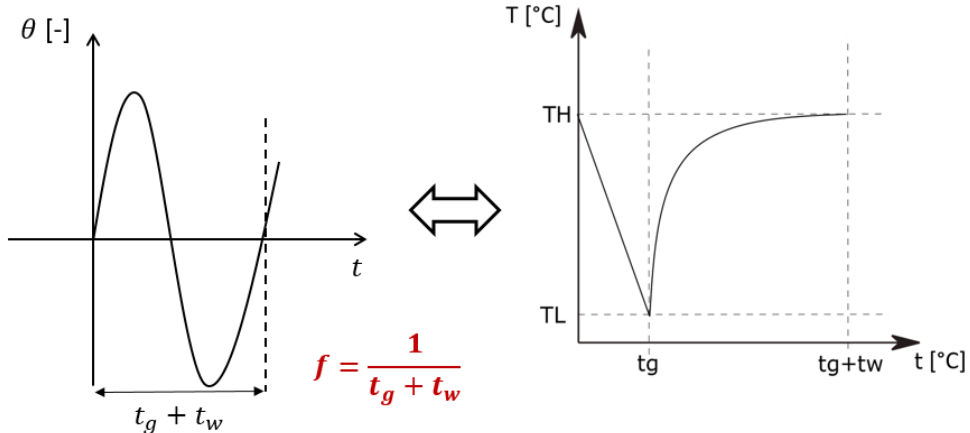


Figure 5.12: Equivalence between the harmonic variation and the temperature variation imposed in the initial problem.

The plate will be made of INOX 316L, its thermal diffusion is  $\alpha = 3,75 \cdot 10^{-6} m^2.s^{-1}$ , which is supposed to be constant. According to Unal [15], the following orders of magnitude for  $t_g$  and  $t_w$  are assumed to be:

$$t_g \approx 5 \cdot 10^{-3} s \text{ and } t_w \approx 1 \cdot 10^{-2} s \quad (5.14)$$

The frequency of the temperature variation is then equal to  $60 Hz$ .

Figure 5.13 shows the evolution of the bandwidth (blue curve) and time delay (red curve) within the plate as a function of the thickness. It indicates that after  $100 \mu m$  (green vertical limit) the information is not correctly detectable according to the blue curve: an attenuation by a factor of 2 is noted. This is the first limit that can be fixed for the thickness of the plate. Moreover the time delay is almost  $0.75 s$  for a  $100 \mu m$  thickness.

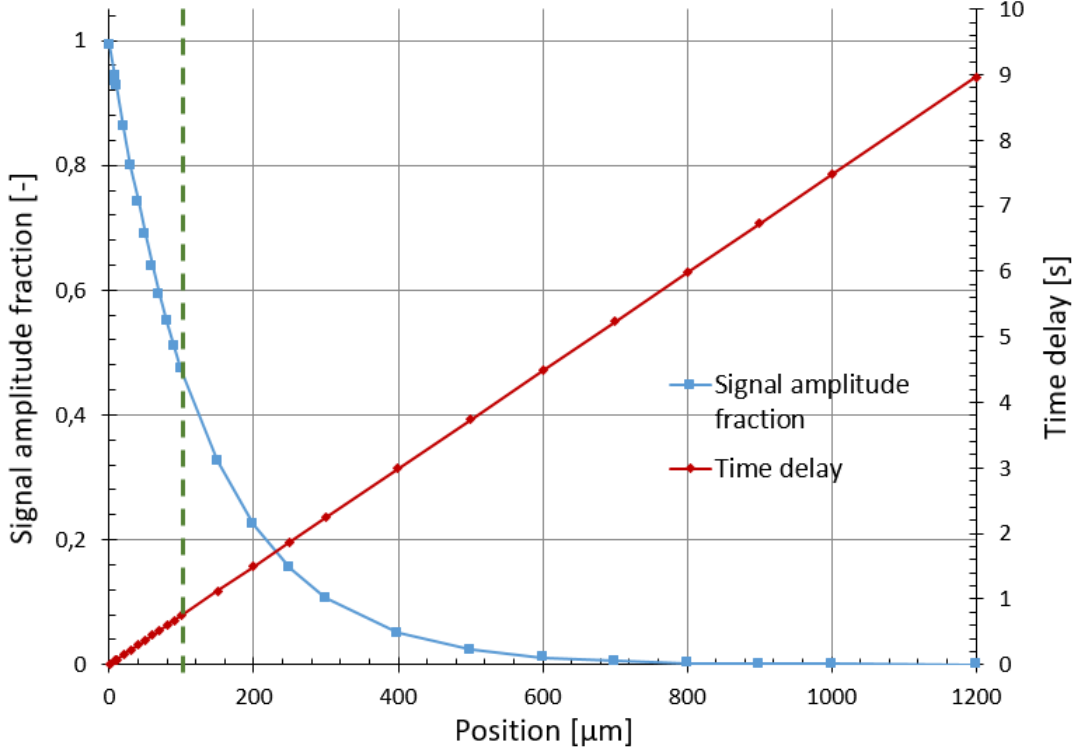


Figure 5.13: Variation of  $\bar{\theta}$  within the plate, blue curve shows the signal attenuation as a function of the thickness, red curve shows the time delay on the initial information as a function of the thickness.

## 1D solving

In 1D, the diffusion equation (5.3) can be written as:

$$\boxed{\rho C_P \frac{\partial T}{\partial t} = \lambda \frac{\partial^2 T}{\partial x^2} + q''' \quad (5.15)}$$

$$\boxed{\text{Boundary conditions: } \frac{\partial T}{\partial x}(0, t) = 0 \quad T(e, t) = T_{d,wet}(t) \quad (5.16)}$$

$$\boxed{\text{Initial condition: } T(x, 0) = T_{d,initial}(x) \quad (5.17)}$$

where  $T_{d,initial}(x)$  is the solution of the steady state problem defined by Equation (5.6) and (5.7) expressed in Equation 5.18.

$$\boxed{T_{d,initial} = \frac{q'''}{2\lambda}(x^2 - e^2) + T_H \quad (5.18)}$$

The solution of Equation (5.6) is a parabolic profile as shown in Figure 5.14 as it is a one-dimensional problem.

After meshing the plate with a regular mesh size along the axis (see Figure 5.15), equations (5.15) to (5.17) are solved by finite differences using a second-order centered scheme for the Laplacian (5.19) and an implicit scheme for time dependence (5.20).

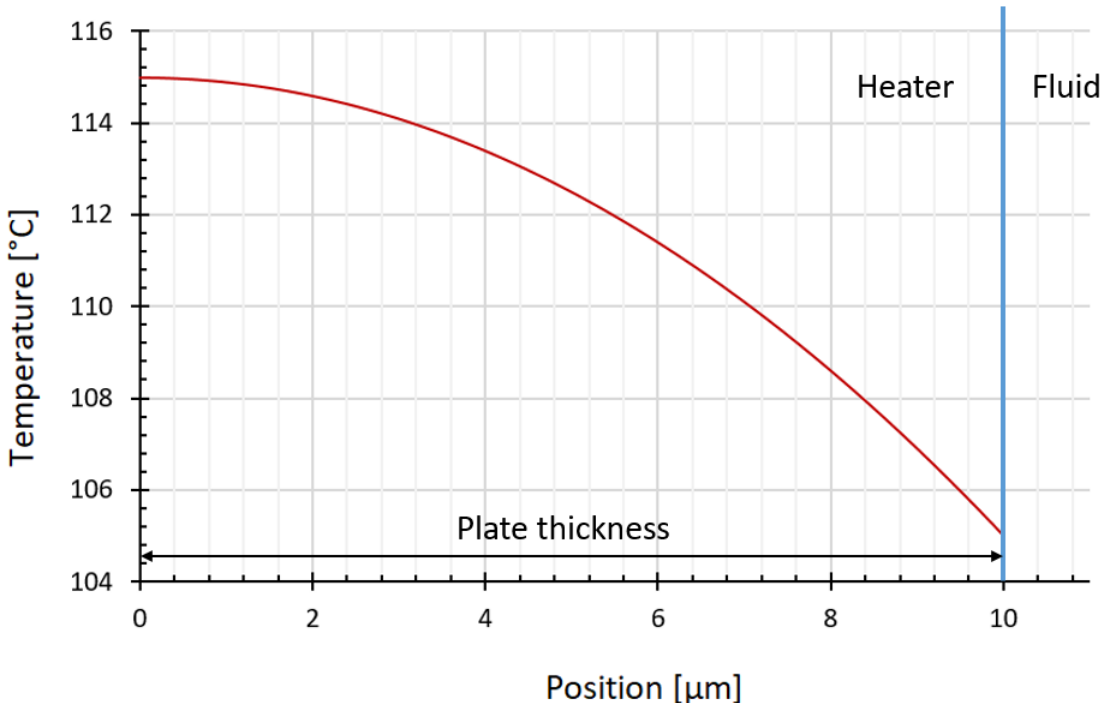


Figure 5.14: 1D steady state problem solution: temperature within the plate (thickness  $10 \mu m$ ).

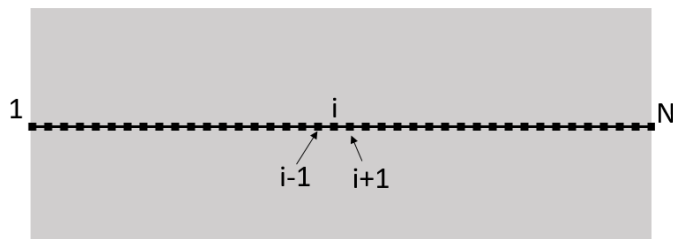


Figure 5.15: Meshing for finite differences resolution.

$$\begin{aligned}
 & \text{for } 2 < i < N - 1 \quad \frac{\partial^2 T}{\partial x^2} = \frac{T_{i+1} - 2T_i + T_{i-1}}{\Delta x^2} \\
 & \text{for } i = 1 \quad \frac{\partial^2 T}{\partial x^2} = \frac{T_2 - T_1}{\Delta x^2} \\
 & \text{for } i = N \quad T_N = T_{d,wet}
 \end{aligned} \tag{5.19}$$

$$\text{for } 1 < i < N \quad \left( \frac{\partial T}{\partial t} \right)^{n+1} = \frac{T_i^{n+1} - T_i^n}{\Delta t} \tag{5.20}$$

with  $N$  the number of points in the meshing over  $x$ ,  $n$  the number of time points. The temperature  $T(0, t)$  is then calculated. This temperature will be noted  $T_{dry}$ .

## Thickness selection

The 1D solving of the direct heat conduction problem leads to a first result regarding the plate thickness.

Figure 5.16 displays the variation of the temperature of the dry side of the heater for the previous time depending boundary conditions (Section 5.2.2) as a function of the plate thickness. It appears that for thicknesses higher than  $100 \mu\text{m}$  (yellow curve), the calculated dry temperature strongly differs from the wetted temperature.

Figure 5.16 (bottom) points out the time phase shift for a thickness ranging from  $10 \mu\text{m}$ -green curve to  $100 \mu\text{m}$ -yellow curve. For a thickness equal to  $100 \mu\text{m}$ , the phase shift represents almost 20% of the time scale we aim to measure, which implies that this thickness cannot be exceeded. The temperature variation of  $5^\circ\text{C}$  initially imposed on the wetted side results in a variation of  $4.2^\circ\text{C}$  on the dry side of the plate of  $100 \mu\text{m}$  thickness. The amplitude for the temperature variation between the wet and dry side is similar, the attenuation is small enough to be acceptable. We wish to limit the attenuation to  $1^\circ\text{C}$  because of the capabilities of a commercial infrared camera: the resolution of a camera, i.e. its ability to detect a temperature variation, is of the order of  $1^\circ\text{C}$ . This result is in accordance with the preliminary study of order of magnitude in Section 5.2.2 and confirms that this thickness cannot exceed  $100 \mu\text{m}$ .

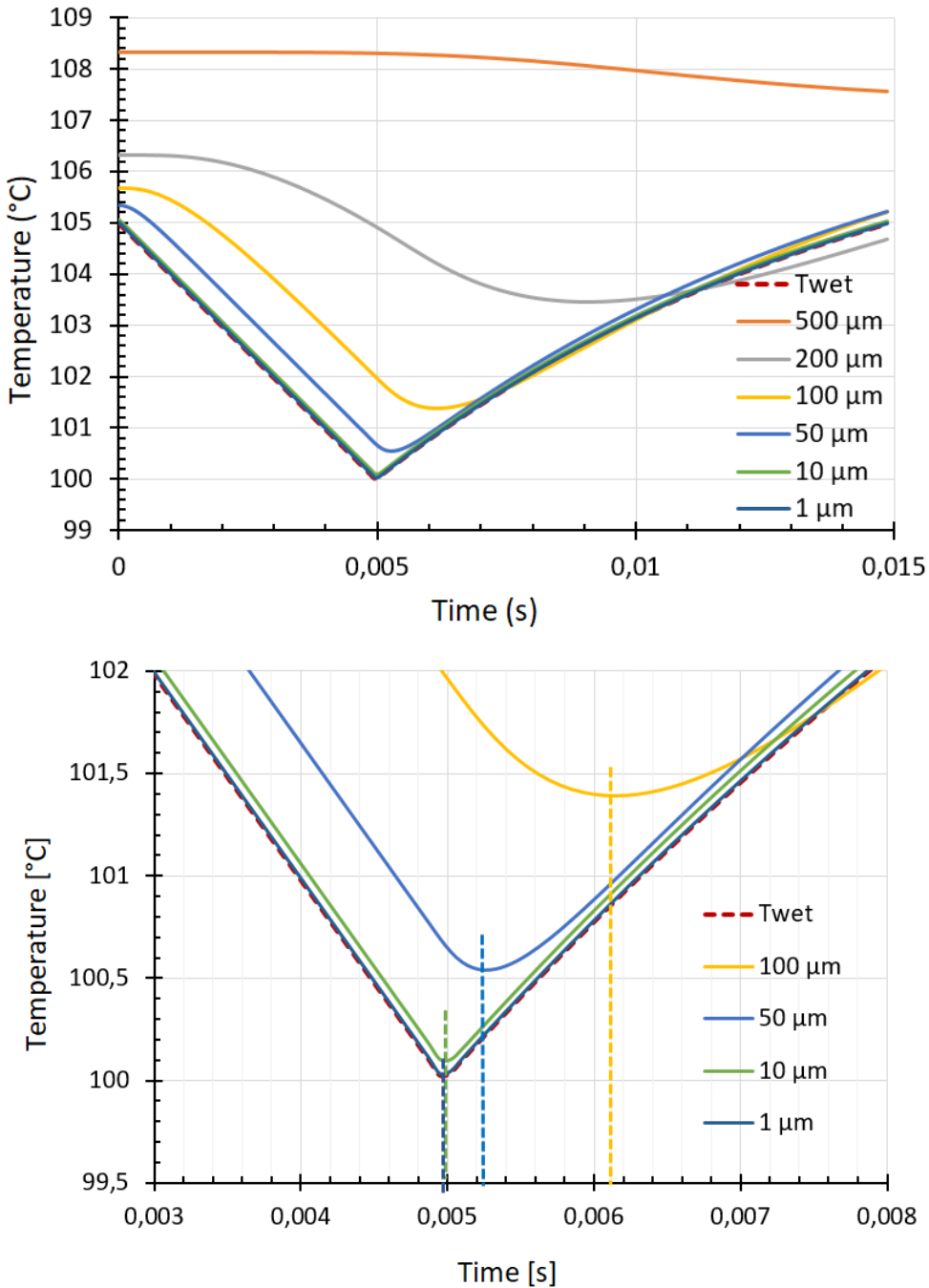


Figure 5.16: Direct problem solution: temperature on the external face (dry temperature) as a function of the thickness of the plate. This problem solution was solved with the following values:  $N = 1000$ ,  $n = 50$ ,  $t_g = 0.005 \text{ s}$ ,  $t_w = 0.01 \text{ s}$ ,  $\Delta t = 0.00031 \text{ s}$ ,  $P = 1 \text{ bar}$ ,  $I = 400 \text{ A}$ ,  $\Delta T = 5 \text{ }^\circ\text{C}$ .

### 5.2.3 Inverse problem

#### Measurement techniques

As introduced in Section 5.1.2, the temperature of the heated plate is intended to be measured on its external face (dry side,  $T_{dry}$ ) using an infrared camera. The temperature of the wetted side of the plate  $T_{wet}$  will be deduced from the dry temperature by solving the heat diffusion equation within the plate. Since boundary conditions are imposed on a single face of the plate (dry side), the heat conduction within the plate is called an inverse problem; such problems are ill-posed according to Hadamard [116, 117]. This implies that the solution of this probem is very sensitive to potential uncertainties in the boundary conditions. In our case this behaviour is emphasized by the thickness of the heater.

The purpose here is to determine if the measurement of the dry temperature will make it possible to deduce the wetted temperature, the one of interest, with an acceptable uncertainty without resorting to numerical regulation techniques. Indeed, these techniques imply knowing what we are measuring in order to filter and recover the information of interest. Without this prior knowledge there is no guarantee that we are not eliminating the information we wish to measure. The following section is dedicated to the study of this key-point.

#### Methodology

In Section 5.2.2, the wetted temperature was imposed and the dry temperature was calculated. The idea here is to try (i) to check whether, in the context of the inverse problem, it is possible to reconstruct the wet temperature  $T_{wet}$  that had been imposed from the dry temperature calculated previously  $T_{d,dry}$ , and (ii) to check the impact of an uncertainty (or measurement noise) on  $T_{dry}$  on the construction of the wet temperature  $T_{wet}$ . This methodology is described Figure 5.10 in Section 5.2.1.

As the previous study showed, it is a 1D framework.

The inverse problem is therefore characterised by the solution of the following system:

$$\boxed{\rho C_P \frac{\partial T}{\partial t} = \lambda \frac{\partial^2 T}{\partial x^2} + q'''} \quad (5.21)$$

$$\boxed{\text{Boundary conditions: } \begin{aligned} \frac{\partial T_i}{\partial x}(0, t) &= 0 \\ T_i(0, t) &= T_{d,dry}(t) \end{aligned}} \quad (5.22)$$

The dry temperature is taken as the result of the direct 1D problem calculated in Section 5.2.2.

The initial condition is given by:

$$T_i(x, 0) = T_{i,initial}(x) \quad (5.23)$$

where  $T_{i,initial}(x)$  is the solution of the steady state problem:

$$\boxed{\begin{aligned} \text{Problem equation: } & \lambda \frac{\partial^2 T_i}{\partial x^2} = -q''' \\ \text{Boundary conditions: } & \begin{aligned} \frac{\partial T_i}{\partial x}(0) &= 0 \\ T_i(0) &= T_{d,dry}(0, 0) \end{aligned} \end{aligned}} \quad (5.24)$$

The wet temperature  $T(e, t)$  is then calculated solving the heat conduction equation with conditions described from 5.22 to 5.24. This temperature is noted  $T_{i,wet}$  and will be compared to  $T_{d,wet}(t)$ .

## Results

The inverse problem was solved with finite differences as the direct problem was. Figure 5.17 shows the successive steps to solve the inverse problem. First, the direct problem was solved imposing a temperature variation over the wetted side of the plate (internal face)  $T_{d,wet}$ . As a result, we calculate the temperature variation obtained on the external face of the plate  $T_{d,dry}$ . The inverse problem is then solved imposing on the external face the temperature resulting from the direct problem calculation  $T_{d,dry}$ . The solution of the inverse problem is then the calculated temperature on the internal face  $T_{i,wet}$ , which then has to be compared with the one imposed first  $T_{d,wet}$ .

As it can be noticed on Figure 5.17, we are calculating exactly the same wetted temperature than the one imposed at the beginning for any parameter (blue and green curve).

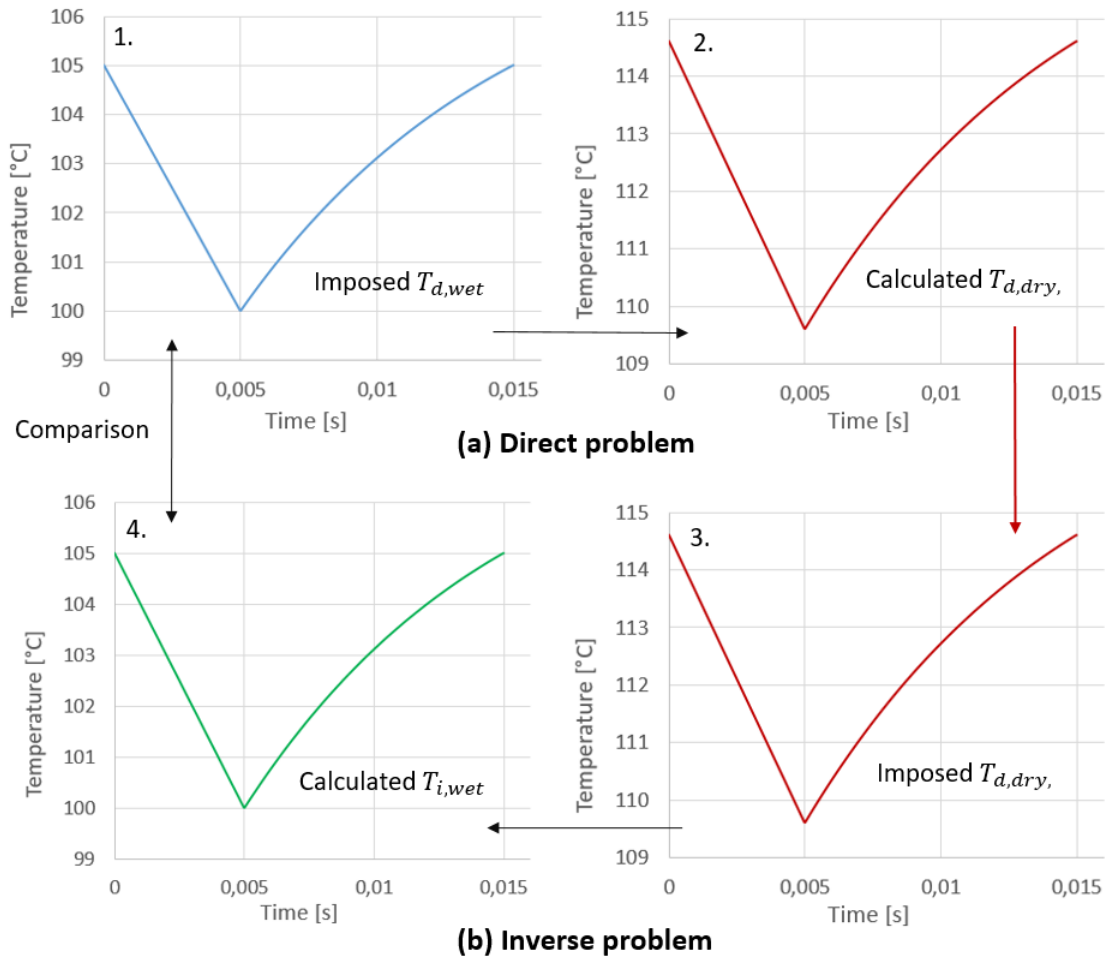


Figure 5.17: Steps to solve the inverse problem, (a) solving the direct problem by imposing the wet temperature (blue curve), (b) solving the inverse problem by imposing the dry temperature (red curve), calculated before.

As all inverse problems, the solution is known to be very sensitive to boundary conditions uncertainties. To characterise this effect, a random uncertainty (white noise) of  $\pm 0.5^{\circ}\text{C}$  is applied to the measurement on the outside (dry temperature). This value of  $\pm 0.5^{\circ}\text{C}$  is chosen to be consistent with the expected measurement uncertainty of the temperature measurement by a properly calibrated IR camera.

Imposing this uncertainty to the dry side temperature  $T_d(0, t)$ , results in an amplification of the noise of the wetted temperature as expected. The amplification factor is strongly dependent of the plate thickness.

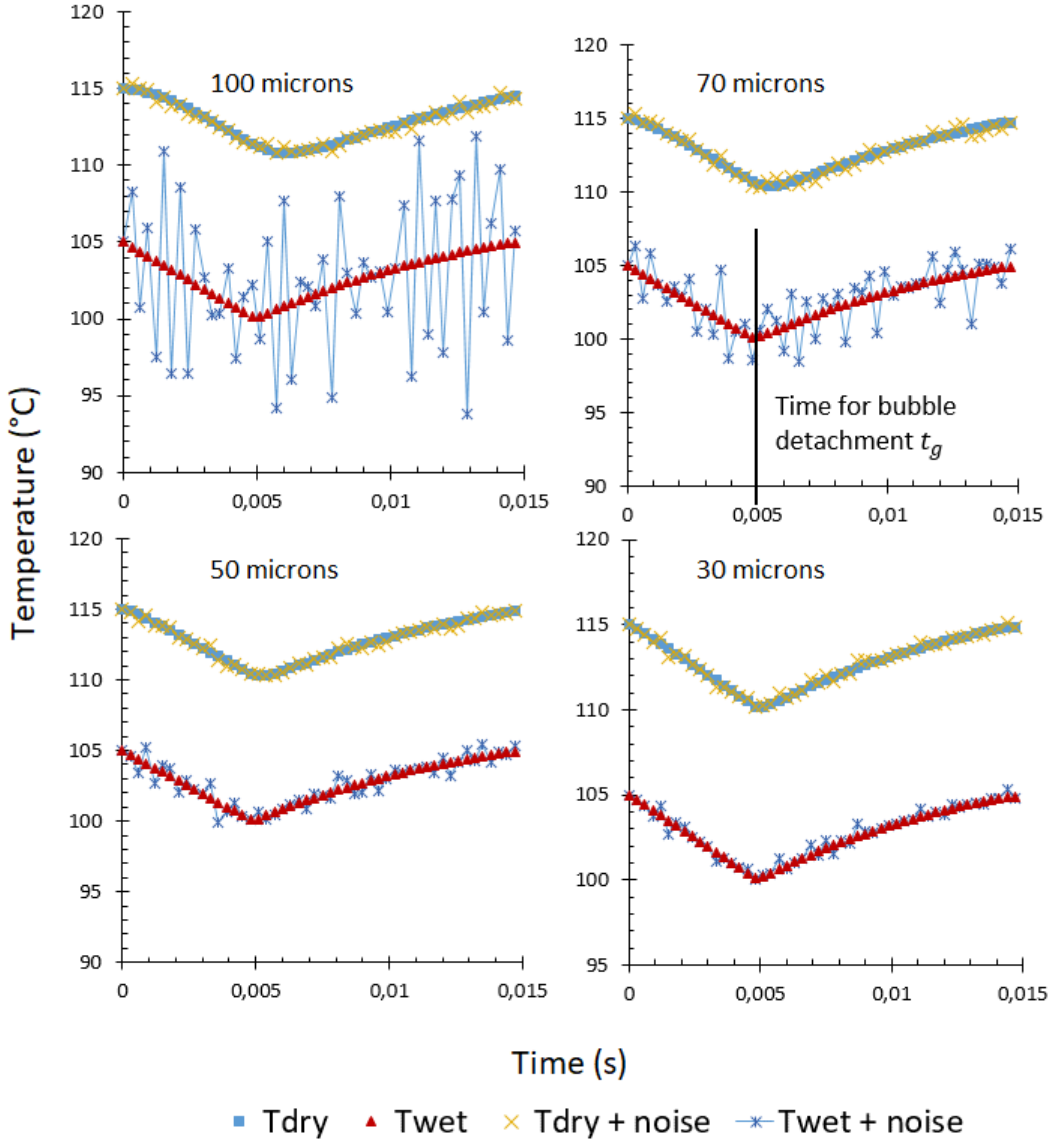


Figure 5.18: Illustration of the noise amplification solving the inverse problem for various thicknesses. This problem solution was solved with the following values:  $N = 1000$ ,  $n = 50$ ,  $t_g = 0.005 \text{ s}$ ,  $t_w = 0.01 \text{ s}$ ,  $\Delta t = 0.00031 \text{ s}$ ,  $P = 1 \text{ bar}$ ,  $I = 400 \text{ A}$ ,  $\Delta T = 5^{\circ}\text{C}$ .

Figure 5.18 shows the influence of the plate thickness on the accuracy of the calculated wetted temperature. The blue and red triangles depict the initial results for the dry and

wetted temperature (without any uncertainties). The yellow crosses correspond to the dry temperature taking into account for the uncertainty (imposed white noise). The blue crosses are the result of the inverse problem with the noisy dry temperature. For  $100 \mu\text{m}$ , the amplification leads to an impossibility of finding back the time scales that are aimed to be measured ( $t_g$  and  $t_w$ ). Decreasing the thickness leads to decrease the noise on the reconstructed wetted temperature, making it easier to determine  $t_g$  and  $t_w$  timescales.

The amplification of the measurement noise by the inverse calculation as a function of the plate thickness is listed in Table 5.1.

Table 5.1: Amplification factor of uncertainties by inverse calculation depending of plate thickness.

Thickness [ $\mu\text{m}$ ]	Root mean square $T_{dry}$ [ $^{\circ}\text{C}$ ]	Maximum error $T_{dry}$ [ $^{\circ}\text{C}$ ]	Root mean square $T_{wet}$ [ $^{\circ}\text{C}$ ]	Maximum error $T_{wet}$ [ $^{\circ}\text{C}$ ]
100	4.5	10.63	0.23	0.5
70	1.43	3.49	0.27	0.5
50	0.55	1.41	0.2	0.5
30	0.28	0.82	0.18	0.5

A  $70 \mu\text{m}$  thickness enables to detect the change of slope (identified on the Figure 5.18) that corresponds to the time of the bubble detachment, which makes it a priori possible to measure the bubble detachment frequency from the wall. However, the apparent noise shows an oscillation of about  $5^{\circ}\text{C}$  around the actual temperature value.

For the study of boiling that is envisaged on the future device, a more accurate temperature measurement should be considered. Classical wall boiling models (described in the previous chapters) show that wall superheats during boiling are of the order of 3 to  $6^{\circ}\text{C}$ . It is therefore important to be more accurate than these temperature differences in order to be able to use the temperature measurements for modelling purposes: the choice is set around  $2^{\circ}\text{C}$  variation.

For a  $50 \mu\text{m}$  thickness, the noise is reduced. The identification of the quantities of interest in time and temperature is more accurate ( $2^{\circ}\text{C}$  variation around the actual temperature value). This value of  $50 \mu\text{m}$  is then chosen to be the new upper limit for the plate thickness.

To verify that this result is maintained for several temperature cycles at the same nucleation site, the amplification is identified for two successive cycles. The figure 5.19 shows the result for two successive cycles and a thickness of 100 microns keeping the same values for the inlet quantities of the problem.

The amplification due to the inverse calculation of the wetted temperature is identified as before. Table 5.2 lists the amplifications for two successive temperature cycles for the same thicknesses as above, and it can be seen that the amplifications are identical.

The conclusions drawn for a single cycle are therefore retained.

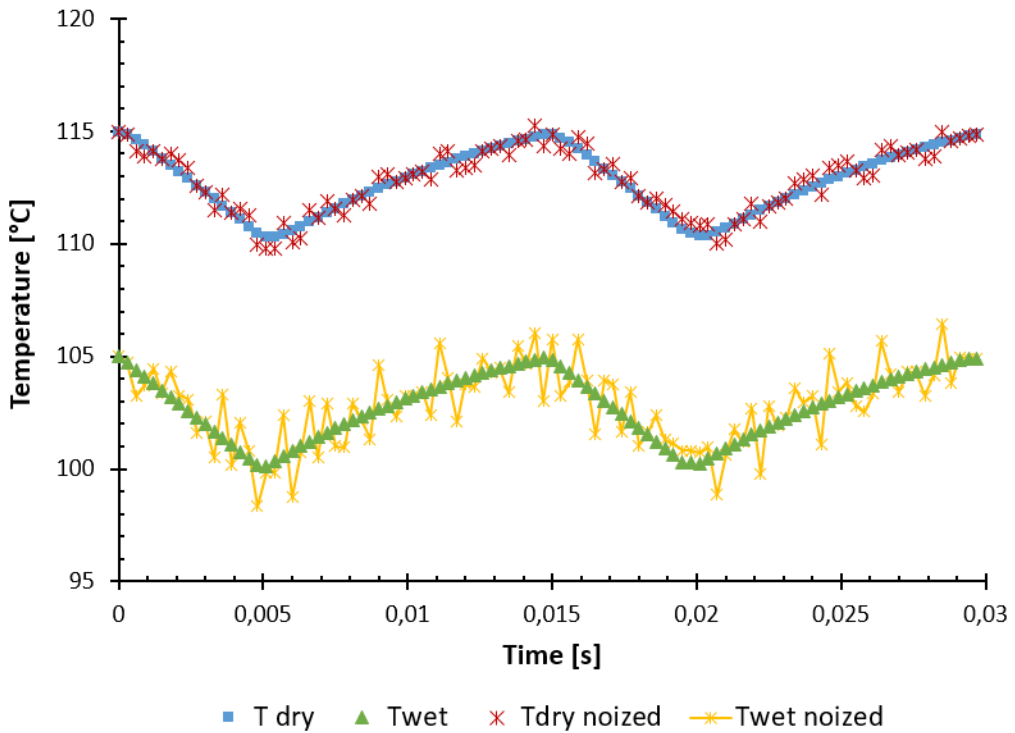


Figure 5.19: Illustration of the noise amplification solving the inverse problem for  $100 \mu\text{m}$  plate thickness. This problem solution was solved with the following values:  $N = 1000$ ,  $n = 100$ ,  $t_g = 0.005 \text{ s}$ ,  $t_w = 0.01 \text{ s}$ ,  $\Delta t = 0.00031 \text{ s}$ ,  $P = 1 \text{ bar}$ ,  $I = 400 \text{ A}$ ,  $\Delta T = 5^\circ\text{C}$ .

Table 5.2: Amplification factor of uncertainties by inverse calculation depending of plate thickness for two successive temperature variation cycles.

Thickness [ $\mu\text{m}$ ]	Root mean square $T_{dry}$ [ $^\circ\text{C}$ ]	Maximum error $T_{dry}$ [ $^\circ\text{C}$ ]	Root mean square $T_{wet}$ [ $^\circ\text{C}$ ]	Maximum error $T_{wet}$ [ $^\circ\text{C}$ ]
100	3.67	12.18	0.23	0.5
70	1.4	3.28	0.24	0.5
50	0.65	1.68	0.22	0.5
30	0.32	0.68	0.22	0.5

## 5.3 Spatial resolution of the measurements

In this Section, we aim to determine the spatial resolution of this method, using the 2D model for this problem. This 2D study should confirm the 1D approach developed above. The 1D approach was given for bubble diameters that are an order of magnitude larger than the plate thickness studied:  $D \gg e$ . It is important to verify the behaviour of the plate with a bubble whose diameter is of the order of the thickness of the plate:  $D \approx e$ . The 2D effects in this problem are inherent to the fact that we have a plate powered by the direct Joule effect and therefore with an internal heat source. The resistance of the plate drives the flux distribution and any change in temperature impacts this distribution and can create inhomogeneities or oppose a temperature change. First, the 2D model is presented with a comparison between the 2D and 1D result for a large bubble ( $D \gg e$ ). Then a sensitivity study is carried out to establish the thickness at which a bubble of a fixed size (pressure dependent) can be detected by an IR camera on the dry side (in the case of  $D \approx e$ ). Finally, we are interested in the minimum distance between two bubbles for them to be detected independently of each other by an IR camera on the dry side of the plate.

### 5.3.1 2D diffusion influence

In order to assess the validity of a one-dimensional approach, some calculations using a two-dimensional description of the heater were performed. In such case, the general diffusion

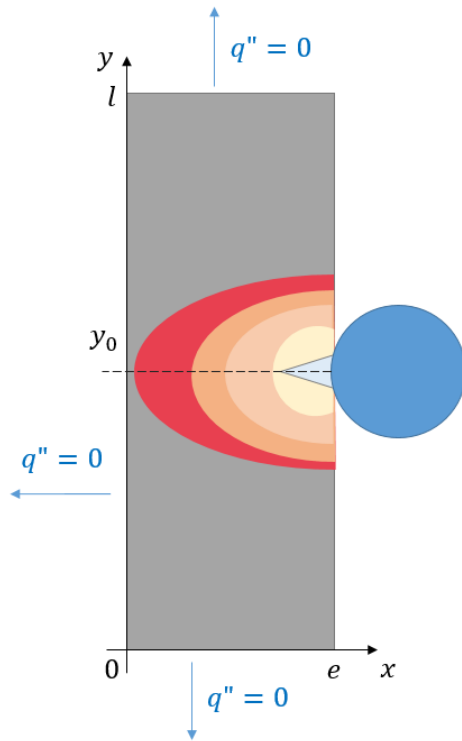


Figure 5.20: Diagram of the 2D model with a bubble growing on  $y = y_0$ . The plate dimension is  $e \times l$ .

equation (5.3) can be written for a 2D approach as:

$$\boxed{\rho C_P \frac{\partial T}{\partial t} = \lambda \left( \frac{\partial^2 T}{\partial x^2} + \frac{\partial^2 T}{\partial y^2} \right) + q'''} \quad (5.25)$$

where  $x$  and  $y$  are the space variables (see Figure 5.20).

The boundary conditions are:

$$\boxed{\begin{aligned} \text{Boundary conditions: } & \frac{\partial T}{\partial x}(0, y, t) = 0 \\ & T(e, y, t) = T_{d,wet}(y, t) \\ & \frac{\partial T}{\partial y}(x, 0, t) = 0 \\ & \frac{\partial T}{\partial y}(x, l, t) = 0 \end{aligned}} \quad (5.26)$$

The temperature on the wetted side of the plate  $T_{wet}$  is given by:

$$\boxed{\begin{aligned} \text{for } t < t_g \text{ and } y = y_0 & T_{d,wet}(x = e, y = y_0) = \frac{T_L - T_H}{t_g} t + T_H \\ \text{for } t_g < t < t_g + t_w \text{ and } y = y_0 & T_{d,wet}(x = e, y = y_0) = T_L + \frac{T_L - T_H}{1 - e^{-1}} \left( 1 - e^{-\frac{t - t_g}{t_w}} \right) \\ \forall t \text{ and } y \neq y_0 & T_{d,wet} = T_H \end{aligned}} \quad (5.27)$$

where  $y_0$  is the position of a nucleation site on the plate (see Figure 5.20).

The initial condition is:

$$T(x, y, 0) = T_{d,initial}(x, y) \quad (5.28)$$

where  $T_{d,initial}(x, y)$  is the solution of the steady state problem where the boundary conditions are ( $T_H$  is same as defined on Figure 5.8):

$$\boxed{\begin{aligned} \text{Problem equation: } & \lambda \left( \frac{\partial^2 T}{\partial x^2} + \frac{\partial^2 T}{\partial y^2} \right) = -q''' \\ \text{Boundary conditions: } & \frac{\partial T}{\partial x}(0, y) = 0 \\ & T(e, y) = T_H \\ & \frac{\partial T}{\partial y}(x, 0) = 0 \\ & \frac{\partial T}{\partial y}(x, l) = 0 \end{aligned}} \quad (5.29)$$

The 2D steady state temperature distribution is presented in Figure 5.21.

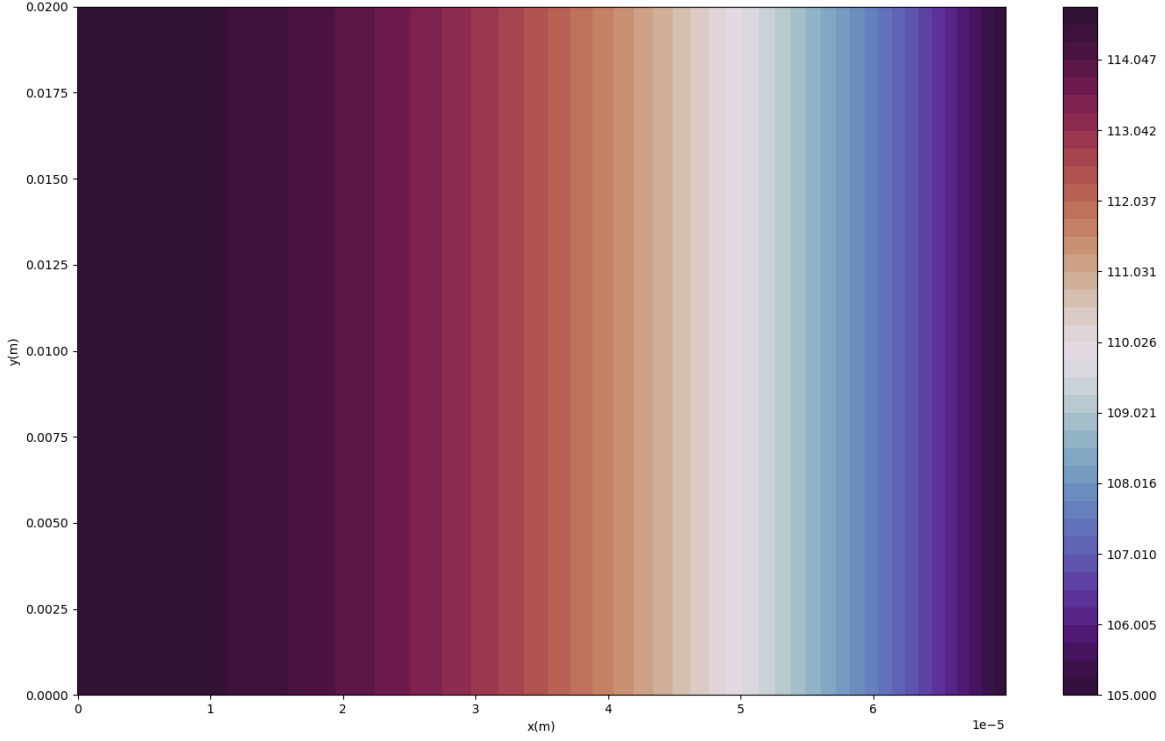


Figure 5.21: Steady temperature used as the initial condition in the 2D model.

Equations 5.25 to 5.29 are solved by finite difference using a second-order central scheme for the Laplacian and an implicit scheme for time dependence. The temperature  $T(0, t)$ , noted  $T_{dry}$ , is then calculated. Figure 5.22 displays, for different thicknesses, the influence of the 2D description of the heater temperature beneath the nucleation site at  $y = y_0$ . This figure aims to point out the diffusion effect between 1D and 2D modellings. The yellow curves depict the 1D calculation of the direct conduction problem within the plate, whereas the blue curves depict the 2D calculations of this problem. It shows that the gap between 1D and 2D simulations is decreasing with the thickness: the difference in terms of plate temperature comes from a maximum gap of  $0.21^\circ\text{C}$  at  $100\ \mu\text{m}$  to  $0.07^\circ\text{C}$  at  $50\ \mu\text{m}$ . We can then conclude that it is useless to consider a 2D approach, at least, as long as the bubble size is larger than the thickness of the plate.

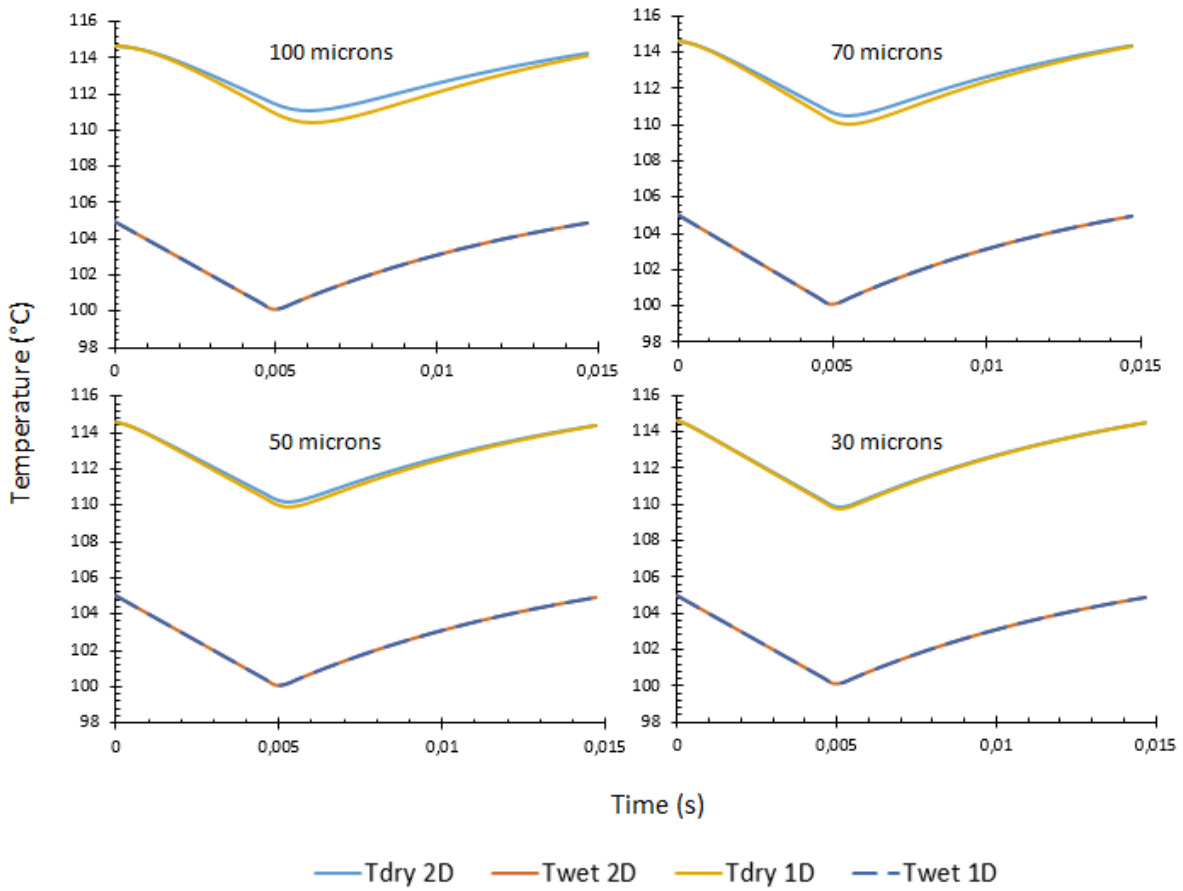


Figure 5.22: Illustration of the 2D diffusion effect over the dry temperature for various thicknesses at  $y = y_0$ ,  $x = e$  for wet temperature,  $x = 0$  for dry temperature. This problem solution was solved with the following values:  $N_x = 50$ ,  $N_y = 200$ ,  $n = 50$ ,  $t_g = 0.005 \text{ s}$ ,  $t_w = 0.01 \text{ s}$ ,  $\Delta t = 0.00031 \text{ s}$ ,  $P = 1 \text{ bar}$ ,  $I = 400 \text{ A}$ ,  $\Delta T = 5 \text{ }^{\circ}\text{C}$ .

### 5.3.2 Thermal influence area of a bubble growth

When a bubble appears at a nucleation site, a temperature variation appears under the bubble. Figure 5.23 shows graphically the area of influence of a bubble on the wall temperature. Without a bubble the temperature is constant (right), when a bubble grows on the wall (left), the temperature variation that we study in 1D appears on a zone that we define here as being the size of the bubble diameter. The temperature variation on the dry side then appears to be attenuated in amplitude, and the influence area is expended because of 2D diffusion effect. It is important to check that this temperature variation is measurable in two steps: (i) check that the amplitude  $A$  of this variation is measurable and therefore larger than the resolution of the camera (its ability to detect a temperature variation), (ii) that the size of the spot  $d$  is larger than a camera pixel, to be able to detect it.

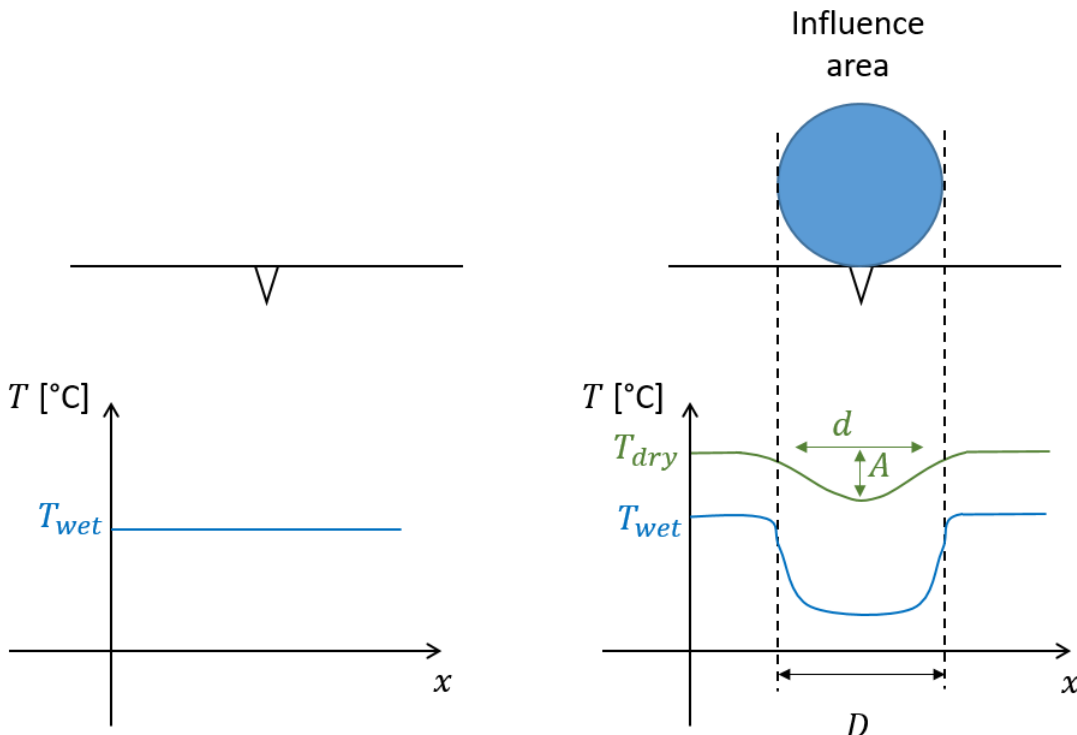


Figure 5.23: Influence area during a bubble growth on a nucleation site. This area can be characterised by his size  $d$  and the amplitude of the thermal disturbance  $A$  for the dry side of the plate.

Let us recall that the aim of these measurements is to detect the timescales of the bubble growth on the plate from low to high pressure conditions. Unal correlation [15] gives an order of magnitude of the Sauter diameter of the bubble as a function of thermal hydraulic conditions. For our prototypical conditions, the bubble diameter ranges from  $40 \mu\text{m}$  to  $800 \mu\text{m}$ , for pressure values respectively from 110 to 1 bar.

For each of these conditions (pressure, bubble size), the maximum thickness over which the bubble is not well detected by IR measurements has to be determined.

IR camera generally presents a theoretical temperature resolution of  $50 \text{ mK}$  (a good cali-

bration must be carried out beforehand). As a first criterion, we will consider that a variation of the wall temperature of  $1^{\circ}\text{C}$  is enough to detect a bubble attached to the wall. In order to consider bubble timescales to be measurable, a second criteria was set. The detachment of the bubble will induce a slightly higher temperature variation so that a second step corresponding to a variation of  $2^{\circ}\text{C}$  of the wall temperature is considered. Moreover, conventional detectors for high-speed, high-performance cameras have pixel sizes in the range of 10 to  $25\ \mu\text{m}$ . The bubble detection criterion for the size of the influence area  $d$  is therefore set at 2 pixels or  $50\ \mu\text{m}$ .

As an example, Figure 5.24 shows for a  $120\ \mu\text{m}$  bubble size (corresponding bubble size for  $P = 50\ \text{bar}$ ) and a temperature variation of  $5^{\circ}\text{C}$  under his nucleation site, the limit thickness selection, with a red dashes curve named  $1^{\circ}\text{C}$  limit for the detection first criterion and a blue dashes curve named  $2^{\circ}\text{C}$  limit for the measurement second criterion.

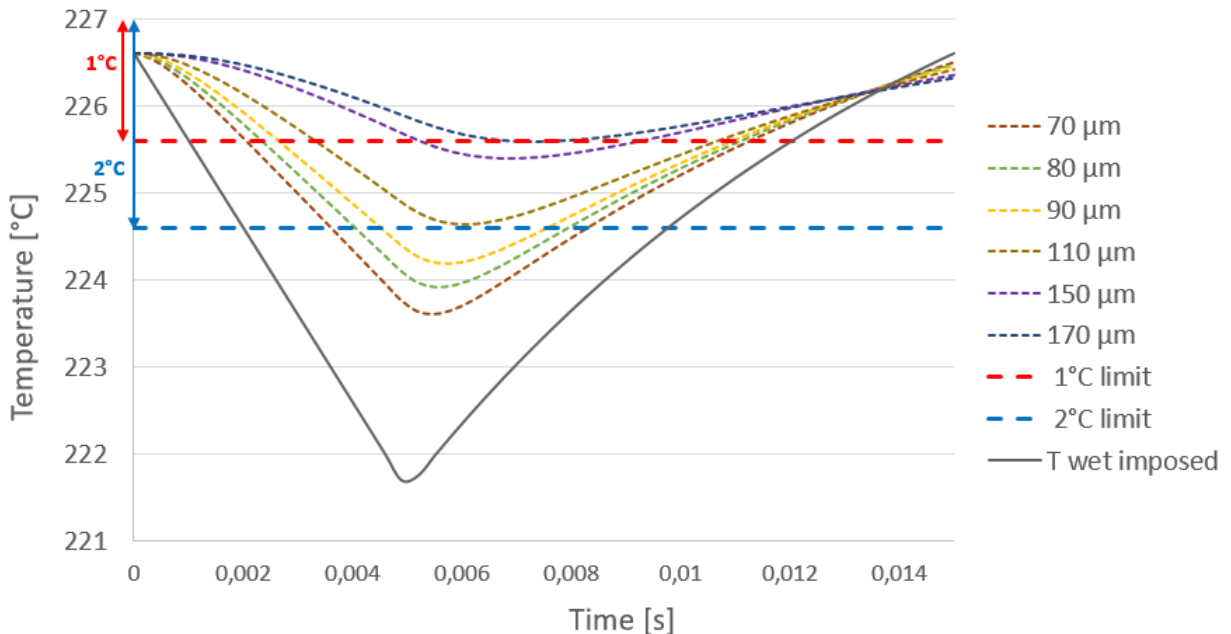


Figure 5.24: Example of determination of the limit thickness for  $20\ \text{bar}$  pressure, a  $120\ \mu\text{m}$  bubble diameter was imposed.

The determination of the thickness is done in two steps:

- a first step consists in identifying the thickness corresponding to the camera-readable amplitude of the dry-side temperature variation (example Figure 5.24, criteria 1 gives a  $170\ \mu\text{m}$  thickness, criteria 2 gives  $110\ \mu\text{m}$  thickness.),
- a second step determines the dry-side influence area considering the two temperature criteria (see Figure 5.25, criteria 1 thickness is valid ( $d_1 = 60\ \mu\text{m}$ ), but criteria 2 was corrected to  $100\ \mu\text{m}$  thickness ( $d_2 = 60\ \mu\text{m}$ )).

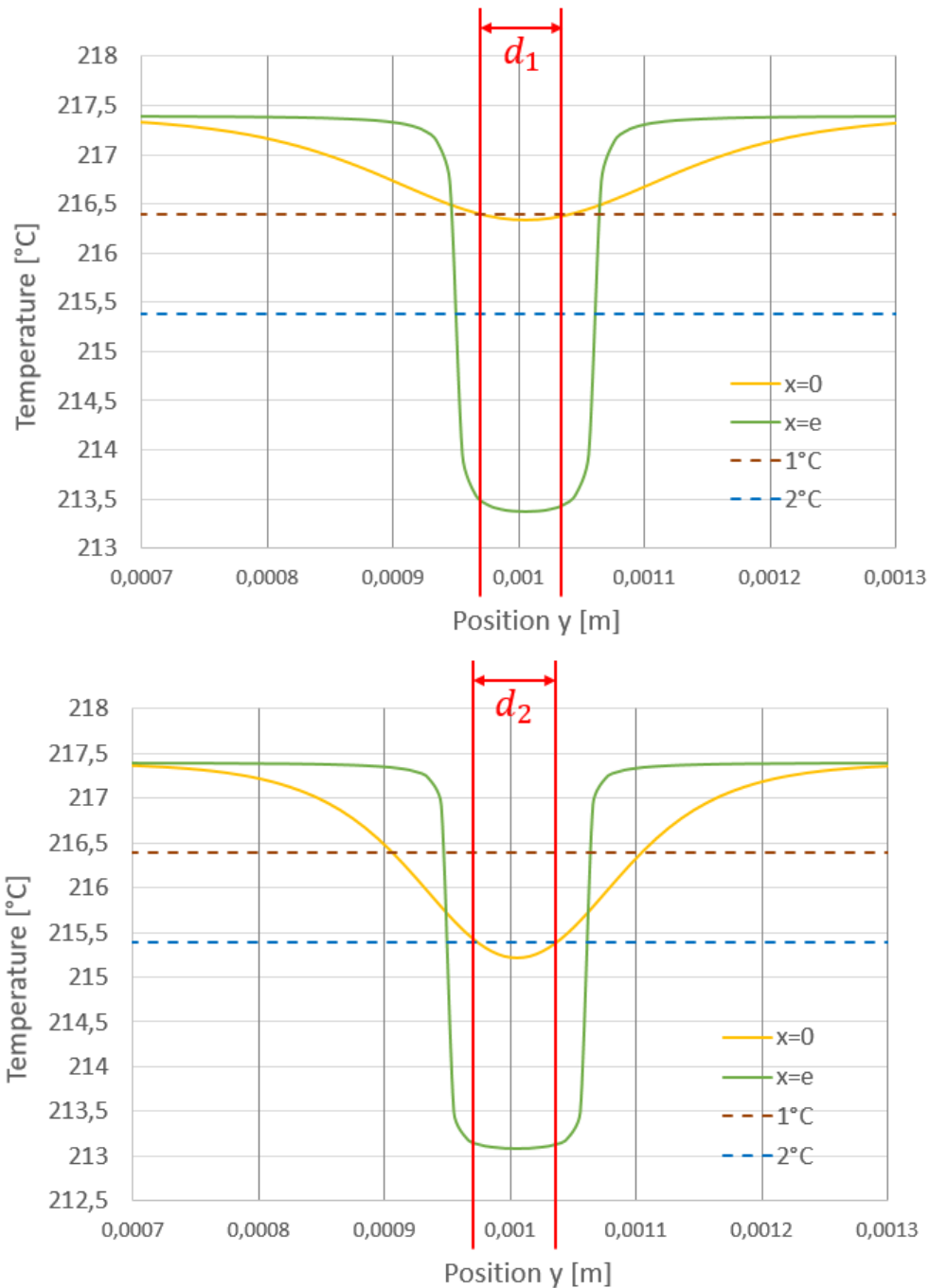


Figure 5.25: Example of verification of the zone of influence of temperature variation according to criteria 1 and 2. Here, for a pressure of 20 bar, for a thickness of 170  $\mu\text{m}$  (top), criterion 1 is respected, the zone of influence is 60  $\mu\text{m}$ , for the second criterion (bottom) it is necessary to reach 100  $\mu\text{m}$  thickness to detect the influence area on the dry side.

Table 5.3 summarises for each couple of pressure and bubble size, the thickness corresponding to the first and second criteria defined above. These values were identified after the two steps of checking amplitude and area of influence against the parameters of an IR camera.

Table 5.3: Spatial resolution: thickness range associated to bubble size detection (pressure dependent).

Bubble size ( $\mu m$ )	Pressure (bar)	First criterion: $1^\circ C$ detection thickness ( $\mu m$ )	Second criterion: $2^\circ C$ measurement thickness ( $\mu m$ )
800	1	250	190
120	20	170	100
70	50	100	50
50	80	70	40
40	110	65	35

This result shows that a  $50 \mu m$  thickness is a good compromise to be able to detect bubbles over the plate, to measure the timescales of the bubble growth and to maintain a sufficient thickness to ensure the representativeness of the surface. For higher pressure values, bubble size calculated with Unal correlation [15] decreases and the temperature variation under this bubble could be more complicated to capture.

### 5.3.3 Discretization between two bubbles growing on the plate

With the same 2D model, the space meshing between two bubbles depending on the thickness of the plate is also checked as shown in Figure 5.26. For a fixed thickness, the space between two bubbles of the same size is increased until they can be detected independently from each other from the dry side of the plate (see Figure 5.26).

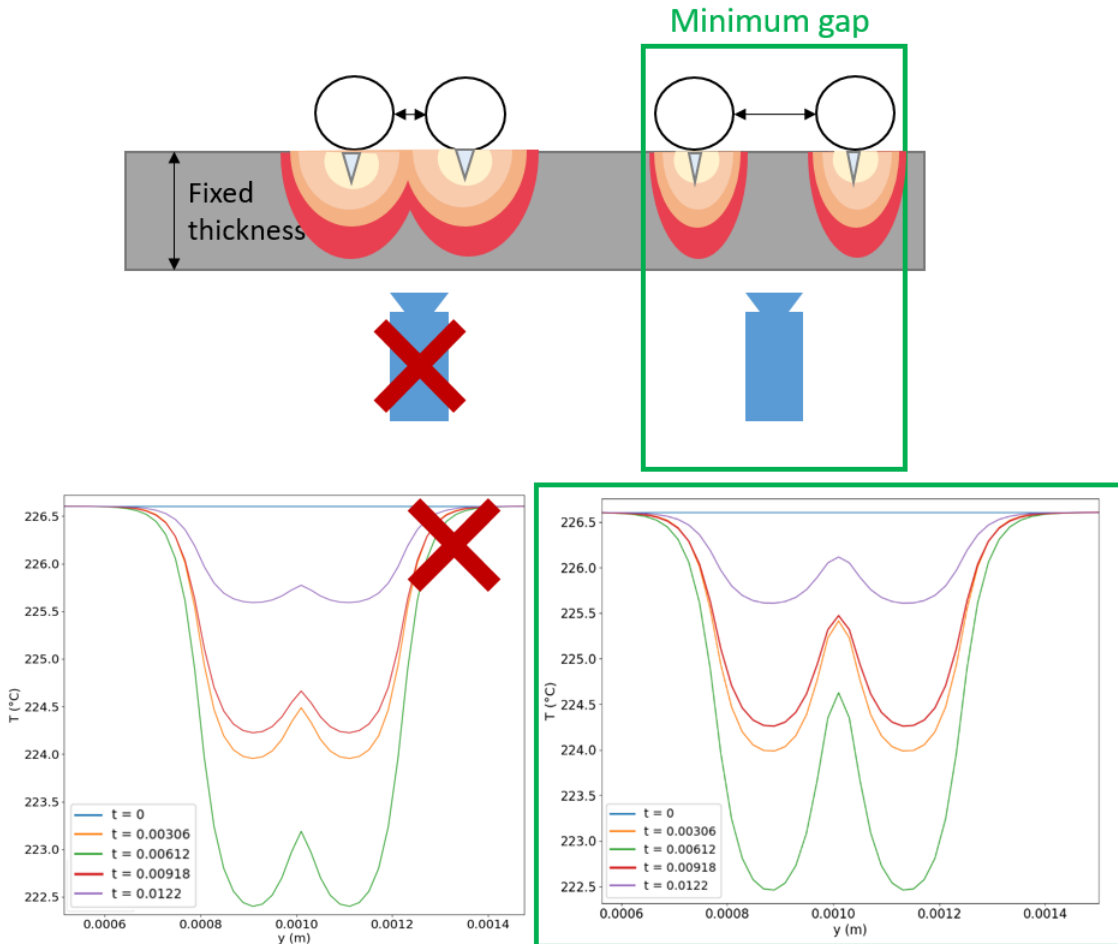


Figure 5.26: Example of determination of the minimum gap for two bubbles to be discernable. For the first example (left) the bubbles are too close, the temperature on the dry side will not allow to discretize two objects but one big bubble growing on the plate. For the second example, after expanding the distance between the bubbles, the temperature field allows to detect two different spots.

Table 5.4 summarises the minimum gap between two bubbles to be detected independently (and not seen as one). Thickness of  $50 \mu\text{m}$  will provide a discretisation of  $40 \mu\text{m}$  for bubbles with a diameter of  $200 \mu\text{m}$  and  $100 \mu\text{m}$  for bubbles with a diameter of  $50 \mu\text{m}$ .

Table 5.4: Meshing of the method

Thickness ( $\mu m$ )	Bubble size ( $\mu m$ )	Minimum gap for detection ( $\mu m$ )
70	200	60
70	50	120
50	200	40
50	50	100
30	200	20
30	50	60

## 5.4 Influence of the boundary condition on the dry side

The previous results were demonstrated from a simple boundary condition on the outer boundary of the plate: a null heat flux condition. It is now interesting to consider the results with a different boundary condition. The previous model has therefore been modified by applying a heat flux condition on the outer boundary of the plate (see Figure 5.27).

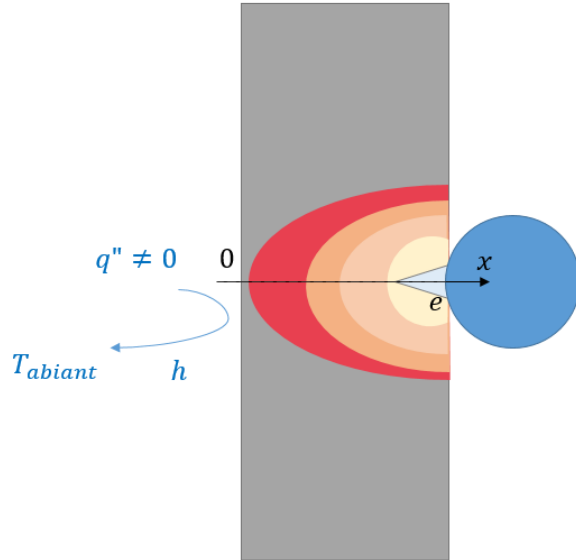


Figure 5.27: Diagram of the model with new boundary condition depending of the surrounding environment.

In 1D, the diffusion equation (5.3) is still written as:

$$\boxed{\rho C_P \frac{\partial T}{\partial t} = \lambda \frac{\partial^2 T}{\partial x^2} + q'''}$$
 (5.30)

$$\boxed{\text{Boundary conditions: } -\lambda \frac{\partial T}{\partial x}(0, t) = h(T(0, t) - T_{ambient}) \\ T(e, t) = T_{d,wet}(t)}$$
 (5.31)

$$\boxed{\text{Initial condition: } T(x, 0) = T_{d,initial}(x)}$$
 (5.32)

$$\boxed{T_{d,initial} = \frac{q'''}{2\lambda} x^2 + (x - \frac{\lambda}{h}) \frac{T_{wet} - T_{ambient} + \frac{q'''e^2}{2\lambda}}{e - \frac{\lambda}{h}} + T_{ambient}}$$
 (5.33)

This system of equations is solved with the same finite difference method as was the isolated problem previously. The result has been checked for a zero heat transfer coefficient ( $h = 0$  corresponding to the isolated problem): the same result as with an isolated interface is obtained.

A low ambient temperature of  $20^\circ\text{C}$  is imposed. The maximum heat transfer coefficient value for natural convection in air is  $25 \text{ W.m}^{-2}.\text{s}^{-1}$ . This value is used to identify the change

for the dry temperature calculation and then the reverse calculation for the wet temperature. The heat transfer coefficient for forced convection air can reach  $300 \text{ W.m}^{-2}.\text{s}^{-1}$ . With this new coefficient the problem and the possible boundary conditions are well framed and a final comparison to validate our conclusions can be proposed.

With the same input data as before, the isolated model can be compared to the model with heat losses.

Figure 5.28 compares the results for a fixed thickness of  $50 \mu\text{m}$  between the models: the initial isolated plate model is compared with the heat loss condition model for different values of the heat transfer coefficient  $h$ . An increase in temperature is identified when the exchange coefficient at the wall increases. The values of the three models are nevertheless very close, so there is no significant change in the direct modelling result.

The amplification due to the inverse calculation of the wetted temperature is identified as in Section 5.2.3 (example of inverse result for this model is presented Figure 5.29). Tables 5.5 and 5.6 lists the amplifications for the same thicknesses as previously identified.

Table 5.5: Amplification factor of uncertainties by inverse calculation depending on plate thickness for the heat loss flux boundary problem  $h = 25 \text{ W.m}^{-2}.\text{s}^{-1}$ .

Thickness [ $\mu\text{m}$ ]	Root mean square $T_{dry}$ [ $^{\circ}\text{C}$ ]	Maximum error $T_{dry}$ [ $^{\circ}\text{C}$ ]	Root mean square $T_{wet}$ [ $^{\circ}\text{C}$ ]	Maximum error $T_{wet}$ [ $^{\circ}\text{C}$ ]
100	4.37	8.7	0.24	0.5
70	1.11	2.79	0.19	0.5
50	0.73	1.87	0.25	0.5
30	0.41	0.93	0.26	0.5

Table 5.6: Amplification factor of uncertainties by inverse calculation depending on plate thickness for the heat loss flux boundary problem  $h = 300 \text{ W.m}^{-2}.\text{s}^{-1}$ .

Thickness [ $\mu\text{m}$ ]	Root mean square $T_{dry}$ [ $^{\circ}\text{C}$ ]	Maximum error $T_{dry}$ [ $^{\circ}\text{C}$ ]	Root mean square $T_{wet}$ [ $^{\circ}\text{C}$ ]	Maximum error $T_{wet}$ [ $^{\circ}\text{C}$ ]
100	4.49	10.48	0.24	0.5
70	1.4	3.84	0.26	0.5
50	0.66	1.57	0.24	0.5
30	0.31	0.74	0.21	0.5

A change in the amplification of the measurement noise by the inverse calculation can be identified with this change of boundary condition: this variation is not significative. This model with a heat loss flux does not lead to a change in the conclusions drawn earlier.

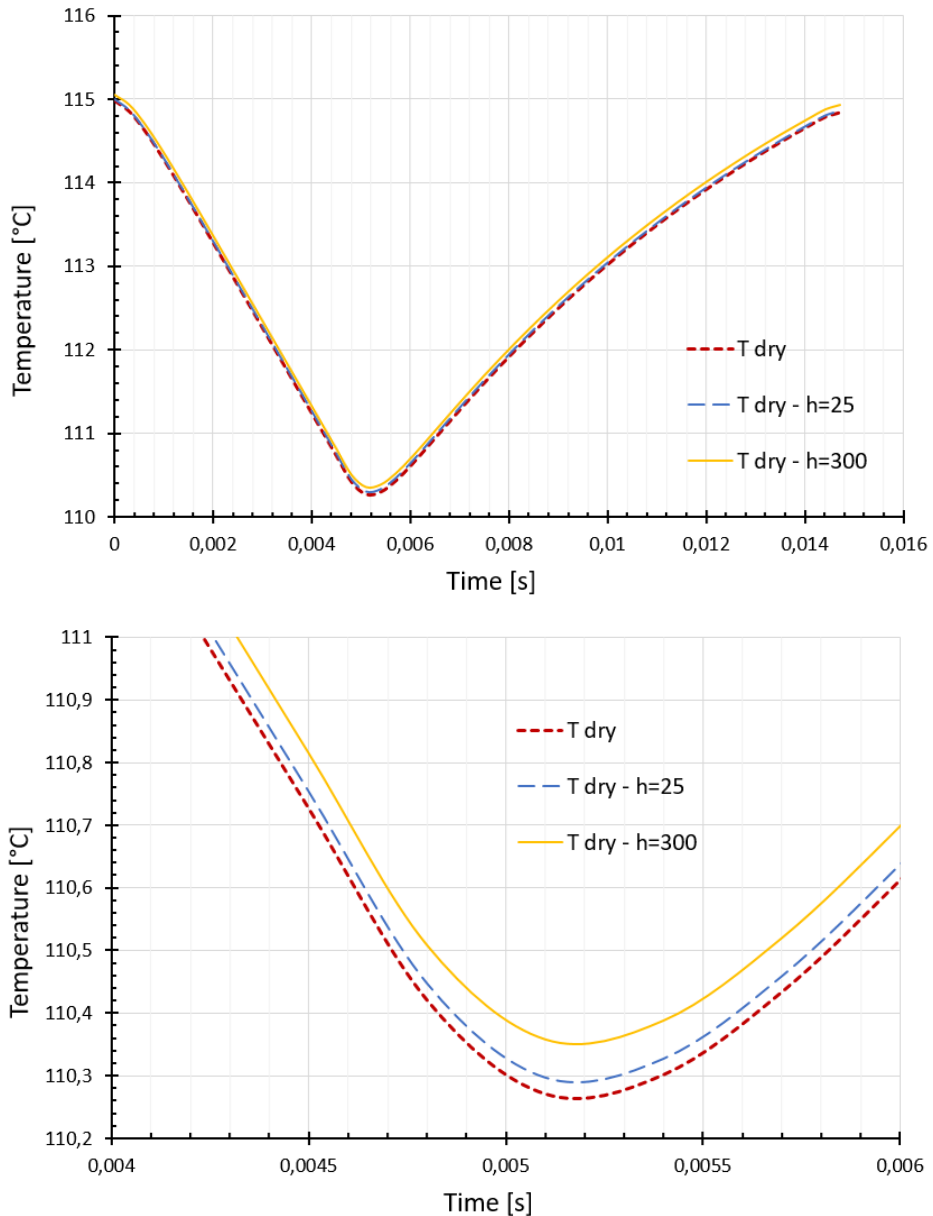


Figure 5.28: Comparison between the isolated plate model and the heat loss condition model for a fixed thickness of  $50 \mu\text{m}$  (top image). Focus on the slope change (bottom image). This problem solution was solved with the following values:  $N = 1000$ ,  $n = 50$ ,  $t_g = 0.005 \text{ s}$ ,  $t_w = 0.01 \text{ s}$ ,  $\Delta t = 0.00031 \text{ s}$ ,  $P = 1 \text{ bar}$ ,  $I = 400 \text{ A}$ ,  $\Delta T = 5 \text{ }^\circ\text{C}$

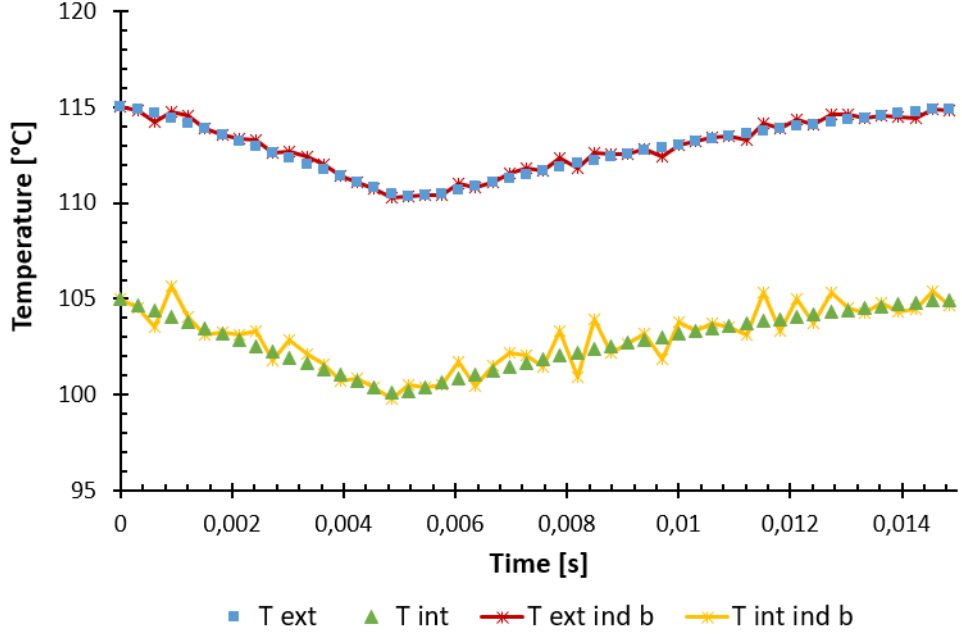


Figure 5.29: Result of the inverse calculation for the isolated plate model for a  $50\ \mu m$  plate thickness. This problem solution was solved with the following values:  $N = 1000$ ,  $n = 50$ ,  $t_g = 0.005\ s$ ,  $t_w = 0.01\ s$ ,  $\Delta t = 0.00031\ s$ ,  $P = 1\ bar$ ,  $I = 400\ A$ ,  $\Delta T = 5\ ^\circ C$ ,  $h = 300\ Wm^{-2}s^{-1}$ .

## 5.5 Conclusion for the heater design

The aim of this study was to define the geometry of the heating plate allowing thermographic measurements.

A study of the thermal behaviour of the plate was presented. First of all, the study of the conduction in the plate allows to fix a maximum limit for the plate thickness. This first limit was set at  $100\ \mu m$  to correctly capture the temperature variation and time delay. As the measurements are made on the external face of the plate, it will be necessary to reconstruct the wetted temperature from these measurements by solving the inverse conduction heat transfer problem through the heated plate. Solving the inverse problem, a second limit over the thickness of the plate is fixed. This limit aims to minimise the amplification of uncertainties due to the inverse character of this problem. This second limit is set at 50 microns.

In a third step, a study was presented to determine the spatial resolution of this method. Through a 2D approach, for every range of pressure, the thickness to detect the associated bubble size was selected. In addition, the minimum discernable gap between two bubbles was determined. To enhance this result, more realistic boundary conditions could be imposed and should confirm the choice for the  $50\ \mu m$  thickness.

The future test section will allow optical access to the flow and infrared measurements. The direct Joule heating plate will have a thickness determined by this study of  $50\ \mu m$ .

## 5.6 Power supply for direct Joule heating

Now that the thickness of the heating plate for infrared thermography measurements is fixed, the direct Joule heating method has to be defined. Indeed, it is necessary to dimension correctly the power supply to heat the plate and visualise boiling under various thermal hydraulic conditions. This is based on existing models that describe the onset of boiling and its development as a function of wall temperature, thermal hydraulic conditions and the power to be injected (presented in Chapter 2). As presented previously, the boiling flow starts with the appearance of the first bubble (ONB), followed by significant bubble production (OSV). We are therefore interested in predicting the power to be injected to reach these two points, which will give us a range of power to be provided to observe boiling flow. The boiling crisis point is also calculated as a limit that could be approached during testing.

### 5.6.1 Onset of Nucleate Boiling power

The location of the Onset of Nucleate Boiling (ONB) marks the onset of activation of the first nucleation sites. This point is determined with the following steps:

- First, the average fluid temperature at all elevation along the test section is calculated by setting a temperature condition at the inlet and performing the power balance along the section (the fluid being single-phase up to the desired ONB elevation point).
- The wall temperature for each elevation is then calculated from the fluid temperature (conditions for the Nusselt calculation).
- Finally, the parietal superheat, corresponding to these power and temperature conditions, necessary for the ONB point to be reached is calculated.

From these calculations, the power input is varied until the calculated wall temperature (step 2) is equal to the target temperature of ONB (step 3). The power is thus calculated for the different thermal hydraulic conditions involved. With the plate thickness fixed, it is possible to calculate its electrical resistance and to determine the necessary current ( $I = \sqrt{\frac{P}{R}}$ )/voltage ( $U = RI$ ) ratio.

For the future test campaign the following models (presented previously in Chapter 2) were selected:

- The Gnielinski model for the calculation of the Nusselt number.

$$Nu_{Gnielinski} = \frac{\frac{C_f}{2}(Re - 1000)Pr}{1 + 12.7 \left(\frac{C_f}{2}\right)^{0.5} (Pr^{2/3} - 1)} \quad (5.34)$$

- The equation for the calculation of the wall temperature.

$$T_p = T_l + \frac{q'' D_H}{\lambda_l Nu_{Gnielinski}} \quad (5.35)$$

- The Forst and Dzakovic model for the calculation of the wall superheat.

$$(T_w - T_{sat})_{ONB,FD} = \left( \frac{8\sigma\phi T_{sat}}{\lambda_{l,sat} L \rho_g} \right)^{0.5} Pr_{l,sat} \quad (5.36)$$

The thermal hydraulic conditions targeted are the following:

- Pressure from 20 to 120 bar.
- Subcooling from 5 to 15°C.
- Mass velocity in the test section from 1000 to 2000  $kg.m^{-2}.s^{-1}$

The now sized hot plate has the following characteristics:

- Size:  $5 \times 1.5\text{ cm}$ .
- Thickness:  $50\text{ }\mu\text{m}$ .
- Materials: Stainless steel 316L.

For these conditions, the powers to be injected through the test section and the associated voltage-current pairs are presented in Table 5.7.

Table 5.7: Range of power for ONB to be reached at the middle of the test section.

Pressure [bar]	Subcooling [°C]	Mass velocity $[kg.m^{-2}.s^{-1}]$	Power [W]	Voltage [V]	Current [A]
20	5	1000	54.14	1.59	34.05
20	15	1000	145.71	2.61	55.86
20	5	2000	99.03	2.15	46.05
20	15	2000	262.62	3.5	74.99
120	5	1000	62.89	1.71	36.7
120	15	1000	167.01	1.79	59.8
120	5	2000	113.16	2.3	49.22
120	15	2000	297.73	3.73	79.85

### 5.6.2 Onset of Significant Void power

We now calculate the OSV (Onset of Significant Void) point, which is the point at which there is significant bubble creation: the beginning of fully developed saturated boiling.

Most OSV models have very small temperature differences. This is very close to the saturation temperature, but this is valid for the near-wall temperature, not for the average temperature over the cross-section of the fluid flow. The most accurate models are those of Saha and Zuber [86] for the empirical models and Levy [17] for the analytical models. However, Levy's model is qualified at low pressure (up to 4 bar maximum). The Saha and Zuber model is therefore the one selected for this calculation.

From this model, the difference between the liquid temperature and the saturation temperature at the OSV point can be established. Iterations are performed in the same way as for ONB point calculation, varying the injected power until the desired difference is obtained. This deviation is defined in two categories according to the flow rate, depending on the Peclet number with a change at  $Pe=70000$ .

$$\begin{cases} \Delta T_{OSV,SZ} = 0.0022 \left( \frac{\phi D_h}{\lambda_l} \right) & \text{if } Pe \leq 70000 \\ \Delta T_{OSV,SZ} = 153.8 \left( \frac{\phi}{G_{en} C_{pl}} \right) & \text{if } Pe > 70000 \end{cases} \quad (5.37)$$

The power to be injected to reach the OSV point in the middle of the test section is obtained from the characteristics of the heating plate mentioned above and the thermal hydraulic conditions to be imposed at the test section inlet.

The powers to be injected to reach the OSV through the heating plate and the associated voltage-current pairs are presented in Table 5.8.

Table 5.8: Range of power for OSV to be reached at the middle of the test section.

Pressure [bar]	Subcooling [°C]	Mass velocity [kg.m <sup>-2</sup> .s <sup>-1</sup> ]	Power [W]	Voltage [V]	Current [A]
20	5	1000	118.4	2.35	50.35
20	15	1000	334.63	3.95	84.65
20	5	2000	236.8	3.33	71.21
20	15	2000	669.24	5.59	119.71
120	5	1000	170.21	2.82	60.37
120	15	1000	444.6	4.56	97.57
120	5	2000	340.42	3.99	85.38
120	15	2000	889.19	6.44	137.99

### 5.6.3 Critical heat flux limit

We now identify the critical flow: it is important to be able to predict the critical flow in the tests in order to be able to control along with the pressure, flow and flow ranges when

getting close to this heat flux.

The critical flux is calculated from the thermal hydraulic conditions at saturation.

The different existing models for the critical flow were used with our conditions. A lower limit can therefore be established that should not be exceeded in order not to risk reaching this critical heat flux. This heat flux could be useful for future experiments to investigate critical heat flux under these conditions. The Katto model is the most widely used for forced convection flows, Table 5.9 presents the powers associated with the thermal hydraulic conditions.

Table 5.9: Range of power for CHF to be reached in the test section.

Pressure	Subcooling	Mass velocity	Power	Voltage	Current
[bar]	[°C]	[kg.m <sup>-2</sup> .s <sup>-1</sup> ]	[W]	[V]	[A]
20	5	1000	3702.9	1454.63	2.55
20	15	1000	4552.35	1612.86	2.82
20	5	2000	4432.35	1591.47	2.78
20	15	2000	5943.16	1842.85	3.22
120	5	1000	1924.87	1048.77	1.83
120	15	1000	2943.99	1297.03	2.27
120	5	2000	2488.04	1192.37	2.09
120	15	2000	4288.99	1565.52	2.74

#### 5.6.4 Power supply design

The power supply must be able to deliver the different power ranges presented above with independant control of current and voltage, with a precision allowing the low voltages calculated for the ONB point to be reached. In addition, it must be capable of delivering a significant power to enable the critical flow to be approached in future tests. This requires the power supply to be equipped with a dimmer for voltage and current.

The minimum capacity required is  $0.5\text{ V}$  at  $30\text{ A}$  to reach ONB. It is then necessary to be able to gradually increase the power up to  $8\text{ V}$  under  $200\text{ A}$  for OSV configuration. Then have an estimated capacity margin up to  $4\text{ V}$  and  $1500\text{ A}$  to be able to reach critical heat flux.

# Chapter 6

## Instrumentation selection

This section aims to define and characterise the instrumentation required to perform the desired measurements through the visualisation of bubbles and IR thermography of the heated wall (see diagram Figure 6.1). Shadowgraphy references have been studied and led to a test strategy to have a better understanding and a better control over the measurement technique. For this purpose, a reduced scale model has been created to test different optical setups. Two test campaigns were carried out and are presented in this chapter. Moreover, some literature research was performed to define the steps which will be necessary to implement IR measurement technique.

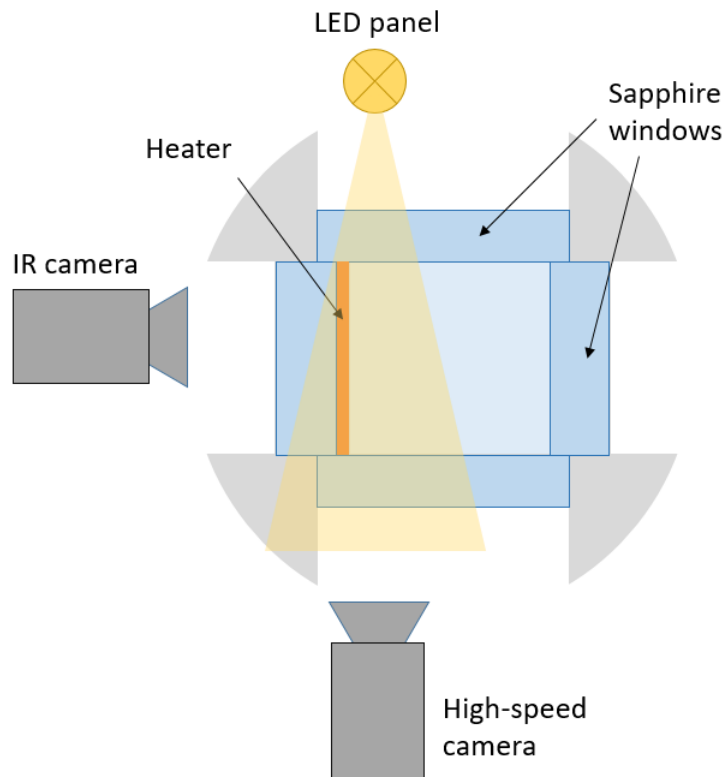


Figure 6.1: Shadowgraphy measurements diagram.

## 6.1 Shadowgraphy

We wish to carry out measurements with direct visualisation of the flow and more particularly of the bubbles created at the wall. For this purpose, the method of visualisation by shadowgraphy was chosen. It consists of placing the object to be observed between the light source and the measuring device: the high-speed camera. The shadowgraphy setup is described in the diagram Figure 6.2.

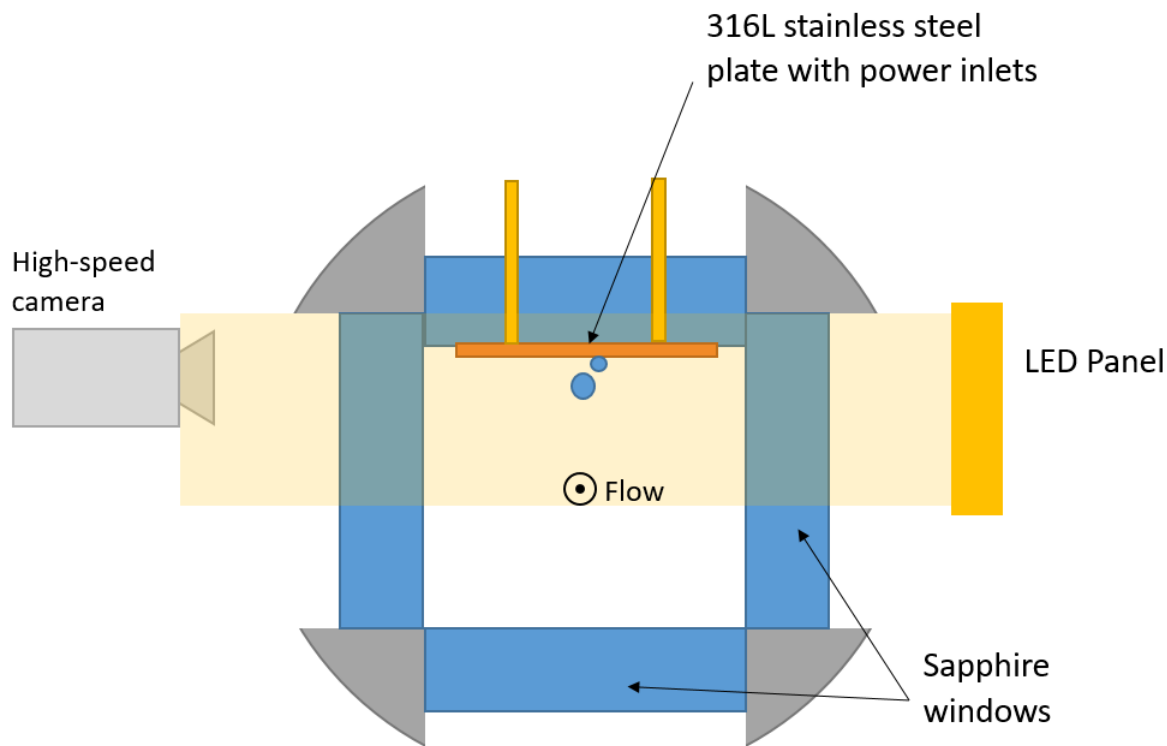


Figure 6.2: Shadowgraphy measurements diagram.

This kind of setup has been used in several non-intrusive measurement campaigns in the literature.

The method of shadowgraphy visualisation of bubble formation in a convective flow with a heated wall was used by March [4] in high pressure and high temperature configurations. It was set up to visualise the different modes of the boiling flow and to perform void ratio and interfacial area measurements using image analysis tools such as stereology and mathematical morphology (see Figure 6.3).

As a reminder, the facility used was capable of reaching the so-called PWR reactor condition, with a fuel assembly of 9 rods. A material analysis for a window at these temperature and pressure gave diamond as the best material, but being expensive it was replaced by sapphire. Several problems were identified: the temperature gradient close to the wall influences the visualisation of the flow and a deformation of the sheath profile makes it difficult to discern bubbles close to the heating wall. In addition, an index gradient, caused by strong temperature gradients at the interface, distorts the shape of the bubbles and can create a mirage effect. During the tests, the sapphire was attacked by water at high temperature and



Figure 6.3: Example of visualisation by shadowgraphy at 155bar, reprinted from March [4].

March noted a darkening of the image and ripples of the sheath line for the highest conditions (pressure and temperature). These observations, linked to the pressure and temperature gradient, should be taken into account when working in PWR conditions.

Lin and Chen [33] carried out an experiment with direct visualisation using R134a as coolant fluid. Several measurements were performed: critical heat flux was measured as well as the bubble diameter (at detachment and as a function of time) and the observation of nucleation sites.

Input parameter measurements were done using classic instrumentation as thermocouples and pressure transducers. Two high-speed cameras were used for direct visualisation of the flow: one for bubble flow and bubble departure diameter, another camera was used for nucleation site observations. To access the flow with direct visualisation, crystal glass windows of 20 mm were installed. Two types of test sections are examined in this work, one flat test section and one augmented test section (technical name "hypervapotron" see Figure 6.4). Images from direct visualisation were very clear (see Figure 6.5) in this work due to low pressure and low temperature experiment allowed by the use of a coolant fluid.

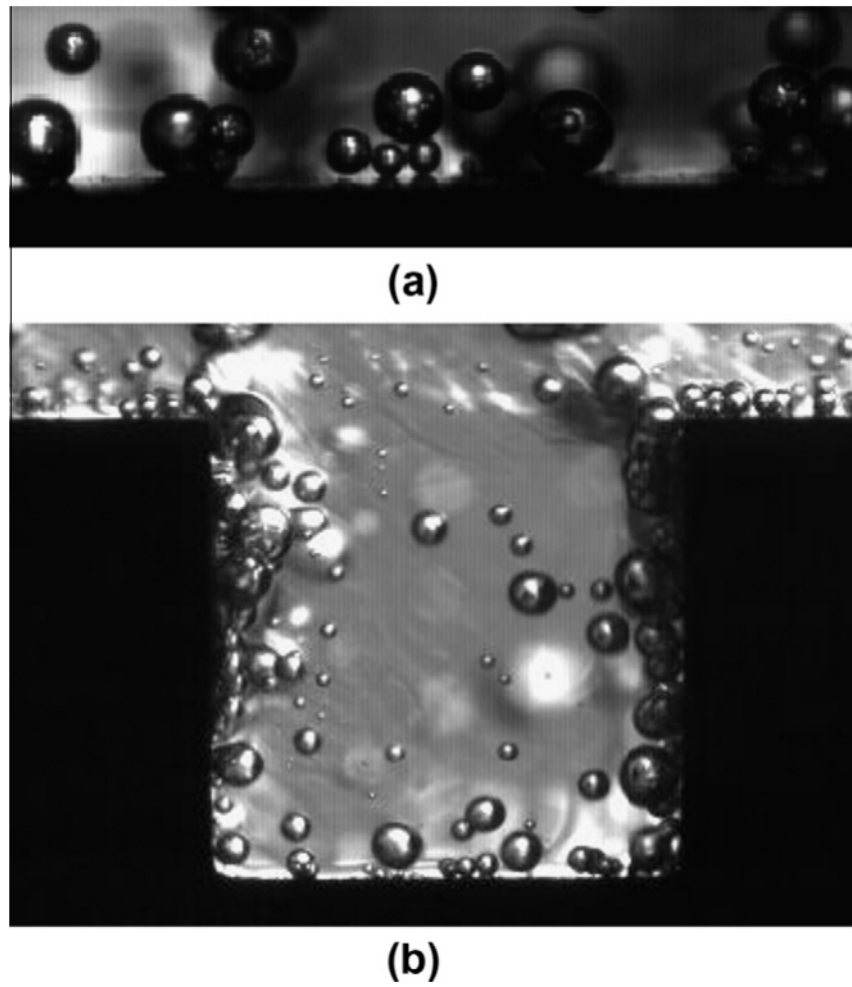


Figure 6.4: Images used for measuring the bubble departure diameter (a) flat surface, (b) hypervapotron, ( $P = 0.4\text{ MPa}$ ,  $V_{bulk} = 0.2\text{ m/s}$ ,  $T_{wall} - T_{sat} = 4.3^\circ\text{C}$ ,  $q_0 = 0.23\text{ MW/m}^2$ ), reprinted from Lin and Chen [33].

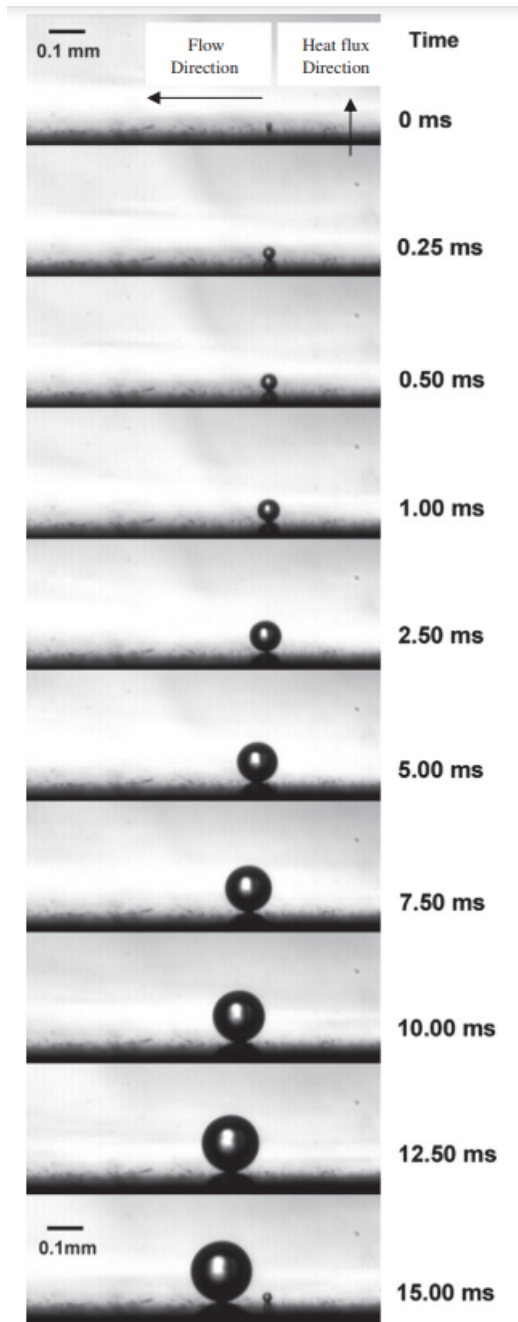


Figure 6.5: Sample images of bubble growth ( $P = 0.4\text{ MPa}$ ,  $V_{bulk} = 0.2\text{ m/s}$ ,  $T_{wall} - T_{sat} = 1.1^\circ\text{C}$ ,  $\Delta T_{sub,in} = 12.8^\circ\text{C}$ , location: bottom of hypervapotron cavity), reprinted from Lin and Chen [33].

Nucleation site density was measured by direct visualisation of the bubbles on the wall as shown in Figure 6.6. This method of measurement can be problematic when there are many bubbles in the flow (high equilibrium quality). It can be difficult to distinguish between bubbles still at their nucleation site on the wall and bubbles passing into the field of the camera.

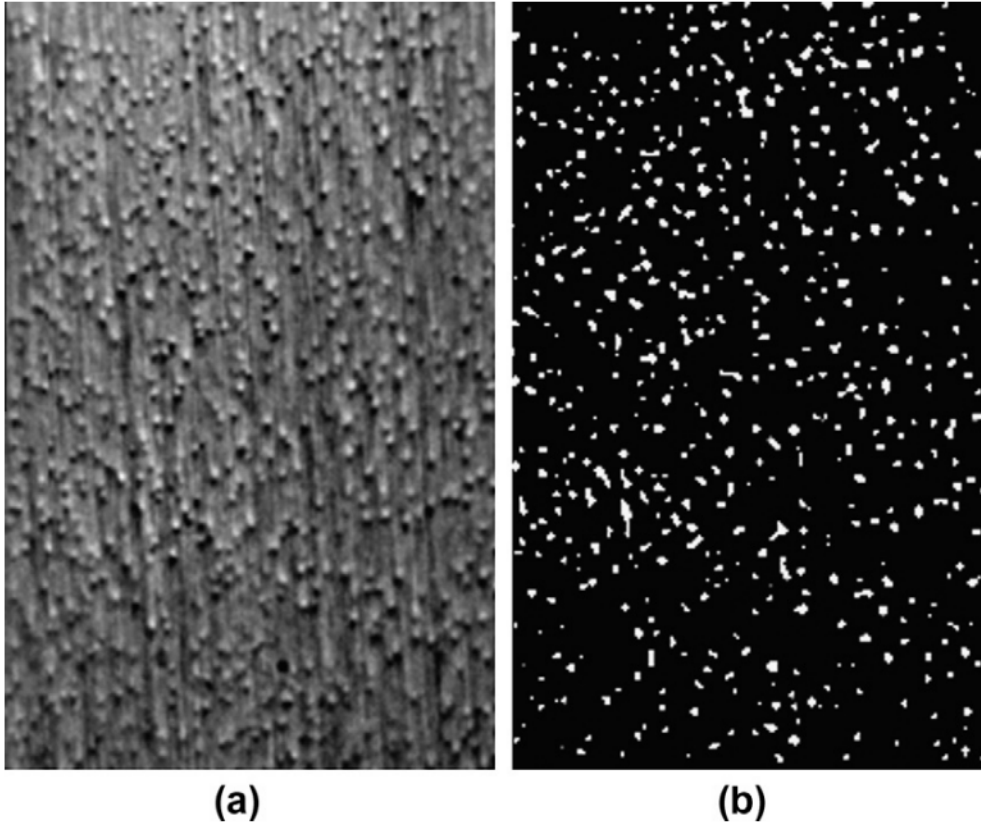


Figure 6.6: Images used for nucleation site density measurements (a) raw image (b) post-processed image, from Lin and Chen [33].

A method of image analysis after shadowgraphy visualisation was also developed by Euh et al. [30]. In this study, flow is vertical and in forced convection, in the case of subcooled boiling. The geometry of the test section is annular with a heating rod in the centre, visualised by a high-speed camera. Measurements made at 5000  $i/s$  through pirex windows were taken around the ONB point (Onset of Nucleate Boiling). The analysis method consisted of a frequency measurement by control volume: after defining the control volumes, an algorithm is used to calculate the frequency of bubble passage through this volume. It analysed the local variation of the image intensity on a predefined control volume located at a nucleation site. This method makes it possible to distinguish on an image the bubbles passing in the flow, and crossing the field of the camera, from the bubbles developing on the nucleation sites of the wall.

As presented in Figure 6.7, the algorithm treats independently the bubbles appearing in the control volume ('nucleated bubble') from those entering it through an interface of the control volume ('flowing bubble'). The frequency of detachment can thus be measured without bias.

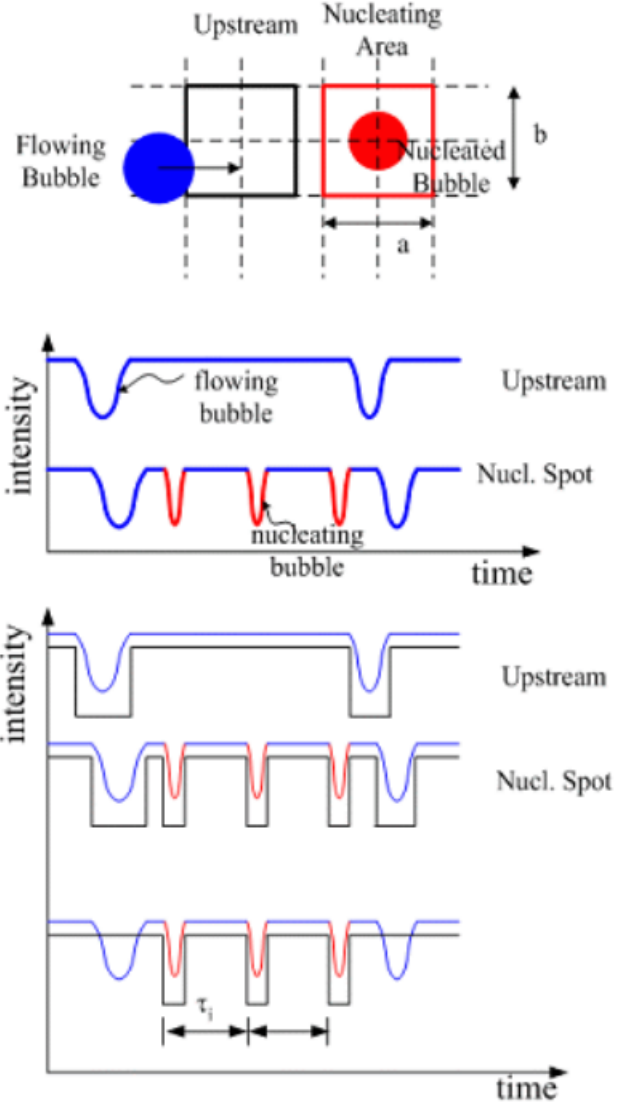


Figure 6.7: Algorithm for an image processing in order to obtain the bubble departure frequency, from Euh et al. [30].

The work of Estrada-Perez et al. [64] highlights the feasibility of setting up a direct flow visualisation and the information that can be recovered with several techniques: Particle Tracking Velocimetry (PTV), Particle Image Velocimetry (PIV) and shadowgraphy in parallel (see Figure 6.8).

Indeed, a direct visualisation method using shadowgraphy and PTV with simultaneous seeding allows to deduce information concerning the flow structure surrounding the bubbles near the wall. Estrada-Perez noted the same distortion effect over measurements as March: Thermally induced Optical Distortions (TOD) found nearby the interface. Three main optical distortion effects are noted due to density changes or boiling bubbles passing through the measurement region. The authors propose a method to limit the errors caused by direct observation. For example, for the distortion of the image due to the temperature gradient: the refractive index varies with temperature due to the change in density and is hampered by

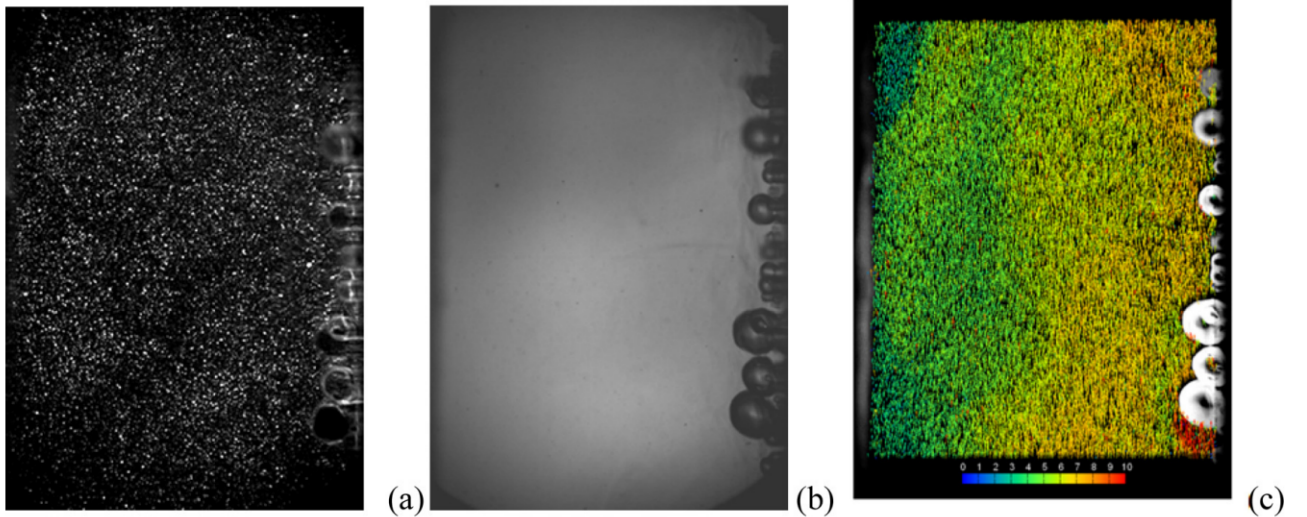


Figure 6.8: Experimental results showing (a) PIV image, (b) shadowgraphy image, (c) velocity field obtained with PTV, reprinted from Hassan [48].

the bubbles in the flow which create additional interfaces which is problematic (problem for PTV in particular) as identified by Euh et al. [30]. A check can be made with a calibration grid to deal with distortion problems. This calibration grid is made with circular patterns and coinciding with the focal plane of the shadowgraphy setup. The PTV centroid location algorithm (mask correlation method) is applied to the calibration grid. Figure 6.9 shows the centroid location process applied to the calibration grid.

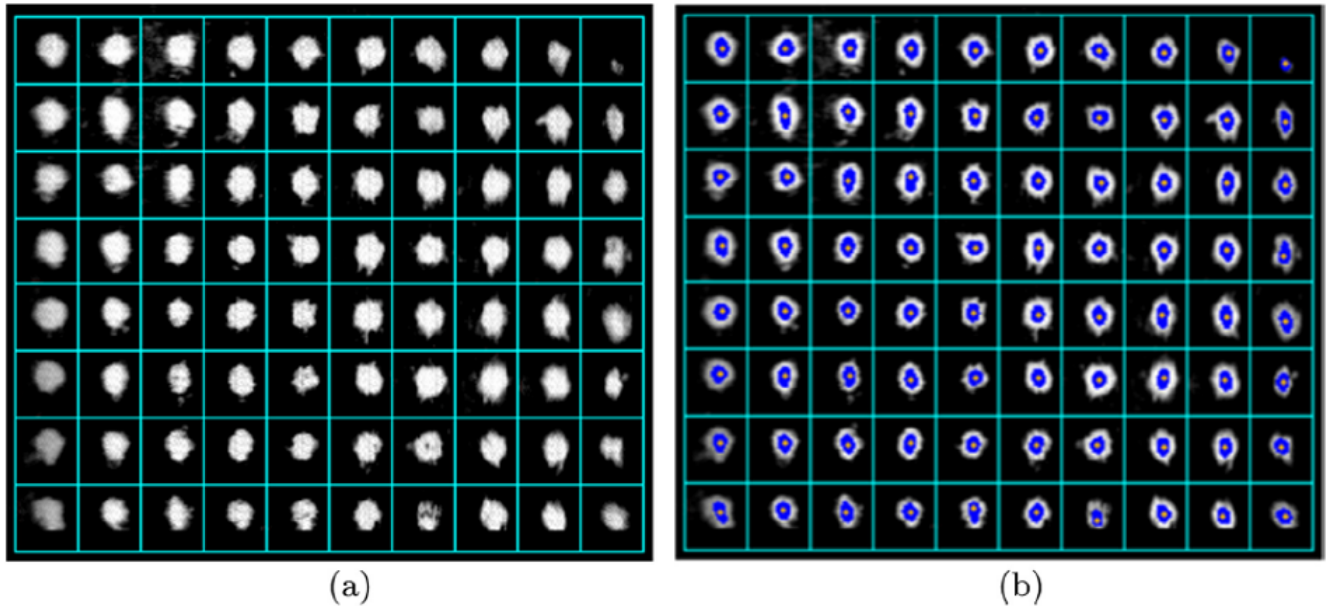


Figure 6.9: Centroid location process, (a) inverted version of the original calibration grid image, (b) output of the PTV centroid location algorithm, reprinted from Estrada-Perez et al. [64].

Estrada-Perez noted a concomitant behavior between distortion and the heat flux: the higher the heat flux, the larger the distortions. They are also larger in the vicinity of the wall. Calibration grid analysis over 1000 images shows that the image is deforming, moving in the flow direction. The maximum value of the random uncertainty due to thermal distortions is calculated at 0.5 pixels (with an estimated error of the algorithm given of 0.1 pixels). This value is valid at the location of the calibration grid, for position nearby the nucleation site they estimate it as 0.16 pixels.

A bias uncertainty was also calculated due to thermally induced optical distortion: an apparent displacement of the grid, uniformly distributed, was observed. As the heat flux rise, the whole image was shifted towards the wall. This bias can be easily corrected, as the displacement is uniformly distributed, with the calibration grid.

Bubbles passing through the measurement region can also cause optical distortion. The curvature of the bubble interface can cause a lens-like effect which causes an optical aberration of the calibration grid as shown in Figure 6.10. This effect causes a variation of the grid points of 15 pixels. Estrada-Perez removed this undesired effect by using the bubbles images as masks to remove them.

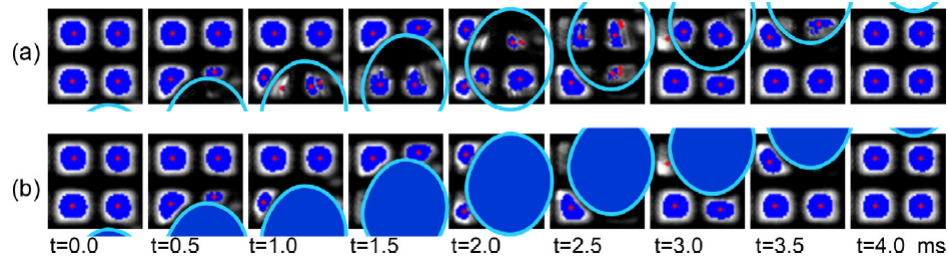


Figure 6.10: Example of centroid location variation due to a bubble optical distortion, reprinted from Estrada-Perez et al. [64]

He noted another problem that can influence the results: the lighting technique can heat the fluid and be an additional energy input to the initial heating method. The visualisation mode of the high-speed camera used (continuous or fragmented) also has an impact: the fragmented mode allows the time between each image to be limited. Furthermore, if there is a synchronisation of the light source with the camera in split mode, the energy contribution of the illumination and its influence can be neglected. After this feasibility study, several works were carried out using the three methods PTV, PIV and shadowgraphy simultaneously ([48] [37]): it allows to obtain different kind of information on the flow structure and near wall boiling. Figure 6.11 shows the analysis that can be done on a bubble on its nucleation site with PTV and shadowgraphy measurements. This work is done with a refrigerant fluid (HFE 301).

These examples in the literature have highlighted difficulties in image analysis for boiling studies. To make potential corrections easier, it is necessary to get the clearest images as possible for image analysis. For this purpose, it is necessary to select the lenses and lighting, which associated, give the best image quality. The following tests were performed in order to correctly define the instrumentation and shadowgraphy setup.

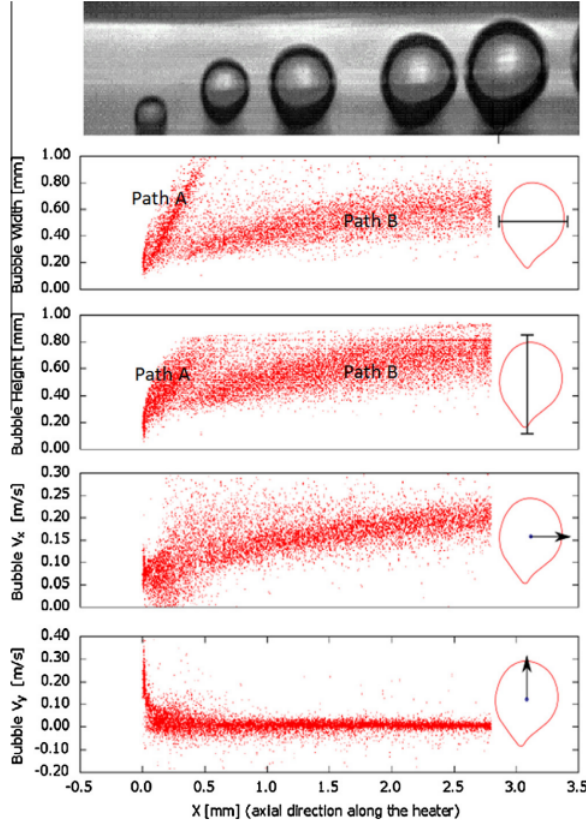


Figure 6.11: High magnification bubble dynamics measurements side view, reprinted from Hassan [48]

## 6.2 Reduced experimental setup

The objective of the following tests was to define the characteristics of an image acquisition/processing system adapted to future high pressure and high temperature tests.

All the tests were carried out on a test facility designed for this purpose. It consists of a glass jar (1) measuring  $10 \times 10 \times 10 \text{ cm}^3$ , a base and a stem (2) allowing the movement of a heated plate (size  $3 \times 1.5 \times 6 \text{ cm}^3$ ) by two  $2 \times 180 \text{ W}$  heating cartridges (3), fitted with a power variator (see Figure 6.12).

For safety reasons, the model is supplied with electricity through a safety transformer. The tests were carried out with conventional demineralised water. The power delivered by the heating elements was adjusted using the manual thermostat.

The camera used was a Photron high-speed camera, model Mini UX100. The images were acquired at a frequency of 4000 images per second with an exposure time of 1/5000 of a second. These settings are suitable for measurements on this facility and at atmospheric pressure. They should be adapted for measurements on the high pressure setup (higher acquisition frequency, for example).

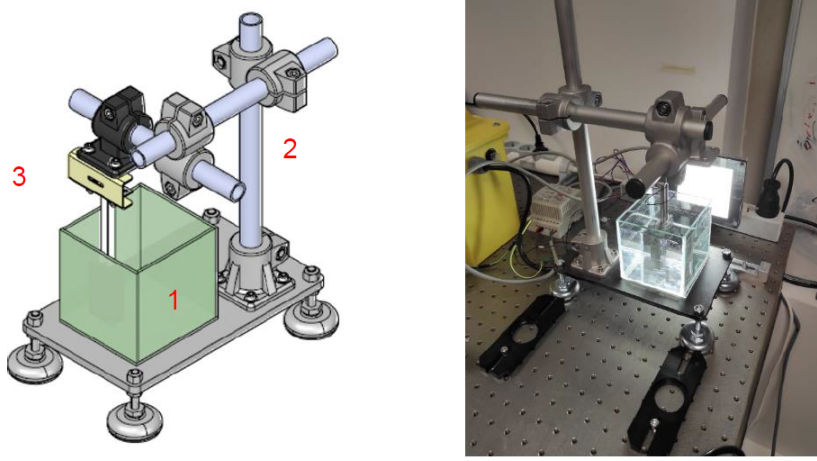


Figure 6.12: Test model, glass jar (1), base and stand (2), plate with heating cartridges (3) implemented.

## 6.3 First test campaign: shadowgraphy

### 6.3.1 First test presentation

It is recalled that this visualisation system must allow the measurement of three quantities in a high temperature, high pressure test section to be dimensioned: the size parameters (diameter, perimeter, etc.) of the bubbles at the time of their detachment, their detachment frequency and the spatial density of the nucleation sites (using thermal cameras). The aim of this first test campaign is to define the right setup for the visible measures.

All the optical setups that were evaluated are transmission shadowgraphy setups; based on this common configuration, the following points were studied:

1. The best characteristic(s) in terms of illumination and light collection lens.
2. The acquisition frequency (in frames per second) and exposure time (in s) adapted to the nucleation, growth and displacement rates of the bubbles after detachment.
3. The magnification of the optical setup allowing a correct measurement of the shape and characteristic dimensions of the bubbles (at least the diameter and perimeter).
4. A first approach to image processing.

### 6.3.2 Choice of optical assembly: lens and lighting

The following combinations of lenses and lighting were tested during this first campaign (see Figure 6.13 and Table 6.1).

The figures presented in Figure 6.14 illustrate the images obtained with these different configurations (Table 6.1), with a fixed thermostat.

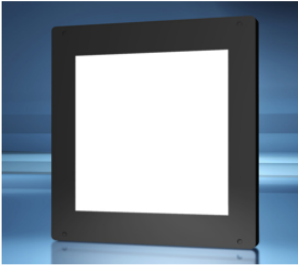
Lens		Light sources	
Macro Tamron SP AF 90mm F2.8		LED panels, PHLOX® SLLUB white LED Backlights 200x200 mm	
Thorlabs MVT23024 - 0.243X Bi-Telecentric lens			
Telecentric lens			
Zoom 6000 Navitar		Collimated lighting, Optoengineering High-performance telecentric illuminators, LTCLHP series	
Zoom Keyence VH-Z20T			
Optoengineering MC3-03X Entocentric macro			

Figure 6.13: Lens and light sources implemented.

Table 6.1: Lens and light source configurations.

Led panels	Collimated lighting
Bi-telecentric lens (Configuration $n^{\circ}1$ )	Bi-telecentric lens (Configuration $n^{\circ}2$ )
Telecentric lens (Configuration $n^{\circ}3$ )	Macro lens Tamron (Configuration $n^{\circ}4$ )
Zoom Keyence lens (Configuration $n^{\circ}5$ )	
Macro lens Tamron (Configuration $n^{\circ}6$ )	
Zoom Navitar lens (Configuration $n^{\circ}7$ )	
Macro entocentric lens (Configuration $n^{\circ}8$ )	

As expected, there is no configuration that reconciles a large depth of field with a high magnification. The images taken with the bi-telecentric lens are those that allow the observation of the largest measurement volume ( $\pm 11\text{ mm}$  depth of field) but with the smallest scale factor. Conversely, the entocentric macro lens provides a tenfold increase in scale factor to the detriment of depth of field ( $\pm 0.7\text{ mm}$ ). As far as lighting is concerned, the use of a collimated point source does not seem to bring any qualitative improvement, neither in terms of contrast nor in terms of sharpness, compared to LED surface lighting. For future tests, these less cumbersome lights will be perfectly adapted.

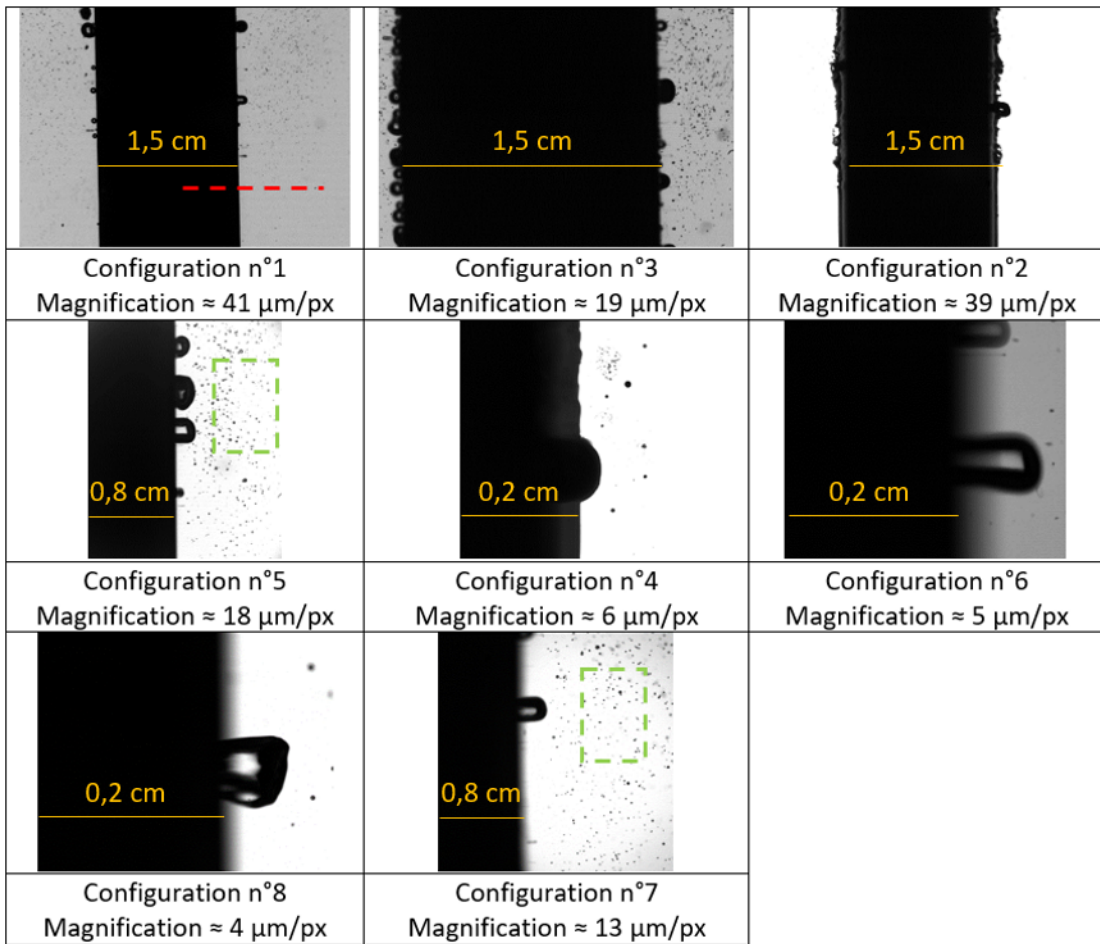


Figure 6.14: Illustration of the images obtained in the different configurations studied.

The analysis of the profiles at the edge of the hot plate (the area of the image that changes abruptly from the lowest to the highest intensity levels) allows us to quantify the sharpness of the images approximately via the slope of this transition. The steeper the intensity slope is, the greater the contrast and therefore the easier it is to detect the edges of objects. This is an important parameter for future image processing, which should allow us to measure the geometry of the bubbles.

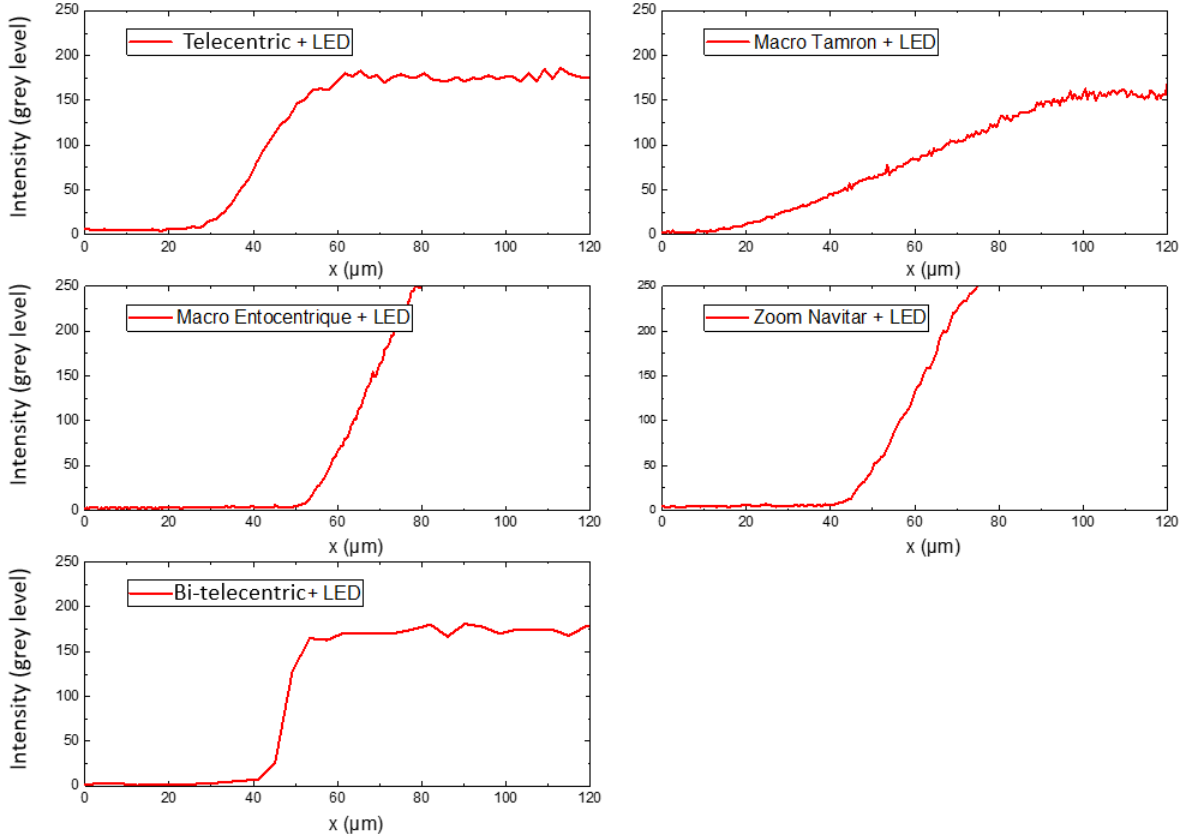


Figure 6.15: Heated plate edge profiles for different configurations with LED panel lighting.

The profiles of all the configurations using the LED panel (cf. Figure 6.15) confirm that the bi-telecentricity makes it possible to obtain the sharpest images and therefore those that will be the easiest to process digitally. We can therefore conclude that the setup combining bi-telecentric lens and homogeneous surface illumination is the most suitable for future tests, at least for the observation of the morpho-geometry of the bubbles at the time of their detachment as well as their detachment frequency. It is important to specify for the dimensioning of the future optical device that the field of view of the bi-telecentric objectives is limited by the dimensions of the entrance lens and that they are constrained to work at a fixed distance from the objects (fixed focal).

High magnification zoom lenses (Navitar or Keyence) are not without their advantages. Figure 6.16 show that it is possible to zoom in sharply on the bubbles once they have detached from the heated wall and condensed; they then become perfectly spherical again and it is therefore possible to measure their size distribution and their velocity. It should be noted that this zone, which is approximately at a constant temperature, does not show deformations due to refraction effects induced by temperature gradients (no optical aberrations), which is also an advantage. Moreover this kind of lenses can allow visualisation focused on a single nucleation site for more precise measurements.

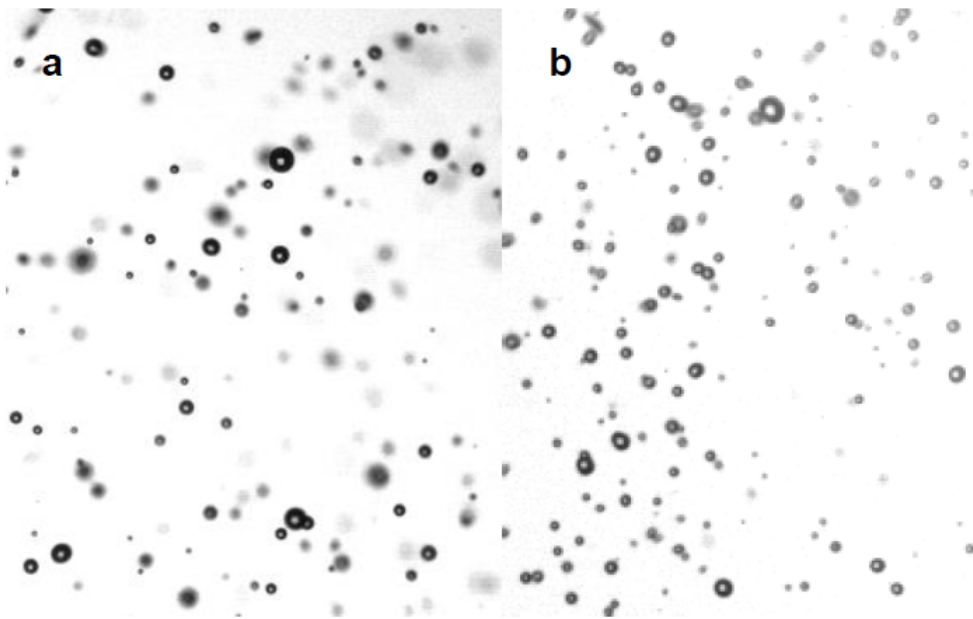


Figure 6.16: Images of flowing bubbles observed with Navitar (a) and Keyence (b) zooms.

### 6.3.3 Validation of the acquisition frequency and shutter time

These tests also allowed us to validate the fact that a frequency of  $4000\text{ i/s}$  allows the birth-detachment sequence of a medium-sized bubble to be broken down into about fifteen images, which seems sufficient to measure detachment frequency and diameter simultaneously (cf. Figure 6.17).

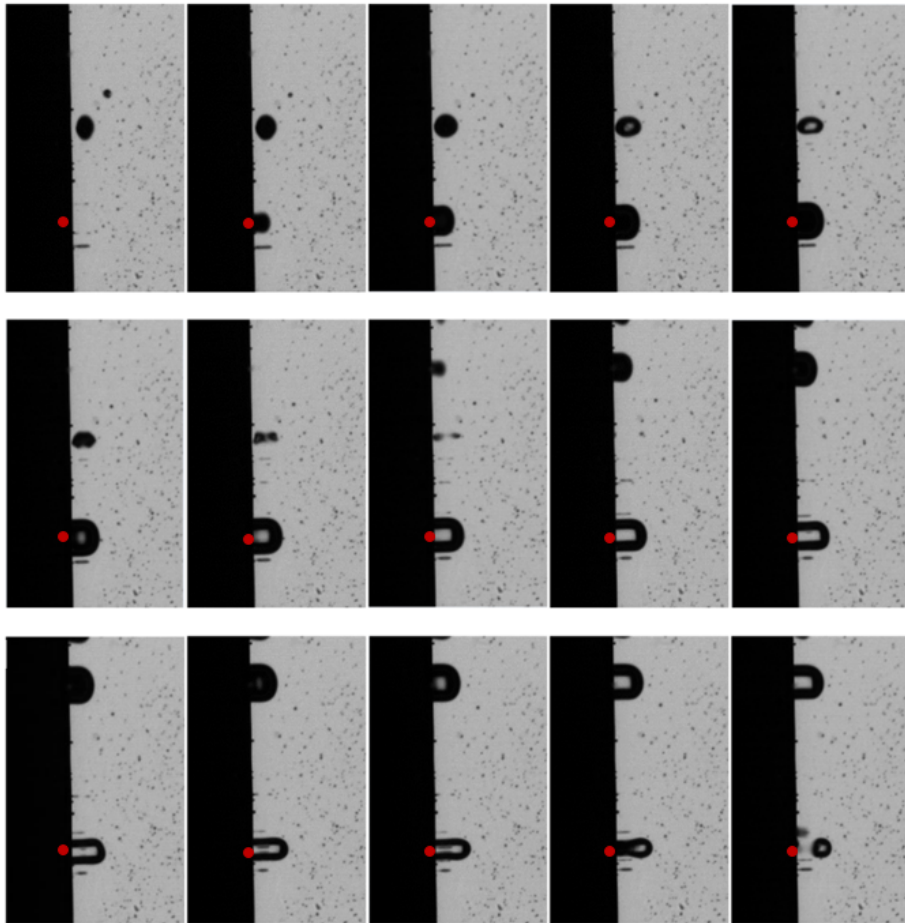


Figure 6.17: Growth/detachment sequence of a bubble on its nucleation site (red dot), from up left to the bottom right, observed with configuration n°1.

Exposure for a relatively short time, 0.2 ms in this case, guarantees the limitation of motion blur during acquisitions. These two values are therefore orders of magnitude to be considered at least for future tests on the high pressure, high temperature setup. The same type of sequence can also be carried out with a higher magnification setup provided that the bubble is appearing in the zone of sharpness, as shown in Figure 6.18 (Keyence lens and LED panel).

This configuration can therefore be considered for the study of more local areas as a complement to larger scale observations with the bi-telecentric configuration.

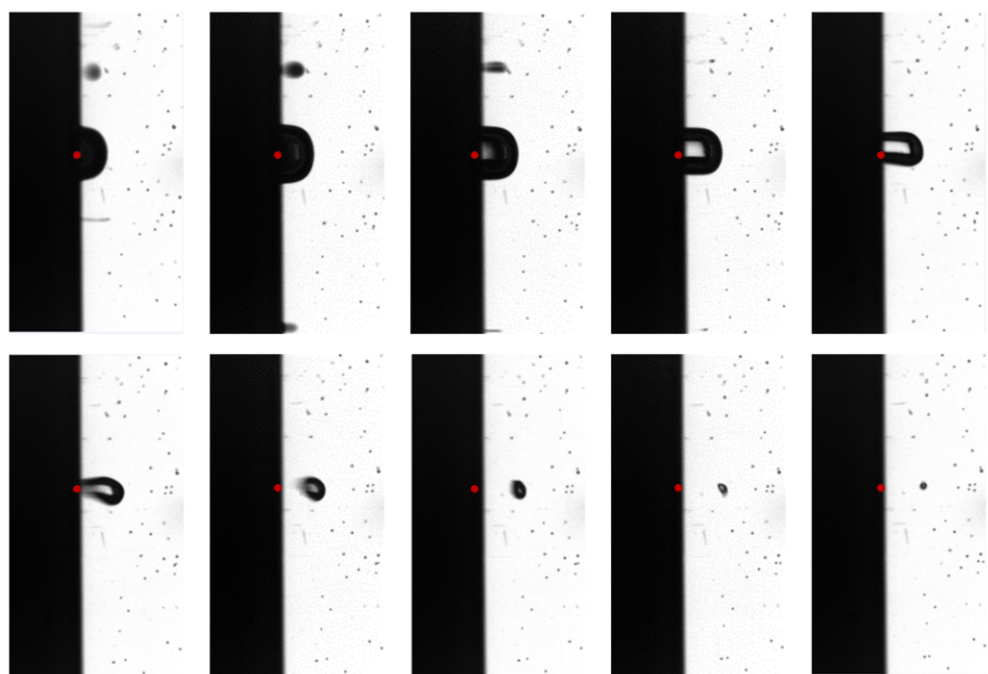


Figure 6.18: Growth/detachment sequence of a bubble on its nucleation site (red dot), from up left to the bottom right, observed with configuration n°5.

### 6.3.4 Evaluation of the influence of the thermal gradient

On the basis of configuration n°1 (bi-telecentric lens and LED panel), which is the one defined to be the most suitable, we carried out some tests to size the deformation zone induced by the thermal gradient. It is recalled that the temperature gradient at the wall creates a blurred zone by locally modifying the refractive index, which hinders the detection of the exact moment of bubble detachment and so its detachment diameter.

To propose a first evaluation of the dimensions of this deformation zone, we observed a horizontal test pattern under three different conditions considering decreasing temperature differences between the pool and the heated wall. The temperature was measured with a laboratory probe thermometer. The images obtained under these conditions are shown in Figure 6.19.

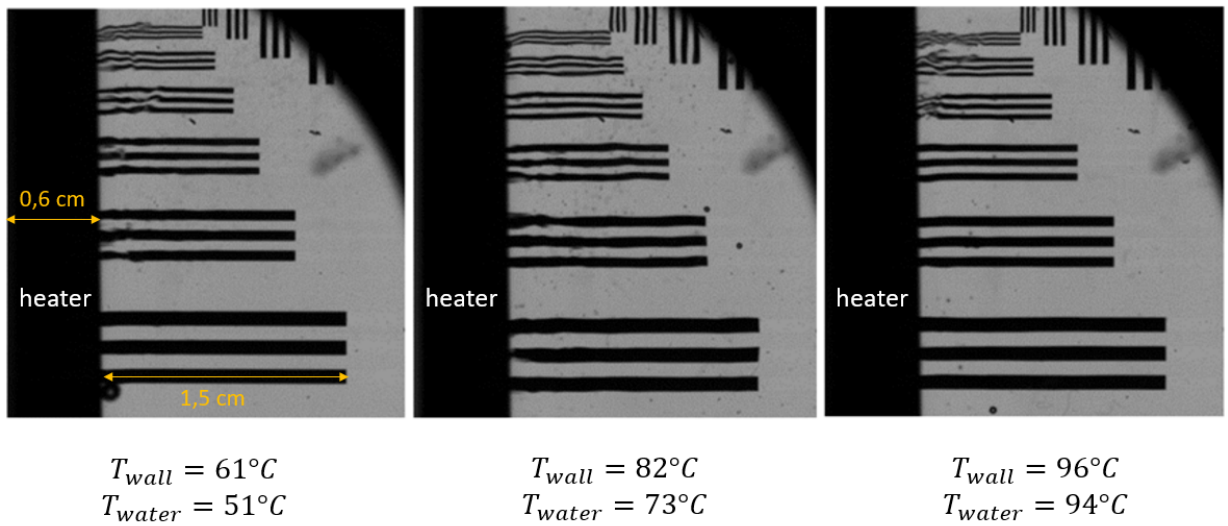


Figure 6.19: Observation of a test pattern in the presence of three thermal gradients, the induced deformations appear as distortion of the horizontal lines.

For all three configurations, distortions of the near-wall strips are observed. The upper bands are more distorted than the lower ones: this is due to the vase configuration. Indeed, once the bubbles detach from the wall they rise towards the surface and drag a mass of warm water towards the top of the surface. This mass of water changes the optical index locally due to its higher temperature. It induces distortions close to the wall which have a fluctuating character in time. This deformation zone can extend over several millimeters from the wall (up to almost 10 mm with the experimental configuration studied here), i.e. several times the characteristic dimension of the objects to be measured. As the temperature of the pool increases (i.e. as the temperature difference with the plate decreases), the effects of the gradient for the lowest strips decrease. The large deformations that persist on the upper strips are due to the passage of bubbles that detach from the wall.

These very partial observations highlight the difficulty introduced by these local refraction effects. Due to natural convection phenomena and the detachment of bubbles, the images are deformed dynamically, which makes it very difficult to set up a hypothetical digital correction a posteriori. In order to take these distortions into account in the final experimental setup, it will be necessary to: i) have a pool temperature as close as possible to the wall temperature, ii) place a transparent test pattern in the background to be able to calculate a 2D dynamic

correction to be applied to the images. This will be the object of the second test campaign described Section 6.4.

### 6.3.5 Other comments

More anecdotally, these tests were also an opportunity to evaluate the influence of a stirring movement in the experimental vessel. For this purpose, a magnetic stirrer was set up to create local mixing under the hot plate. Figure 6.20 shows the influence of this local agitation on the detachment of the bubbles.

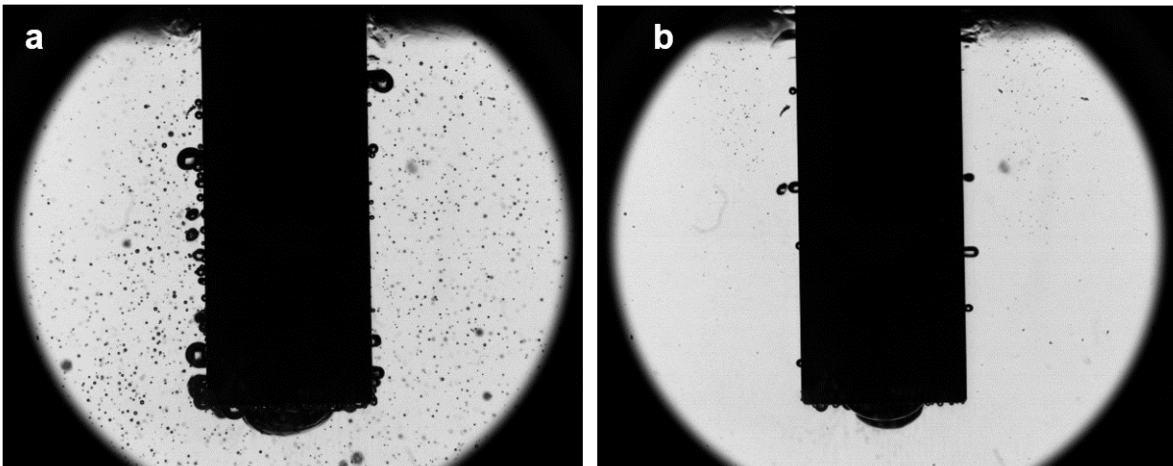


Figure 6.20: Observation of bubble growth and detachment (thermostat in position 4), with agitation (a) and without agitation (b).

It can be seen very clearly that the agitation creates recirculations which favour the detachment of the bubbles; the latter are then found in greater numbers in the continuous phase. The quality of the image is not affected, but this greater quantity of bubbles in the flow can be disturbing, especially if a dynamic correction of the distortion is made using a test pattern placed at the back of the observation volume. In principle, in the high pressure facility, the flow being in forced convection, there should not be as many bubbles moving into the field.

The last alternative test was an observation test on the smallest surface of the hot plate. The idea of this last configuration was to validate that observing on smaller surfaces improves image quality by minimising the number of overlaps and the thickness along the optical axis of the thermal gradient. The sequence of images presented in Figure 6.21 shows that there is indeed a real interest in minimising this area, as it also leads to minimising the number of blurred objects and overlaps. There are fewer bubbles overlapping and preventing accurate measurements without object reconstruction. This is also an important point to take into account for the dimensioning of the model in high pressure, high temperature configuration.

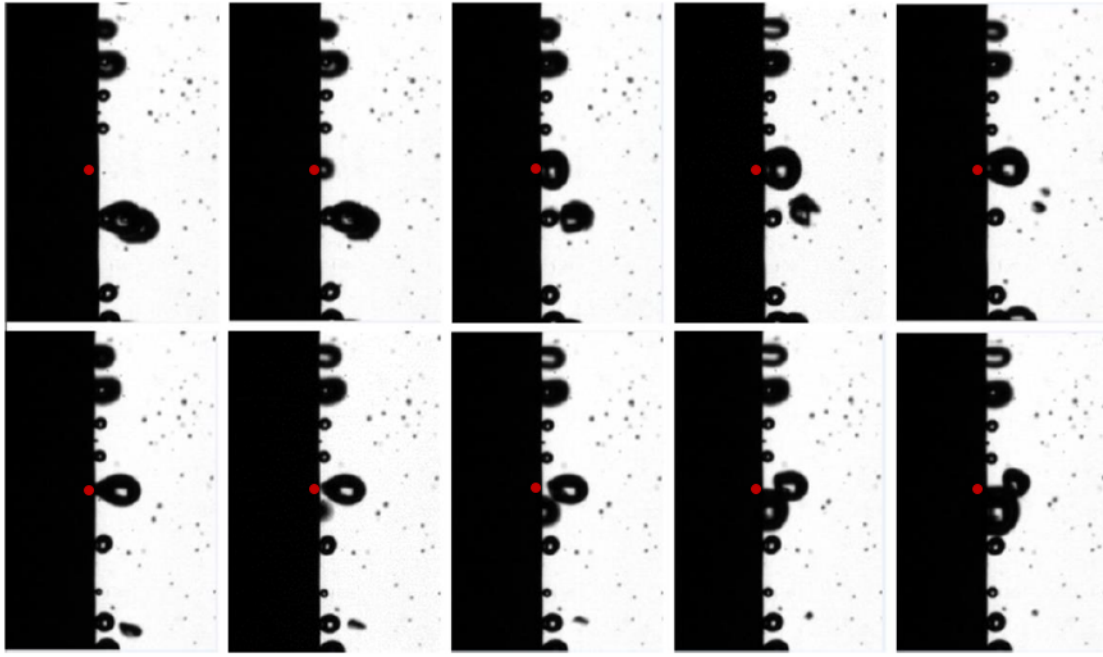


Figure 6.21: Observation on the smallest dimension of the hot plate, identification of a nucleation on his site (red dot).

### 6.3.6 First attempts at image processing

In order to definitively validate that the images have an adequate contrast and resolution, a first image processing was evaluated. Its objective was to verify the possibility of simply detecting bubbles in the near wall. The algorithm used to evaluate those images is relatively simple and is based on the following steps:

- Averaging the images in the sequence to extract the continuous components,
- Subtracting this average from the raw acquisitions,
- Binarisation of the resulting images using a grey level threshold,
- Succession of morphological operations (opening, convex image,...) to isolate the main bubbles,
- Labelling and extraction of the geometric features of interest.

Figure 6.22 illustrates the different steps of this algorithm on a typical image set.

Of course, this treatment is simplistic and will be enhanced for future tests on the high pressure setup. It can nevertheless serve as a basis for future developments. It should be noted that this type of processing can easily be implemented with programming languages (Python, Matlab,...) or with free image processing software (ImageJ, Plugim!,...).

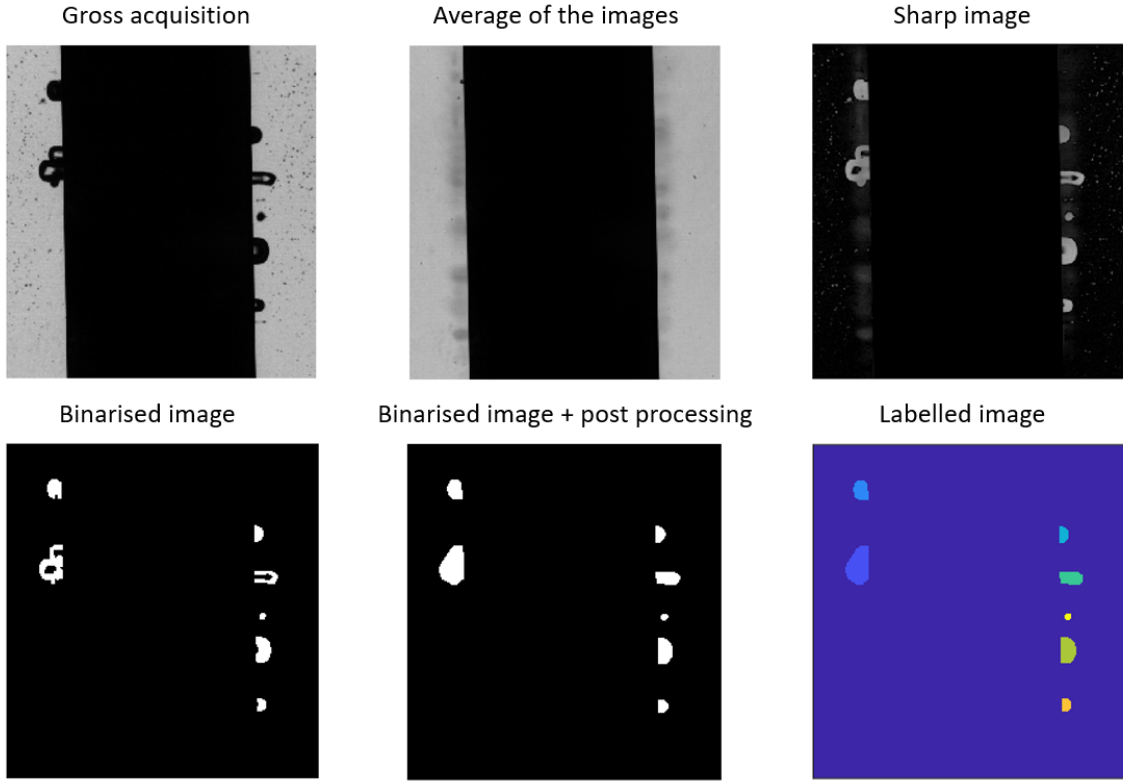


Figure 6.22: Illustration of the different steps of the evaluated image processing.

Using this post processing steps as presented on Figure 6.23, first measurements of bubble sizes could be conducted, results are listed in Table 6.2. The bubbles analysed in this image are smaller than  $100\mu m$ , even smaller bubbles can be expected to be measured during the high pressure, high temperature forced convection campaign.

Table 6.2: Measured geometric characteristics of the image processing presented in Figure 6.23.

Surface	Center	Minor axis	Major axis	Equivalent diameter	Perimeter
2665	[ 88.5 ; 234.8 ]	76.5	45.9	58.3	196.3
965	[ 92.7 ; 88.8 ]	41.5	30.1	35.1	112.3
504	[ 481.7 ; 174.4 ]	33.3	20.2	25.3	84.2
1044	[ 496.6 ; 257.2 ]	49.9	27.2	36.5	123.9
1261	[ 490.5 ; 397.4 ]	52.9	31.4	40.1	134.3
379	[ 487.6 ; 501.7 ]	25.6	19.5	219	70.3
133	[ 490.7 ; 331.6 ]	14.1	12.2	13.1	38.3

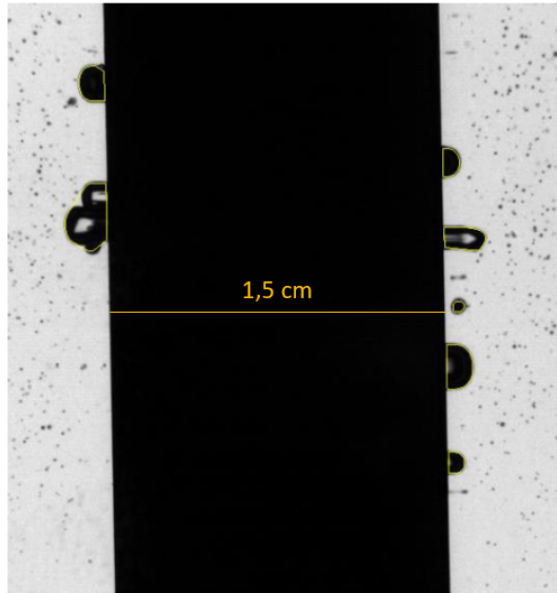


Figure 6.23: Image processing results.

We can add here that several pattern recognition algorithms exist. For example de Langlard et al. [41] proposed a binary decomposition of the image and then a reconstruction with a pattern recognition process. This algorithm makes it possible to determine ellipses within an unidentifiable cluster of ellipses. This pattern recognition process is operated in several phases:

- identification of regions of interest,
- extraction of the contours of the shapes,
- separation of the edges into distinct segments separated by connection points,
- the grouping of these segments,
- fitting with an ellipse for each group of segments,
- selection of good or bad solutions.

This algorithm was tested on synthetic images for a dense bubbly flow and showed good results for quite large groups of bubbles (see Figure 6.24).

It has also been tested on gas-liquid flows and shows good results (see Figure 6.25), however it is limited to well defined bubble shapes: circular or elliptical.

This type of treatment can be useful to determine the size of bubbles at the interface at their site of nucleation but also to characterise the bubbles in the core of the flow.

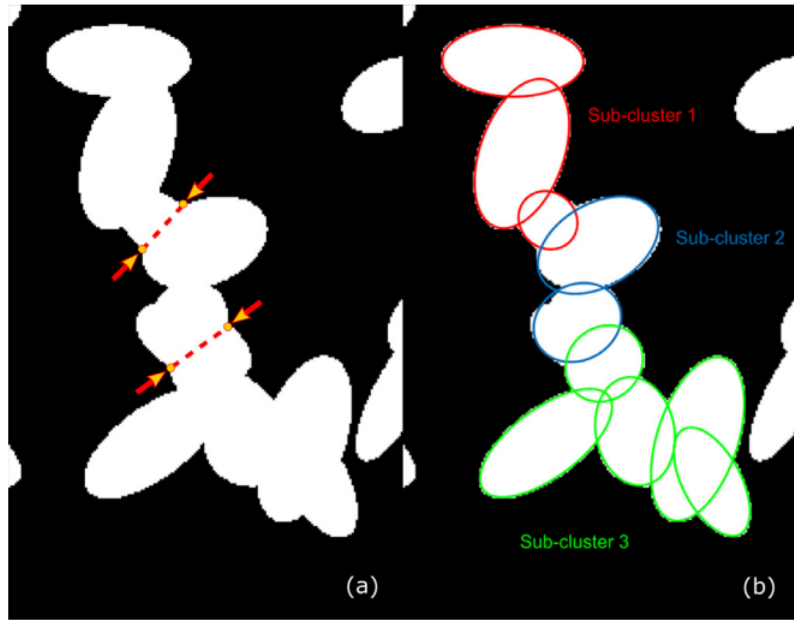


Figure 6.24: Image processing results, illustration of cluster decomposition and ellipse fitting in the case of a cluster involving 17 segments, (a) Initial cluster and detected split, (b) resulting subclusters and ellipse fitting, reprinted from deLanglard et al. [41].

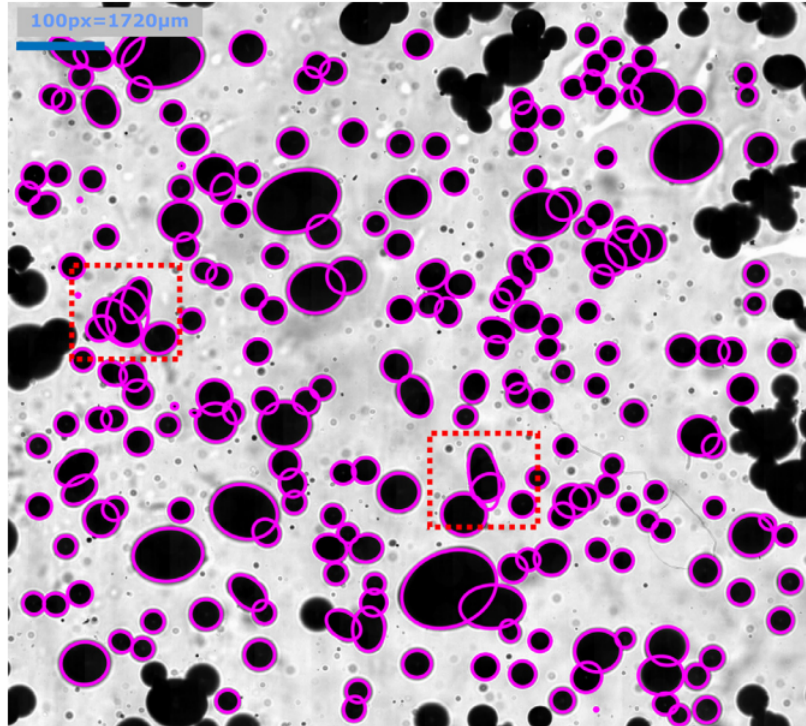


Figure 6.25: Performances of the proposed algorithm on an experimental acquisition, 181 ellipses have been detected, the red boxes highlight the two bad fits. Note that clusters touching the border are not considered, reprinted from deLanglard et al. [41].

Deep learning is now used for many applications including the study of boiling water flows. Suh et al. [118] proposes to use these methods to measure and characterise the nucleation, coalescence and detachment of the heating surface. In his study, he presents pool boiling tests, with a copper plate heated by a block in a jar with temperature measurements by thermocouples (see Figure 6.26). A light source illuminates the bubbles, which are viewed by a high-speed camera using an shadowgraphic setup.

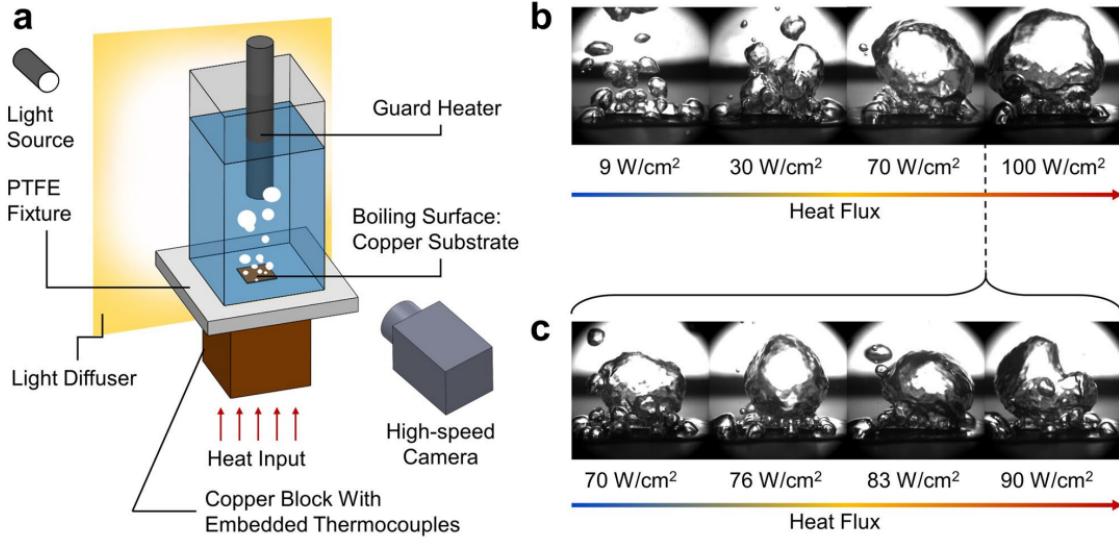


Figure 6.26: Experimental setup and imaging techniques. (a) All pool boiling experiments are conducted on a pool boiling rig with fixed thermal attachment, consistent imaging distance, and an identical plain copper substrate. (b) Temporal bubble images captured from the high-speed camera confirm that it is challenging to differentiate bubble changes with small heat flux steps (c) However, the changes in bubble appearance become more noticeable when heat flux steps are relatively large, reprinted from Suh et al. [118].

During the tests, the heat flux sent through the plate was gradually increased. With these images, separated into three parts: a training part, a test part and a validation part. The code was trained to recognise the size and number of bubbles associated with a particular heat flux. The Figure 6.27 shows that the relationship between bubble size and heat flow can be correlated and retrieved from simple unlabelled images (validation). This could lead to better trend analysis over boiling and automate measurements and image processing.

The use of deep learning makes it possible to automate measurement techniques. This will not be used in this study for boiling characteristics measurements but it could be implemented afterwards to analyse some trends.

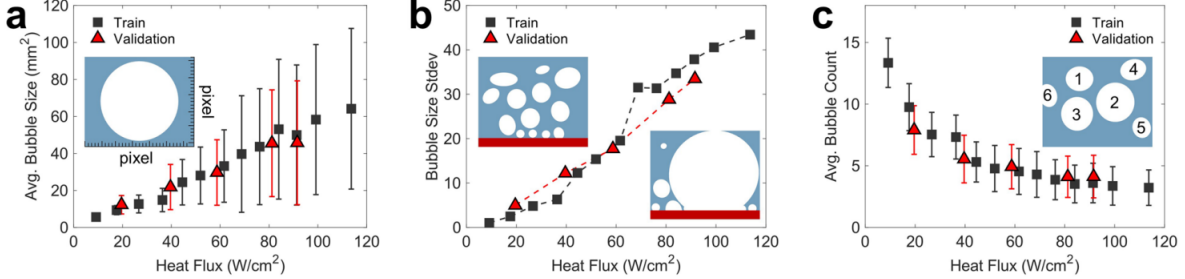


Figure 6.27: Bubble statistics with varying heat flux. (a) The average bubble size and boiling heat flux display a linear relationship. The error bars represent the standard deviation. (b) The bubble size standard deviation, in turn, characterizes bubble size differences of a given step and also exhibits a near-linear trend. Low heat fluxes have small standard deviations, which means bubbles sizes are relatively uniform. As heat flux increases, the difference becomes small and large bubbles become increasingly noticeable and is reflected in the plot. (c) The average bubble count decreases exponentially due to vigorous bubble coalescence as boiling heat flux increases, reprinted from Suh et al. [118].

### 6.3.7 First campaign conclusions

From this first session of tests, it is possible to formulate a certain number of recommendations for the setup currently being designed. On the acquisition frequency and exposure time: the tests were carried out with an acquisition frequency of 4000  $i/s$  and an exposure time of 1/5000 of a second. These parameters are suitable for measurements at atmospheric pressure but will have to be adapted for tests on the high pressure facility. They nevertheless give an order of magnitude of the adapted frequencies of acquisition. On the optical setup: the bi-telecentric lens associated with a LED panel seems to be the best configuration for suitable images for processing bubble detection. This type of lens limits the optical aberrations due to perspective without eliminating the distortions linked to the thermal gradient. High magnification zooms are also of interest because they allow detailed study of specific areas, such as a particular nucleation site. It is therefore advisable to use at least two types of lens to instrument the model, a bi-telecentric lens for "wide field" observations and a high magnification zoom lens for more local observations. On the distortions linked to thermal gradients: the tests showed that this effect was the major obstacle to carry out quality measurements. In order to limit measurement errors, it will be necessary to correct each image and therefore to maybe implement a dynamic calibration adapted to the different test conditions on the high pressure, high temperature setup. It is therefore important to consider, right from the design of the test section, a transparent test pattern system with a regular pattern that will allow the construction of a transfer function to correct these deformations. Finally, visualisation of the narrowest surface of the plate limits the aberrations induced by the thermal gradient as well as the effects of overlapped bubbles by projection on the camera sensor. There is therefore an interest in reducing the size of the heating plate to limit these sources of error. A new set of tests should be performed to better characterize this distortion and understand the thermal gradient effect on future measurements. On image processing: these initial tests show that, in this respect, it will be relatively easy to find one or more algorithms adapted to measure the geometric characteristics of the bubbles.

## 6.4 Second test campaign: thermal gradient influence

### 6.4.1 Second test presentation

The objective of this second session of tests was to better understand and quantify the effects of optical distortions, due to temperature gradients between the pool and the heater, observed during the first campaign.

During this first test campaign (Section 6.3), the characteristics of an image acquisition system adapted to future tests on the DIOGEN test section were defined. These future tests should allow us to measure the three characteristic parameters of nucleate boiling at high pressure, high temperature, namely: the bubble diameter at detachment, the detachment frequency and the nucleation site density. The optical setup used is therefore the one retained following the first test campaign: a transmission shadowgraphic setup, with LED panel lighting, a fast camera equipped with bi-telecentric or zoom lenses. The objective of this campaign is to better understand the mirage phenomena that appears in the vicinity of the heated wall. To this end, a new series of acquisitions was carried out to study, in particular:

1. The effect of the index gradient on the visualisation of a test pattern and objects of known dimensions.
2. The type of associated distortions.
3. The dimensions of the spatial area affected by these distortions.
4. The impact of the size of the heating object on the dimensions of the distorted area.

All the tests were carried out on the same setup already used for the qualification tests of the visualisation system (Figure 6.12).

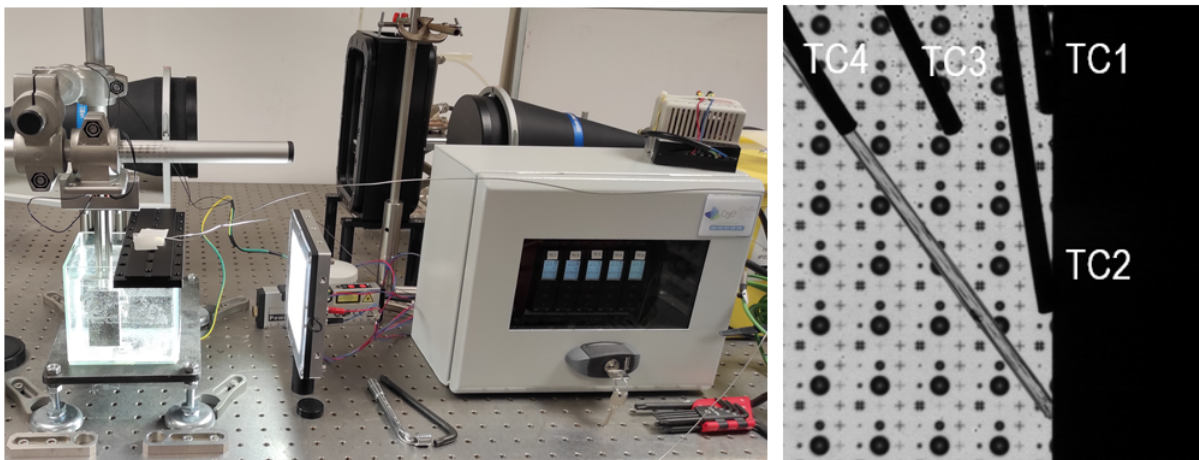


Figure 6.28: Lens and light sources implemented.

A new temperature measurement device was added. It consists of five thermocouples with a digital display (see Figure 6.28).

The transmission optical setup validated during the first campaign was repeated, following the configuration shown in Figure 6.29. The camera was placed on an optical rail to allow precise focusing directly on the objects to be studied. The whole experimental setup

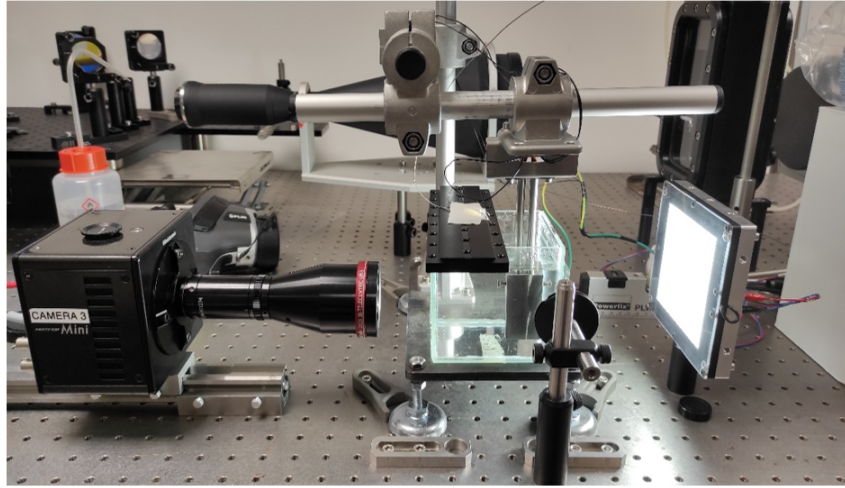


Figure 6.29: Optical transmission setup.

was fixed on an optical plate in order to guarantee the alignments.

To characterise/quantify the distortions due to thermal gradients, different objects with known geometries were used:

- A test pattern with a known pattern (see Figure 6.30) placed between the back side of the tank and the LED panel,
- An optical fibre of  $600 \mu\text{m}$  diameter, placed against the heating plate in different planes,
- An optical fibre of  $200 \mu\text{m}$  diameter, placed against the heating plate in different planes.

The stripped optical fibres have the double advantage of being accurately sized and transparent objects, thus representative of the measurements in the final model. The visualisation of these size objects allowed to quantify the dimensions of the area impacted by the thermal gradient and to propose a first qualification of the distortion induced on the objects.

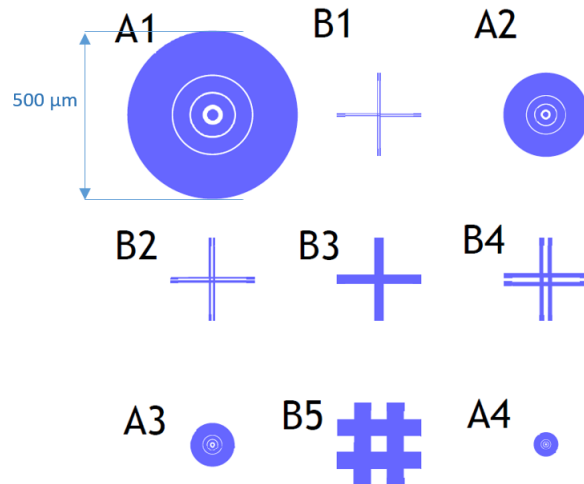


Figure 6.30: Pattern of the test pattern used (Model R3L3S5P Thorlabs).

Three types of lenses were used: a bi-telecentric lens, and two zoom lenses chosen during the first test campaign (Section 6.3). To better understand what is observed with these lenses, their respective depths of field were verified experimentally:

- The bi-telecentric lens has a depth of field of 2.7cm, which allows the entire 20mm plate to be seen,
- The Opto-engineering MC303X zoom lens has a depth of field of less than 1mm,
- The second zoom lens has a depth of field ranging from a few hundred micrometres to a maximum of 2.5 mm depending on the aperture setting.

The bi-telecentric lens therefore allows the entire nucleation zone to be observed and the two zooms to focus on a particular site in order, for example, to measure the frequency of bubble detachment. This complementarity may be of interest for future tests on the DIOGEN test section.

#### 6.4.2 Transition from transient to steady state

In the first stage, the temperature of the fluid was raised from room temperature by imposing a heating power on the plate through the heating cartridges. The temperature of the fluid thus rises in stages until boiling occurs. The experimental setup includes a test pattern at the back of the system, and a 600 or 200  $\mu\text{m}$  diameter optical fibre pressed against the plate which is observed with the bi-telecentric lens, as presented in Figure 6.31.

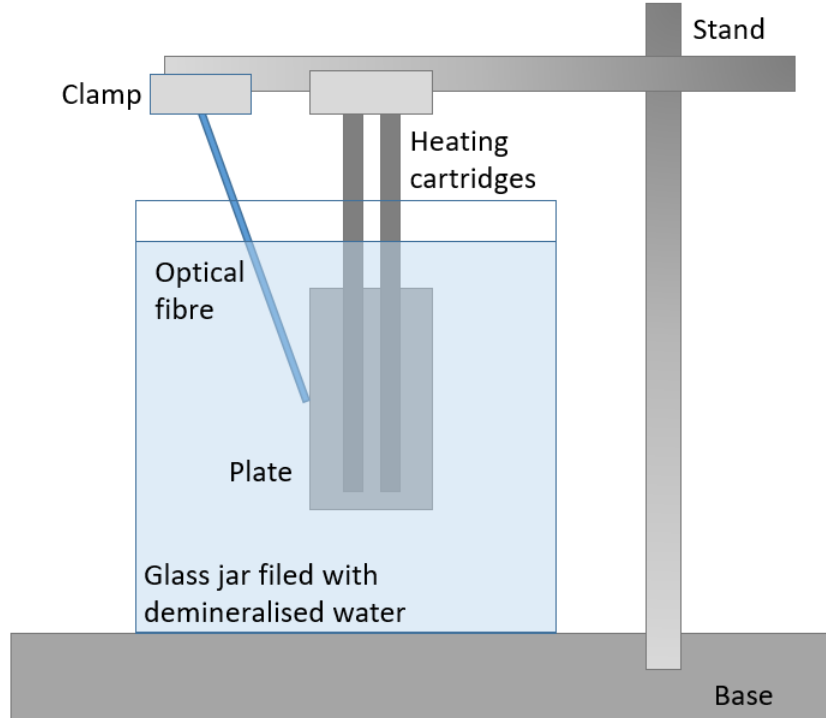


Figure 6.31: Diagram of the experimental setup with the positioning of the fibre against the wall.

The two tables below (Figure 6.32 and Figure 6.33) show pictures taken at regular intervals of temperature. In the first image in Figure 6.32, the arrow represents the direction of the natural convective flow induced by the hot plate, from the bottom to the top of the tank.

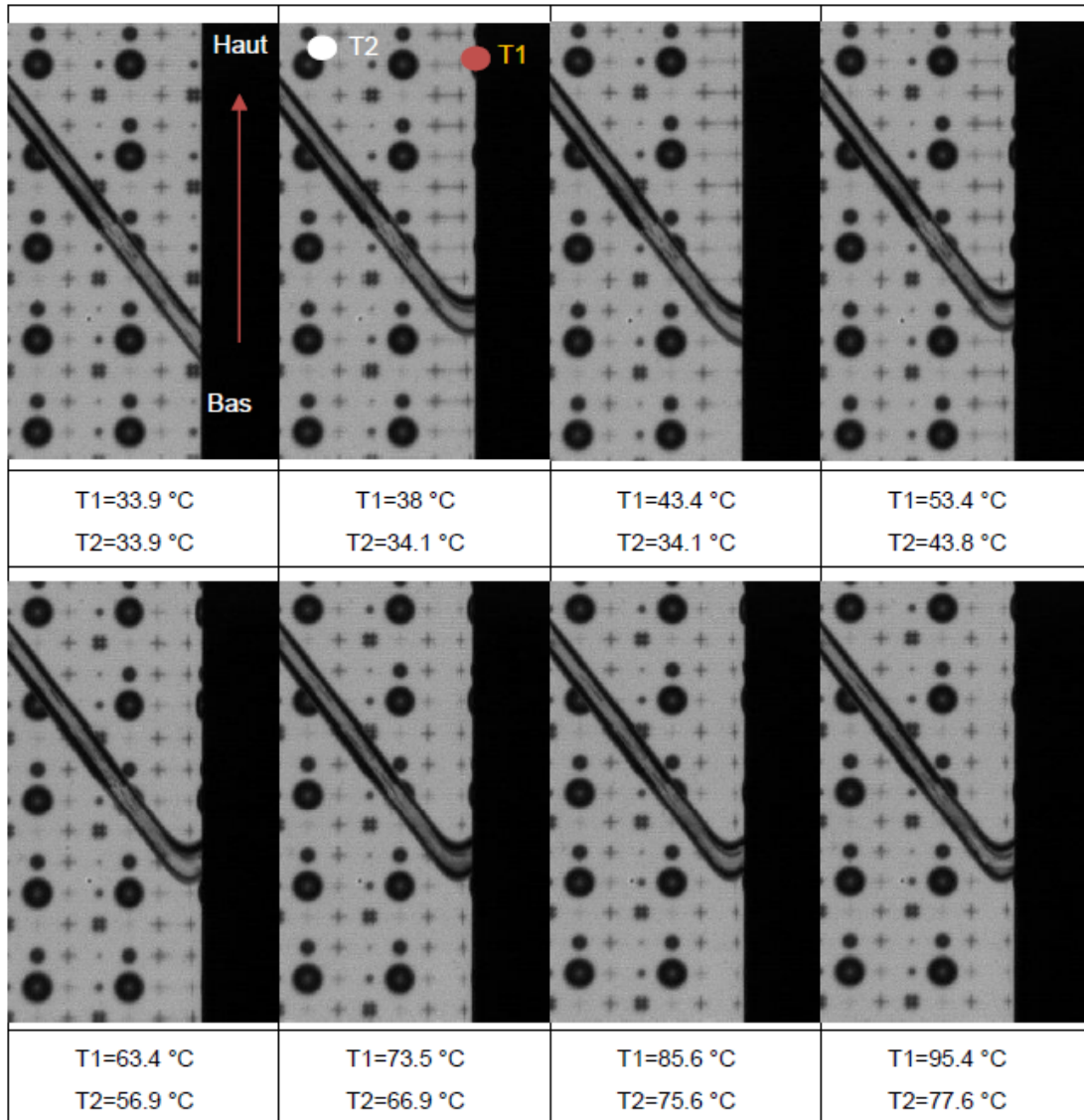


Figure 6.32: Visualisation with a bi-telecentric objective of a  $600 \mu\text{m}$  optical fibre against the heating wall with a test pattern in the background. The points T1 and T2 shown in the second image give the position of the thermocouples, the values of which are shown below each image.

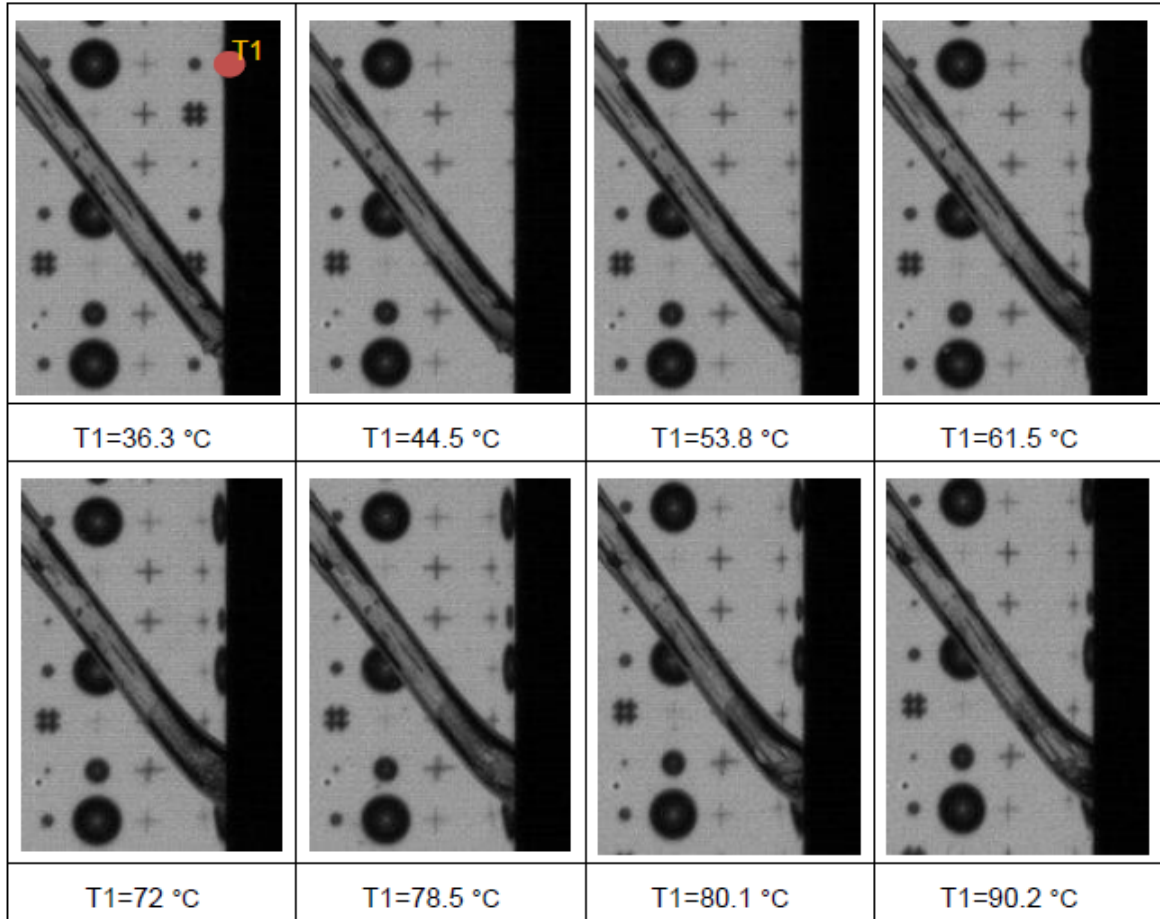


Figure 6.33: Visualisation with a bi-telecentric objective of a  $600 \mu\text{m}$  optical fibre against the heating wall with a test pattern in the background. The point T1 shown in the first image give the position of the thermocouple, the values of which are shown below each image.

As the plate and fluid heat up, the following phenomena are systematically observed:

1. The disappearance of part of the pattern (circled in Figure 6.34, figure a) and its reappearance just before boiling (circled in Figure 6.34, figure c).
2. A curvature of the fibre towards the top of the image along the direction of convective flow (Figure 6.34, figure b).
3. A movement of the test pattern that appears to rise before stabilising until boiling occurs (Figure 6.34, figure c).

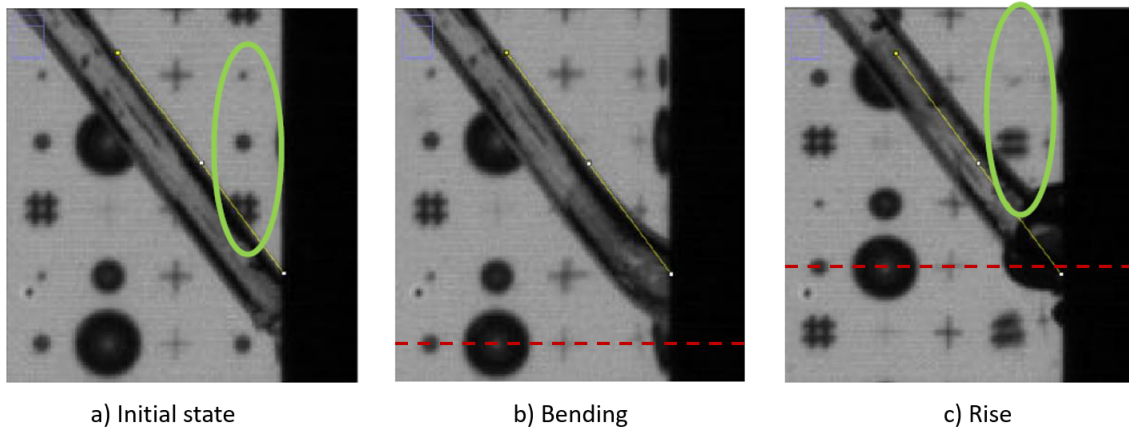


Figure 6.34: Stages of deformation during temperature rise, (a) initial state without heating source, (b) bending of the optical fibre and deformation of the pattern, (c) general rise of the image (red dashes) and reappearance of the pattern.

This effect, called the mirage effect, is visible over a thickness of about 600 microns. There is also a mirror effect: the patterns seem to appear on the near wall symmetrically to those on the other side, and squashed against the wall (see Figure 6.35).

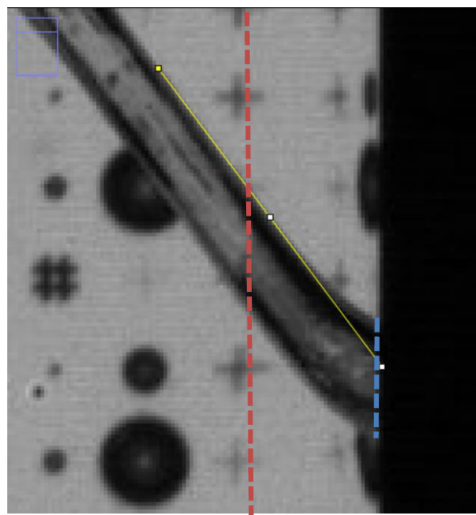


Figure 6.35: Image b) Figure 6.34.

The upward movement of the test pattern can be quantified (pattern presented in Figure 6.30): for example in the case of Figure 6.34, there is an overall upward movement of 850 microns of this pattern. This phenomenon of deformation (rising of the global image) in the direction of the natural convective flow was also observed by Estrada-Perez et al. [64]. The displacement of the optical fibre can also be measured: the deformation shifts the end of the fibre by 420 microns, then the same phenomenon of upward movement as for the pattern of the test pattern is observed, but to a lesser extent: 390 microns. This difference is explained by the position of the test pattern behind the tank, unlike the fibre which is positioned in the middle of the plate. The further away the object observed is from the objective, the greater the deformation, which is logically directly proportional to the thickness of the hot water layer. The measurement uncertainty on the impacted zone is fixed at 2 pixels (eye measurements on the images), i.e. 60 microns here. These measurements give a rough indication of the thickness of the observation zone impacted by these "mirage" effects for the test conditions investigated.

For each of the tests, the interface at the contact between the fibre (initial size 600 or 200 microns) and the heating wall (dotted blue in Figure 6.35) can be measured. Figure 6.36 shows the evolution of the deformation (ratio between the size of the contact area between the fibre and the wall and the real size of the fibre) as a function of temperature. This figure allows us to identify a stabilisation level of the deformation around 64°C. It can be assumed that during boiling the deformation observed will be a stabilised deformation of the objects at the wall.

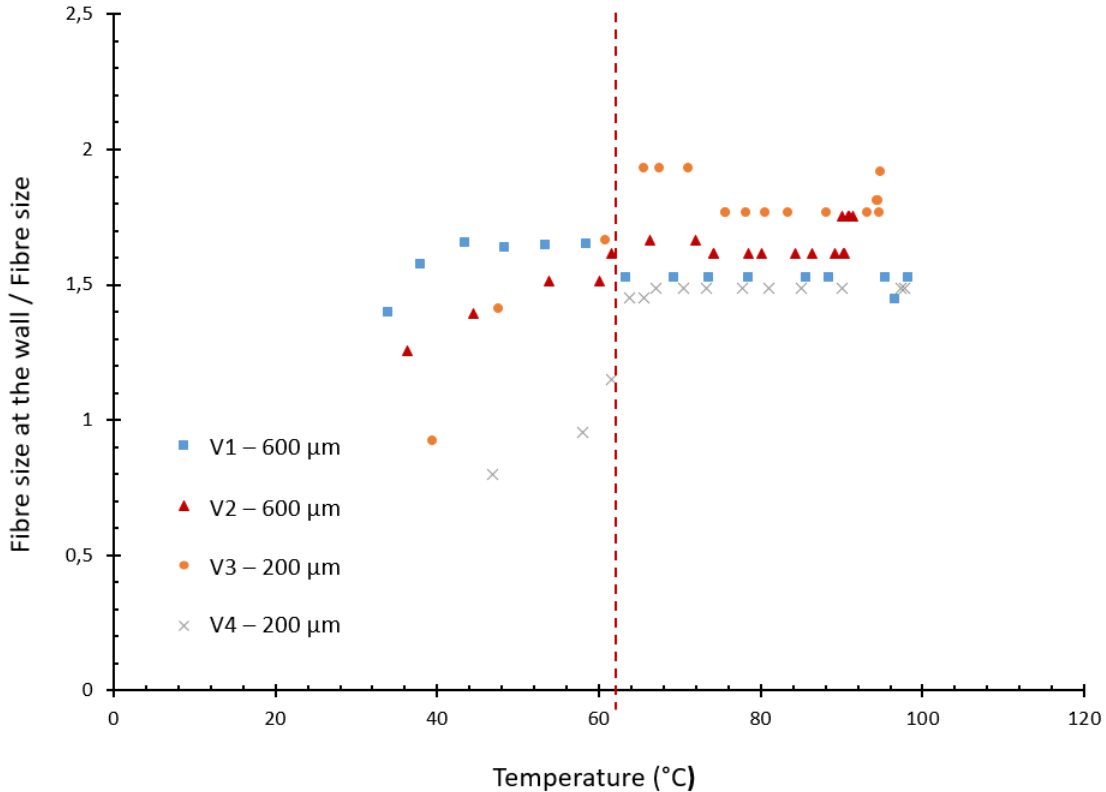


Figure 6.36: Evolution as a function of wall temperature of the fibre size observed against the wall for the different tests (Figure 6.32 for V1, 6.33 for V2, 6.37 for V3 and 6.38 for V4).

### 6.4.3 Deformation zone

For all the tests carried out, it is possible to measure the thickness of the near-wall zone affected by the deformation. For the three tests presented below (Figure 6.37, 6.38 and 6.39) carried out with the zoom or bi-telecentric lenses, these dimensions are presented in Table 6.3 according to the side of the plate considered (large side width 3cm, small side width 1.5cm).

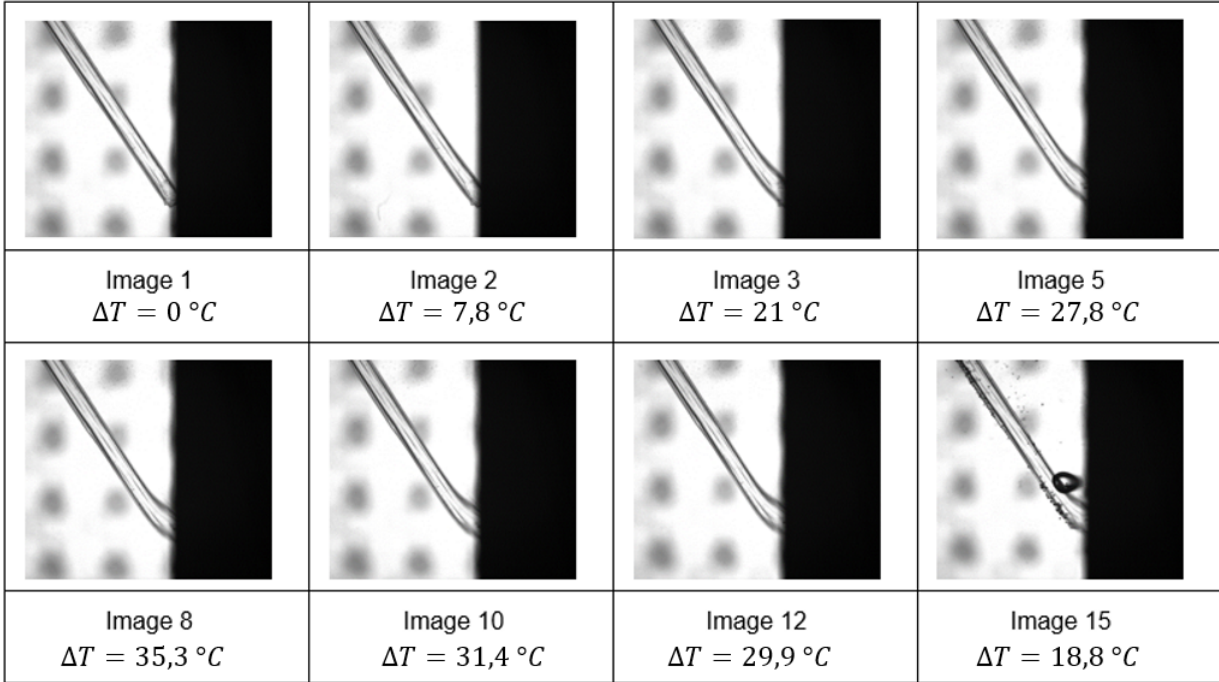


Figure 6.37: Visualisation with a zoom lens of a  $200 \mu\text{m}$  optical fibre against the wall with a test pattern in the background (short side).

Table 6.3: Thickness of the near wall zone affected by the deformation.

Tests	Figure	Used lens	Plate	Setup	Deformation zone
V1	6.32	Bi-telecentric	Wide (3 cm)	Patern + 600 microns fiber	0.98 mm
V2	6.33	Bi-telecentric	Wide	Patern + 600 microns fiber	1.01 mm
V3	6.37	Zoom	Short (1.5 cm)	Patern + 200 microns fiber	0.35 mm
V4	6.38	Optoengineering	Short	Patern + 200 microns fiber	0.32 mm
V5	6.39	Zoom	Short	200 microns fiber	0.36 mm

These results confirm the link between the thickness of the impacted zone and the observed plate dimensions. The thickness of the deformed zone near the wall depends logically on the thermal power transferred to the fluid and therefore on the surface of the heating plate. The larger the surface area, the greater the thickness of the high temperature fluid optically passed through and the larger the deformation zone. These observations confirm, if necessary, that it is important to limit the dimensions of the heating plate in the final facility as much as possible to favour the quality of the observations.

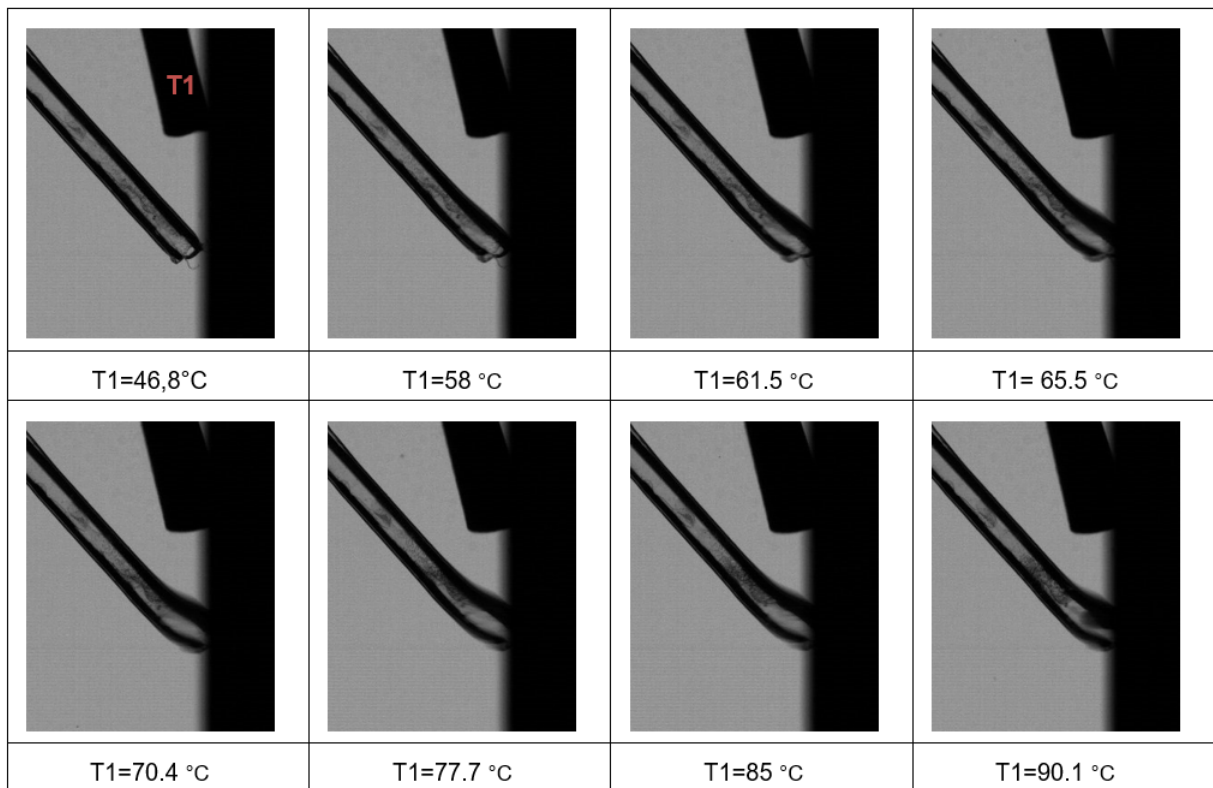


Figure 6.38: Visualisation with a zoom lens of a  $200 \mu\text{m}$  optical fibre against the wall (short side).

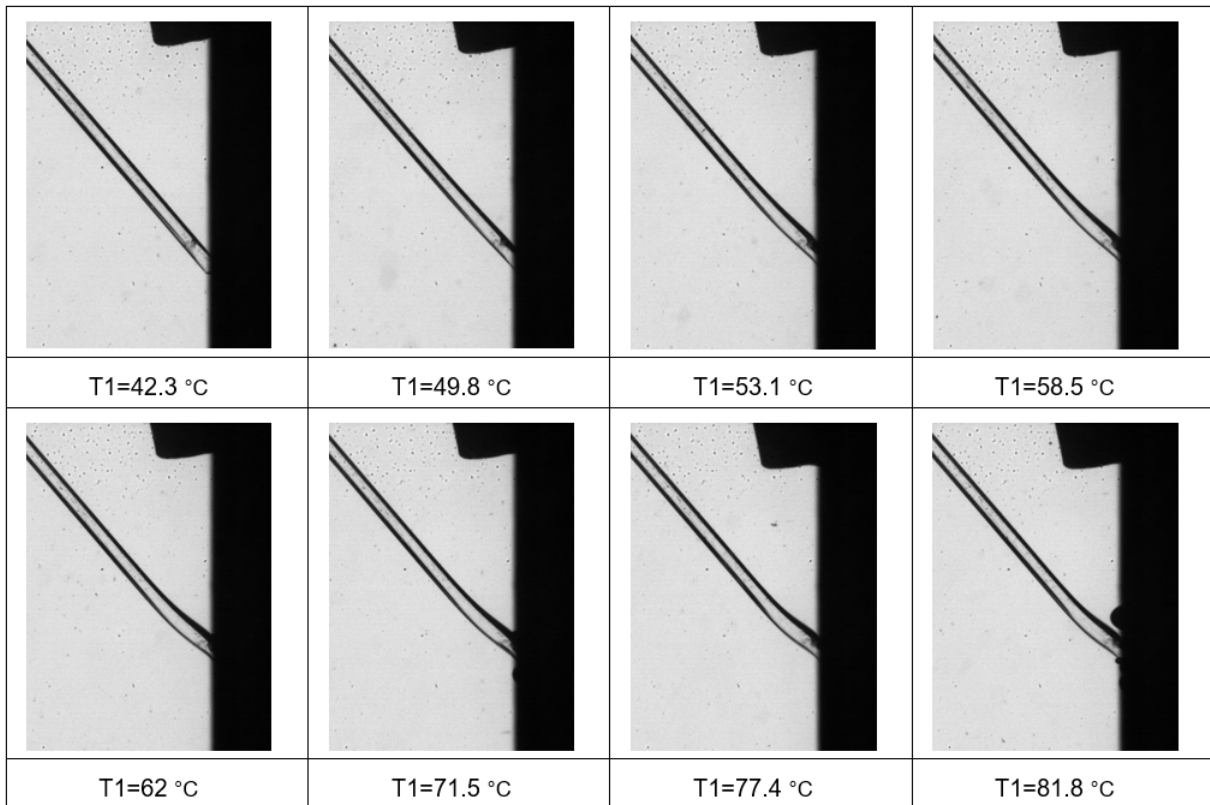


Figure 6.39: Visualisation with a zoom lens of a  $200 \mu\text{m}$  optical fibre against the wall (short side).

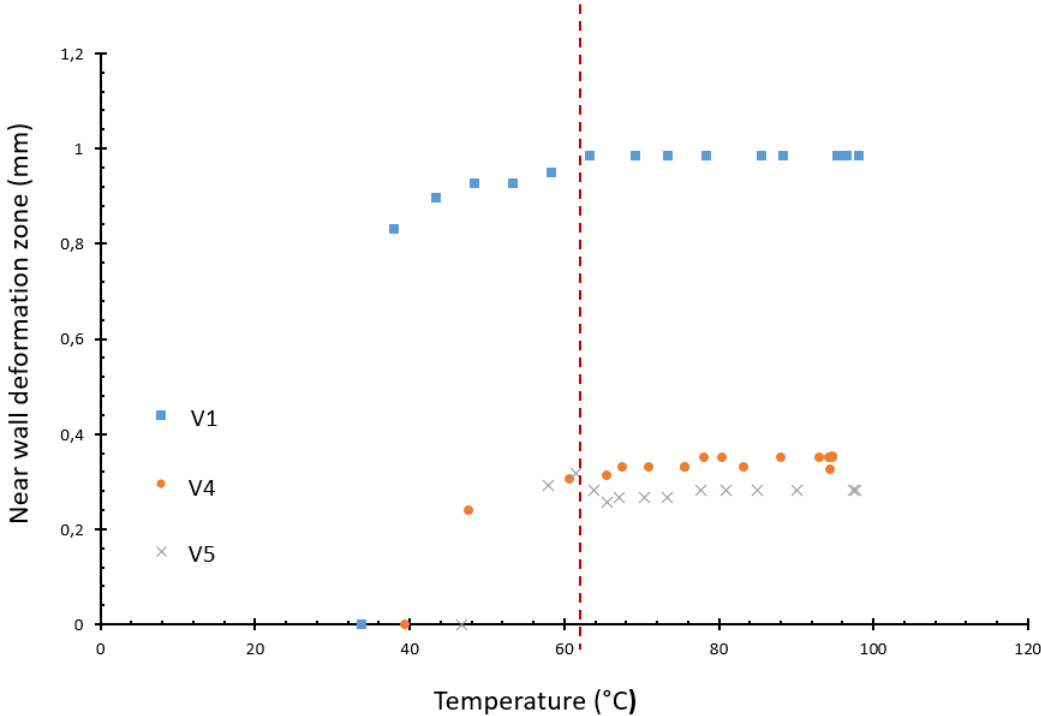


Figure 6.40: Evolution of the thickness of the near-wall deformation zone as a function of the wall temperature for the different tests (Visualisation 1, 4 and 5).

For each of the tests presented above, the evolution of the thickness of the near-wall deformation zone can also be measured. Figure 6.40 shows its evolution during the temperature rise of the fluid for the different tests. Again, an asymptote can be identified around  $64^{\circ}\text{C}$  which corresponds to the stabilisation observed for the fibre/wall contact zone (see subpart 6.4.2). For future tests on the DIOGEN test section, the deformation zone being constant when boiling appears, it should be possible to correct these effects at high pressure and high temperature.

#### 6.4.4 Impact of deformation on objects

To highlight the impact of this deformation on the near-wall objects over the entire observation area, the 200 micron fibre was placed along the heating plate at a fixed distance (120  $\mu\text{m}$  for Figure 6.41, 500  $\mu\text{m}$  for Figure 6.42). Fluid temperature values are measured along the wall (TC1) and in the jar (TC 2, 3, 4, 5).

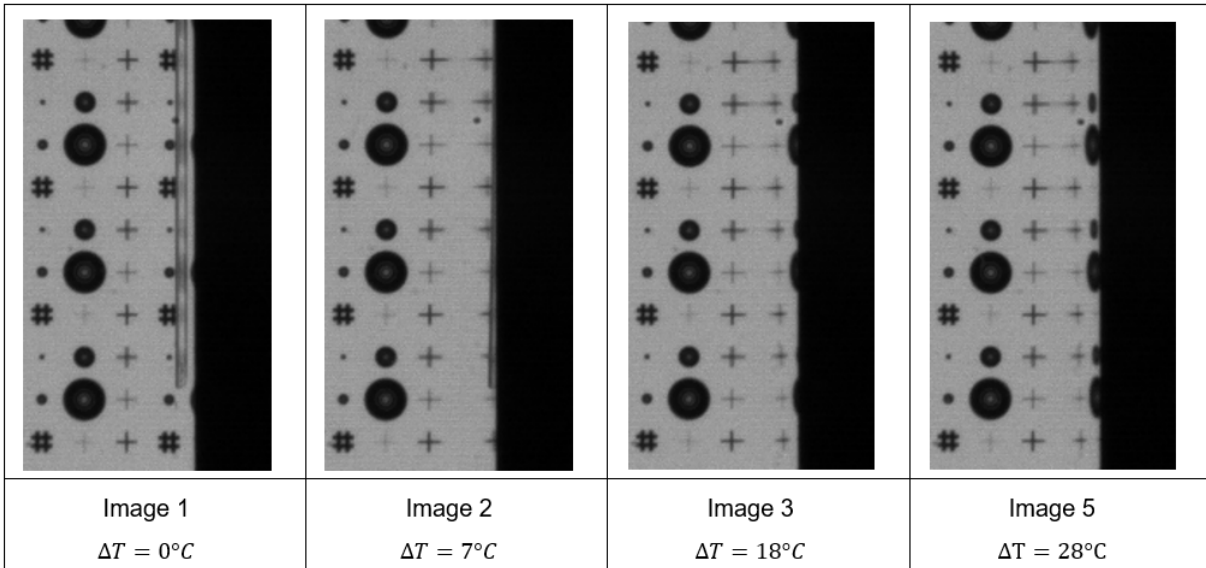


Figure 6.41: Visualisation with a bi-telecentric objective of a 200  $\mu\text{m}$  optical fibre at 120  $\mu\text{m}$  from the wall.

For the first near-wall position (at about 120 microns, Figure 6.41), as the temperature rises, the mirage effect causes the fibre to disappear completely, as it was the case for the test pattern (see Section 6.4.2). An effect is still visible when the fibre is moved away to about 500 microns from the plate (Figure 6.42), which confirms the thickness of the deformation zone measured previously and shows that the gradient is "constant" over the whole height of the plate. It can also be noted (Figure 6.42) that the deformation persists after image 10 ( $\Delta T = 35^\circ\text{C}$ ) until image 23 ( $\Delta T = 13^\circ\text{C}$ ), image 10 corresponds to the maximum gradient value.

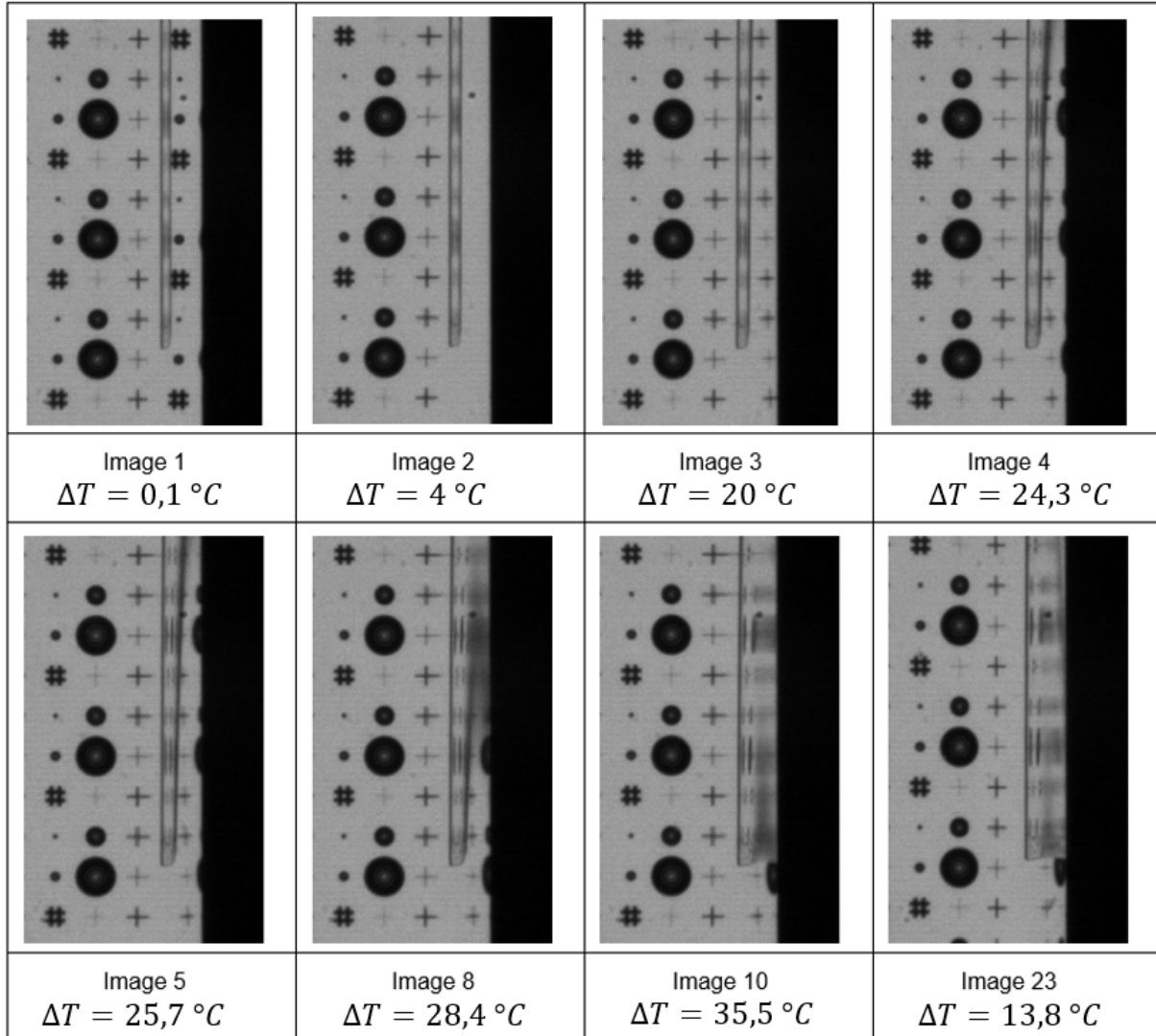


Figure 6.42: Visualisation with a bi-telecentric lens of a  $200 \mu\text{m}$  fibre optic at  $500 \mu\text{m}$  from the wall.

#### 6.4.5 Effect of the thickness of hot water passed through

To better understand the effect of the hot water zone size the light passed through, on the deformation of the images, a final test was carried out by placing a graduated ruler on the upstream and downstream edges of the heating wall. This setup is illustrated in Figure 6.43. Again, a regular sequence of images was taken during the temperature rise.

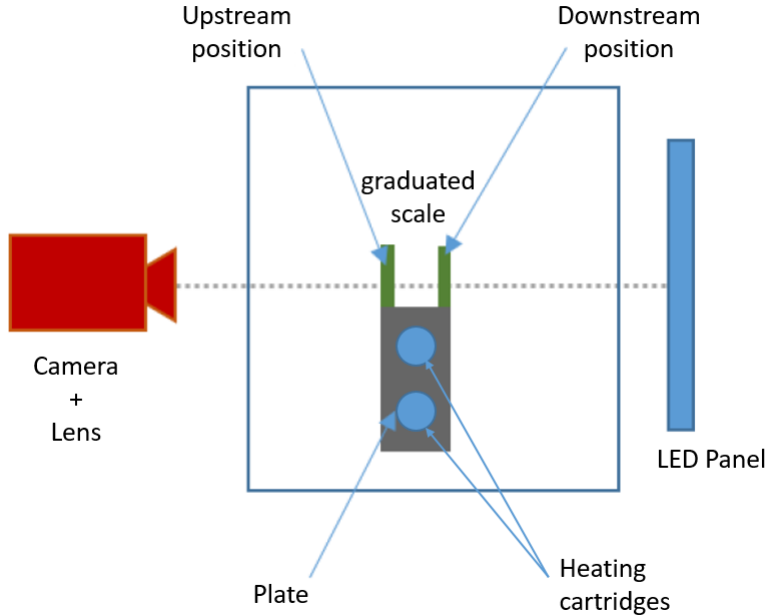


Figure 6.43: Schematic diagram of the assembly with two graduated scale positions against the wall.

Figure 6.44 and 6.45 show images taken for the two positions of the ruler. These observations logically confirm that there is a relationship between the thickness of the optically traversed "hot" water and the distortion. In the first images obtained with the upstream position (see Figure 6.44), the ruler is very little distorted, contrary to what is observed for the downstream position (see Figure 6.45).

Figure 6.46 shows the intensity profile of the ruler in the upstream position for  $45.3^{\circ}\text{C}$  (blue profile) and  $86.7^{\circ}\text{C}$  (red profile). These intensity profiles make it possible to detect the shift of the graduations between these two images: there is a shift of  $0,08\text{ mm}$ . For the downstream position, no shift was detected for different temperature conditions. Nevertheless, the part in contact with the plate seems to experience a mirage effect: a part of the graduations of the ruler disappears near the wall (Figure 6.45). This is the mirror effect observed on the images with the test pattern (Figure 6.34). Indeed, near the wall the symmetrical part of the ruler is positioned at  $1.07\text{ mm}$  from the plate (see red line in Figure 6.47). This may explain why no shift is detected since the reflection of the scales located more than one millimetre away from the wall is visible.

The position of the object on the plate therefore has an impact on the visualisation. The same observation will be true for the nucleation sites of the bubbles in the final facility, which again pleads for limiting the width of the heating plate as much as possible.

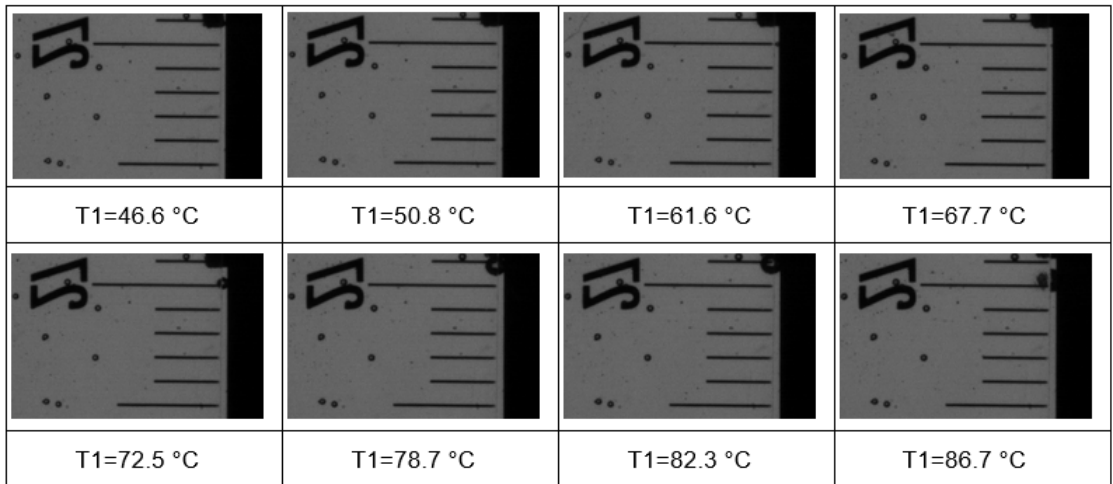


Figure 6.44: Visualisation with a bi-telecentric lens of a ruler positioned against the hot plate in the upstream position.

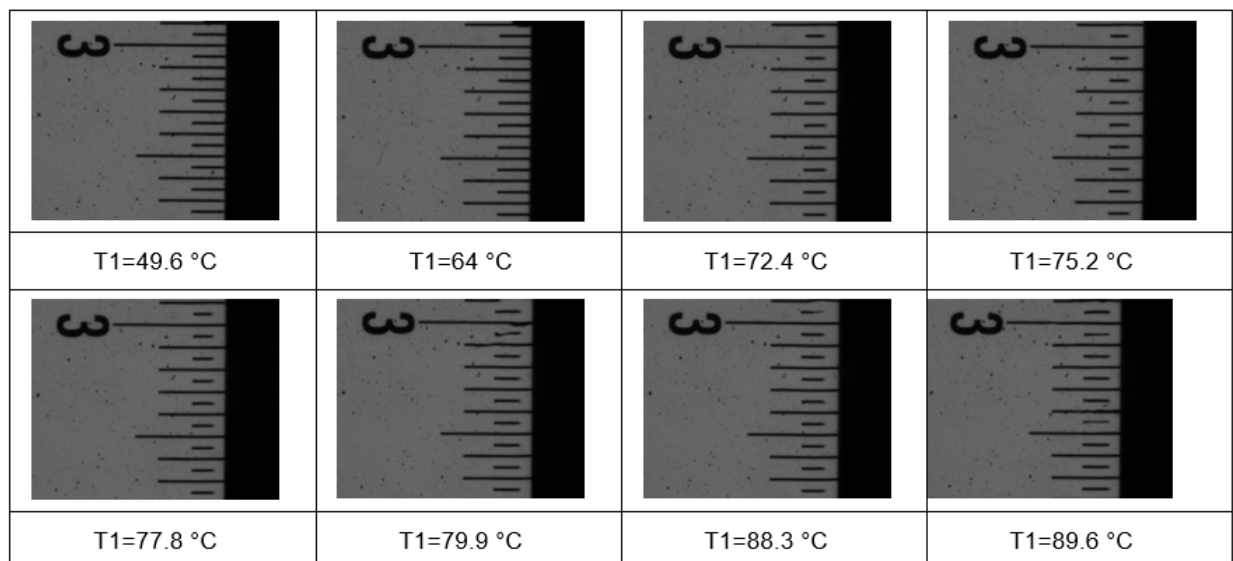


Figure 6.45: Visualisation with a bi-telecentric lens of a ruler positioned against the hot plate in the downstream position.

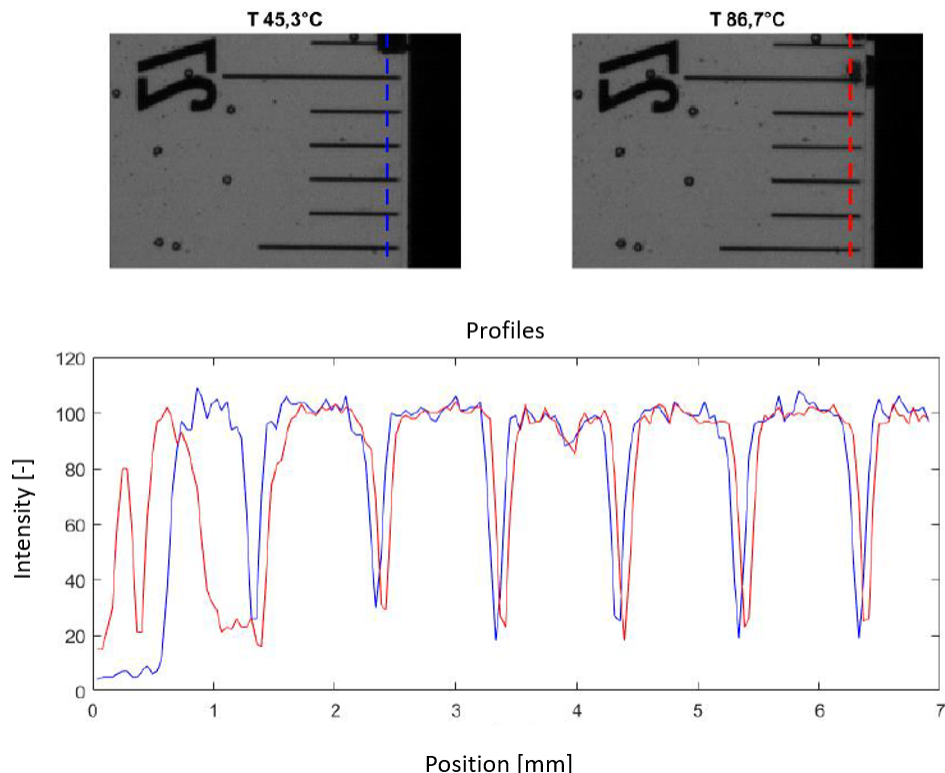


Figure 6.46: Positional deviation of the scales of the ruler placed in the upstream position as for two temperature values.

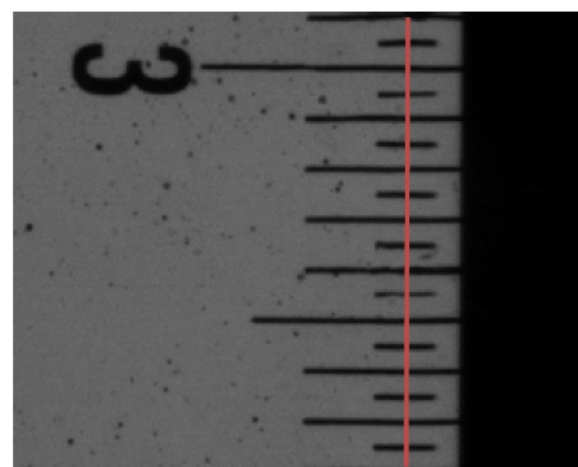


Figure 6.47: Positional deviation of the scales of the ruler placed in the upstream position as a function of temperature.

#### 6.4.6 Second campaign conclusions

The objective of these new tests was to propose a first evaluation of the influence of the temperature gradient on the visualisation of near-wall boiling. The setup used is identical to the one used for the first campaign. During this second campaign, it was associated with a system for measuring temperature using thermocouples, making it possible to carry out temperature mapping in the vessel.

The observations made during this campaign confirm the existence of distortions linked to the thermal gradient over a thickness of several hundred micrometers, which is sufficiently large to have an impact on the measurement of the size of the bubbles at detachment. This phenomenon must be taken into account when measuring the average size of bubbles at detachment, but it can be neglected if we are only interested in the bubble departure frequency. During the temperature rise, the deformation presents a transient: disappearance then reappearance of a part of the test pattern, curvature of the fibre towards the top of the image following the direction of the convective flow, movement of the test pattern which seems to rise before stabilising until the appearance of boiling. This transient is observed for the different configurations before reaching a steady state before boiling. It was possible to identify a stabilisation plateau of the deformation around  $64^{\circ}C$  for this configuration. Once this plateau is reached, the deformation remains constant and reproducible, which means that it can be corrected.

In terms of image deformation, we also note certain effects that could be more complex to take into account. This is particularly the case for the "mirror effect" in the near wall. This effect is less important for objects close to the lens. More generally, the thickness of the deformed zone in the near wall is directly proportional to the size of the heating plate. It will therefore be interesting to try to minimise it for the dimensioning of the future high pressure, high temperature test section.

At this stage, those elements could lead to investigate the possibility of digital correction using optical simulation software. For the measurements on the high pressure, high temperature test section, 2D modelling of the temperature field under test conditions coupled with a ray-tracing calculation could be an effective solution to implement. It will allow to anticipate the optical index gradients that will be obtained and thus to estimate the mirage effects that will be expected during these future tests. The main difficulty is to know the evolution of indices as a function of temperature above  $100^{\circ}C$  (little data in the literature).

The future boiling tests will be carried out in high pressure, high temperature and forced convective flow. The DIOGEN test section will be composed of sapphire windows allowing optical access to the flow. The same transmission optical setup will be used to measure bubble sizes and detachment frequency.

## 6.5 Infrared thermography

The aim is to carry out time and space resolved measurements of the temperature of the heated plate. For this purpose we have chosen the method of IR thermography. This consists of using a high-speed measuring device, an IR camera, calibrated for the target temperature range. The IR thermography setup is described in the diagram Figure 6.48. In this work we intend to perform coupled shadowgraphic and IR measurements. This synchronisation will allow to avoid the issue of wall distortion due to the thermal gradient regarding the identification of detachment instant (Section 6.1). Indeed, the temperature under a bubble varies with a known variation of decay and growth during nucleation (presented in Chapter 5).

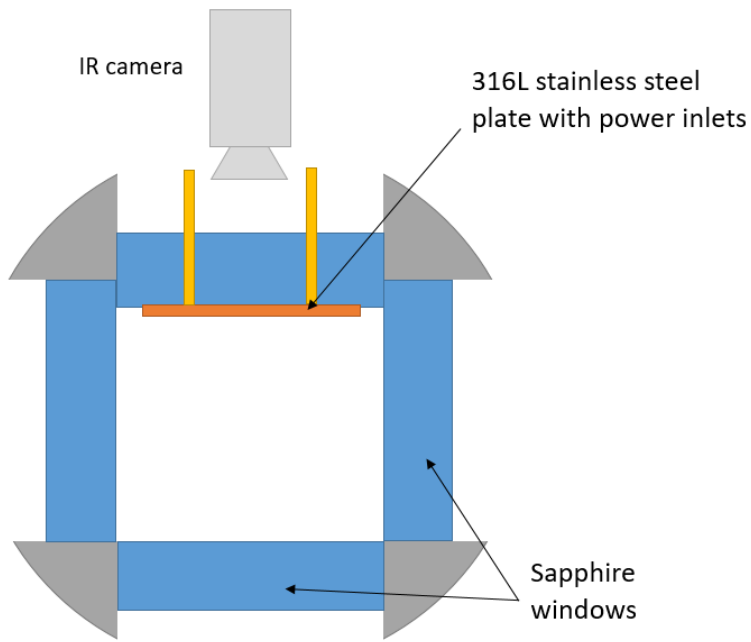


Figure 6.48: Diagram of the IR thermography setup.

Several articles present solutions using an infrared camera to visualise the temperature field on the heating element. In thermography, radiation is associated with a temperature. Stephan Boltzmann's law describes the total energy radiated per unit surface area of a body as directly proportional to its temperature (see Equation ??).

$$M = \epsilon \sigma_{SB} T^4 \quad (6.1)$$

with  $\epsilon$  is the emissivity of the surface,  $\sigma_{SB} = 5.67 \times 10^{-8} W/m^2 K^4$  is the Stephan Boltzmann's constant and  $T$  is the temperature of the surface. The IR camera sensor converts the radiation it detects into an electrical signal. The emissivity of a material (excluding black bodies) depends on its temperature. This variation makes temperature measurements by infrared thermography more complex and requires calibration with the use of surface whose emissivity is constant which allows the temperature to be directly determined. A review of the literature was carried out to establish the key points to be taken into account for the implementation of an IR thermography.

### 6.5.1 Literature review on infrared thermography

Scheiff [36] provides a fairly comprehensive study on setting up a combined shadowgraphic and infrared thermography for transient boiling experiments. The area to be measured by infrared thermography is the back of a metal foil semi-annular heating a semi-annular pipe, the test section is shown in Figure 6.49.

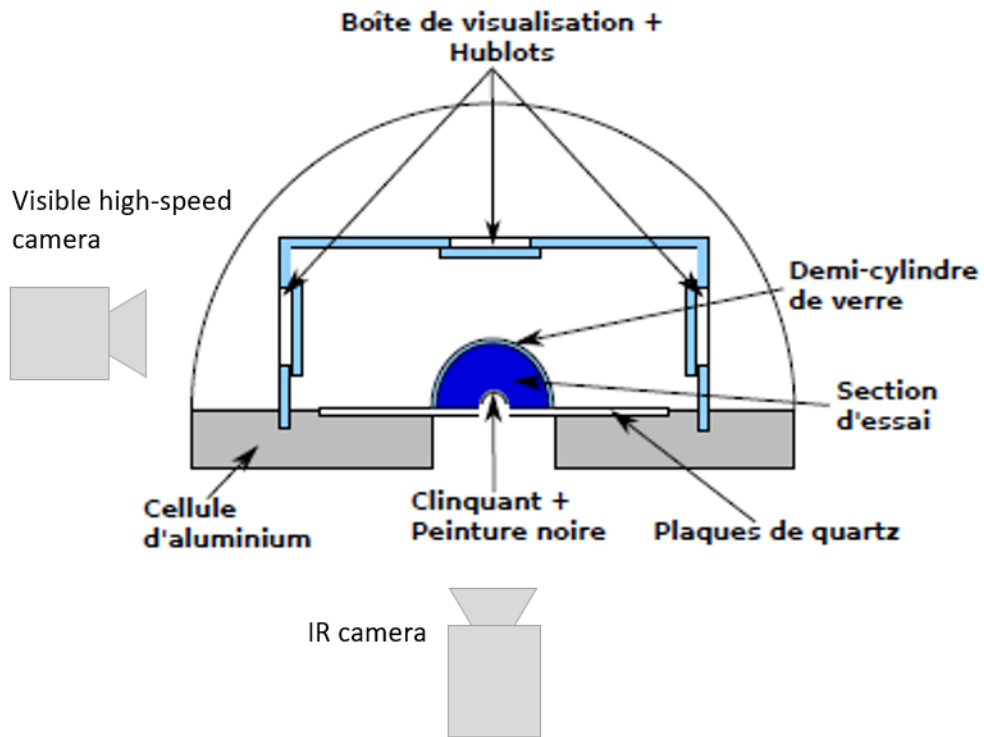


Figure 6.49: Cross-section of the test section, reprinted from Scheiff [36]

The measuring device is done with a synchronisation, carried out between the fast camera (Photron RS3000) and the infrared thermal camera (CAPID JADE III). Calibration of the IR measurements is done with a 4th order polynomial, and a non-uniformity correction (NUC) with two black bodies working between  $20 - 100^{\circ}\text{C}$  and between  $20 - 550^{\circ}\text{C}$ .

Scheiff noted the importance of taking into account for the average atmospheric transmittance, depending on the distance to the object, which should be less than  $2\text{ m}$ , according to the graph 6.50.

Thermographic measurement is also sensitive to the angle of orientation of between the object and the camera. Emissivity of an isotropic body does not depend on the observation angle, otherwise for other material, directional emissivity must be taken into account when doing such measurements. For conductive materials, the emissivity is highly dependent on orientation. For dielectric materials this dependence is reduced, this type of material has a constant emissivity up to an orientation of  $30^{\circ}$ .

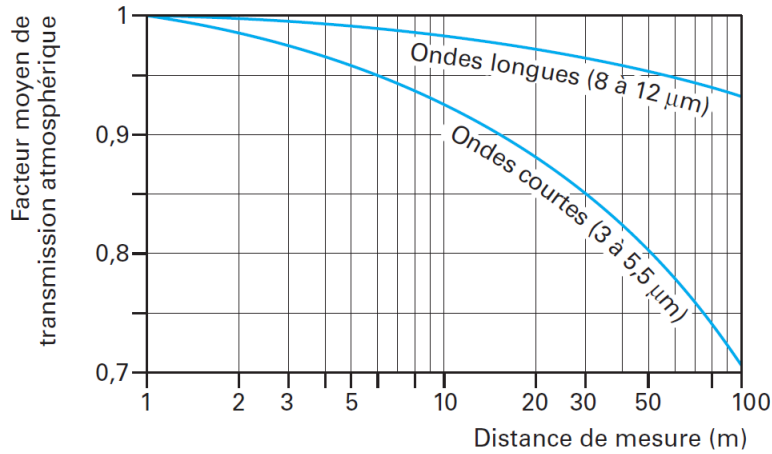


Figure 6.50: Typical curve of the average transmittance of the atmosphere as a function of the measuring distance, for an atmosphere with 50% relative humidity, reprinted from Pajani [119]

A black paint is applied to the back of the foil, and presents a constant emissivity of 0.94 in its range of temperature. In his study, Scheiff details work done on the impact of paint deposition on IR measurement. This type of black paint has very low heat conductivity. The paint application system was optimised: with a spray or airbrush application, the layer of deposited paint was irregular and thick (the shape of the foil does not help). A solution was found with a manual spiral applicator (see Figure 6.51): it consists in a stainless steel rod surrounded by a wire, which diameter is  $30\ \mu m$ .

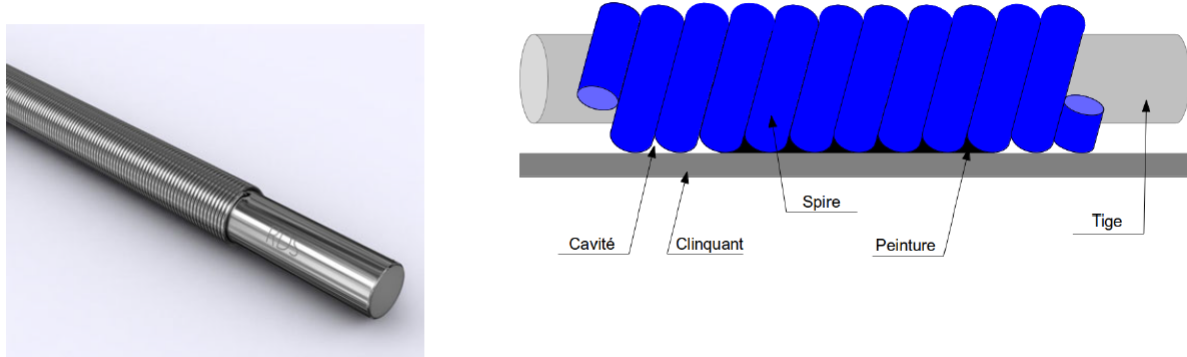


Figure 6.51: Manual spiral applicator: stainless steel rod surrounded by a wire of  $30\ \mu m$ , reprinted from Sheiff [36].

The thickness of the deposit is governed by the thickness of the wire :  $30\ \mu m$ . This solution allow a reproducible and uniform paint layer of  $25 - 30\ \mu m$ . The paint thickness determination is important as it influences the level of IR emissions received by the camera.

The emissivity of different samples was measured by Scheiff with an integral sphere covered with a reflective and scattering infrafold coating for the  $1.5 - 15\ \mu m$  range. Emissivity measurements consists in the illumination of the sample in a given direction, then measure-

ment of reflections by a detector. Those measurements were performed for different thickness samples between 5 to 150  $\mu\text{m}$ .

Yoo et al. [27] aims to perform measurements of two-phase flow parameters in a convective boiling system which involves a large heated area. For this purpose, he developed a strategy for coupled visible and IR thermography measurements. The test channel is  $10 \times 10 \text{ mm}^2$  square geometry, the fluid flows (3M NOVEC 7000) upward through a vertical test section of 305 mm height. The test section (Figure 6.52) is enclosed by transparent acrylic walls except for the heated wall side. According to Yoo, the composition of the materials chosen for their optical properties must be selected according to the application and in particular the test conditions involved. Also, according to Yoo and many authors working on the subject ([36] [51]), optical distortions are avoided or limited with the coupling of the two visible and IR visualisation techniques. For an accurate infrared measurement, a correct calibration must be in place.

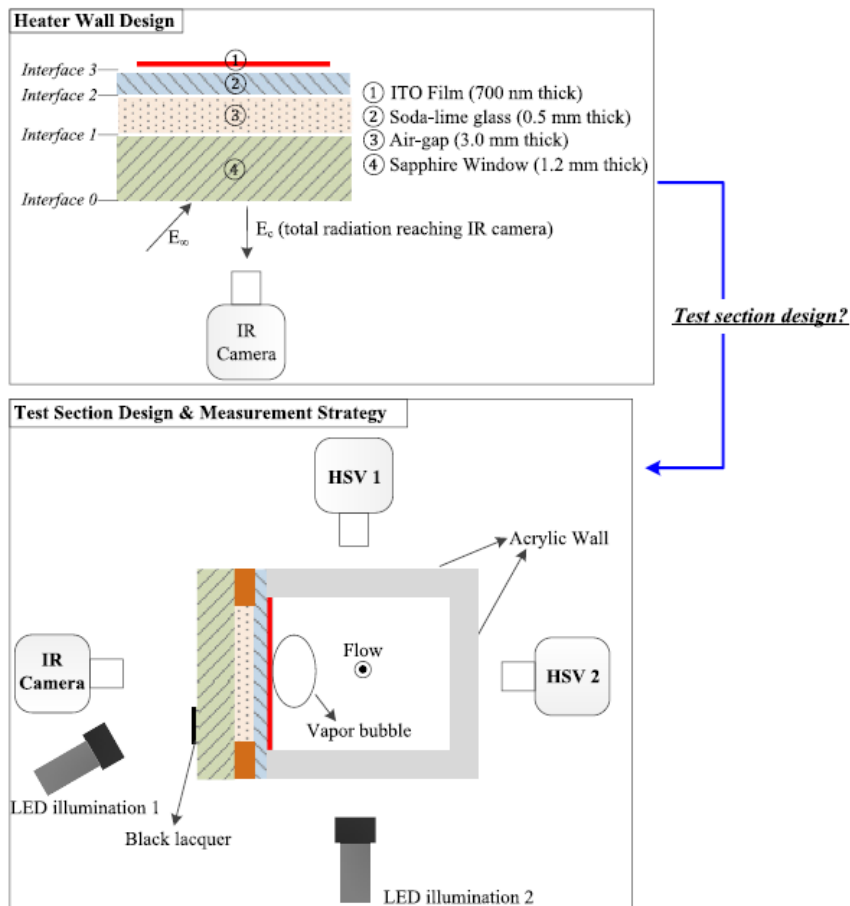


Figure 6.52: Heater wall design (top) and measurement strategy (bottom) in the subcooled flow boiling experiment (view from the top of channel), reprinted from Yoo et al. [27].

Yoo highlighted two types of heater design for IR measurements:

- Thin metal foil heater which he considers the best solution for capturing the transient wall temperature but for a small heated area,
- Using an ITO deposit on a substrate.

Yoo chose the second option and deposited a  $0.7 \mu\text{m}$  ITO film on an IR-transparent  $0.5 \text{ mm}$  soda-lime glass substrate enclosed with a sapphire window to prevent heat loss (trapped air between the sapphire and the glass insulate the wall). In his work, Yoo presents the experimental procedure to measure optical properties of the materials that make up the heating element. Using gold-coated mirrors, the heater was first tested from both sides (presented Figure 6.53). ITO temperature was measured from the ITO side and also through the semi-transparent media at the same time. Due to his thickness, ITO temperature measured from both side should be the same if the optical properties of the materials used are correct. Black laquer was applied on the sapphire to obtain the boundary condition at the outer surface. This technique led to adjust ITO properties (input data of the solving algorithm) to ensure the best performance in temperature measurements.

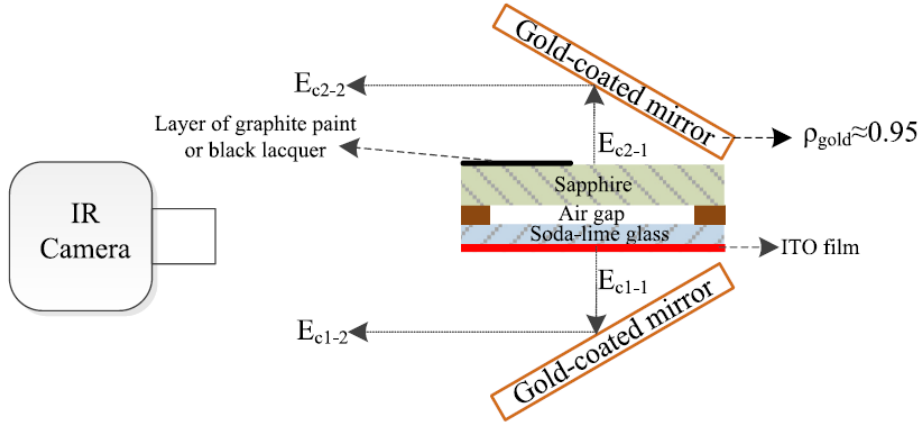


Figure 6.53: Experimental setup to validate the ITO film's optical properties, reprinted from Yoo et al. [27].

Kim et al. [120] measured the temperature of a multilayer consisting of silicon substrate coated with a thin thermal insulator (partially transparent to IR). The objective of this work was to demonstrate the feasibility of an IR thermography solution to measure the local heat transfer produced by two-phase flow with high temporal and spatial resolution over relatively large areas. The use of an insulator aims to amplify the temperature variations and provide a higher signal for the IR camera. Temperature can be measured by coating selected area with a thin IR opaque film: an opaque black paint is applied on top of the polyimide tape. The temperature profile within the multilayer is obtained by unsteady heat conduction simulations. This conduction is supposed to be unidimensional according to the authors because the temperature gradient is much larger in one direction.

The temperature measured by the camera results from three contributions: emission from the black paint, emission from each of the layers and reflection from surroundings. The temperature of each layer needs to be determined with a coupled conduction and radiation problem. Some experimental results are needed to calculate the real temperature from the emission received by the camera (as identified by Yoo). This includes to determine the optical properties<sup>1</sup> of the materials used for the heater. To do so, a blackbody (large cylindrical cavity, see Figure 6.54) is used with a controlled temperature. It was positioned in front and behind each material (see Figure 6.55) to determine whether its absorptivity or its reflectivity.

<sup>1</sup>absorption and transmission

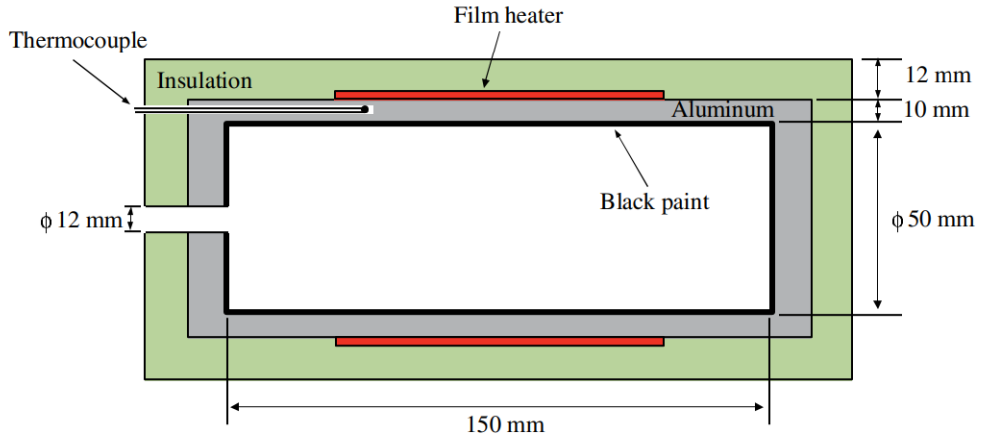


Figure 6.54: Blackbody construction used for optic characteristics measurements, reprinted from Kim et al. [120].

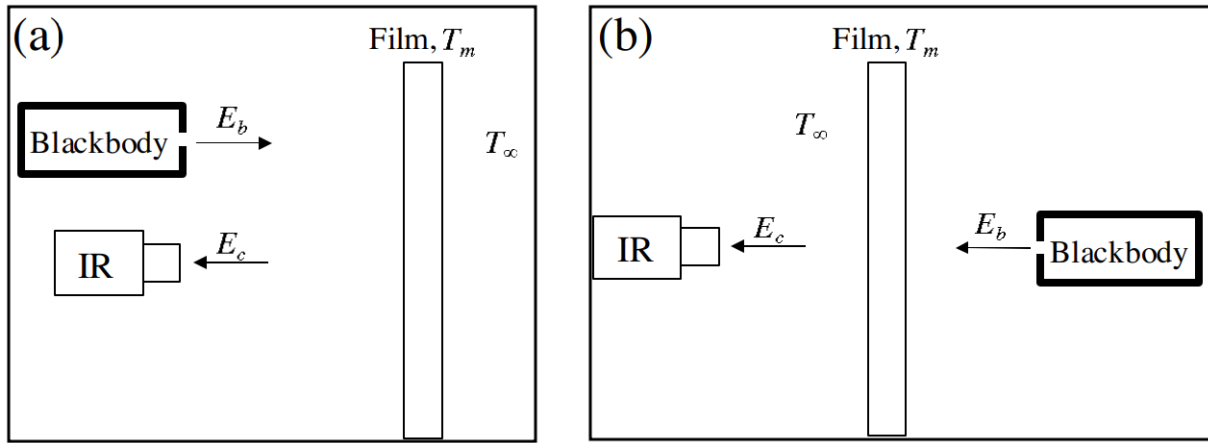


Figure 6.55: Schematic of experimental setup used to measure the reflectivity and transmittivity of a single layer, (a) apparent reflexivity measurement, (b) apparent transmittivity measurement, reprinted from Kim et al. [120].

Experiential uncertainties impact concerning the calculated heat flux were determined by moving from a small value each experimental parameter at a time and running the algorithm. Sensitivity of the variables at varying flux was found and the parameters that resulted in the highest error are sum-up in Table 6.4. Determining the values of the optical and thermal characteristics of the materials used seems to be a major source of error in the IR measurements. Care must be taken to control the sources of error and therefore to test the properties of the materials.

Table 6.4: Parameters with largest effect on uncertainty analysis, reprinted from Kim et al. [120].

Experimental constant	Value	Uncertainty
Emissivity of the black coating	0.90	0.01
Absorptivity of the polyimide tape	$7110 (m^{-1})$	$500 (m^{-1})$
Polyimide thickness	$15 \mu m$	$2 \mu m$
Adhesive thickness	$15 \mu m$	$2 \mu m$
Reflectivity of silicon-air interface	0.34	0.017
Reflectivity of silicon-polyimide interface	0.34	0.017
Thermal conductivity of polyimide	$0.12 W/m - K$	$0.01 W/m - K$
Thermal conductivity of adhesive	$0.20 W/m - K$	$0.01 W/m - K$

As in Yoo et al. study [27], Kim uses gold coated mirrors to evaluate the experimental technique and algorithm beforehand. Figure 6.56 shows the same type of setup as Yoo. Temperature is measured from both sides and checked to be the same for different ranges.

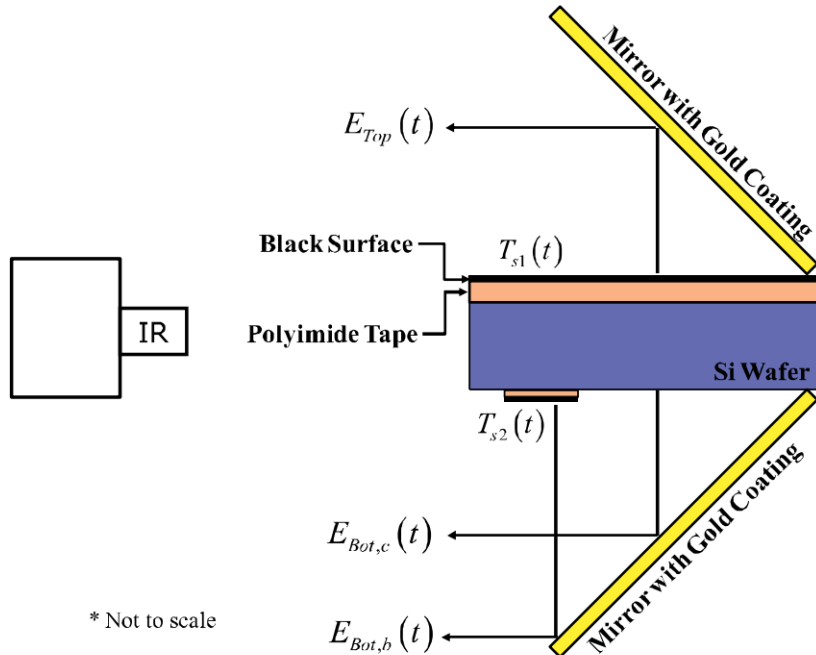


Figure 6.56: Experimental setup for validation of temperature measurement, from Kim et al. [120].

For these tests, a Sillicium wafer was heated by a thin film heater, black coating was deposited on top of this wafer. The technique used to produce the black coating was silk screening and its thickness is  $6 \mu m$ . The paint used is a 20 % carbon black in vinyl chloride/vynil acetate copolymer after curing (Nadar GV111). This technique seems to produce a thinner thickness than the techniques described by Sheiff [36]. Silk screening is another

technique which should be considered for our setup.

Hapke et al. [44] worked on a  $1.5\text{ mm}$  inner diameter cylindrical test section, made of nickel base alloy 2.4816, used to determine the ONB (Onset of Nucleate Boiling) while measuring wall superheat. The temperature measurement was done with a IR thermography system: AGEMA Thermo vision 900. This system is sensitive to long wave spectrum ( $8 - 12\text{ }\mu\text{m}$ ).

To enable measurement, the test section was coated uniformly with a lacquer (with a constant emissivity  $\epsilon = 0.94$ ). Calibration measurement allow to calculate the local distribution of the emissivity due to inhomogeneities of the lacquer coat. This calibration was made without heating: the inner fluid temperature was kept constant and so the temperature of the wall can be calculated (through the resolution of a conductive problem). Emissivity was then calculated comparing the temperature measured by thermography and the one calculated by conduction.

To analyse these experiments, the conductive problem within the wall was solved with the external face boundary condition measured and the inner temperature calculated. This study do not really take into account for transient temperature changes supposed to be very small.

Bucci<sup>2</sup> [121] developed a radiative/conductive model for the IR measurement of an ITO deposit on a sapphire substrate. This study aims to set up an IR measurement method for tests on nucleate boiling.

In the course of their study, they identified calcium fluoride as the most suitable material for IR measurement. However, this material is fragile and limits its use. Sapphire is a strong, but semi-transparent material adding uncertainties to the temperature measurement (sapphire absorbs and emits in the targeted spectral range). The absorption coefficient of sapphire is variable with temperature (it decreases with temperature rising), so it is important to take it into account. They do not use a black paint with a constant emissivity in this study. The classical calibration based on the average of the optical properties cannot be applied as implemented in the work of Yoo et al. [27] or Kim et al. [120]. The camera is therefore constantly receiving IR radiation emitted by the ITO deposit, but also by the sapphire, as well as IR reflections from the environment on the sapphire (see Figure 6.57). Bucci developed a conduction model based on the characteristics of the IR camera (IRC806 camera, 2500 fps, pixel size: 116 microns). The solving method is a 3D finite volume method. The temperature distribution though the substrate is calculated by solving the heat balance equation within the substrate. The radiative model combined ITO emission, sapphire emission and background reflection. This model was compared and validated with single-phase transient conduction. This model improved the accuracy of the ITO temperature measurement compared to calibration based results.

---

<sup>2</sup>whose setup is described in Chapter 1, 4 and 5

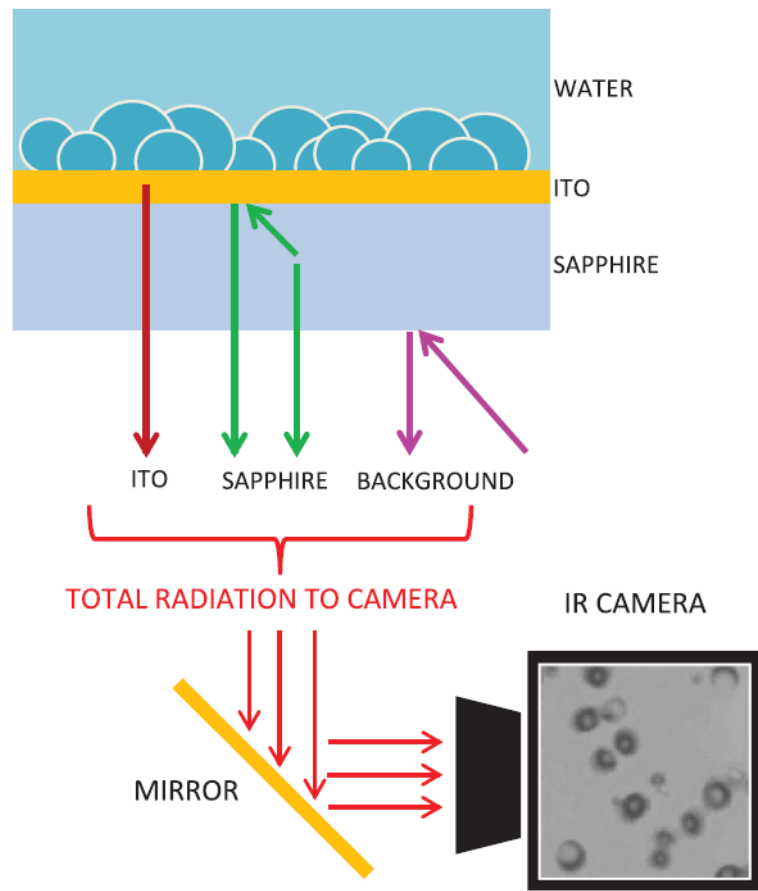


Figure 6.57: Different contributions to the radiation measured by the IR camera (not to scale), reprinted from Bucci [121].

### **6.5.2 Strategy for IR thermography implementation**

On the basis of these various studies, a strategy for implementing an infrared thermography measurement technique on the high pressure, high temperature test section was determined. This strategy is based on several steps, described below but not yet implemented.

The first step was the choice of the heating element and the definition of its geometry (presented in Chapter 5). The plate will be made of stainless steel 316L, its geometry is  $5 \times 1 \text{ cm}^2$  with a thickness of  $50 \mu\text{m}$ .

Since that we fixed the geometry of the heating element, the second step is the application of a constant emissivity black paint, which must be chosen according to the particularities of this study. Indeed, the spectral range must be known according to the type of infrared camera used, the targeted temperature range (from low pressure to high pressure) must also be taken into account for the choice of the paint. The technique of deposit on the stainless steel plate must also be mastered. For this, a preliminary test campaign and analysis of several deposition techniques must be considered. The testing of several of the above-mentioned techniques must be set up to allow the control of the deposit thickness, since it can strongly impact the measurements.

Then the calibration of the camera according to the plate characteristics and the range of temperature targeted must be conducted. Simple calibration does not seem to be sufficient for this type of study as presented before. It is necessary to characterise the materials optically before assembly and to correct these characteristics with the techniques presented above (use of black bodies for optic characteristics, mirror system with gold coating to correct the measurement algorithm...). Nevertheless, in this litterature review, temperature comparison between the two faces of the heater using mirrors with gold coating were performed in ambiant air. It is questionable whether a calibration in air can really take into account the thermal behaviour of the heating element in contact with a boiling flow.

Once these steps have been carried out, a radiation conduction model seems necessary to eliminate possible uncertainties due to the environment and the materials used. A parametric sensitivity study on the sources of experimental error will be appreciated to correctly determine the measurement uncertainty of this method.

# **Part III**

## **Experimental design and testing**



# Chapter 7

## Preparation of the experiments

### 7.1 Test matrix

The tests considered should provide a database allowing to compare nucleate boiling models by independently measuring the three characteristic parameters: bubble detachment frequency, bubble detachment diameter and active nucleation site density. To do so, the measurements must be performed with a wide range of thermal hydraulic conditions. Firstly, measurements of these parameters must be done for prototypical PWR thermal hydraulic conditions, for which there is a lack of data. In addition, operating a wider range of the thermal hydraulic conditions will also be interesting to capture the influence of the different parameters like pressure, inlet temperature, mass flow velocity. Indeed, measurements over a wide pressure range are important to observe the change in phenomenology. In particular, those tests should help to confirm the observations stated by Hosler [28] and March [4].

The test matrix is therefore built up from a large pressure variation, with a specific point at 70 bar (noted by Hosler [28] as the pressure at which there is a change in flow topology). In addition, several inlet temperature are proposed, to study different values of subcooling. Several flow velocities are also proposed. The data from the test matrix are summarised in Table 7.1. 84 thermal hydraulic conditions are then identified.

Table 7.1: Test matrix.

Parameters	Values
Pressure [bar]	20 – 40 – 60 – 70 – 80 – 100 – 120
Subcooling [°C]	20 – 15 – 10 – 5
Mass velocity [kg/m <sup>2</sup> .s]	2000 – 1500 – 1000

### 7.2 Modified test facility

The time constraints inherent in the completion of this thesis work and the technological problems raised during the pre-design of the test facility led to a downgrading of the constraints with regard to the thermographic measurement (detailed later). In the first phase of

the study, the aim was to carry out infrared measurements on the heating plate. Therefore, the window had to allow these wavelengths to pass. Sapphire was chosen to be the window material as its characteristics are:

- Transparency for optical measurements,
- Transparency for transmission of the desired wavelengths,
- Robustness on high pressure and high temperature environment
- Electrical insulation not to interfere with Joule heating.

The initial concept was then a sapphire window, on which the heating plate would be assembled to generate boiling on the side in contact with the fluid while IR observations will be carried out on the external face. In Chapter 5, we determined that the heater plate thickness should be equal to  $50 \mu\text{m}$ . This thickness constraint affects the method of plate mounting on the sapphire window. Nevertheless, no reliable technique solution could be found concerning the window equipped with the heating plate with sealed passages for direct Joule effect heating. Several concepts were presented before. They are summed up in Figure 7.1.

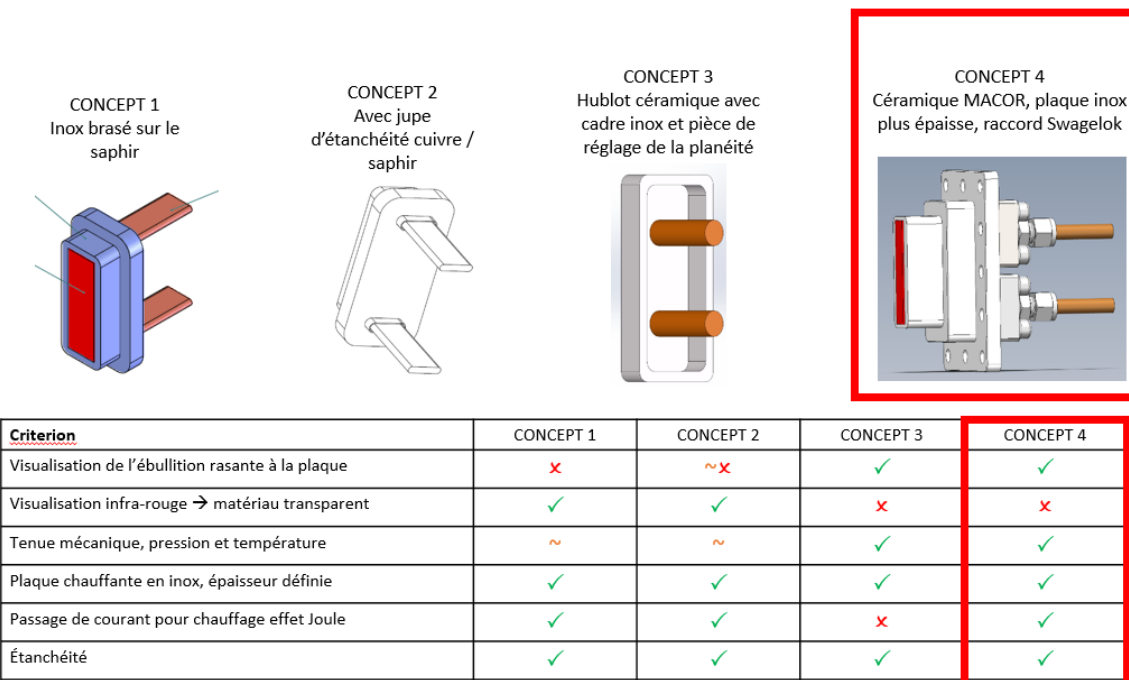


Figure 7.1: Evolution of the heated window concept.

Facing the technical incapacity and time constraints, the sapphire heating window and thus, thermographic measurements were abandoned. A new design could then be dimensioned to perform only shadowgraphic measurements.

This new test section will be equipped with sapphire windows on three of its sides, and a porthole equipped with the heating plate without the possibility of thermographic measurement. Nevertheless, the design takes into account the possibility of changing this window with a window allowing infrared measurement if the technical solution is found in the future.

Discussions on the infrared window will continue and, according to recent exchanges, should require special brazing tests.

### 7.2.1 Design

The test section must enable to characterise nucleate boiling in the prototypical conditions of PWR. To achieve this, the test section must provide:

- Means of visualisation,
- Elements to produce well-located boiling,
- Pressure and temperature measurements at the inlet and outlet.

The input data for the design of the test section are as follows:

- $30 \times 30 \text{ mm}$  square flow channel,
- Power to be supplied up to  $5 \text{ kW}$ ,
- Plate thickness:  $50 \mu\text{m}$  (for IR measurements, else, without constraint),
- Process connection DN: DN20 (for DIOGEN facility),
- PN = 420 or class 2500 Lbs.

The dimensioning conditions of the components are as follows:

- Pressure:  $150 \text{ bar}$ ,
- Temperature:  $340^\circ\text{C}$ ,
- Fluid: Demineralised and deaerated water.

The first part of the test section design resulted in the following design Figure 7.2.

The new test section design is shown in Figure 7.3. The test section consists of the three sapphire windows for flow visualisation as presented in Chapter 4. For the heating part, as the constraint of the infrared measurement was lifted, the heating plate will be thicker (about  $1 \text{ mm}$  thick), with two brazed copper electrodes. The aim was to design a window with the following characteristics:

- Electrical insulation,
- Thermal insulation,
- Mechanically resistant to pressure / temperature,
- Easily machinable.

After carrying out this research, a material emerged: MACOR. This technical ceramic has the advantage of being machinable in the same way as steel, it is a good electrical insulator, its cost is lower. In order to maintain the heating plate in the test section, a flange made of MACOR was sized (see Figure 7.4).

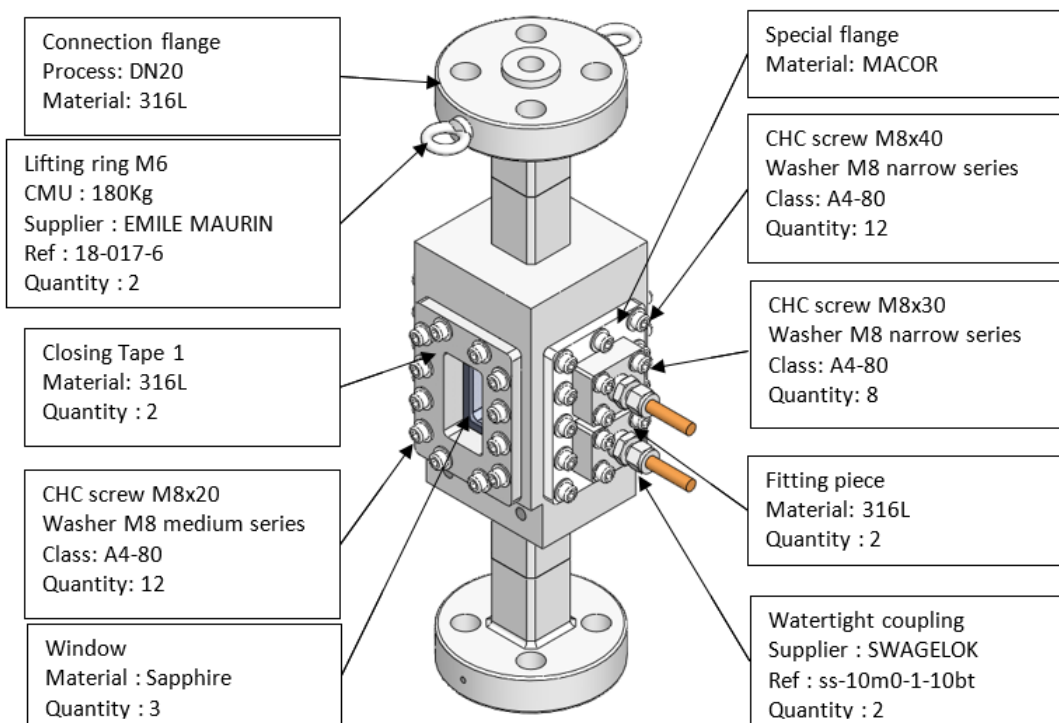


Figure 7.2: Modified test facility description.

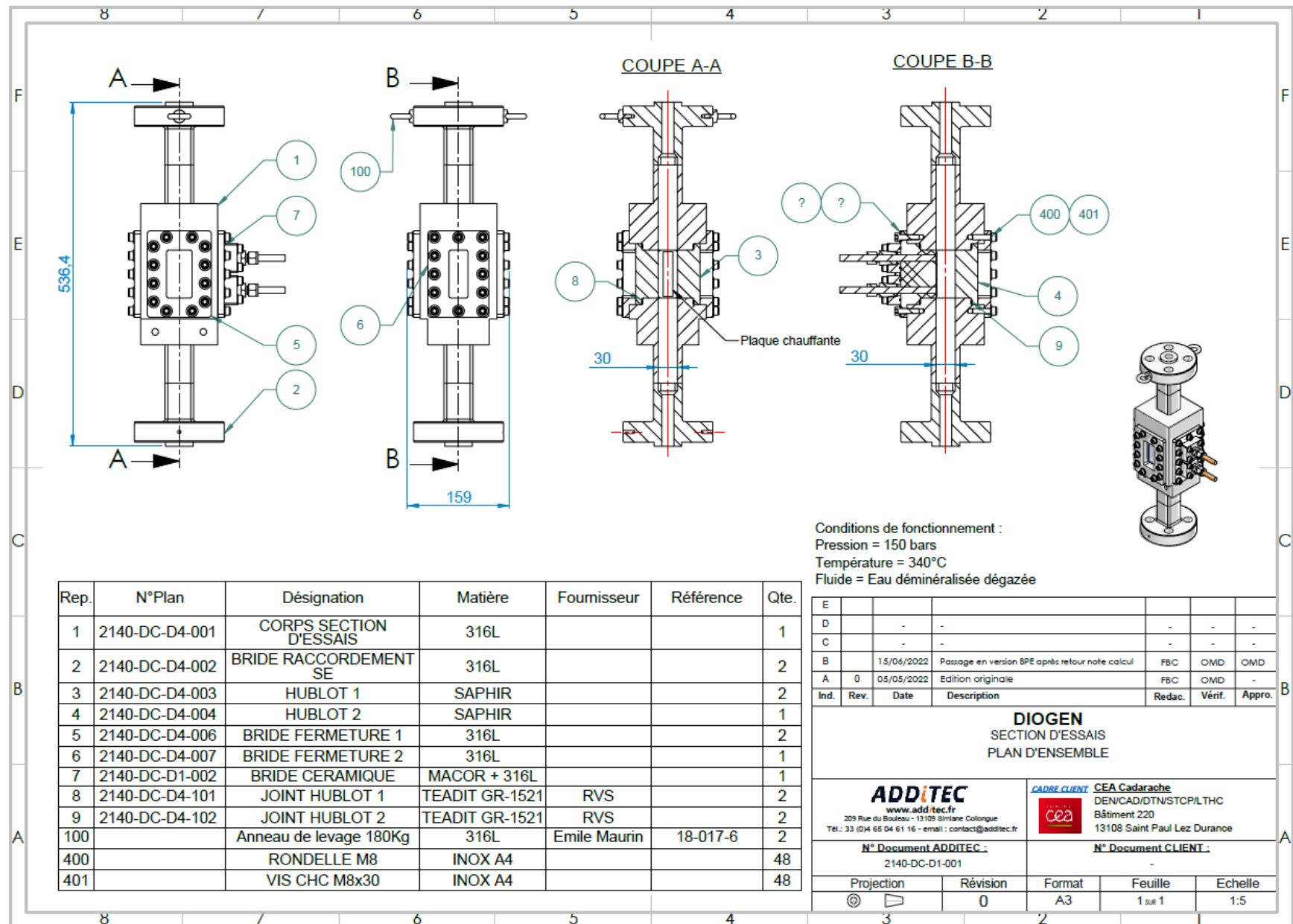


Figure 7.3: Modified test facility plan.

The MACOR flange (see Figure 7.4) allows the plate with the copper electrodes (see left Figure 7.5) to be fixed with two stainless steel plates attached directly to the MACOR flange. These plates allow the insertion of couplings to ensure watertightness around the electrodes.

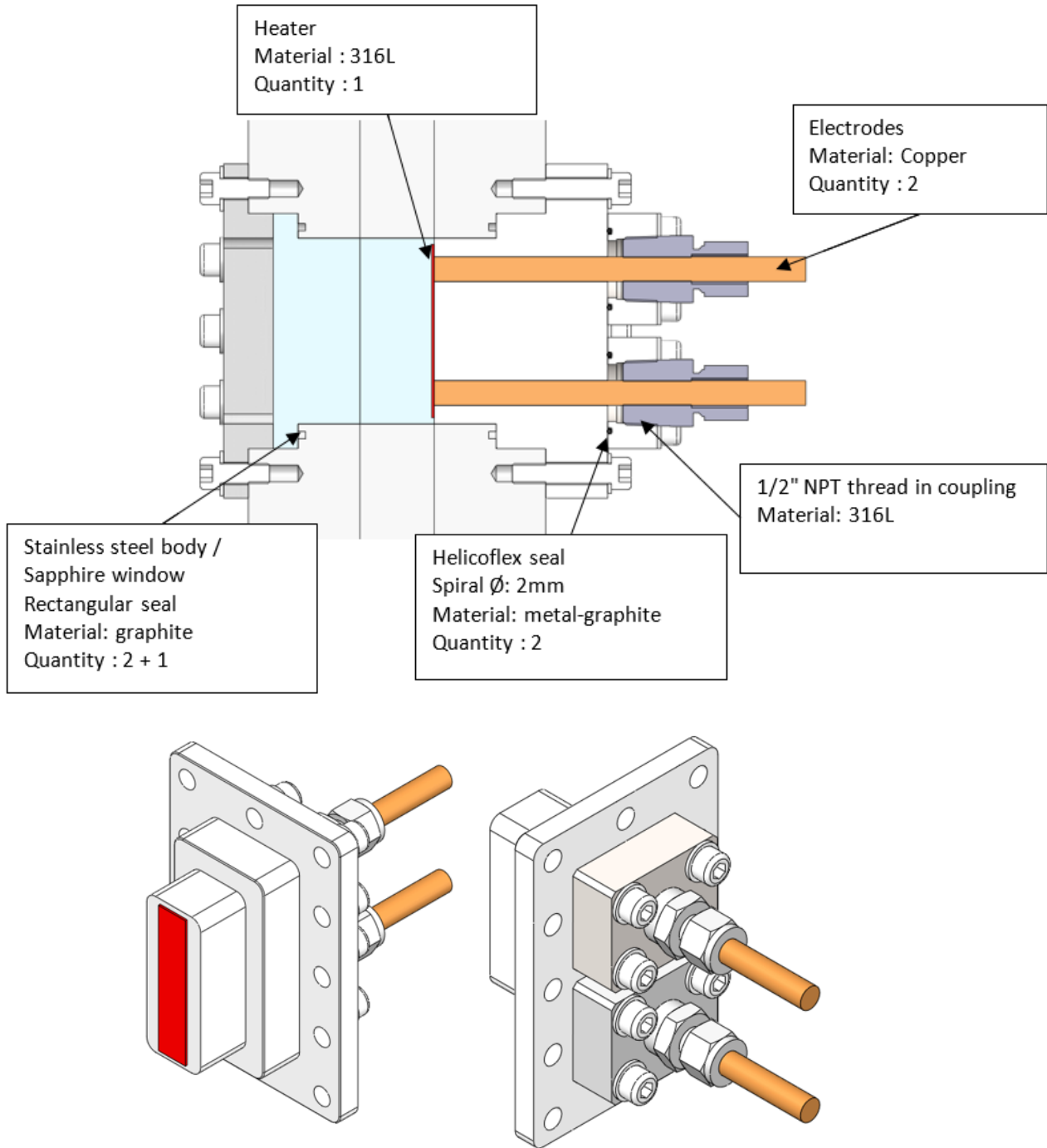


Figure 7.4: MACOR flange equipped with the heating plate.

The watertight assembly is then attached to the body of the test section to close the test section formed by the other three sapphire windows (see right Figure 7.5).

The DIOGEN test section is an equipment that is designed according to the conditions

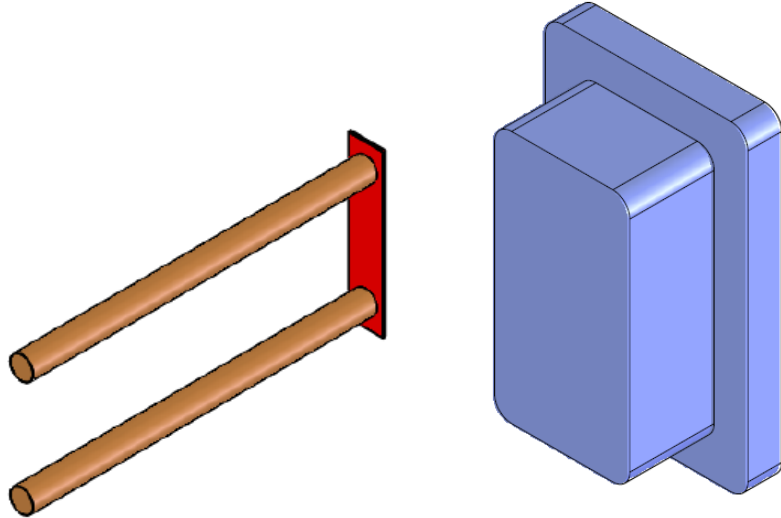


Figure 7.5: Heater design (left) and sapphire window (right).

described previously. It is therefore subject to the Pressure Equipment Directive (PED) because its design pressure is greater than  $0.5 \text{ bar}$  relative (or  $1.5 \text{ bar}$  absolute). It is therefore necessary to define the risk category to which this section belongs. This is done by means of:

- Its design pressure,
- Its volume.

The type of fluid (gas or liquid), divided into two categories:

- Category 1: includes fluids known as "dangerous",
- Category 2: includes other "non-hazardous" fluids.

The temperature must also be taken into account in order to determine the phase of the fluid, liquid or gas. In the DIOGEN section, the fluid is superheated water. The total volume of the DIOGEN section is  $0.38 \text{ L}$ .

The DIOGEN test section is therefore (Figure 7.6) in category 0, the so-called "State of the art" category. The CEA manufacturer is therefore free to define the modalities of control of its equipment.

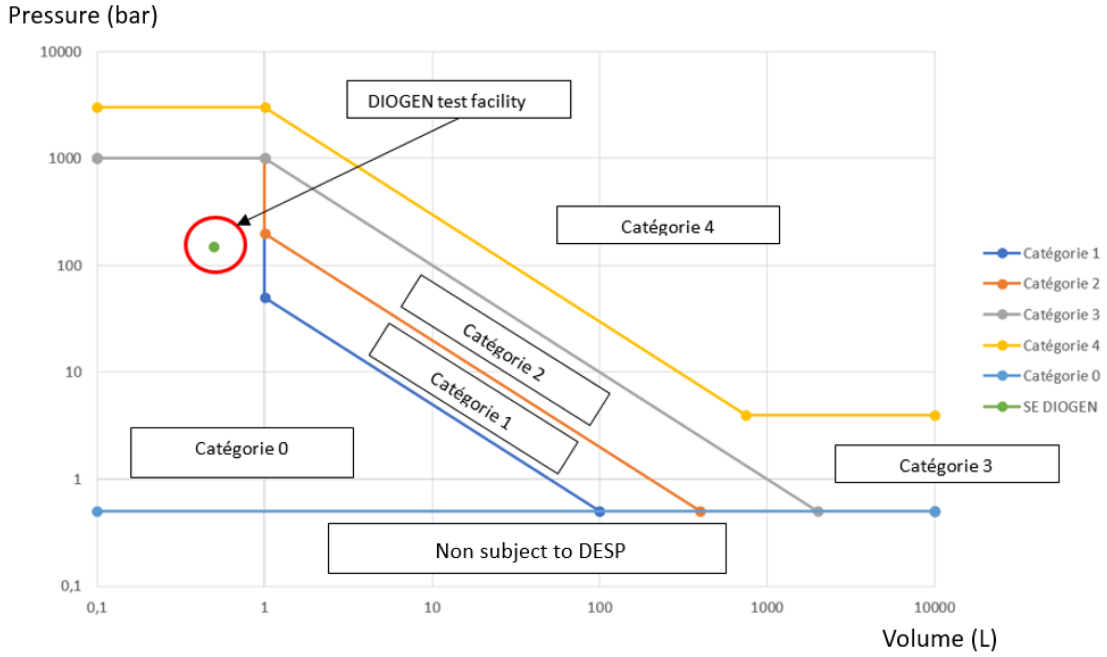


Figure 7.6: DESP category graph, stating the constraints over an ESP equipment.

### 7.2.2 Assembly and problems

All the parts were manufactured by different suppliers. The two copper electrodes were brazed to the stainless steel plate (see Figure 7.7). The body of the test section was machined from a block of 316L stainless steel, the flanges for the sight glasses were also machined from 316L stainless steel. The fitted flange was machined from MACOR, with the passages for the electrodes.

When mounting the stainless steel plates, which seal the copper electrodes, to the MACOR flange, a crack was detected when the first screw was tightened. The plates were dismantled (see Figure 7.8) to identify the origin of the break, which was identified at the threaded hole for the screw insertion.

This breakage is due to the fact that the plates must be tightened to the torque associated to the silver gasket positioned between the plate and the MACOR to ensure the seal. From the beginning of the tightening (of 25% of the required torque value) the MACOR broke, proving that this material is not adapted for our configuration. This breakage halted the possible tests with this test section.

It was decided to check the assembly of the sapphire windows by inserting them into the body (see Figure 7.9) of the facility.

The flange is then tightened to the torque imposed by the graphite gaskets allowing the sapphire to be sealed. This tightening is done in a snail-like way to impose an homogeneous stress on the sapphire. When the flange was tightened of 10% of the required torque value to the body of the test section, the sapphire window broke (see Figure 7.10). The reason for the breakage is that the window touched the stainless steel body of the test section at this point. Sapphire is a very compressive material but it does not tolerate being stressed against another material.

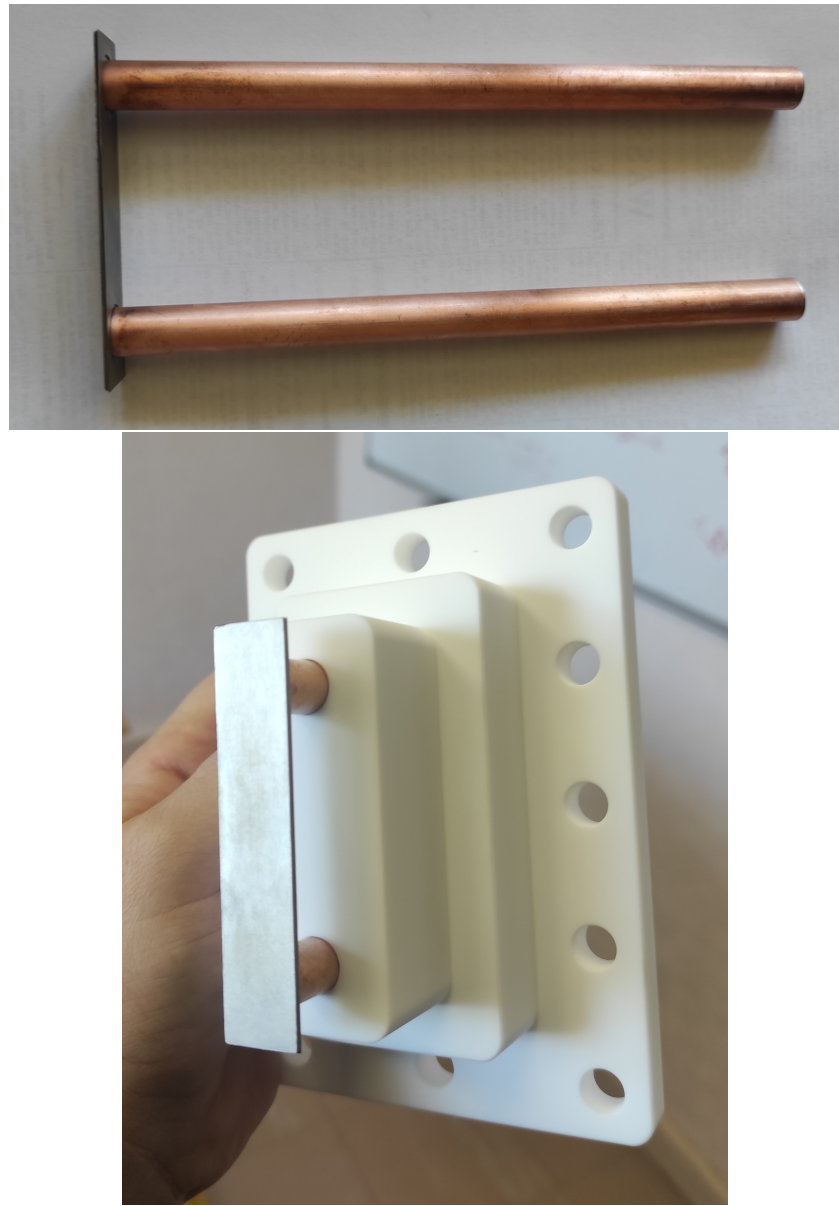


Figure 7.7: Heating plate and its two copper current inlets inserted in the MACOR flange.



Figure 7.8: Breakage of the MACOR when assembling the plates, crack observed as soon as the first screw was tightened, when disassembling a breakage was observed with the threaded MACOR.

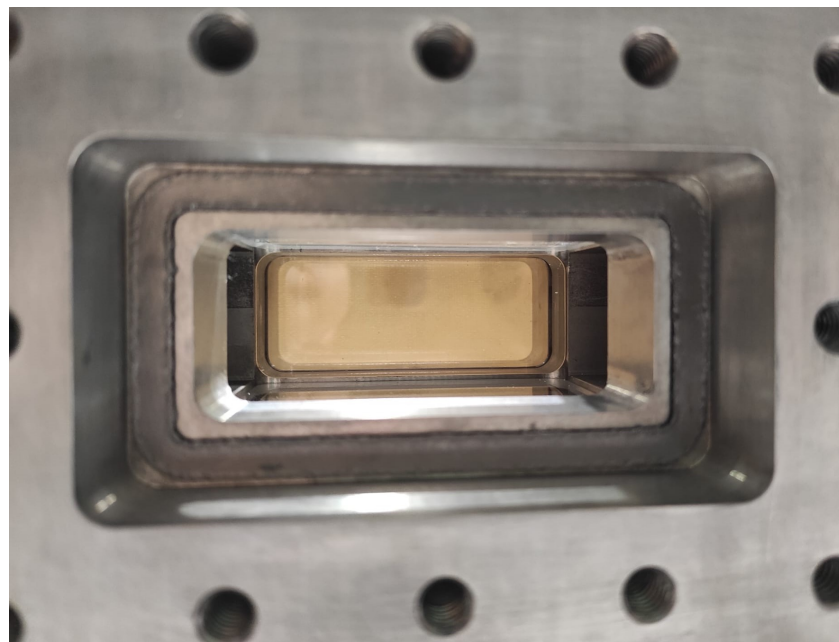


Figure 7.9: The sapphire window is fitted by inserting it into its compartment in the test section body after first inserting a gasket for sealing. The sapphire is then held in place by a stainless steel counter flange screwed to the body of the test section.

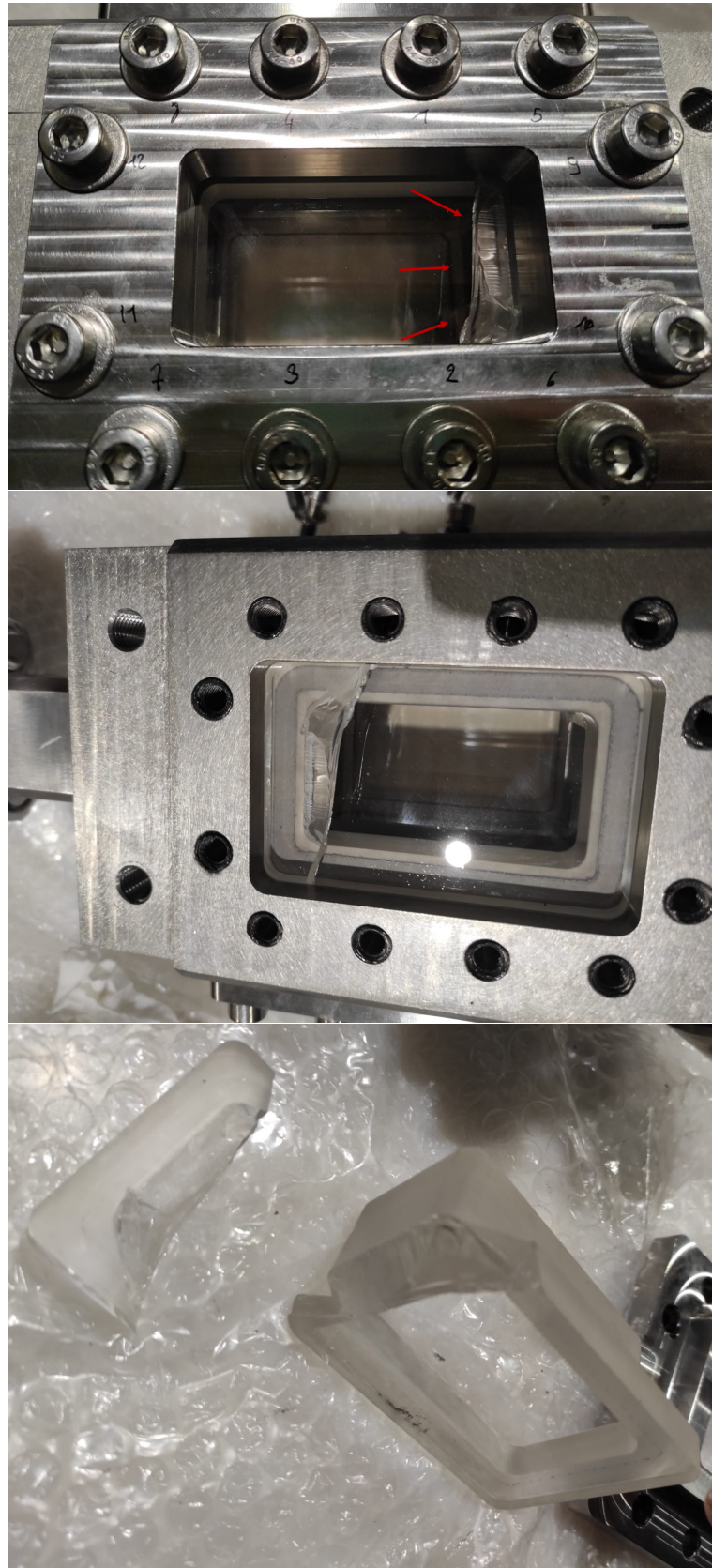


Figure 7.10: Sapphire window broken in two pieces during assembly.

## 7.3 Back-up plan

As a result of the problems encountered during the pre-assembly phase at the manufacturer's premises, it is necessary to make modifications to the parts to enable the sapphire windows to be fitted, as well as to consider an alternative solution for the heating flange. The CEA has a thermalhydraulic test loop operating at conditions of 170 bar and 350 °C on which visualisation has been performed in the past using sapphire and zirconia windows (March [4]). During these tests, the windows were circular in shape. The sapphire window was brazed on, while the zirconia window had a system to hold it in place in the sightglass holder: the pressure of the circuit was then used to press the zirconia window onto its holder to achieve a seal.

As a result, inspired by this feedback, the CEA wishes to consider an alternative "emergency" solution to be able to carry out tests, even in degraded conditions for this thesis associated with this project. The idea is to be able to visualise boiling in high pressure and high temperature conditions. The main objective of this back-up solution is no longer to perform quantitative tests but to prove that such tests (visualisation at high pressure and high temperature operating conditions) are technically feasible.

### 7.3.1 Design

The changes of the test section are presented as follows. The first step is the replacement of the MACOR flange with the heating plate with the following assembly: a unique stainless steel 316L bloc heated by three heating cartridges presented Figure 7.11.

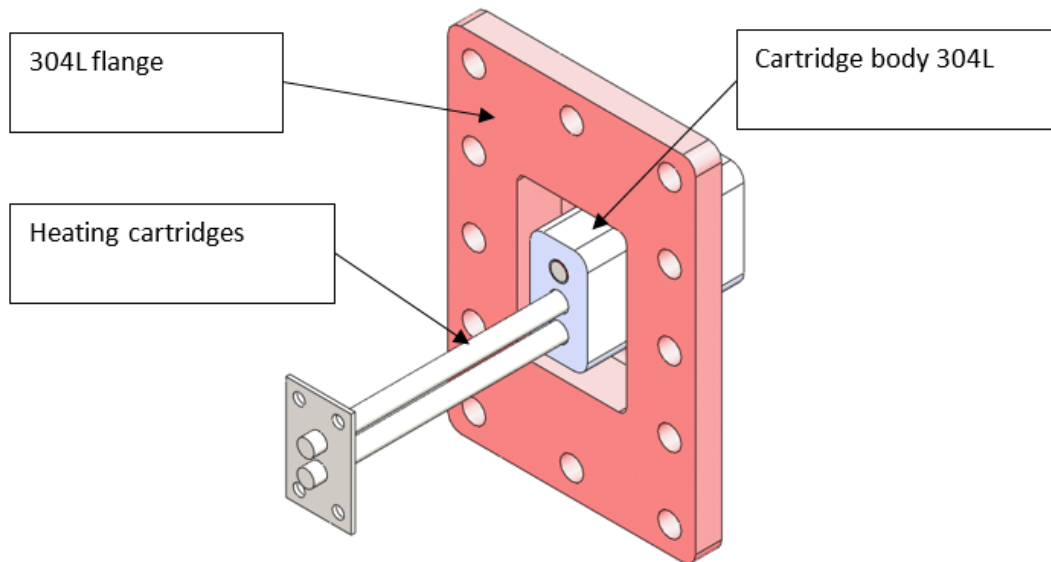


Figure 7.11: Inox heating flange.

For the mounting of the sapphire windows, the idea is to limit the stress when tightening the assembly. For this purpose, it is proposed to use previous concept using the fluid pressure to ensure the seal as presented Figure 7.12. It is then necessary to modify the body of the test section originally manufactured as well as the flanges for the sapphire windows:

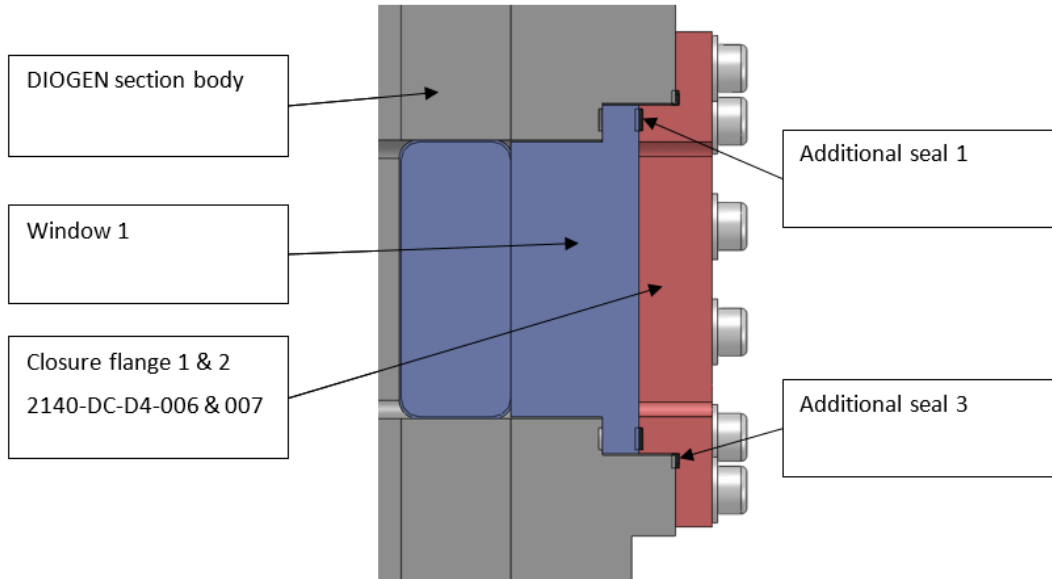


Figure 7.12: Sapphire window and new sealing strategy.

- Addition of two seal grooves in the closing flange 1 to achieve double sealing,
- Addition of two seal grooves in closure flange 2 to achieve double sealing,
- Enlarging the sapphire sightglass housings to give 0.5 mm clearance,
- Machining a flange for the heater assembly,
- Machining of a solid plate to replace the broken sapphire window. If the assembly is validated, it will be necessary to supply a new sapphire window.

The elements are then assembled on the body of the test section as shown in Figure 7.13. The heating flange is inserted with a gasket into the body of the test section and torqued to ensure a tight seal. The heating cartridges can then be inserted into the heating block. For sapphire sightglasses, a system involving two gaskets between the sapphire and the counter flange and the increase of the gaps ensure that there is no stressful contact between the sapphire and the stainless steel.

3D views of the new concept are shown Figure 7.14.

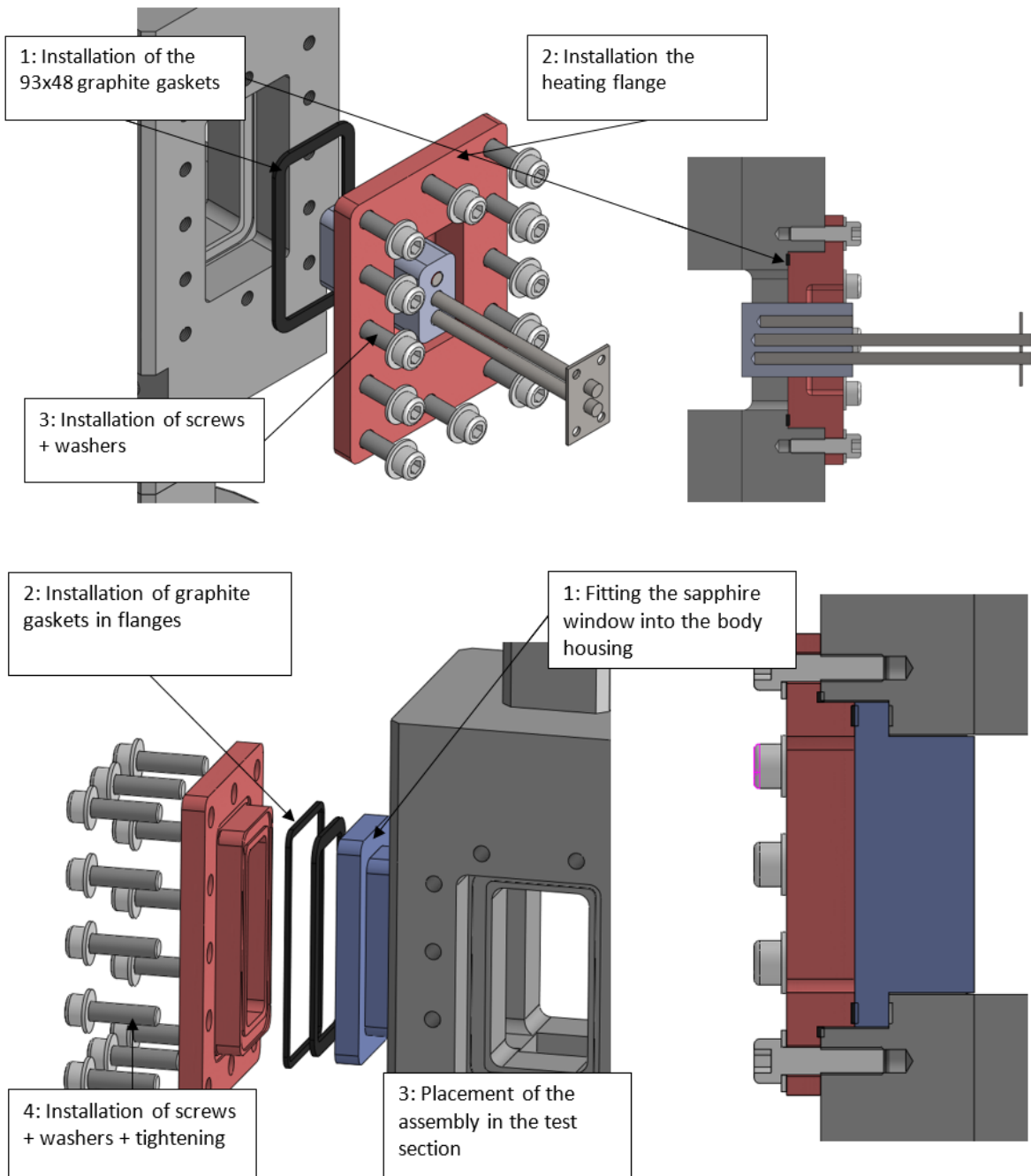


Figure 7.13: Installation of the heating flange (top) and the sapphire windows (bottom) in stages.

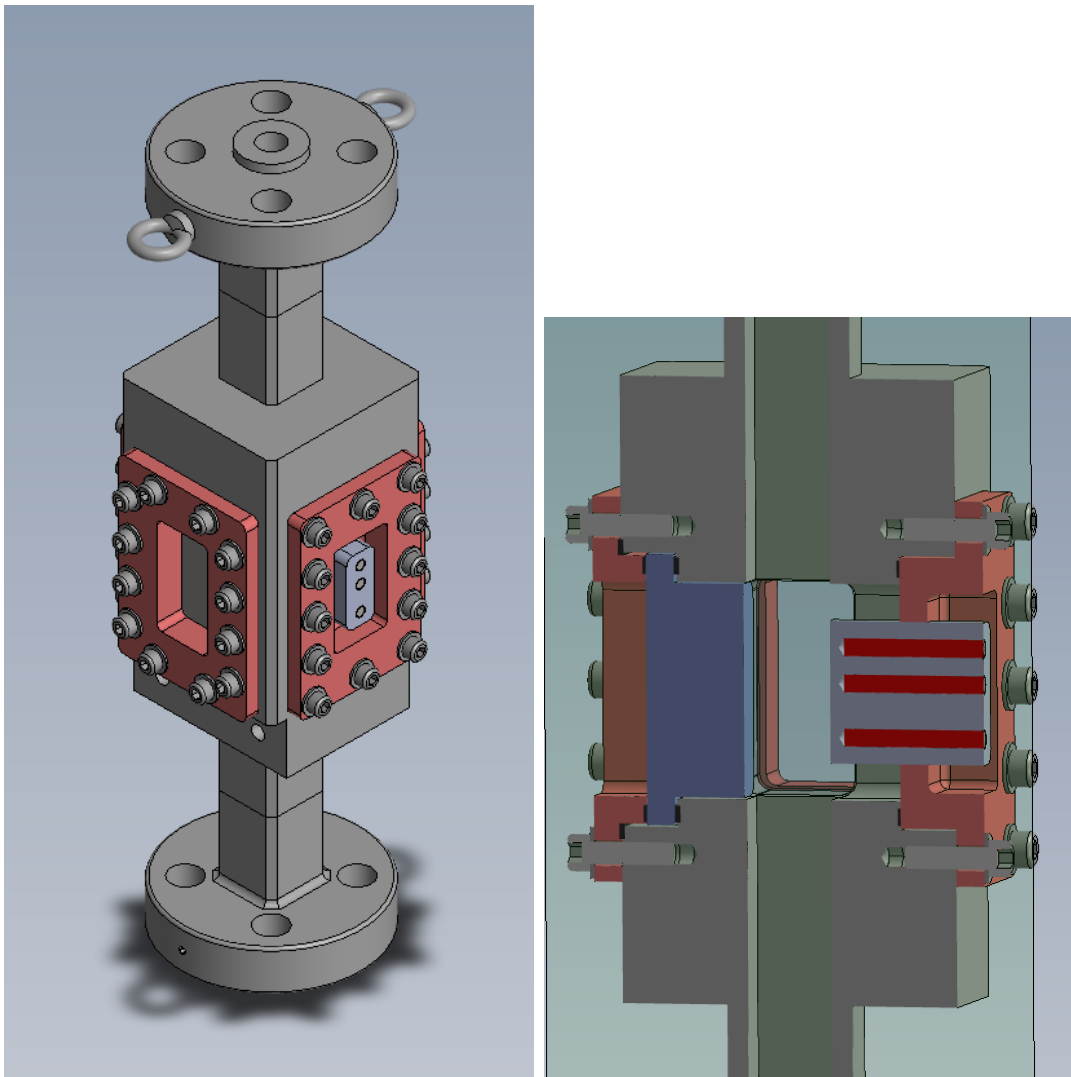


Figure 7.14: Back-up test section 3D views from the outside and cut view of the cartridges heater.

The flanges have been remanufactured to incorporate the two-gasket sealing system (see Figure 7.15). The plate to replace the broken window can be replaced later by a sapphire window if the assembly is validated.



Figure 7.15: Stainless steel plate to replace broken window and the flange remanufactured with gasket grooves to ensure sealing at the test section body and sapphire levels.

The heating flange was manufactured (Figure 7.16) from a block of stainless steel. This is a complex machining operation to allow a block heated by three cartridges to be fitted to the test section frame. The front of the block has a surface that will be in contact with the flow.

The stainless steel heating flange was inserted into the body of the test facility and

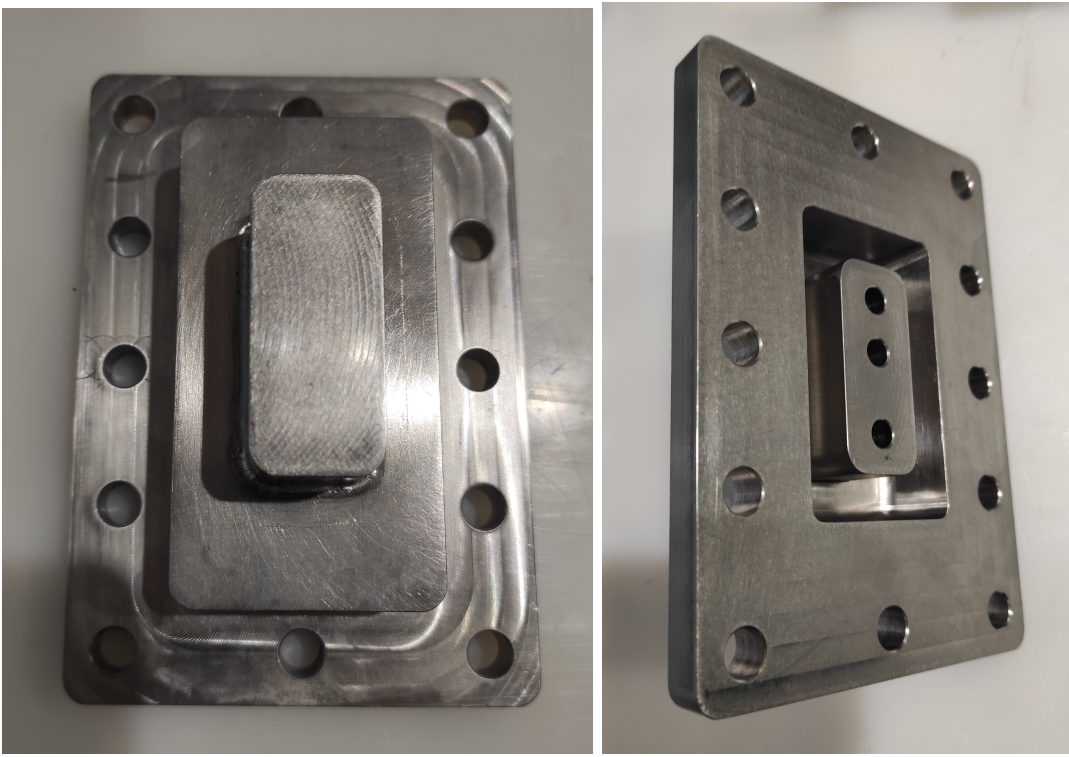


Figure 7.16: Heating flange.

torqued, along with the plate replacing the sapphire window that was broken during the first assembly. The windows were then fitted with the double gasket system described earlier (Figure 7.12). Tightening was progressive in a snail-like pattern to limit stress. With the enlargement of the sapphire inserts, the assembly was a success.

The Figure 7.17 shows the windows assembled on the body of the test section, as well as visual access to the hot plate through the remaining side window. At the time of assembly, in order to limit the risk of breaking the windows, an initial tightening test was carried out with the broken window and was successfully completed (without any additional breakage). The windows were tightened and the tightening can be adjusted according to the hydraulic test if the seal is not made.



Figure 7.17: Assembled test section DIOGEN.

### 7.3.2 Hydraulic test

Once the assembly was completed without any breakage problems, a hydraulic pressure test was carried out. The purpose of this test is to verify the mechanical strength of the entire test section up to 1.5 times the working pressure value of 150 bar. To do this, the test section is filled with demineralised water and connected to a manual pump (see Figure 7.18), which allows the test pressure to be built up gradually. This pressure increase is carried out in 25 bar steps with a 5 minute pause per step.

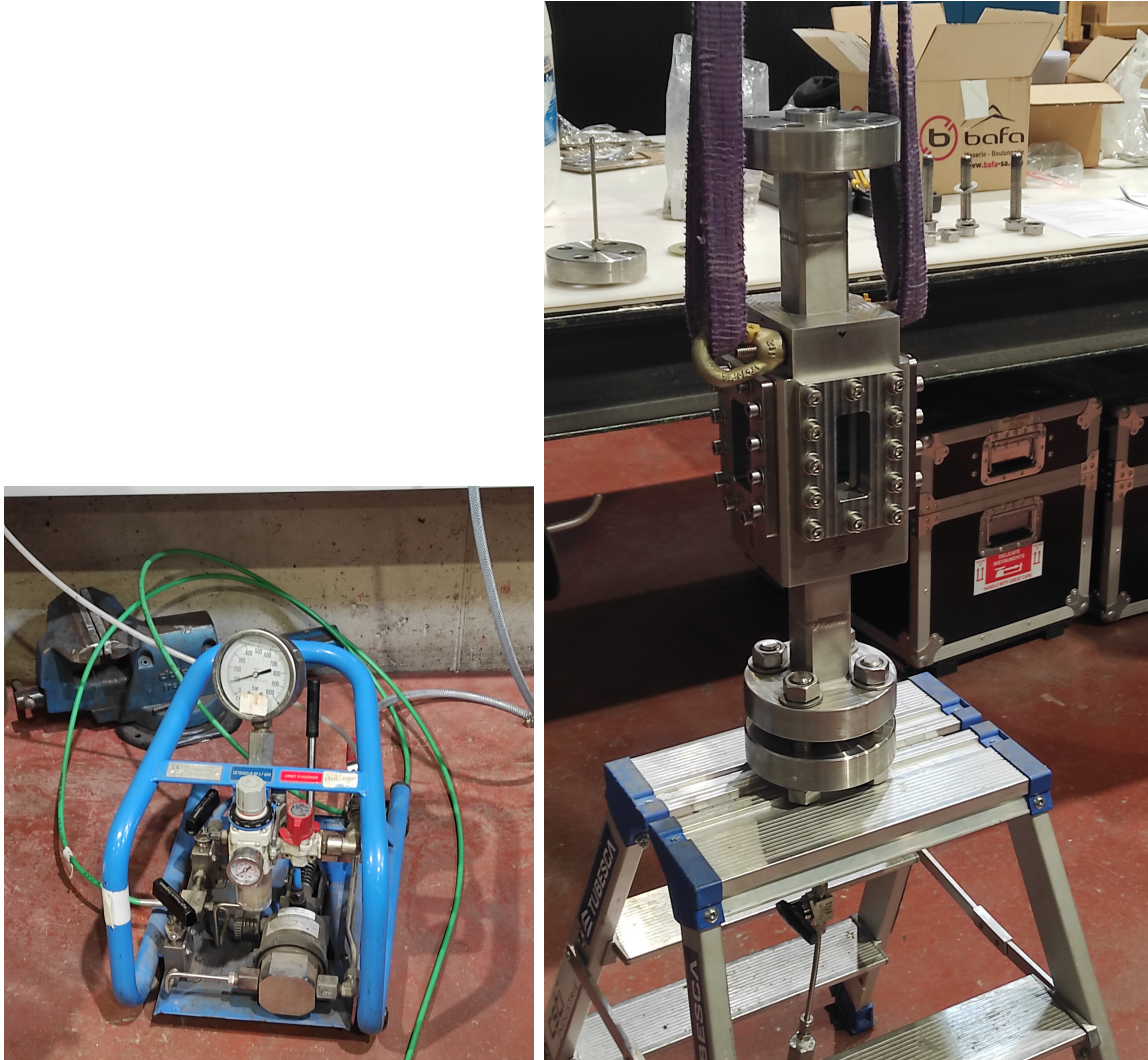


Figure 7.18: Hand pump (left) and DIOGEN test section connected (right) for the hydraulic and mechanical strength test.

An initial pressure build-up is carried out to expel the air at 1, then 3 and 6 bar. Once the air was expelled, the first stage of 25 bar is reached. Leaks are noted at the side window (see Figure 7.19).

Tightening was progressively increased to 25 N.m. The pressure steps are then carried out, with a persistent but reduced leak on the windows. For each step, a 5 minutes stop time is taken with a pressure drop measurement summarised in the Table 7.2.

At 220 bar and above, a significant leakage is noted at the seal between the stainless

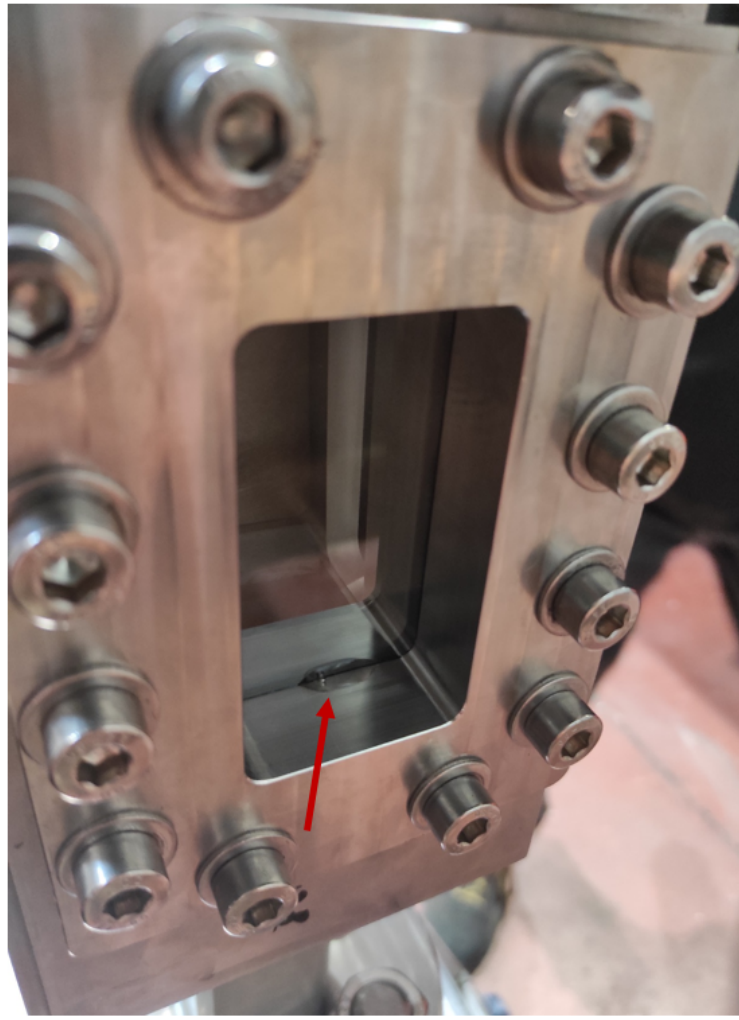


Figure 7.19: Leak on the sapphire window during hydraulic test.

Table 7.2: Hydraulic tests: pressure drop.

Step	Initial pressure [bar]	Pressure after 5 min [bar]	Pressure drop [bar]
[‐]			
1	51	47	4
2	102	92	10
3	151	131	20
4	175	164	11
5	203	185	18

steel flange and the body of the test section. The 225 bar level was then reached despite the significant leakage to check the mechanical stability of the test section and in particular the sapphire windows. No deformation was observed in the entire test section and no defects

were found in the sapphire windows.

After this step, the pressure was lowered to 100 bar to dry the test section, no leakage was observed at the windows. A final stage at 150 bar was carried out, with a wait of 30 minutes, a leak persisted at the windows but provided one drop within the waiting time. The pressure drop in 30 minutes static is 15 bar. This watertightness defect was judged acceptable for our use.

Once the mechanical strength of the test section was validated, the test section DIOGEN could be installed on an existing loop at the CEA to provide the desired thermal hydraulic conditions: BIKINI. BIKINI is a thermal hydraulic installation with a wide range of operative conditions up to the primary conditions of a PWR. It allows the implementation of test sections with upward or downward flow. The pressurisation of this installation is ensured by a thermal pressuriser.

A first water start-up was carried out with a pressurisation of the whole installation to check the global leakage. The circuit is first drawn to vacuum for the filling phase. Once the circuit is filled with water, the drains at the primary pump and the water level are opened to evacuate the air. A charge pump is then activated and the pressure is gradually built up to the system operating pressure of 150 bar. During this pressure build-up, the DIOGEN mock-up behaved as expected: no deformation or breakage of the windows. A leakage persists at low pressure as observed during the mechanical resistance test, but it decreases when the pressure increases: the pressure of the fluid increases the compression of the gaskets, ensuring the sealing. Several leaks were detected on the BIKINI loop at the level of valves or sensors which were tightened. The validation criterion for the leakage test is a pressure drop of less than 4 bar in 10 minutes. The test was successfully completed with a loss of 3.2 bar in 10 minutes. That has completely validated the test section allowing to perform real tests. Figure 7.20 shows the implementation of the DIOGEN setup on the experimental facility BIKINI.

Actions such as the wiring of the heating cartridges, as well as the installation of the thermal insulation could then be carried out.



Figure 7.20: DIOGEN test section implemented on BIKINI installation.

## 7.4 New test matrix

The new test section no longer has three windows but only two: one in front of the heating window and one on the side. This new configuration, presented in Figure 7.21, does not allow for the shadowgraphic setup originally planned. Nevertheless, the visualisation with front lighting should give readable images at least to investigate from a qualitative point of view the influence of the pressure on the flow structure in the vicinity of the heater plate.

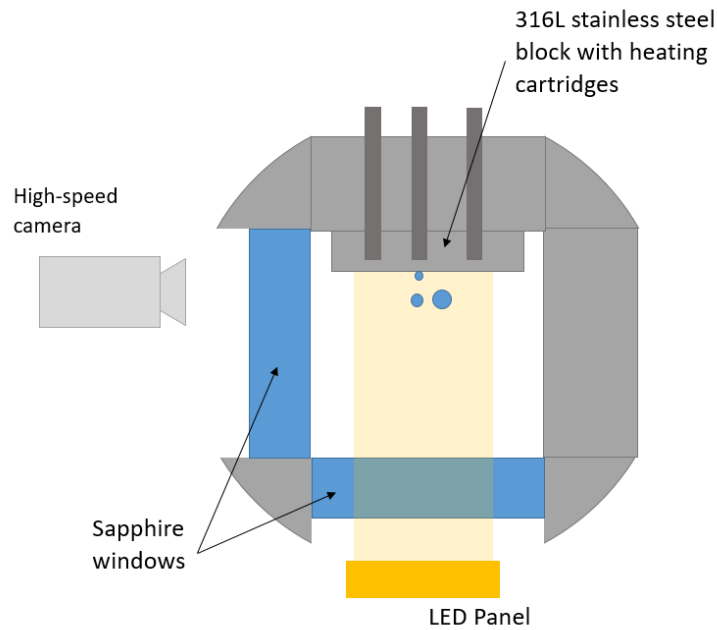


Figure 7.21: New visualisation configuration with the back-up test section.

An adapted test matrix is then proposed for this first campaign on BIKINI, compared to the one initially planned and described in Section 7.1.

Table 7.3: Adapted test matrix for BIKINI/DIOGEN test campaign.

Test	Pressure	Subcooling	Saturation temperature	Inlet temperature	Mass velocity	Targeted boiling point
[ - ]	[ bar ]	[ °C ]	[ °C ]	[ °C ]	[ kg/m².s ]	[ - ]
1	40	20	250	230	2000	ONB
2	40	10	250	240	2000	ONB
3	60	20	275	255	2000	ONB
4	60	10	275	265	2000	ONB
5	70	20	285	265	2000	ONB
6	70	10	285	275	2000	ONB
7	80	20	295	275	2000	ONB
8	80	10	295	285	2000	ONB
9	100	20	310	290	2000	ONB
10	100	10	310	300	2000	ONB
11	120	20	325	305	2000	ONB
12	120	10	325	315	2000	ONB

The conditions are restricted in order to be able to observe nucleated boiling on the surface of the block heated by the heating cartridges for several pressure values. For each of the thermal hydraulic conditions presented in Table 7.3, power will be injected gradually from the cartridge heaters to reach the ONB then to go on to reach higher void fraction (close to the OSV).

This first campaign should demonstrate the feasibility of high pressure, high temperature measurements, but also provide initial qualitative results on nucleate boiling at low and high pressure. If this campaign is successful, it will be the first step towards a device allowing shadowgraphic and thermographic measurements to be made and answering the questions raised in this manuscript.

## 7.5 Test campaign

The DIOGEN model was installed on the BIKINI thermal hydraulic installation at CEA Cadarache (Figure 7.20). The optical setup with a high-speed, high-precision PHOTRON V2640 camera and a macro lens was positioned grazing the heating block. This camera has  $13.5\ \mu m$  pixel size and a resolution of *12 bits*. Its minimum frequency is  $100\ Hz$  up to  $6600\ Hz$  in full frame ( $4\ Mpxl$ ). A collimated LED light was positioned on the same side of the test section, above the camera and with a slight angle of incidence (see Figure 7.22).

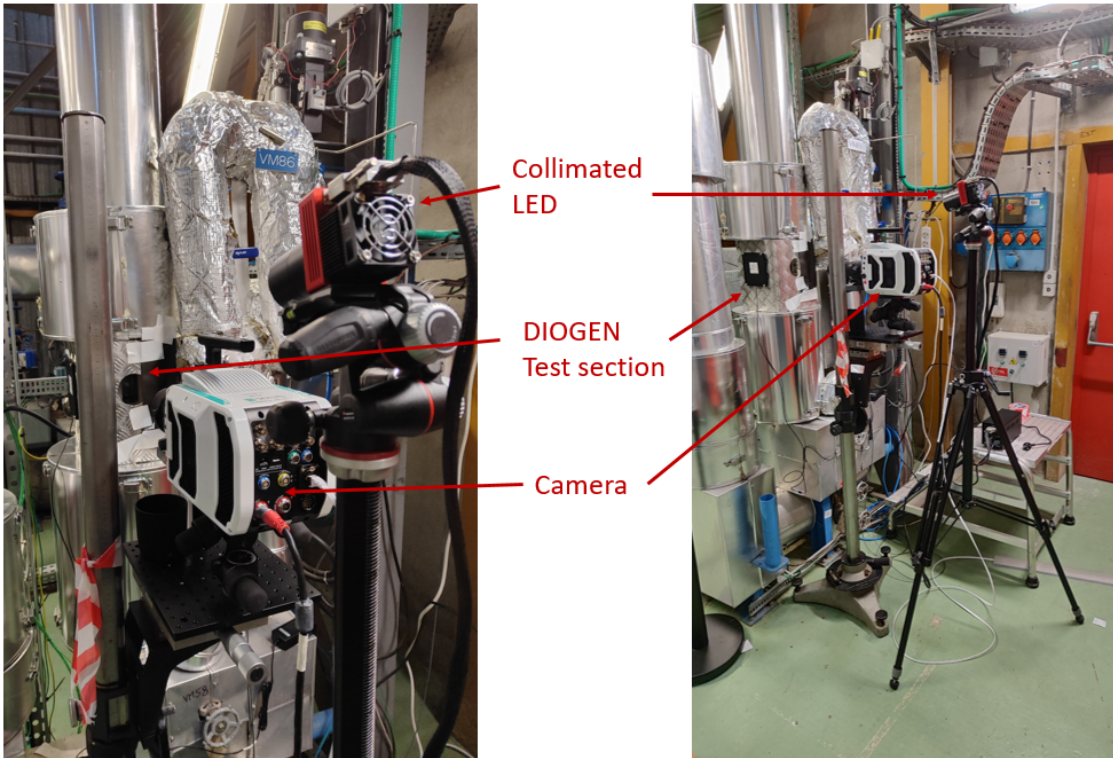


Figure 7.22: Visualisation configuration and optic setup with the back-up test section.

The pressure in BIKINI is controlled by a thermal pressuriser: a heating rod heats the water in the pressuriser and increases the pressure in the circuit. The pressuriser then acts as a pressure stabiliser with a vapour phase and a liquid phase which are adjusted in real time

using the heating rods. The installation is said to follow precise temperature rise procedures: to avoid leakage problems due to differential expansion the temperature in the circuit can rise by  $15^{\circ}\text{C}/\text{h}$ .

The test matrix was followed to make the first points. However, the heating system proved to be faulty: the flange was heated faster than the front of the block where boiling was expected to occur. The boiling was therefore triggered in a corner of the test section and not on the block. A simulation using Ansys Fluent (Figure 7.23) confirmed that the power injected by the heating cartridges does not reach the targeted area.

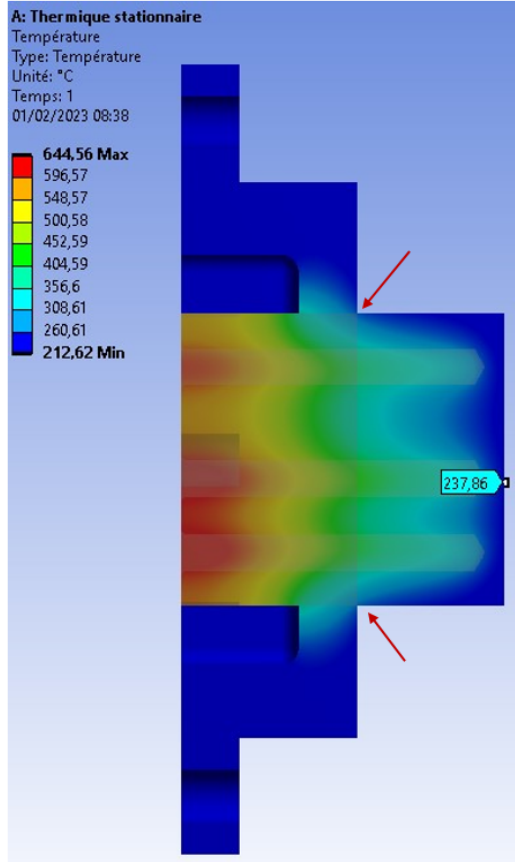


Figure 7.23: Result of the Ansys Fluent modelling of the heating flange. The power injected through the cartridges is fixed at  $300\text{ W}$ , the boundary conditions were imposed as natural convection with an exchange coefficient of  $10\text{ W/mK}$  with the surrounding air. The flange heats up faster on the inner edges (see red arrows) than on the face of the heating block.

Boiling could therefore not be observed for the lowest pressure of the test matrix. However, visualisation was possible at higher pressure, in particular at  $120\text{ bar}$ . The subcooling could be reduced to the minimum value allowed by the system (a safety device for the pump prevents approaching saturation). This allowed boiling to take place on the heating block. Two types of recordings were carried out, with a full frame of  $2048 \times 1952\text{ pxl}$  allowing the recording at  $6600\text{ i/s}$  (Figure 7.24) and with a smaller window of  $768 \times 480\text{ pxl}$  allowing to go up to  $28000\text{ i/s}$  (Figure 7.25). The capacity of the camera allows to go beyond this speed but the brightness capacity of the optical setup was limiting.

$$P = 120 \text{ bar} \quad Q = 1,21 \text{ m}^3/\text{h} \quad T_{in} = 321^\circ\text{C}$$

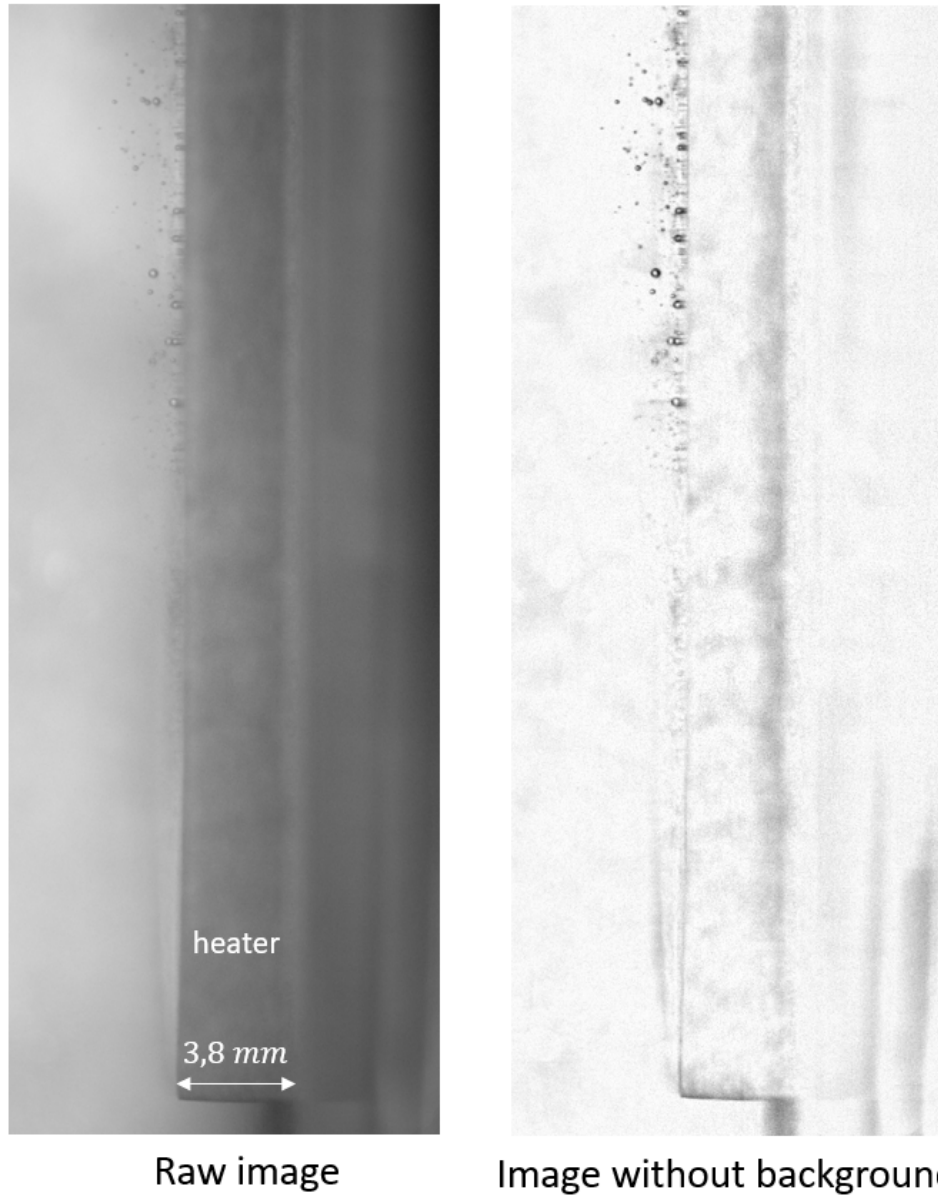


Figure 7.24: Example of a full frame image  $2048 \times 1952 \text{ ppxl}$  with  $6600 \text{ i/s}$  record for:  $P = 120 \text{ bar}$ ,  $Q = 1.21 \text{ m}^3/\text{hr}$ ,  $T_{in} = 321^\circ\text{C}$  corresponding to a subcooling of  $\Delta T_{sub} = 3.7^\circ\text{C}$ . Raw image (left) and image without background (right).

$$P = 120 \text{ bar} \quad Q = 1,21 \text{ m}^3/\text{h} \quad T_{in} = 321^\circ\text{C}$$

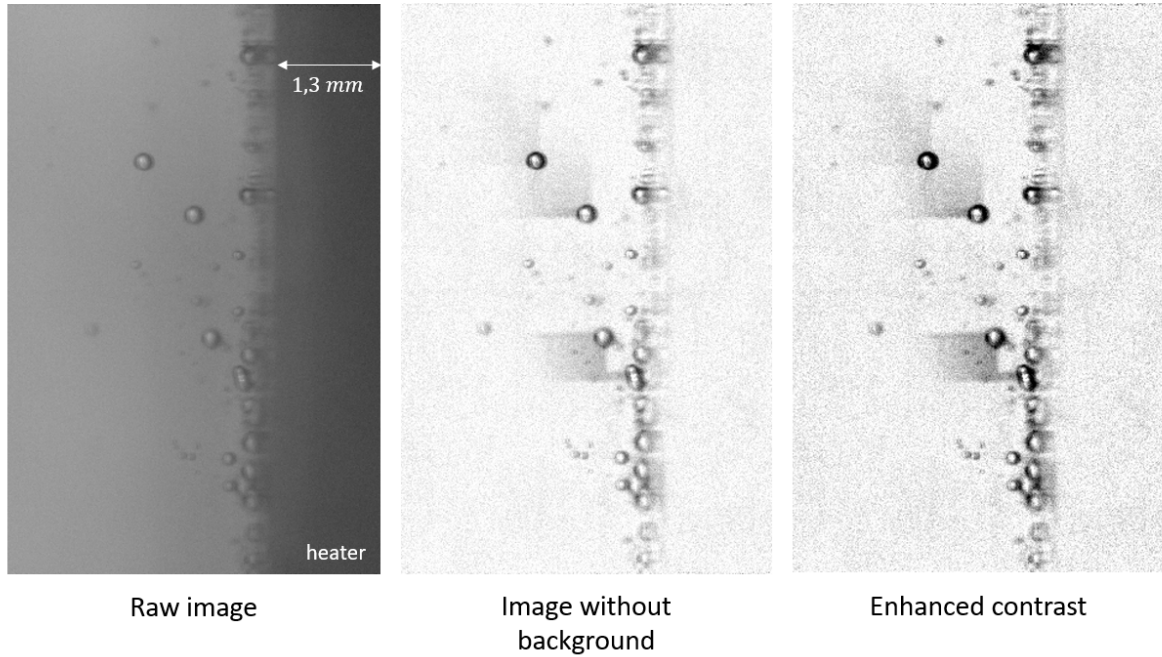


Figure 7.25: Example of a reduced frame image  $768 \times 480 \text{ pxl}$  with  $28000 \text{ i/s}$  record for:  $P = 120 \text{ bar}$ ,  $Q = 1.21 \text{ m}^3/\text{hr}$ ,  $T_{in} = 321^\circ\text{C}$  corresponding to a subcooling of  $\Delta T_{sub} = 3.7^\circ\text{C}$ . Raw image (left), image without background (center) and enhanced contrast image (right).

The images obtained show several weaknesses that prevent from performing quantitative measurements. Firstly, the depth of field of a macroscopic lens constrains the visualisation in a reduced plane and limits the possibility to see bubbles at their nucleation site. Indeed, bubbles can be created outside the focal plane and appear after having been detached by re-entering the plane. It can be seen in the Figure 7.26 that bubbles are present but are not sharp and therefore cannot be measured. In this example, a bubble is discerned against the heated wall but cannot be detected, this bubble then moves into the focal plane and can be identified. Several bubbles appear when entering the focal plane or disappear when leaving it. This complicates the visualisation and measurements. Adapted lenses with larger focal planes should be considered for future tests.

$$P = 120 \text{ bar} \quad Q = 1,21 \text{ m}^3/\text{h} \quad T_{in} = 321^\circ\text{C}$$

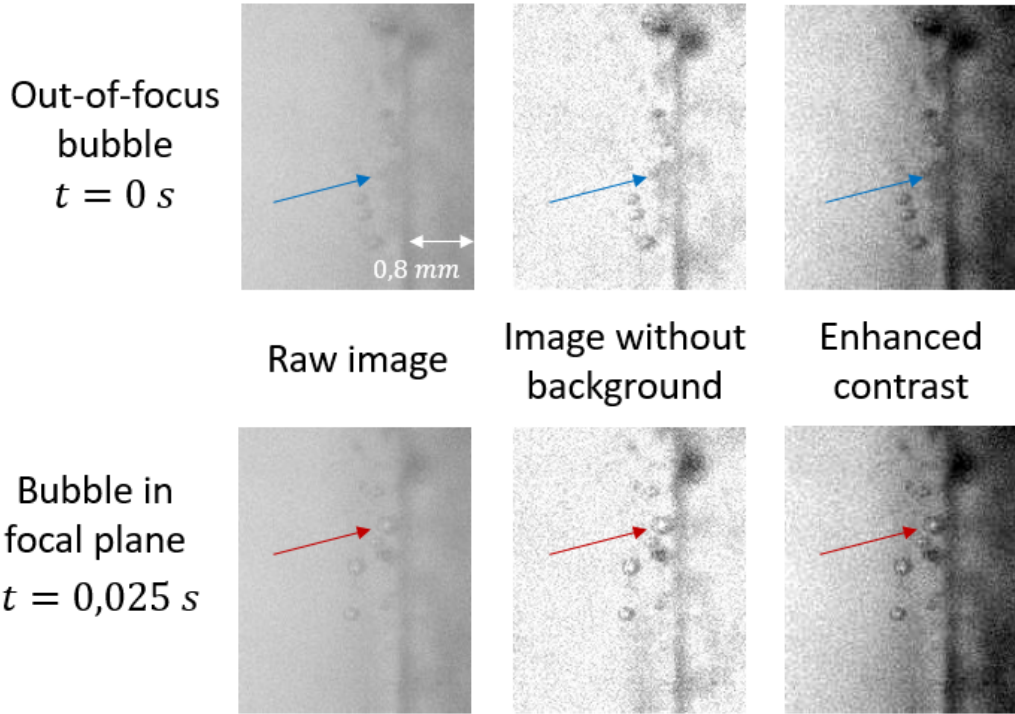
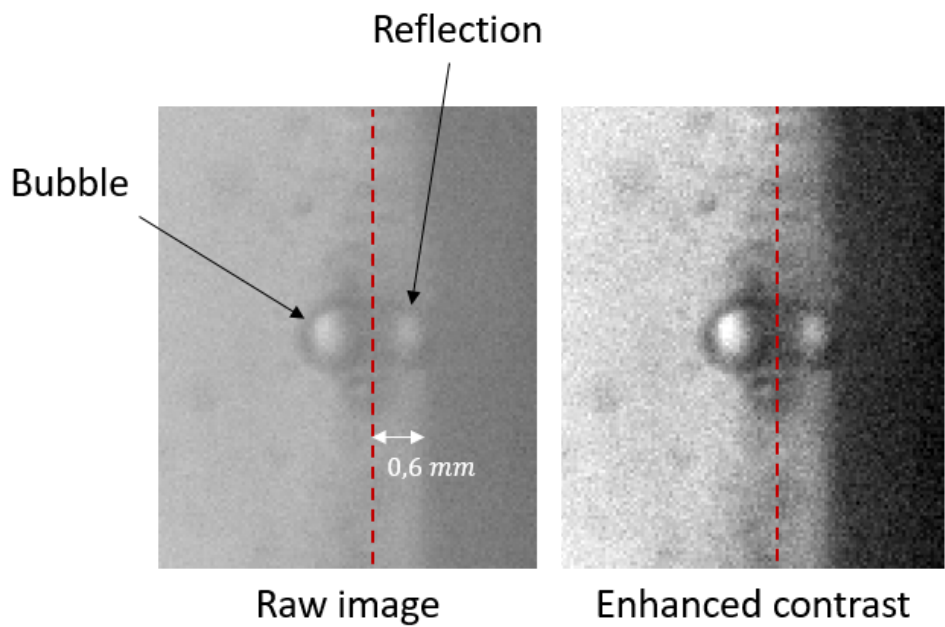


Figure 7.26: Bubble out of focal plane (top) appearing in plane (bottom) for:  $P = 120 \text{ bar}$ ,  $Q = 1.21 \text{ m}^3/\text{h}$ ,  $T_{in} = 321^\circ\text{C}$  corresponding to a subcooling of  $\Delta T_{sub} = 3.7^\circ\text{C}$ . Raw images (left), images without background (center) and enhanced contrast images (right).

In addition, as the lighting is on the same side as the camera but at a different angle, many reflections are noticed on the wall and the bubbles. The same phenomenon that was noted during the low pressure tests to characterise the optical system (Chapter 6) appears in these images. A near wall mirror effect is noted (see Figure 7.27), in this image two bubbles can be identified but only one really exists, the other is a reflection of the first on the plate. This effect is enhanced here by the incidence angle of the light source but can also be associated with distortions due to the near wall temperature gradient. This mirror effect causes a loss of information in the near wall (over  $0.6 \text{ mm}$  in this image) and an accentuated blurred area in the near wall which contributes to the difficulty of visualising a bubble at a nucleation site. These near-wall phenomena constitute what is referred to in the literature as a mirage effect: one cannot tell whether the bubble is still attached to the wall or not. This echoes to Chapter 6, a calibration system should allow to limit this distortion effect over measurements. Several ideas could arise with a shadowgraphic configuration. One of them is to create a test pattern directly on the sapphire window in the back of the system (window the nearest to the LED panel) or to use a projection of a test pattern on the heater. All these elements strongly limit the ability of visualising a bubble at its nucleation site in this degraded configuration (inability to perform shadowgraphic measurements).



$$P = 120 \text{ bar} \quad Q = 1,21 \text{ } \text{m}^3/\text{h} \quad T_{in} = 321 \text{ } ^\circ\text{C}$$

Figure 7.27: Near wall mirror effect with a symmetry axis (red dashes) close to the wall (0.6 mm) for:  $P = 120 \text{ bar}$ ,  $Q = 1.21 \text{ } \text{m}^3/\text{h}$ ,  $T_{in} = 321 \text{ } ^\circ\text{C}$  corresponding to a subcooling of  $\Delta T_{sub} = 3.7 \text{ } ^\circ\text{C}$ . Similar effect detected on the low pressure vessel tests presented in Chapter 6.

Nevertheless, several observations could be noted. Firstly, several coalescence phenomena could be captured in the near wall. An example is given in Figure 7.28. Two bubbles close together become one larger bubble. This phenomenon appears several times for our high pressure conditions. Secondly, as presented in the literature review Chapter 1, the phenomenon

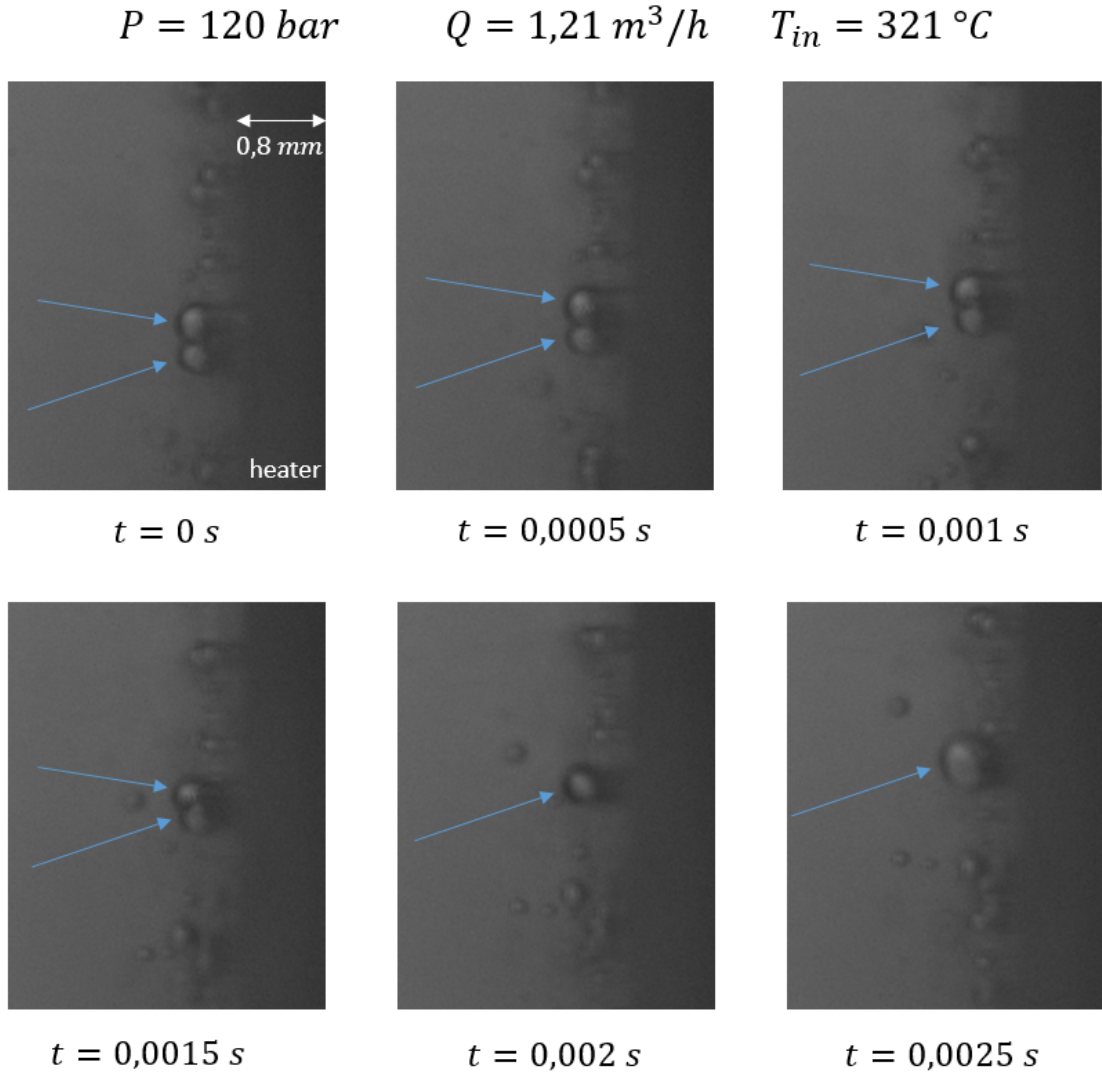


Figure 7.28: Coalescence phenomenon between two bubbles observed for:  $P = 120 \text{ bar}$ ,  $Q = 1.21 \text{ m}^3/\text{h}$ ,  $T_{in} = 321^\circ\text{C}$  corresponding to a subcooling of  $\Delta T_{sub} = 3.7^\circ\text{C}$ .

of sliding on the wall of a bubble was observed on several occasions. This phenomenon, of which an example is given in Figure 7.29, is very frequent in the configurations that were studied during this test campaign. A bubble can slide up the entire length of the heating plate without detaching from it (identified on a full frame image). Bubble size models based on this phenomenon are therefore worth analysing and may provide answers to the disparities in detachment bubble diameter measurements.

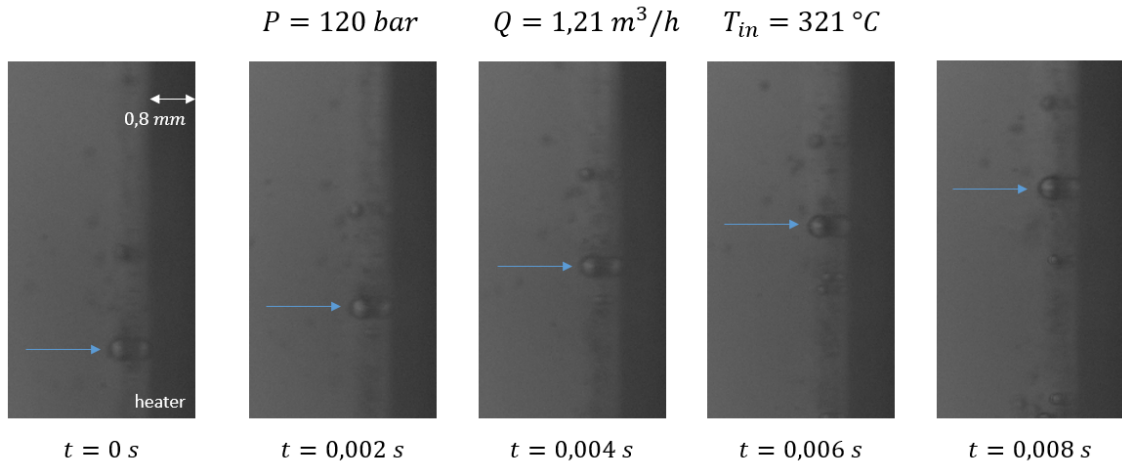


Figure 7.29: Bubble sliding on the plate (going  $3.5 \text{ cm}$ ), phenomenon captured for:  $P = 120 \text{ bar}$ ,  $Q = 1.21 \text{ m}^3/\text{h}$ ,  $T_{in} = 321^\circ\text{C}$  corresponding to a subcooling of  $\Delta T_{sub} = 3.7^\circ\text{C}$ .

Finally, a particular phenomenon was observed several times during the tests. A bubble detaches itself from the wall, moves forward in the flow and comes back to rest against the wall before detaching itself again. An example of the observation of this phenomenon is shown in Figure 7.30. The observation of this rebound in the wall was observed on several occasions during the tests. The degraded configuration used for these tests does not allow us to conclude at this stage, but similar observations have been made in some DNS (Direct Numerical Simulation) simulations of boiling flow.

$$P = 120 \text{ bar} \quad Q = 1,21 \text{ m}^3/\text{h} \quad T_{in} = 321^\circ\text{C}$$

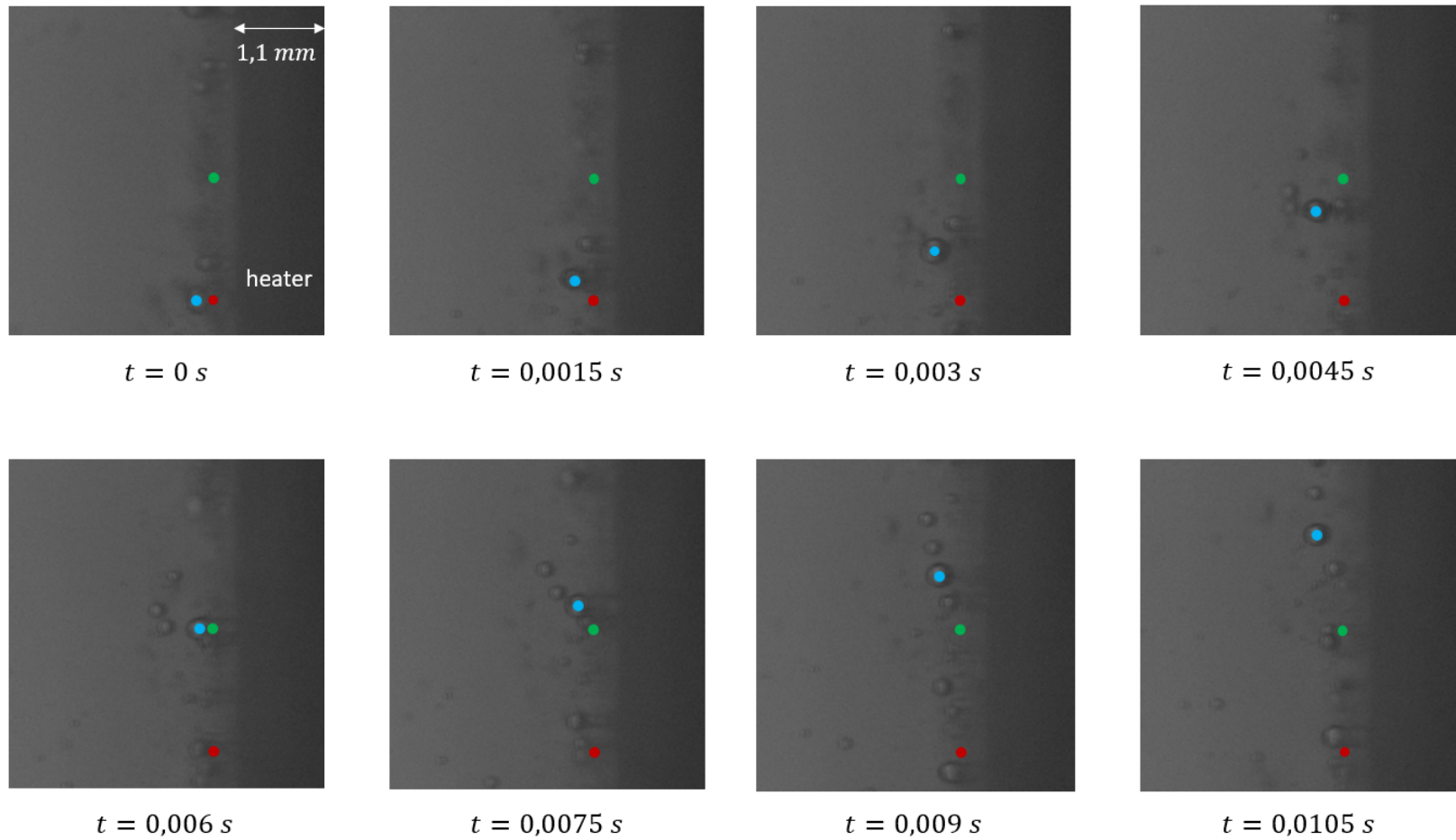


Figure 7.30: Observation of a bubble (blue dot) detaching from the wall (red dot) and reattaching to the wall (green dot) before detaching again. This visualisation was made for:  $P = 120 \text{ bar}$ ,  $Q = 1.21 \text{ m}^3/\text{h}$ ,  $T_{in} = 321^\circ\text{C}$  corresponding to a subcooling of  $\Delta T_{sub} = 3.7^\circ\text{C}$ .

The observations made here cannot lead to firm statements or quantitative measurements. Indeed, the test section used was carried out as a back-up and the boundary conditions are not mastered. The heating block inserted with the flange, described in Figure 7.31, shows a deflection before the camera field.

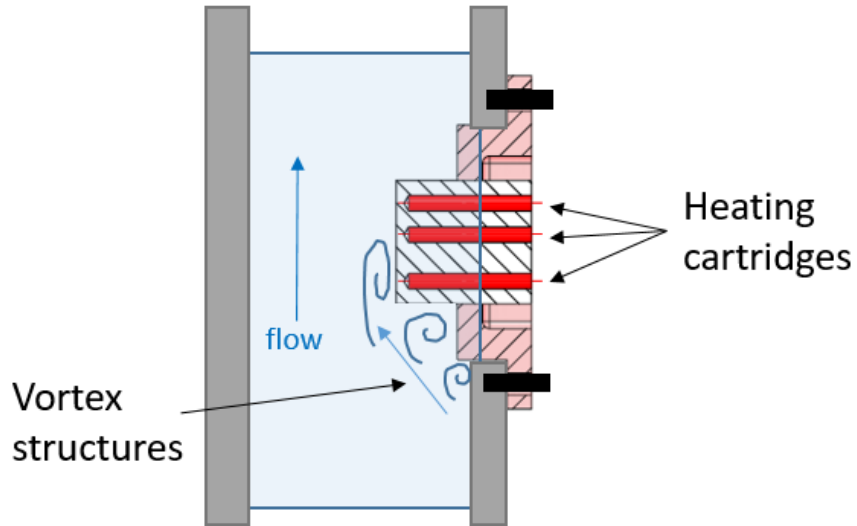


Figure 7.31: Schematic diagram of the test section depicting the deflection of the heating plate and its impact on the flow.

This upward step disrupts the flow, with vortex structures being released and disrupting the boiling on the wall. These structures could be identified with a strange bubble displacement: bubbles in the flow can be seen distinctly circling as these structures pass along the heated wall. It was also observed that a release of a colder water structure can pull all the bubbles away from the wall and there is a delay before boiling reappears. The upward flow in the test section is therefore not stationary, not controlled and well known. Observations such as bubbles sticking to the wall may be due to the particularities of this flow.

Nevertheless, this degraded test section allowed us to carry out visualisation at high pressure and to identify some phenomena known in the literature. These initial tests suggest that high pressure measurements will be feasible with a complete model (possibility of making measurements using shadowgraphy and a high-performance heating system).



# Conclusion and future prospects

## Conclusion

Boiling crisis is a phenomenon that can affect the safety of nuclear reactors. Unfortunately, despite more than 50 years of research, the physical mechanisms involved are not yet fully understood. This work aims to study nucleate boiling in order to understand the underlying physics leading up to DNB triggering. To achieve this goal, particular attention is drawn to phenomena occurring in the vicinity of the heated wall, and characterisation of the detachment bubble diameter, the detachment frequency and the nucleation site density is of prime importance. In terms of modelling, those parameters (combined in the so-called wall heat flux partitioning model) are highly sensitive in the two-fluid model, which currently is the state of the art model for multiphase flows. Therefore, being able to measure them as accurately as possible is a major step towards accurate modelling of nucleate boiling. However, measurements and studies of nucleate boiling are often carried out at low pressure or with simulating fluids. High pressure measurements are rare because they are complex to set up and perform. A review of the literature has highlighted the lack of measurements for prototypical PWR conditions and justified the need of specific measurements at high pressure operating conditions.

In this work, we intended to design an experiment to measure the aforementioned parameters for the prototypical thermal hydraulic conditions of a PWR. A multi-step strategy has been proposed and implemented:

- In a first step, a review of existing models has been performed and has led to determine some orders of magnitude for the parameters of interest, *i.e.* the bubble size at detachment and the detachment frequency. These orders of magnitude have been used to design the future instrumentation. By showcasing the different existing models, this literature review also paves the way for future comparison and validation with high pressure data. The purpose of the high pressure tests is to check whether the models established at low pressure remain relevant at actual PWR conditions.
- Then, a thermal hydraulic facility has been designed according to the targeted thermal hydraulic conditions. This experimental rig aims to set the thermal hydraulic conditions at the boundaries of the test section where the measurements will be performed. This installation is currently being manufactured at CEA/Cadarache.
- The pre-design of the test section is an important part of this work. After a critical review of similar prototypes, several concepts and potential technical solutions have been studied. The major technological obstacles to overcome before building the test section have been identified.

- Special attention was paid in this work on infrared thermographic measurements. To determine the heating element and in particular its thickness, a model was developed to characterize the thermal behaviour of the heater. Its originality comes from that it takes into account for boiling process on the wetted side of the heater. Since the wetted temperature must be deduced from the dry temperature measurement, an inverse heat conduction problem was solved. It was finally shown that  $50\ \mu m$  thickness for the heater strongly limits the noise amplification due to the ill-posed problem without any regularisation method while ensuring satisfactory representativeness of an industrial surface.
- Some preliminary tests were carried out on an experimental device operating at atmospheric pressure. Those tests have clearly stated that regarding our measurements, shadowgraphy using bi-telecentric lens coupled with LED pannels was the best optical configuration. They also highlighted the impact of the liquid temperature gradient in the vicinity of the heated wall which induces an index gradient and causes distortions that can have a significant impact on near-wall measurements. A specific study to quantify this effect was performed and showed its impact is constant when boiling occurs and it should decrease with pressure.
- A first concept of an experimental setup to be tested in high pressure and high temperature conditions was developed. The first concept had three sapphire windows and a heated MACOR window to allow the shadowgraphic measurements selected during the preliminary test phase. Unfortunately, this prototype test section could not be operated, as one sapphire window and the MACOR porthole broke during assembly. A back-up plan was found with great urgency, to demonstrate the feasibility of high pressure measurements. Shadowgraphic measurements were unfortunately made impossible because of the design of this back-up test section. Nevertheless and despite non-optimal experimental conditions, some images demonstrating the feasability of such measurements were obtained for high pressure up to 120 bar.

## Prospects

Preliminary tests have demonstrated the feasibility of high pressure, high temperature measurements using a test section equipped with transparent sapphire windows. However, some points need to be improved before performing real and quantitative measurements.

- Firstly, since the feasibility of the measurements has been demonstrated, the whole test section must be re-manufactured. The missing sight glass must be replaced and the heating porthole, which has shown defects, must be improved. Once these repairs are performed, the test section will then be ready to carry out shadowgraphic measurements of the bubbles close to the heated wall and thus hopefully provide data on the diameter and frequency of detachment as well as dependence of flow regime on pressure.
- In parallel, work concerning IR thermography measurements still needs to be improved. The thickness of the heating plate has been fixed to allow a thermographic measurement. Nevertheless, technical solution to implement this heated plate still needs to be developed, in particular the assembly technique between the metallic plate and sapphire windows.

- Systematic measurements should allow to create a reliable and validated database regarding the targeted thermal hydraulic conditions. Several test campaigns are needed to establish credible data banks.

As far as the thermal study of the heater is concerned, this preliminary study can also be completed. Indeed, several aspects deserve to be taken into account, especially for the boundary conditions that are considered:

- Since the plate will be fixed on a sapphire window, the different layers of materials can modify the thermal behaviour of the wall (sapphire, brazing).
- For the development of the IR thermography measurement, a constant emissivity paint must be applied to the back of the plate, which can also impact on the thermal behaviour of the heater.
- More realistic boundary conditions on both sides of the heater can be applied. For example on the wetted side, determining the sensitivity to  $t_g$  and  $t_w$  could lead to improvements.

As mentioned before, IR measurements can prove to be an issue, the problem being that the IR camera does not only measure the radiative heat flux emitted by the heated plate (through the paint which is deposited on its back), but also that from the substrate over which the heater is fixed, as well as the close environment. The main difficulty is then to be able to determine the contribution only due to the heater. In order to predict this, an improvement to the thermal model developed in the present work could be performed by taking into account the coupling between the conduction within the heater and the radiative heat transfer. Another potential use of such a thermal model can be proposed. Usually, boiling flows are modelled using the well known two-fluid balance equations considering the heater as a boundary condition (through the heat flux partitioning model). Very few studies, up to our knowledge, consider coupling between the flow and the thermal behaviour of the heater ([122]). One intermediate approach could be to study the thermal behaviour of the heating plate<sup>1</sup> considering the flow in the vicinity of the wall as a realistic boundary condition. Our model can be seen as a basis for such development. In that sense, it is a continuation of models initially proposed by Bricard et al. [123] of Le Corre et al. [124], who focused on CHF modelling using a similar approach.

Another output of the present work is the confirmation that designing and implementing an experiment to study boiling flow at PWR operating conditions is far from easy. Much remains to be done in order to get the facility to an operating stage, and to obtain the desired measurements. Despite the fact that using a simulant fluid raises some questions about the transposition to steam/water conditions, it is our belief that this approach should not be ruled out. It can be an interesting compromise between:

- On the one hand an highly representative experiment performed for prototypical operating conditions (PWR) that is very complex to implement and achieve, and as a consequence is a source of big uncertainties (distortions due to refractive index gradients on the vicinity of the heated wall, coupled conductive and radiative model for IR measurements...),

---

<sup>1</sup>By solving the energy balance equation within the heated plate.

- On the other hand, an experiment whose representativeness could be discussed but which is simpler to implement. However, the use of simulant fluid is well admitted regarding CHF prediction. Furthermore, François [71] gave some elements that suggest a potential extension of those scaling laws to transpose quantities such as local void fraction. It then seems reasonable to assume that this validity extension could also be applied to physical mechanisms occurring in the vicinity of the heater.

The key is then to determine which is more impacting between the errors due to this assumption, and the uncertainties induced by the difficulty of making accurate measurements in steam/water flows.

# Bibliography

- [1] Shiro Nukiyama. The maximum and minimum values of the heat  $q$  transmitted from metal to boiling water under atmospheric pressure. *International Journal of Heat and Mass transfer*, 27, July 1984.
- [2] Jil Guéguen. *Contribution à la modélisation multidimensionnelle des écoulements bouillants convectifs en conduite haute pression pour l'application au cas des réacteurs à eau pressurisée*. phdthesis, Université de Grenoble, August 2006.
- [3] Michaël Montout. *Contribution au développement d'une Approche Prédictive Locale de la crise d'ébullition*. phdthesis, Université de Toulouse, January 2009.
- [4] Philippe March. *Caractérisation et modélisation de l'environnement thermohydraulique et chimique des gaines de combustible des réacteurs à eau sous pression en présence d'ébullition*. phdthesis, Aix Marseille Université, December 1999.
- [5] Jean-Marc Delhaye. *Thermohydraulique des réacteurs nucléaires*. Génie atomique. EDP sciences, 2008. ISBN 978-2-86883-823-0.
- [6] H. Cubizolles. *Etude stéréologique de l'évolution de la topologie des écoulements diphasiques à haute pression*. phdthesis, Ecole Centrale Lyon, January 1996.
- [7] Etienne Manon. *Contribution à l'analyse et à la modélisation locale des écoulements bouillants sous-saturés dans les conditions des Réacteurs à Eau sous Pression*. phdthesis, Ecole Centrale Paris, November 2000.
- [8] Fabrice François, Henda Djeridi, Stephane Barre, and Michel Klédy. Measurements of void fraction, liquid temperature and velocity under boiling two-phase flows using thermal-anemometry. *Nuclear Engineering and Design*, 381, September 2021.
- [9] Michel Klédy. *Développement d'une méthode de mesure du champ de vitesse et de température liquide en écoulement diphasique bouillant en conditions réacteurs ou simulantes*. phdthesis, Université de Grenoble, May 2018.
- [10] J.G. Collier and J.R. Thome. *Convective boiling and condensation*. Oxford science publication. Clarendon press oxford, 3rd ed edition, 1994.
- [11] Jean-Marc Delhaye. Transferts de chaleur : ébullition ou condensation des corps purs. *Physique énergétique*, January 1990. doi: 10.51257/a-v1-a1560. URL <https://www.techniques-ingénieur.fr/doi/10.51257/a/v1/a1560>.

- [12] N. Kurul and M.Z. Podowski. Multidimensional effects in forced convection subcooled boiling. *Proceeding of the 9th International heat Transfer Conference*, pages 19 – 24, 1990.
- [13] Robert Cole. Bubble frequencies and departure volumes at sub-atmospheric pressures. *AICHE Journal*, 13(4):779–783, July 1967. ISSN 0001-1541, 1547-5905. doi: 10.1002/aic.690130434. URL <https://onlinelibrary.wiley.com/doi/10.1002/aic.690130434>.
- [14] G. Kocamustafaogullari and M. Ishii. Interfacial area and nucleation site density in boiling systems. *International Journal of Heat and Mass Transfer*, 26(9):1377–1387, September 1983. ISSN 00179310. doi: 10.1016/S0017-9310(83)80069-6. URL <https://linkinghub.elsevier.com/retrieve/pii/S0017931083800696>.
- [15] H.C. Ünal. Maximum bubble diameter, maximum bubble-growth time and bubble-growth rate during the subcooled nucleate flow boiling of water up to 17.7 MN/m<sup>2</sup>. *International Journal of Heat and Mass Transfer*, 19(6):643–649, June 1976. ISSN 00179310. doi: 10.1016/0017-9310(76)90047-8. URL <https://linkinghub.elsevier.com/retrieve/pii/0017931076900478>.
- [16] Patrick Bricard. *Modélisation de l'ébullition sous-saturée et de la crise d'ébullition par caléfaction en convection forcée*. phdthesis, Ecole Centrale Paris, December 1995.
- [17] S. Levy. Forced convection subcooled boiling—prediction of vapor volumetric fraction. *International Journal of Heat and Mass Transfer*, 10(7):951–965, July 1967. ISSN 00179310. doi: 10.1016/0017-9310(67)90071-3. URL <https://linkinghub.elsevier.com/retrieve/pii/0017931067900713>.
- [18] H.C. Ünal. Determination of the initial point of net vapor generation in flow boiling systems. *International Journal of Heat and Mass Transfer*, 18(9):1095–1099, September 1975. ISSN 00179310. doi: 10.1016/0017-9310(75)90227-6. URL <https://linkinghub.elsevier.com/retrieve/pii/0017931075902276>.
- [19] Young Min Kwon and Soon Heung Chang. A mechanistic critical heat flux model for wide range of subcooled and low quality flow boiling. *Nuclear Engineering and Design*, 188(1):27–47, April 1999. ISSN 00295493. doi: 10.1016/S0029-5493(99)00025-4. URL <https://linkinghub.elsevier.com/retrieve/pii/S0029549399000254>.
- [20] Akira Inoue, Tatsuo Kurosu, Toshimasa Aoki, Makoto Yagi, Toru Mitsutake, and Shinichi Morooka. Void fraction distribution in BWR fuel assembly and evaluation of subchannel code. *J. Nucl. Sci. Technol.*, 32(7):12, 1995.
- [21] R. Sugrue and J. Buongiorno. A modified force-balance model for prediction of bubble departure diameter in subcooled flow boiling. *Nuclear Engineering and Design*, 305: 717–722, August 2016. ISSN 00295493. doi: 10.1016/j.nucengdes.2016.04.017. URL <https://linkinghub.elsevier.com/retrieve/pii/S0029549316300450>.
- [22] C.H. Lee and I. Mudawwar. A mechanistic critical heat flux model for subcooled flow boiling based on local bulk flow conditions. *International Journal of Multiphase Flow*, 14(6):711–728, November 1988. ISSN 03019322. doi: 10.1016/0301-9322(88)90070-5. URL <https://linkinghub.elsevier.com/retrieve/pii/0301932288900705>.

- [23] Robert Cole. A photographic study of pool boiling in the region of the critical heat flux. *AICHE Journal*, 6(4):533–538, December 1960. ISSN 0001-1541, 1547-5905. doi: 10.1002/aic.690060405. URL <https://onlinelibrary.wiley.com/doi/10.1002/aic.690060405>.
- [24] P Stephan and J Hammer. A new model for nucleate boiling heat transfer. *Heat and Mass Transfer*, 30(2):119–125, 1994.
- [25] D.C. Groeneveld, A. Ireland, J. Kaizer, and A. Vasic. An overview of measurements, data compilations and prediction methods for the critical heat flux in water-cooled tubes. *Nuclear Engineering and Design*, 331:211–221, May 2018. ISSN 00295493. doi: 10.1016/j.nucengdes.2018.02.031. URL <https://linkinghub.elsevier.com/retrieve/pii/S0029549318301961>.
- [26] Junping Gu, Qinggong Wang, Yuxin Wu, Junfu Lyu, Suhui Li, and Wei Yao. Modeling of subcooled boiling by extending the RPI wall boiling model to ultra-high pressure conditions. *Applied Thermal Engineering*, 124:571–584, September 2017. ISSN 13594311. doi: 10.1016/j.applthermaleng.2017.06.017. URL <https://linkinghub.elsevier.com/retrieve/pii/S1359431117318859>.
- [27] Junsoo Yoo, Carlos E. Estrada-Perez, and Yassin A. Hassan. An accurate wall temperature measurement using infrared thermometry with enhanced two-phase flow visualization in a convective boiling system. *International Journal of Thermal Sciences*, 90:248–266, April 2015. ISSN 12900729. doi: 10.1016/j.ijthermalsci.2014.12.007. URL <https://linkinghub.elsevier.com/retrieve/pii/S1290072914003524>.
- [28] E.R. Hosler. Flow patterns in high pressure two-phase (steam-water) flow with heat addition. In *9th National Heat Transfer Conference*, January 1967.
- [29] R.P. Roy, S. Kang, J.A. Zarate, and A. Laporta. Turbulent subcooled boiling flow - experiments and simulations. *Journal of heat transfer*, 124:73–93, Ferbruary 2002.
- [30] D J Euh, B Ozar, T Hibiki, and M Ishii. Measurement of bubble departure frequency in subcooled boiling flow using an image processing technique. In *NURETH-13*, page 12, 2009.
- [31] Byong-Jo Yun, Byoung-Uhn Bae, Dong-Jin Euh, and Chul-Hwa Song. Experimental investigation of local two-phase flow parameters of a subcooled boiling flow in an annulus. *Nuclear Engineering and Design*, 240(12):3956–3966, December 2010. ISSN 00295493. doi: 10.1016/j.nucengdes.2010.02.004. URL <https://linkinghub.elsevier.com/retrieve/pii/S0029549310001147>.
- [32] Z. Edelman and E. Elias. Void fraction distribution in low flow rate subcooled boiling. *Nuclear Engineering and Design*, 66(3):375–382, September 1981. ISSN 00295493. doi: 10.1016/0029-5493(81)90167-9. URL <https://linkinghub.elsevier.com/retrieve/pii/0029549381901679>.
- [33] Meng Lin and Peipei Chen. Photographic study of bubble behavior in subcooled flow boiling using r-134a at low pressure range. *Annals of Nuclear Energy*, 49:23–32, November 2012. ISSN 03064549. doi: 10.1016/j.anucene.2012.06.001. URL <https://linkinghub.elsevier.com/retrieve/pii/S0306454912001831>.

- [34] Michel Klédy, Fabrice Francois, Henda Djeridi, Stephane Barre, and Jean-Marc Delhaye. Toward a local drift flow model for high-pressure, subcooled, convective boiling flows. *International Journal of Heat and Mass Transfer*, 177, October 2021.
- [35] T.H. Lee, G.C. Park, and D.J. Lee. Local flow characteristics of subcooled boiling flow of water in a vertical concentric annulus. *International Journal of Multiphase Flow*, 28(8):1351–1368, August 2002. ISSN 03019322. doi: 10.1016/S0301-9322(02)00026-5. URL <https://linkinghub.elsevier.com/retrieve/pii/S0301932202000265>.
- [36] Valentin Scheiff. *Étude expérimentale et modélisation du transfert de chaleur de l'ébullition transitoire*. phdthesis, Université de Toulouse, December 2018.
- [37] C.E. Estrada-Perez and Y.A. Hassan. PTV experiments of subcooled boiling flow through a vertical rectangular channel. *International Journal of Multiphase Flow*, 36(9):691–706, September 2010. ISSN 03019322. doi: 10.1016/j.ijmultiphaseflow.2010.05.005. URL <https://linkinghub.elsevier.com/retrieve/pii/S0301932210000960>.
- [38] Dewen Yuan, Deqi Chen, Xiao Yan, Jianjun Xu, Qi Lu, and Yanping Huang. Bubble behavior and its contribution to heat transfer of subcooled flow boiling in a vertical rectangular channel. *Annals of Nuclear Energy*, 119:191–202, September 2018. ISSN 03064549. doi: 10.1016/j.anucene.2018.05.010. URL <https://linkinghub.elsevier.com/retrieve/pii/S0306454918302408>.
- [39] Nicolas Baudin. *Étude expérimentale et modélisation de l'ébullition transitoire*. phdthesis, Université de Toulouse, October 2015.
- [40] Ashutosh Yadav and Shantanu Roy. Axial and radial void fraction measurements in convective boiling flows. *Chemical Engineering Science*, 157:127–137, January 2017. ISSN 00092509. doi: 10.1016/j.ces.2016.04.038. URL <https://linkinghub.elsevier.com/retrieve/pii/S000925091630197X>.
- [41] Mathieu de Langlard, Hania Al-Saddik, Sophie Charton, Johan Debayle, and Fabrice Lamadie. An efficiency improved recognition algorithm for highly overlapping ellipses: Application to dense bubbly flows. *Pattern Recognition Letters*, 101:88–95, January 2018. ISSN 01678655. doi: 10.1016/j.patrec.2017.11.024. URL <https://linkinghub.elsevier.com/retrieve/pii/S0167865517304300>.
- [42] R. Situ, M. Ishii, T. Hibiki, J.Y. Tu, G.H. Yeoh, and M. Mori. Bubble departure frequency in forced convective subcooled boiling flow. *International Journal of Heat and Mass Transfer*, 51(25):6268–6282, December 2008. ISSN 00179310. doi: 10.1016/j.ijheatmasstransfer.2008.04.028. URL <https://linkinghub.elsevier.com/retrieve/pii/S0017931008002755>.
- [43] G. Dix. *Vapor void fraction for forced convection with subcooled boiling at low flow rates*. phdthesis, University of California, 1971.
- [44] Ingo Hapke, Hartwig Boye, and Jürgen Schmidt. Onset of nucleate boiling in minichannels. *International Journal of Thermal Sciences*, 39(4):505–513, 2000.

- [45] Zhiwei Jia Ooi, Vineet Kumar, Joseph L Bottini, and Caleb S Brooks. Experimental investigation of variability in bubble departure characteristics between nucleation sites in subcooled boiling flow. *International Journal of Heat and Mass Transfer*, 118:327–339, 2018.
- [46] R. Sémeria. La cinématographie ultra-rapide et l'ébullition à haute pression. *La Houille Blanche*, 49(6):679–686, October 1963. ISSN 0018-6368, 1958-5551. doi: 10.1051/lhb/1963048. URL <https://www.tandfonline.com/doi/full/10.1051/lhb/1963048>.
- [47] J Garnier, E. Manon, and H. Cubizolles. Local measurements on flow boiling of refrigerant 12 in a vertical tube. *Multiphase science and technology*, 13(111), 2001.
- [48] Yassin A. Hassan. Multi-scale full-field measurements and near-wall modeling of turbulent subcooled boiling flow using innovative experimental techniques. *Nuclear Engineering and Design*, 299:46–58, April 2016. ISSN 00295493. doi: 10.1016/j.nucengdes.2015.11.013. URL <https://linkinghub.elsevier.com/retrieve/pii/S0029549315005439>.
- [49] D. Maitra and K. Subba Raju. Vapour void fraction in subcooled flow boiling. *Nuclear Engineering and Design*, 32(1):20–28, April 1975. ISSN 00295493. doi: 10.1016/0029-5493(75)90087-4. URL <https://linkinghub.elsevier.com/retrieve/pii/0029549375900874>.
- [50] Fabrice Francois, Jean-Marc Delhaye, and Philippe Clement. The distribution parameter  $c_0$  in the drift flow modeling of forced convective flow. *Multiphase Science and Technology*, 23(1):77–100, 2011. ISSN 0276-1459. doi: 10.1615/MultScienTechn.v23.i1.40. URL <http://www.dl.begellhouse.com/journals/5af8c23d50e0a883,1890cf7e25bf629f,2ef0694d29>
- [51] Andrew Richenderfer, Artyom Kossolapov, Jee Hyun Seong, Giacomo Saccone, Etienne Demarly, Ravikishore Kommajosula, Emilio Baglietto, Jacopo Buongiorno, and Matteo Bucci. Investigation of subcooled flow boiling and CHF using high-resolution diagnostics. *Experimental Thermal and Fluid Science*, 99:35–58, December 2018. ISSN 08941777. doi: 10.1016/j.expthermflusci.2018.07.017. URL <https://linkinghub.elsevier.com/retrieve/pii/S089417771831255X>.
- [52] Michael D Bartel, Mamoru Ishii, Takayuki Masukawa, Ye Mi, and Rong Situ. Interfacial area measurements in subcooled flow boiling. *Nuclear Engineering and Design*, 210(1): 135–155, December 2001. ISSN 00295493. doi: 10.1016/S0029-5493(01)00415-0. URL <https://linkinghub.elsevier.com/retrieve/pii/S0029549301004150>.
- [53] Mehmet Arik and Avram Bar-Cohen. Effusivity-based correlation of surface property effects in pool boiling CHF of dielectric liquids. *International Journal of Heat and Mass Transfer*, 46(20):3755–3764, September 2003. ISSN 00179310. doi: 10.1016/S0017-9310(03)00215-1. URL <https://linkinghub.elsevier.com/retrieve/pii/S0017931003002151>.
- [54] D. Sarker, W. Ding, R. Franz, O. Varlamova, P. Kovats, K. Zähringer, and U. Hampel. Investigations on the effects of heater surface characteristics on the bubble waiting period during nucleate boiling at low

- subcooling. *Experimental Thermal and Fluid Science*, 101:76–86, January 2019. ISSN 08941777. doi: 10.1016/j.expthermflusci.2018.09.021. URL <https://linkinghub.elsevier.com/retrieve/pii/S0894177718310884>.
- [55] Chi-Yeh Han and Peter Griffith. The mechanism of heat transfer in nucleate pool boiling—part i. *International Journal of Heat and Mass Transfer*, 8(6):887–904, June 1965. ISSN 00179310. doi: 10.1016/0017-9310(65)90073-6. URL <https://linkinghub.elsevier.com/retrieve/pii/0017931065900736>.
- [56] Andrei Olekhnovitch. Diminution de la température de la paroi observée à proximité du flux de chaleur critique de type d'assèchement. *International Journal of Thermal Sciences*, 47(9):1158–1168, September 2008. ISSN 12900729. doi: 10.1016/j.ijthermalsci.2007.09.004. URL <https://linkinghub.elsevier.com/retrieve/pii/S1290072907002037>.
- [57] Roberta Visentini. *Étude expérimentale des transferts thermiques en ébullition transitoire*. phdthesis, Université de Toulouse, 2012.
- [58] R.P. Roy, V. Velindlada, S.P. Kalra, and P. Peturaud. Local measurements in the two-phase region of turbulent subcooled boiling flow. *Journal of Heat Transfer*, 116: 660–669, August 1994.
- [59] Rong Situ, Takashi Hibiki, Xiaodong Sun, Ye Mi, and Mamoru Ishii. Flow structure of subcooled boiling flow in an internally heated annulus. *International Journal of Heat and Mass Transfer*, 47(24):5351–5364, November 2004. ISSN 00179310. doi: 10.1016/j.ijheatmasstransfer.2004.06.035. URL <https://linkinghub.elsevier.com/retrieve/pii/S0017931004002790>.
- [60] R.P. Roy, V. Velindlada, and S.P. Kalra. Velocity field in turbulent subcooled boiling flow. *Journal of heat transfer*, 119:754–766, November 1997.
- [61] R. Sugrue, J. Buongiorno, and T. McKrell. An experimental study of bubble departure diameter in subcooled flow boiling including the effects of orientation angle, subcooling, mass flux, heat flux, and pressure. *Nuclear Engineering and Design*, 279: 182–188, November 2014. ISSN 00295493. doi: 10.1016/j.nucengdes.2014.08.009. URL <https://linkinghub.elsevier.com/retrieve/pii/S0029549314004646>.
- [62] B.J. Yun, B.U. Bae, D.J. Euh, G.C. Park, and C.-H. Song. Characteristics of the local bubble parameters of a subcooled boiling flow in an annulus. *Nuclear Engineering and Design*, 240(9):2295–2303, September 2010. ISSN 00295493. doi: 10.1016/j.nucengdes.2009.11.014. URL <https://linkinghub.elsevier.com/retrieve/pii/S0029549309005731>.
- [63] Valentin Scheiff, Nicolas Baudin, Pierre Ruyer, Julien Sebilleau, and Catherine Colin. Ébullition nucléée lors d'un transitoire de température. Technical report.
- [64] C.E. Estrada-Perez, Junsoo Yoo, and Yassin A. Hassan. Feasibility investigation of experimental visualization techniques to study subcooled boiling flow. *International Journal of Multiphase Flow*, 73:17–33, July 2015. ISSN 03019322. doi: 10.1016/j.ijmultiphaseflow.2015.02.017. URL <https://linkinghub.elsevier.com/retrieve/pii/S0301932215000440>.

- [65] Y.A. Hassan, C.E. Estrada-Perez, and Jun Soo Yoo. Measurement of sub-cooled flow boiling using particle tracking velocimetry and infrared thermographic technique. *Nuclear Engineering and Design*, 268:185–190, March 2014. ISSN 00295493. doi: 10.1016/j.nucengdes.2013.04.044. URL <https://linkinghub.elsevier.com/retrieve/pii/S0029549313004421>.
- [66] G.E. Thorncroft, J.F. Klausner, and R. Mei. An experimental investigation of bubble growth and detachment in vertical upflow and downflow boiling. *International Journal of Heat and Mass Transfer*, 41:3857–3871, 1998.
- [67] E.L. Bibeau and M. Salcudean. A study of bubble ebullition in forced-convective subcooled nucleate boiling at low pressure. *International Journal of Heat and Mass Transfer*, 37(15):2245–2259, October 1994. ISSN 00179310. doi: 10.1016/0017-9310(94)90367-0. URL <https://linkinghub.elsevier.com/retrieve/pii/0017931094903670>.
- [68] J.F. Klausner, R. Mei, D.M. Bernhard, and L.Z. Zeng. Vapor bubble departure in forced convection boiling. *International Journal of Heat and Mass Transfer*, 36(3):651–662, February 1993. ISSN 00179310. doi: 10.1016/0017-9310(93)80041-R. URL <https://linkinghub.elsevier.com/retrieve/pii/001793109380041R>.
- [69] In-Cheol Chu, Hee Cheon No, and Chul-Hwa Song. Bubble lift-off diameter and nucleation frequency in vertical subcooled boiling flow. *Journal of Nuclear Science and Technology*, 48(6):936–949, June 2011. ISSN 0022-3131, 1881-1248. doi: 10.1080/18811248.2011.9711780. URL <http://www.tandfonline.com/doi/abs/10.1080/18811248.2011.9711780>.
- [70] Junsoo Yoo, Carlos E. Estrada-Perez, and Yassin A. Hassan. Development of a mechanistic model for sliding bubbles growth prediction in subcooled boiling flow. *Applied Thermal Engineering*, 138:657–667, June 2018. ISSN 13594311. doi: 10.1016/j.applthermaleng.2018.04.096. URL <https://linkinghub.elsevier.com/retrieve/pii/S1359431117369727>.
- [71] Fabrice François. *Etude et caractérisation des écoulements diphasiques dans un réacteur à eau sous pression embarqué en similitude Fréon*. PhD thesis, Grenoble INPG, 2001.
- [72] Chaitanya R. Mali, V. Vinod, and Ashwin W. Patwardhan. Comparison of phase interaction models for high pressure subcooled boiling flow in long vertical tubes. *Nuclear Engineering and Design*, 324:337–359, December 2017. ISSN 00295493. doi: 10.1016/j.nucengdes.2017.09.010. URL <https://linkinghub.elsevier.com/retrieve/pii/S0029549317304508>.
- [73] O. Baker et al. Design of pipe lines for simultaneous oil and gas flow. *Oil Gas J*, 26 (13.6), 1954.
- [74] BK Kozlov. Types of flow of gas-liquid mixtures and stability boundaries in vertical tubes. *Zhur. Tekh. Fiz.*, 24, 1954.
- [75] ER Quandt. Measurement of some basic parameters in two-phase annular flow. *AICHE Journal*, 11(2):311–318, 1965.

- [76] Manon Bottin. Effect of surface state and fluid properties on critical heat flux - literature review and experiments. In *ICAPP 2019*, 2019.
- [77] Xiande Fang, Yuliang Yuan, Anyi Xu, Lu Tian, and Qi Wu. Review of correlations for subcooled flow boiling heat transfer and assessment of their applicability to water. *Fusion Engineering and Design*, 122:52–63, November 2017. ISSN 09203796. doi: 10.1016/j.fusengdes.2017.09.008. URL <https://linkinghub.elsevier.com/retrieve/pii/S0920379617308086>.
- [78] Tenglong Cong, Xindi Lv, Xiang Zhang, and Rui Zhang. Investigation on the effects of model uncertainties on subcooled boiling. *Annals of Nuclear Energy*, 121: 487–500, November 2018. ISSN 03064549. doi: 10.1016/j.anucene.2018.08.001. URL <https://linkinghub.elsevier.com/retrieve/pii/S0306454918304122>.
- [79] J.T. Rogers, M. Salcudean, Z. Abdulla, D. McLeod, and D. Poirier. The onset of significant void in up-flow boiling of water at low pressure and velocities. *International Journal of Heat and Mass Transfer*, 30(11):2247–2260, November 1987. ISSN 00179310. doi: 10.1016/0017-9310(87)90218-3. URL <https://linkinghub.elsevier.com/retrieve/pii/0017931087902183>.
- [80] FW Dittus and LMK Boelter. Heat transfer in automobile radiators of the tubular type. *International communications in heat and mass transfer*, 12(1):3–22, 1985.
- [81] Volker Gnielinski. Heat transfer coefficients for turbulent flow in concentric annular ducts. *Heat transfer engineering*, 30(6):431–436, 2009.
- [82] AE Bergles and WM Rohsenow. The determination of forced-convection surface-boiling heat transfer. *Journal of Heat Transfert*, pages 365–372, 1964.
- [83] E Jo Davis and GH Anderson. The incipience of nucleate boiling in forced convection flow. *AICHE Journal*, 12(4):774–780, 1966.
- [84] Walter Frost and Gerald S Dzakowic. Graphical estimation of nucleate boiling heat transfer. *Industrial & Engineering Chemistry Process Design and Development*, 6(3): 346–347, 1967.
- [85] Fred W Staub. The void fraction in subcooled boiling—prediction of the initial point of net vapor generation. *ASME*, 1968.
- [86] P. Saha and N. Zuber. Point of net vapor generation and vapor void fraction in sub-cooled boiling. In *5th International heat transfer conference*, volume 4, January 1974.
- [87] Novak Zuber. On the stability of boiling heat transfer. *Transactions of the American Society of Mechanical Engineers*, 80(3):711–714, 1958.
- [88] John H. Lienhard. *A heat transfer textbook*. Phlogiston Press, 3rd ed edition, 2001. ISBN 978-0-9713835-0-0.
- [89] Samson Semenovich Kutateladze. *Heat transfer in condensation and boiling*, volume 3770. US Atomic Energy Commission, Technical Information Service, 1959.

- [90] R.W. Bowring. Physical model, based on bubble detachment, and calculation of steam voidage in the sub cooled region of a heated channel. Technical Report HPR-10, HAL-TEN reactor project, December 1962.
- [91] Y. Katto. A prediction model of subcooled water flow boiling CHF for pressure in the range 0.1–20 MPa. *International Journal of Heat and Mass Transfer*, 35(5):1115–1123, May 1992. ISSN 00179310. doi: 10.1016/0017-9310(92)90172-O. URL <https://linkinghub.elsevier.com/retrieve/pii/0017931092901720>.
- [92] Y. Katto. A physical approach to critical heat flux of subcooled flow boiling in round tubes. *International Journal of Heat and Mass Transfer*, 33(4):611–620, April 1990. ISSN 00179310. doi: 10.1016/0017-9310(90)90160-V. URL <https://linkinghub.elsevier.com/retrieve/pii/001793109090160V>.
- [93] Y. Katto. Prediction of critical heat flux of subcooled flow boiling in round tubes. *International Journal of Heat and Mass Transfer*, 33(9):1921–1928, September 1990. ISSN 00179310. doi: 10.1016/0017-9310(90)90223-H. URL <https://linkinghub.elsevier.com/retrieve/pii/001793109090223H>.
- [94] RA DeBortoli. *Forced-convection heat transfer burnout studies for water in rectangular channels and round tubes at pressures above 500 psia*, volume 188. Bettis Plant, 1958.
- [95] David D Hall and Issam Mudawar. Critical heat flux (chf) for water flow in tubes—i. compilation and assessment of world chf data. *International Journal of Heat and Mass Transfer*, 43(14):2573–2604, 2000.
- [96] P. J. de Munk. Two-phase flow experiments in a 10m long sodium heated steam generator test section. In *International Meeting on Reactor Heat Transfer*, Karlsruhe, October 1973.
- [97] J. Borée. Ecoulements diphasiques eau-vapeur avec changement de phase. Technical Report 106, IMFT-Interface.
- [98] VI Tolubinsky and DM Kostanchuk. Vapour bubbles growth rate and heat transfer intensity at subcooled water boiling. In *International Heat Transfer Conference 4*, volume 23. Begel House Inc., 1970.
- [99] G. Kocamustafaogullari. Pressure dependence of bubble departure diameter for water. *International Communications in Heat and Mass Transfer*, 10(6):501–509, November 1983. ISSN 07351933. doi: 10.1016/0735-1933(83)90057-X. URL <https://linkinghub.elsevier.com/retrieve/pii/073519338390057X>.
- [100] H.J. Ivey. Relationships between bubble frequency, departure diameter and rise velocity in nucleate boiling. *International Journal of Heat and Mass Transfer*, 10(8):1023–1040, August 1967. ISSN 00179310. doi: 10.1016/0017-9310(67)90118-4. URL <https://linkinghub.elsevier.com/retrieve/pii/0017931067901184>.
- [101] Novak Zuber. *Hydrodynamic aspects of boiling heat transfer*. PhD thesis, University of California, 1959.

- [102] Ankur Miglani, Daniel Joo, Saptarshi Basu, and Ranganathan Kumar. Nucleation dynamics and pool boiling characteristics of high pressure refrigerant using thermochromic liquid crystals. *International Journal of Heat and Mass Transfer*, 60:188–200, 2013.
- [103] M Lemmert and JM Chawla. Influence of flow velocity on surface boiling heat transfer coefficient. *Heat Transfer in Boiling*, 237(247), 1977.
- [104] Eckhard Krepper, Bostjan Končar, and Yury Egorov. Cfd modelling of subcooled boiling—concept, validation and application to fuel assembly design. *Nuclear engineering and design*, 237(7):716–731, 2007.
- [105] Nilanjana Basu, Gopinath R Warrier, and Vijay K Dhir. Onset of nucleate boiling and active nucleation site density during subcooled flow boiling. *J. Heat Transfer*, 124(4):717–728, 2002.
- [106] SR Yang and RH Kim. A mathematical model of the pool boiling nucleation site density in terms of the surface characteristics. *International journal of heat and mass transfer*, 31(6):1127–1135, 1988.
- [107] Takashi Hibiki and Mamoru Ishii. Active nucleation site density in boiling systems. *International Journal of Heat and Mass Transfer*, 46(14):2587–2601, July 2003. ISSN 00179310. doi: 10.1016/S0017-9310(03)00031-0. URL <https://linkinghub.elsevier.com/retrieve/pii/S0017931003000310>.
- [108] Sai Raja Gopal Vadlamudi and Arun K. Nayak. CFD simulation of departure from nucleate boiling in vertical tubes under high pressure and high flow conditions. *Nuclear Engineering and Design*, 352:110150, October 2019. ISSN 00295493. doi: 10.1016/j.nucengdes.2019.110150. URL <https://linkinghub.elsevier.com/retrieve/pii/S002954931930161X>.
- [109] Stéphane Pujet. *Modélisation de l’écoulement autour d’une bulle de vapeur en formation sur une paroi chauffante en ébullition convective sous saturée*. phdthesis, Institut national polytechnique de Toulouse, October 1998.
- [110] Janani Srree Murallidharan, B.V.S.S.S. Prasad, B.S.V. Patnaik, G.F. Hewitt, and V. Badalassi. CFD investigation and assessment of wall heat flux partitioning model for the prediction of high pressure subcooled flow boiling. *International Journal of Heat and Mass Transfer*, 103:211–230, December 2016. ISSN 00179310. doi: 10.1016/j.ijheatmasstransfer.2016.06.050. URL <https://linkinghub.elsevier.com/retrieve/pii/S0017931016306925>.
- [111] Yves Cojan, Gilles Kervern, and Jean-Paul Pocholle. Propagation du rayonnement dans les matériaux. *Optique Photonique*, 1998-05. doi: 10.51257/a-v1-e4035. URL <https://www.techniques-ingénieur.fr/doi/10.51257/a/v1/e4035>.
- [112] Louise Bernadou, Fabrice François, Manon Bottin, Henda Djeridi, and Stephane Barre. Analytical study of the impact of thickness over thermal transfer in a plate with boiling flow. In *NURETH-19*, Brussels, Belgium, March 2022.

- [113] Louise Bernadou, Fabrice François, Manon Bottin, Henda Djeridi, and Stephane Barre. Toward the design of a representative heater for boiling flow characterization under PWR's prototypical thermalhydraulic conditions. *Applied Sciences*, 13(3):1534, January 2023. ISSN 2076-3417. doi: 10.3390/app13031534. URL <https://www.mdpi.com/2076-3417/13/3/1534>.
- [114] Y. Y. Hsu. On the size range of active nucleation cavities on a heating surface. *Journal of Heat Transfer*, 84(3), August 1962.
- [115] Zeyong Wang and Michael Z Podowski. A new mechanistic model of nucleation site density. *Transactions of the American Nuclear Society*, 116, 2017.
- [116] G.L. Lagier, H. Lemonnier, and N. Coutris. A numerical solution of the linear multidimensional unsteady inverse heat conduction problem with the boundary element method and the singular value decomposition. *International Journal of Thermal Sciences*, 43(2):145–155, February 2004. ISSN 12900729. doi: 10.1016/j.ijthermalsci.2003.06.002. URL <https://linkinghub.elsevier.com/retrieve/pii/S1290072903001339>.
- [117] Guy-Laurent Lagier. *Application de la méthode des éléments de frontière à la résolution du problème inverse de conduction de la chaleur multidimensionnel: régularisation par troncature de spectre*. phdthesis, Institut national polytechnique de Grenoble, November 1999.
- [118] Youngjoon Suh, Ramin Bostanabad, and Yoonjin Won. Deep learning predicts boiling heat transfer. *Scientific Reports*, 11(1):5622, March 2021. ISSN 2045-2322. doi: 10.1038/s41598-021-85150-4. URL <https://www.nature.com/articles/s41598-021-85150-4>.
- [119] Dominique Pajani. Thermographie - principes et mesure. *Contrôle non destructif*, March 2013. doi: 10.51257/a-v2-r2740. URL <https://www.techniques-ingenieur.fr/doi/10.51257/a/v2/r2740>.
- [120] T.H. Kim, E. Kommer, S Dessiatoum, and J. Kim. Measurement of twophase flow and heat transfer parameters using infrared thermometry. *International Journal of Multiphase Flow*, 40:56–67, 2012.
- [121] Matteo Bucci. A mechanistic IR calibration technique for boiling heat transfer investigations. *International Journal of Multiphase Flow*, page 13, 2016.
- [122] Zeyong Wang and Michael Z. Podowski. Analytical modeling of the effect of heater geometry on boiling heat transfer. *Nuclear Engineering and Design*, 344: 122–130, April 2019. ISSN 00295493. doi: 10.1016/j.nucengdes.2018.12.020. URL <https://linkinghub.elsevier.com/retrieve/pii/S0029549318309014>.
- [123] B. Bricard, P. Peturaud, and Jean-Marc Delhaye. Understanding and modelling dnb in forced convective boiling: Modelling of a mechanism based on nucleation site dryout. *Multiphase Science and Technology*, 9(4):329–379, 1997. ISSN 0276-1459.

- [124] Jean-Marie Le Corre, Shi-Chune Yao, and Cristina H. Amon. A mechanistic model of critical heat flux under subcooled flow boiling conditions for application to one- and three-dimensional computer codes. *Nuclear Engineering and Design*, 240(2):235–244, 2010. ISSN 0029-5493. doi: <https://doi.org/10.1016/j.nucengdes.2008.12.007>. URL <https://www.sciencedirect.com/science/article/pii/S0029549308006225>. Twelfth International Topical Meeting on Nuclear Reactor Thermal Hydraulics (NURETH-12).